Exploring the properties of hot haloes around simulated galaxies

Ashley James Kelly

Abstract: The existence of hot, accreted gaseous coronae around massive galaxies is a central prediction of galaxy formation models in the ΛCDM cosmology. While observations now confirm that extraplanar hot gas is present around late-type galaxies, the origin of the gas is uncertain. We investigate the origin and properties of the hot gas that surrounds galaxies in the cosmological hydrodynamical EAGLE simulations. In summary, we find that haloes of mass $\geq 10^{12}$ $M_{\odot}$ host hot, accreted atmospheres as predicted by White & Frenk (1991). However, supernovae heated gas (feedback) in the innermost region of the halo typically dominates the X-ray emission.

Modern hydrodynamical simulations model various physical processes in the real Universe; however, many are included using 'subgrid models'. Although subgrid models have successfully modelled feedback effects, it remains unclear if, and by how much, the differing implementations affect other halo properties. This thesis uses 'zoom-in' simulations of a Local Group-like region evolved with both the Auriga and Apostle galaxy formation models. We find that feedback processes can be classified into two broad categories: 'ejective' and 'preventative', and future observations may constrain these two regimes.

The large dynamic mass range makes it computationally expensive to run simulations of galaxy formation. Therefore, we explore the basis function expansion technique (BSE), which can efficiently approximate the potential of a simulated galactic halo. We demonstrate that the Herquinst-Ostriker BSE can successfully reproduce the orbits of particles taken from n-body simulations. We also describe two further developments, including the addition of a thin, time-dependent disc and a method to model massive satellite galaxies within the halo efficiently.

Exploring the properties of hot haloes around simulated galaxies

Ashley James Kelly

A thesis presented for the degree of
Doctor of Philosophy

Institute for Computational Cosmology
Department of Physics
Durham University
United Kingdom

July 2022

Dedicated to

Francis Logan

Contents

Declaration

The content presented in Chapter 3 has been published in:

Kelly, A. J., Jenkins, A., Frenk, C. S. *The origin of X-ray coronae around simulated disc galaxies.* MNRAS, **502**(2) (2021), 2934. 2005.12926.

The content presented in Chapter 4 has been published in:

Kelly, A. J., Jenkins, A., Deason, A., et al. *Apostle-Auriga: effects of different subgrid models on the baryon cycle around Milky Way-mass galaxies.* MNRAS, **514**(3) (2022), 3113. 2106.08618.

The author of the thesis was primarily responsible for all aspects of these publications. Other work completed over the course of the preparation of this thesis appears in:

Borrow, J., **Kelly, A. J.** *Projecting SPH Particles in Adaptive Environments* (2021). 2106.05281.

Grand, R. J. J., Marinacci, F., Pakmor, R., Simpson C. M., **Kelly, A. J.** et al. *Determining the full satellite population of a Milky Way-mass halo in a highly resolved cosmological hydrodynamic simulation.* MNRAS, **507**(4) (2021), 4953. 2105.04560.

Nightingale, J., Hayes, R., **Kelly, A. J.**, et al. *PyAutoLens: Open-Source Strong Gravitational Lensing.* The Journal of Open Source Software, **6**(58) (2021), 2825. 2106.01384.

Narayanan, D., Turk, M. J., Robitaille, T., **Kelly, A. J.**, et al. *POWDERDAY: Dust Radiative Transfer for Galaxy Simulations.* ApJS, **252**(1) (2021), 12. 2006.10757

The work in this thesis is based on research carried out in the Institute for Computational Cosmology, Department of Physics, Durham University, United Kingdom. No

part of this thesis has been submitted elsewhere for any other degree or qualification and it is all my own work unless referenced to the contrary in the text.

Acknowledgements

Kids from council estates in Manchester don't get to do PhDs without a large amount of help and an even larger amount of luck. While I don't know who to thank for my luck, there are many people I'd like to thank for their help.

My passion for learning and science didn't develop until I was already in sixth form, and I'm unsure what triggered it. It may have been Star Trek. I'm not sure; however, I know that it was cultivated by Dilip, Scott, Craig and Gill. These were the best teachers that I'd ever had, and fortunately, they arrived in my life at a time when I was ready to learn. I never planned to attend University, but following the excellent advice from my sixth form tutors, I applied to Durham, and my luck continued - I was accepted. I managed to enter a world that I never even knew existed. Fortunately, my luck and support didn't end there. Many more people helped me along this journey.

Firstly, Halim Kusumaatmaja and Chris Nixon, thank you for the faith and confidence you both placed in me. You gave me the chance to experience 'real' research for the first time, and I will never forget that. I'd also like to thank Richard Bower for sharing his enthusiasm for understanding the mysteries of the Universe. Richard's unbridled joy for 'pure' research is an inspiration.

I want to thank Josh Borrow for all the help he's given me, from preparing my initial PhD applications to sharing his inexhaustible knowledge of SPH and subgrid physics. Josh is also the reason that I was involved in both the `yt` project and Google Summer of Code, which have been career-defining experiences in my life. Thank you.

Thank you to everyone involved with Ustinov AFC over the past few years. Football

has been one of the great escapisms from the stress and pressures of a PhD. It's been a pleasure to play with you all, and being your club captain has been a real honour.

To my supervisors, Adrian and Carlos, I will always be immensely grateful for the opportunity that you both gave me. Carlos, thank you for the regular historic digressions about the cosmos and your motivating words; I always felt much more enthused and full of ideas after our meetings. Adrian, thank you for your availability, practicality, and mathematical wizardry. You make a fantastic pair. Thank you both for your continued support, even after I chose to leave academia.

Azi and Nicola, thank you both for being incredible scientists, answering my numerous questions, and going above and beyond to share your knowledge and expertise with me. I'd also like to thank you both for your care, kind and wise words, and continuous support. It was a pleasure having you both join my supervisor meetings; I only wish you'd joined them sooner.

Paolo, Tassos, Tom, Lee, Steve, Helen and everybody else in the Frostbite Physics team at Electronic Arts: thank you! Working with such a talented, motivated, and welcoming group of people solving exciting and challenging physics problems was inspirational. Thank you for creating such a dynamic, stimulating and supportive culture.

Mum, thank you for always giving me so much, even when you had so little. Thank you for your unconditional love and support and for being the guiding light through my darkest years. Dad, from the first day you came into my life, you inspired me. You introduced me to programming and taught me a lifetime's worth of knowledge in just a few years. Thank you for accepting me into your life. Thank you both from the bottom of my heart; I could not have achieved any of this without you.

Henna, it's hard to describe your impact on my life. You have taught me empathy and compassion, and you inspire me to be better and do better every single day. You bring happiness, joy and positivity into everything we do, transforming mundane tasks into some of the best moments of my life. Thank you for everything you've done and continue to do for me! I would not have completed this thesis without you.

Finally, to Aldo, thank you for the memories, for that is all we'll ever have.

This thesis was supported by the Science and Technology Facilities Council (STFC) consolidated grant ST/P000541/1 and an STFC studentship grant ST/S505365/1. This thesis used the DiRAC@Durham facility managed by the Institute for Computational Cosmology on behalf of the STFC DiRAC HPC Facility (www.dirac.ac.uk).

This thesis made use of the following software packages:

- Gadget (Springel, 2005)
- Arepo (Springel, 2010)
- `python` (Van Rossum & Drake, 2009), with the following libraries
  - `numpy` (van der Walt et al., 2011)
  - `scipy` (Jones et al., 2001)
  - `h5py` (Collette, 2013)
  - `matplotlib` (Hunter, 2007)
  - `numba` (Lam et al., 2015)
  - `mpi4py` (Dalcin et al., 2011)
  - `unyt` (Goldbaum et al., 2018)
  - `pyatomdb` (Foster et al., 2016)
  - `read_eagle` (The EAGLE team, 2017)

Chapter 1

Introduction

In the early twentieth century it was widely thought that all visible objects in the night sky belonged to the same single system, the Milky Way. This idea was favoured until the time of the *Great Debate*, where Harlow Shapley and Heber Curtis disputed the nature of the so-called 'spiral nebulae' (Shapley & Curtis, 1921). Shapley believed that distant spiral nebulae were much smaller, and lay within the outskirts of the Milky Way. While Curtis argued that these were large, separate systems, similar to that of the Milky Way but separated by almost a million parsecs. Later in the same decade, Edwin Hubble was able to convince most of the astronomical community that not only are there many other external galaxies in the Universe, but that the Universe is also, in fact, expanding (Hubble, 1926, 1929). This decade saw the birth of extragalactic astronomy and modern cosmology.

In most areas of science new ideas and models are developed and then must be tested through experimentation. However, we cannot set up and study various ensembles of the Universe in a laboratory, each with a different set of parameters. Instead, we must find alternative techniques to help test and develop models of the Universe. Recent increases in computing power have helped computer simulations to become one of the most commonly used tools. Computer simulations can model dynamic systems ranging from an individual atom up to a large volume of the Universe containing thousands of galaxies. Simulations take the initial state of a system and evolve it following the inputted model's rules. At various stages of evolution, the system's

properties can be outputted and compared with observations and measurements taken from a real system. The success of a model is generally measured by its ability to reproduce the statistical properties of the observed system. The last few decades have seen the emergence of an entire field that uses computer simulations to model the formation and evolution of a large number of galaxies over approximately 14 billion years of cosmic time (see Vogelsberger et al., 2020, and references therein).

This thesis will explore some of the most successful cosmological simulations developed. These simulations will be used to explore the gaseous environments surrounding galaxies, comparing results between different simulations and those inferred from the real Universe. This thesis will also examine a new simulation technique to study galactic haloes and discuss how it could be further developed to facilitate the most detailed simulations of galactic haloes.

This chapter will first introduce the standard model of Cosmology, ΛCDM, which describes the Universe's large-scale structure in Section 1.1. Section 1.2 will describe galaxy formation within the framework outlined by ΛCDM. Finally, Section 1.3 will outline some of the challenges with current models and state the research questions that the thesis will attempt to answer.

1.1 ΛCDM

Over the past century, there have been considerable advances in our understanding of the Universe. We now have a successful model of the Universe's evolution referred to as the ΛCDM model (Davis et al., 1985; Maddox et al., 1990; Efstathiou et al., 1990). This model describes the evolution of the Universe from an initial hot, dense, (almost) homogeneous state, often referred to as a 'cosmic soup', to the present day.

The ΛCDM model is made up of three main components baryonic matter, dark matter and dark energy. At the present day it is widely accepted that the energy density of the Universe is distributed as follows: baryonic matter contributes about $\sim 4\%$. Approximately, $\sim 26\%$ is in the form of a collision-less matter commonly

referred to as 'cold dark matter' (CDM), and the remaining $\sim 70\%$ is in the form of dark energy, Λ. There are also small contributions from neutrinos and radiation.

Zwicky (1933) showed that the galaxy velocity distribution in the Coma cluster required a total mass significantly exceeding that inferred from the baryonic mass alone. Smith (1936) also came to the same conclusion while performing a similar analysis of a larger sample of galaxies in the Virgo cluster. A modern analysis of the Coma cluster would account for the baryonic mass of both stars and X-ray emitting hot gas, the latter of which Zwicky neglected; however, this analysis would still conclude that the total cluster mass exceeds the baryonic mass. The evidence for a non-luminous matter, now referred to as dark matter, continued to grow throughout the following century.

Kahn & Woltjer (1959) analysed the kinematics of the Milky Way and Andromeda pair, referred to as the Local Group (LG). Kahn & Woltjer (1959) found that the approach velocity of Andromeda required a total LG mass of order $\sim 10^{12}$ $M_{\odot}$. This inferred LG mass is again much larger than can be accounted for by observable baryonic mass. This conclusion was further supported by measurements of the rotation curves of galaxies, which were found to be (approximately) flat out to large radii, rather than Keplerian (van de Hulst et al., 1957; Rubin & Ford, 1970; Roberts & Rots, 1973; Bosma, 1978; Rubin et al., 1980).

Arguably some of the most convincing evidence for dark matter came from constraints on the baryon energy density obtained from the abundance of light elements produced in Big Bang Nucleosynthesis (Alpher et al., 1948). Comparing the baryonic energy density to the total energy density of matter, which can be inferred from the observations of clusters, demonstrates that baryons make up only a small fraction of total matter in the Universe, thus confirming the presence of a non-baryonic matter component: dark matter.

The evidence for the dark energy comes from a (rare) type of supernova, Type Ia. These supernovae are rare as they involve white dwarf stars which are a late evolutionary stage of some stars, and therefore take a long time to form. The exact mechanism for Type Ia is uncertain; however, it is thought they occur in binary

systems where a small star (white dwarf) explodes after accreting material from a companion. While Type Ia supernovae are rare, the Universe is so large that there are of order $\sim 10^4$ detected and catalogued events in the open supernovae catalogue (Guillochon et al., 2017). Type Ia SNe are particularly interesting as they appear to act as standardisable candles. This means observations of their luminosity profile can be used to measure their distance from the Milky Way. Type Ia supernovae in external galaxies are consistently found to be much fainter than expected in a matter-dominated universe. Thus, requiring that the expansion of the Universe is accelerating, and supporting the existence of dark energy (Riess et al., 1998; Perlmutter et al., 1999).

It is challenging to account for all of the baryons in the Universe. Stars are the most luminous, and therefore most readily detectible, baryonic component. However, stars only contribute of $\sim 7\%$ of the total matter density (Fukugita & Peebles, 2004). The lack of stars leads to two questions: firstly, where are the remaining baryons? Secondly, what prevents the Universe from producing more stars from baryons? These questions motivate the exploration of the theory of galaxy formation.

1.2 Galaxy formation

In the framework of ΛCDM galaxies, groups and clusters are seeded in the early Universe in the form of quantum fluctuations in at early times. As the Universe undergoes a period of rapid inflation, these fluctuations expand into larger over (and under) densities.

The over and under densities continue to grow as the Universe expands. As the Universe expands, it also cools, allowing baryons to decouple from radiation and collapse into the overdensities of dark matter. Once regions of overdensity have grown sufficiently, reaching a critical density, they can turn around from the expansion of the Universe and collapse to form matter haloes. These haloes continue to grow by accreting material from their local environment and continuously merging, hierarchically, with other haloes.

In the early galaxy formation models of White & Rees (1978) and White & Frenk (1991), gas is accreted from the intergalactic medium (IGM) and falls into dark matter potentials. The behaviour of the gas during infall depends on the depth of the potential well, which determines the so-called 'cooling radius' of the halo. The 'cooling radius' is the radius at which the cooling time of the gas is equal to either the dynamical time of the halo or the Hubble time.

In high mass haloes, the cooling radius is smaller than the virial radius and lies deep inside the halo. In these haloes, it is predicted that infalling gas will shock-heat to the virial temperature of the halo and form a hot, quasi-hydrostatic atmosphere of gas (Larson 1974; the idea of an extended, hot gas corona around the Milky Way was first suggested by Spitzer 1956). This hot halo of gas is pressure-supported and will contract towards the centre; as this contraction occurs, the density in the centre of the halo will increase, allowing the cooling time to decrease.

In low mass dark matter haloes, where the cooling radius is much larger than the virial radius, it is thought that all of the accreting gas is cold and does not shock heat. In the event the gas does shock heat, it will likely cool rapidly due to efficient radiative cooling at temperatures $\sim 10^4 - 10^5$ K. The cold gas can then be rapidly accreted onto the central galaxy on timescales comparable to the free-fall time of the halo.

Rees & Ostriker (1977) predict that the transition mass between haloes cooling so efficiently that they collapse at the free-fall rate, and haloes forming quasi-static hot atmospheres of gas is approximately $\sim 10^{12}$ $M_\odot$, similar to that of the Milky Way. This is a prediction that can be tested, as haloes of mass $\geq 10^{12}$ $M_\odot$, should be enveloped in X-ray emission, as they have virial temperatures exceeding a million Kelvin.

In both low and high mass haloes, gas towards the centre of the halo will cool. As the gas cools, it loses pressure support and flows towards the centre of the potential well. The galactic haloes are seeded with a small amount of angular momentum as a result of tidal torques from inhomogeneities in the surrounding matter distribution (Hoyle, 1949; Barnes & Efstathiou, 1987). As the haloes collapse, this angular momentum

is conserved, thus increasing the rotation velocity in the centre of the halo. This collapse continues until a gaseous disc forms with a sufficiently high rotation velocity to prevent further collapse.

In the parts of the galactic disc, the cooling gas will become self-gravitating and collapse under its own gravity. The collapsing gas is able to cool, and collapse further, eventually forming giant molecular clouds (GMCs), which are the sites of star formation in galaxies.

In the picture of galaxy formation presented above, which describes the condensation of baryons into dark matter haloes, was first explored by White & Rees (1978) and White & Frenk (1991). However, in these initial models, gas cooling and star formation are too efficient in low mass galaxies. Consequently, these models produced too many faint galaxies; this is sometimes referred to as the 'overcooling problem'.

The 'overcooling problem' in low mass haloes can be addressed by including an efficient injection of energy from stellar winds and supernova (SN) explosions, a process now commonly referred to as 'feedback'. Stellar feedback can efficiently suppress star formation (SF) by ejecting dense, star-forming gas, generating turbulence that disrupts star-forming regions and driving outflows that eject gas from the interstellar medium (ISM) in the form of a 'hot galactic wind' (Mathews & Baker, 1971; Larson, 1974). Efficient feedback can prevent the excessive gas cooling at high redshift and thus reduce the number of faint galaxies predicted by the model (White & Rees, 1978; White & Frenk, 1991; Pearce et al., 1999; Sommer-Larsen et al., 1999; Thacker & Couchman, 2001).

While the introduction of SNe was able to reduce the number of faint galaxies, the models still produced too many massive galaxies. To correctly produce the correct number of a large galaxies a mechanism by which cooling could be suppressed in the most massive haloes is also required. This is because, in massive haloes, the gas ejected by SNe feedback can cool and re-accrete onto the galaxy, fueling further star formation, on short timescales. Massive haloes, therefore, require a much stronger feedback mechanism.

In the early twentieth century, an unusual class of objects was discovered and termed

'quasars' Fath (1909); Seyfert (1943). Optical observations of these objects showed unusual spectra with broad emission lines at unfamiliar wavelengths. It was later discovered that one of these quasars resides at a redshift of 0.158 (Schmidt, 1963). This discovery established that quasars must be extremely powerful apparent luminosity and distant from the MW. Salpeter (1964) and Lynden-Bell (1969) suggested that the accretion of gas onto extremely massive objects of small sizes, such as supermassive blackholes (SMBHs), could power quasars. Kormendy & Richstone (1995) later found evidence of SMBHs in the centres of many nearby galaxies (Salpeter, 1964; Zel'dovich, 1964; Lynden-Bell, 1969, 1978; Lynden-Bell & Rees, 1971; Rees, 1984). It is now widely accepted that SMBHs power quasars and are referred to as active galactic nuclei (AGN).

Further work by Magorrian et al. (1998) found a tight empirical relationship between the stellar bulge mass of a galaxy and the mass of the SMBH. This relation implies co-evolution between the galaxy and the SMBH, in which the AGN feedback can affect the galactic growth and evolution (Silk & Rees, 1998; King, 2003). Efficient feedback from supernovae SNe and AGN is now a key ingredient of modern galaxy formation models.

It is unclear how the feedback processes from AGN and SNe impact the hot atmospheres, which White & Rees (1978) and White & Frenk (1991) predicted to reside around high mass haloes. It is largely accepted that most haloes of mass $\geq 10^{13}$ $M_{\odot}$, do host quasi-hydrostatic haloes of accreted gas from the IGM. However, the evidence for these atmospheres is less convincing for haloes closer to the transition mass between hot and cold accretion, such as the one around our Milky Way.

1.3 This thesis

In this thesis, we will explore the gaseous atmospheres that surround galaxies. There are two main reasons that gaining a deeper understanding of the gaseous atmospheres is crucial to the future of astronomy. The first is that hot atmospheres are of great cosmological interest. In a ΛCDM universe, hot atmospheres are a fundamental

prediction, and in the absence of feedback processes (such as AGN and SNe), it is simple to infer the total mass of a halo from the measured X-ray luminosity of the hot gas that surrounds it. While the Universe does contain feedback processes, which complicate the picture, it may still be possible to 'weigh' haloes using their coronal X-ray luminosity. The second reason is that hot atmospheres surrounding spiral galaxies provide the primary fuel for ongoing star formation. These hot haloes are also the stage where hot feedback-driven winds mix with the accreting pristine gas from the IGM. Therefore gaining a better understanding of the properties of the hot atmospheres will also provide insight into star formation, cosmological gas accretion and the properties of the galactic winds and processes that drive them.

In Chapter 3 we investigate the origin and X-ray properties of these hot haloes that surround galaxies of halo mass, $10^{11} - 10^{14}$ $M_{\odot}$, in the highly-successful cosmological hydrodynamical EAGLE simulations (Schaye et al., 2015). We aim to identify whether the X-ray emission surrounding these galaxies is due to accreted and shock heated quasi-hydrostatic atmospheres predicted by White & Rees (1978) and White & Frenk (1991), or due to hot super-heated winds produced by feedback processes within the galaxy as claimed by Li & Wang (2013b). We will also explore the so-called 'missing feedback' problem introduced by Wang (2010) which is the apparent low X-ray luminosities observed from low-mass galaxies with high star-formation rates.

In Chapter 4 we will explore the robustness of our conclusions in Chapter 3 by comparing the similarities and differences between the properties and origins of hot atmospheres around MW-mass galaxies in two different simulations, Apostle and Auriga. These are both 'zoom-in' hydrodynamic simulations with the same initial conditions that produce realistic MW-like galaxies at present-day using different subgrid models.

Chapters 3 and 4 demonstrate that hot haloes are ubiquitous around haloes of MW-mass and above. The hot haloes contain a rich interplay of infalling accreting material and hot, feedback-driven outflows. We are interested in how infalling satellite galaxies fit into this picture and how they interact with the gaseous atmosphere.

While self-consistent simulations of all aspects of the galaxy formation picture in full generality are desirable, the calculations are costly. In the case of modern hydrodynamical galaxy simulations of an individual halo, the evolution of the central galaxy dominates the calculation cost. Thus, attempting to study the infall of satellites into a massive halo would result in only a tiny fraction of the compute resources being spent on the objects of interest.

In Chapter 5 we recapitulate a method of approximating the potential of a simulated galactic halo using a basis function expansion technique (Lowing et al., 2011). The basis function expansion of the potential can be used to evolve the infall of satellite galaxies into more massive haloes. We then discuss a range of developments to the method, including adding a thin, time-dependent galactic disc and several corrections. We then perform some experiments using an isolated MW-mass halo, selected from the original Auriga sample, as a test case. Finally, we discuss possible future applications of the method, such as combining the basis function expansion of the potential with a hydrodynamical approximation of the primary halo to investigate the complete hydrodynamical evolution of the infalling satellites into massive haloes.

In this thesis we aim to answer the three broad questions:

I) Do large volume, state-of-the-art cosmological simulations produce hot, accreted haloes around MW-mass haloes and above, as predicted by White & Rees (1978)?

II) Do different galaxy formation simulations, using different subgrid models, produce the same baryon cycle around galaxies?

III) Are there viable computational methods to study the infall of high-resolution low-mass galaxies into higher mass haloes?

We address these three questions in Chapters 3, 4 and 5, respectively.

Chapter 2

Cosmological Hydrodynamical Simulations: Eagle, Apostle and Auriga

Galaxy formation is an incredibly challenging problem to understand as it is an intrinsically interdisciplinary problem involving many processes, spanning a large range of physical scales. Some of the earliest cosmological simulations only included dark matter acting under the influence of gravity (Frenk et al., 1988; Springel, 2005), using methods still readily used today. These dark matter only simulations do not track the evolution and formation of galaxies; they only study the formation and growth of dark matter haloes. Therefore, semi-analytic models were introduced to populate dark matter simulations with galaxies. These models use a range of simplifying assumptions and are added retroactively to the dark matter simulations. Semi-analytic models have successfully reproduced a range of observational constraints from the local Universe (Cole, 1991; White & Frenk, 1991; Lacey & Silk, 1991; Somerville & Primack, 1999; Cole et al., 2000; Lacey et al., 2016).

Over the last few decades, the increase in computing power and resources facilitated the further development of galaxy formation simulations utilising advanced hydrodynamical techniques (Hernquist & Katz, 1989; Springel & Hernquist, 2002; Springel,

2005; Kravtsov et al., 1998; Teyssier, 2002; Springel, 2005, 2010; Bryan et al., 2014; Hopkins, 2015). Modern cosmological galaxy formation simulations combine hydrodynamical fluid solvers alongside 'subgrid' baryonic models to include the effects of complex physics such as cooling, star formation and evolution, feedback and black hole evolution. Subgrid models are required to model processes that occur on scales around, or below, the mass resolution of the simulations, which is typically between $\approx 10^3$ M$_\odot$ $- 10^7$ M$_\odot$.

In this thesis we start by studying the large volume cosmological simulation suite Eagle (Schaye et al., 2015; Crain et al., 2015) in Chapter 3. In Chapter 4 we focus our attention to pairs of MW-mass galaxies which are simulated with two different simulation models. We use both the Auriga galaxy formation model (Grand et al., 2017) (with the Arepo code) and a modified version of the Eagle galaxy formation model (with the Gadget-3 code) to study the same set of initial conditions. These initial conditions are zoom regions identified in the DOVE volume (Sawala et al., 2016; Fattahi et al., 2016) as they reproduce a pair of MW-mass halos analagous to the Local Group. In this thesis we refer to these simulations of the LG analogues as Auriga and Apostle. These two suites of simulations are run with the exact same initial conditions, but use different subgrid models and hydrodynamical solvers. The Auriga simulations in this thesis should not be confused with those in (Grand et al., 2017) which use the same simulation code, and galaxy formation model, to simulate a sample of isolated MW-mass galaxies.

This chapter will discuss a few of the main components of cosmological hydrodynamical simulations used in this work: Auriga (Grand et al., 2017), Apostle (Sawala et al., 2016; Fattahi et al., 2016) and Eagle (Schaye et al., 2015). In this chapter the Apostle and Eagle simulations' implementation can be considered the same. The implementation of Apostle and Eagle only differs by one parameter in the subgrid model and the resolution of the mass elements. These differences are, however, important when considering the conclusions of Chapter 4 where their implications are discussed.

In Section 2.1 we will briefly introduce the two types of cosmological initial conditions

Table 2.1: The cosmological parameters used in this thesis: Ω_m, Ω_b, and Ω_Λ are the average densities of matter, baryonic matter and dark energy in units of the critical density at redshift zero; σ_8 is the square root of the linear variance of the matter distribution when smoothed with a top-hat filter of radius 8 Mpc/h, n_s is the scalar power-law index of the power spectrum of primordial adiabatic perturbations, and h is the Hubble parameter in units of 100 $\mathrm{kms}^{-1}\mathrm{Mpc}^{-1}$.

Simulation name	Ω_m	Ω_b	Ω_Λ	σ_8	n_s	h
Eagle	0.307	0.04825	0.693	0.8288	0.9611	0.6777
Auriga & Apostle	0.272	0.0455	0.728	0.81	0.967	0.704

used in this work, both large volume and 'zoom in' regions. The following sections, Section 2.2 and Section 2.3, will introduce the gravitational problems which must be solved in these simulations and the two main types of hydrodynamical techniques used in this thesis. Section 2.4 will describe subgrid models which are employed to model the baryon physics required for galaxy formation, motivated in Section 1.2.

2.1 Initial Conditions

The first element of the initial conditions is the background cosmology, which defines the composition and primordial power spectrum of the modelled Universe. The primordial power spectrum, at the end of inflation, is generally taken to be a simple power-law defined by the scalar spectral index, n_s. At early times, the density fluctuations, and power spectrum, can be evolved using either linear theory (LT), second-order (2LPT) (Peebles, 1980) or third-order (3LPT) (Michaux et al., 2021) Lagrangian perturbation theory. However, once the amplitude of the fluctuations becomes comparable to the mean matter density, their evolution becomes strongly non-linear and perturbation theory is no longer accurate. When the fluctuations become non-linear, they can no longer be accurately evolved with either of these methods. At which point, it is common to generate a particle distribution with the power spectrum before the non-linear regime, which can evolve to the present using n-body techniques. In general, the initial conditions usually evolve to redshift, $z = 127$, using LT, 2LPT or 3LPT, at which time a particle distribution is created. The ΛCDM model is used for the Auriga, Apostle and Eagle simulations;

however, the choice of model parameters can differ slightly. They are tabulated in Table 2.1. The cosmological parameters of the original AURIGA simulations (Grand et al., 2017), such as the one used in Chapter 5, are the same as those used in the EAGLE simulations shown in Table 2.1.

There are two types of initial conditions used in this thesis, large volume and zoom initial conditions. The large volume initial conditions are uniformly sampled with typical sizes of these ranging from $5 - 300$ Mpc. Zoom in initial conditions combine a low-resolution background volume with a much higher resolution of interest. The high-resolution region of interest is usually centred around a galaxy at the present day, but it is possible to study more extended regions which contain many galaxies.

The EAGLE simulations used in this thesis simulate various large volume, periodic, cubic boxes of side-length 25 Mpc, 50 Mpc and 100 Mpc. The AURIGA, and APOSTLE, simulations in this work use constrained 'zoom in' initial conditions which match some of the mass and kinematic constraints of the Local Group, the Milky Way and Andromeda (see Sawala et al., 2016). The zoom technique allows much more detailed analyses to be performed; however, the results must be interpreted cautiously as they are not necessarily representative of the Universe as a whole.

2.2 Gravity

The gravitational force at a point in a mass distribution can be calculated by solving Poisson's equation. The most direct method for this is to perform an n-body calculation, summing the interactions of every mass element with every other mass element. This is a method which dates back to some early work of Holmberg (1941), which used light bulbs, where the candle power is proportional to mass, to represent mass elements. Lights can effectively be used to represent mass, as the intensity of light reduces with distance squared like the force of gravity. Holmberg modelled some early nebulae each made up of 37 lightbulbs and used a photocell (light sensitive resistor) to estimate the gravitational force on each bulb and integrate them through

time. The work of Holmberg (1941) is probably the earliest example of an n-body gravity simulation of astronomical phenomena.

In modern n-body simulations of gravity direct summation of all mass elements is usually avoided as it has an $O(n^2)$ computational complexity, making it too expensive for large n (where n is the number of mass elements). Modern-day simulations use approximate numerical methods to reduce the computational complexity of the n-body problem. Two of most common algorithms are the octree method (Barnes & Hut, 1986; Barnes & Efstathiou, 1987) and the particle-mesh method (Hockney & Eastwood, 1981). The octree method splits the simulation volume into smaller cells, recursively, to a specified resolution level. The top level cell includes the entire mass of the simulation, this has eight child cells of equal size and so on. The gravity calculation walks the tree starting with the top node and continuously refines the mass distribution until the force calculation is considered accurate enough. This allows the gravitational forces on a particle of distance regions to be computed in much fewer calculations. The computational complexity of this method is $O(n \log n)$. In the particle-mesh method, mass elements are scattered onto a mesh in 3D space using the cloud-in-cell (CIC) method (Hockney & Eastwood, 1981) to generate a density field. The gravitational potential can then be calculated by transforming the density field into Fourier Space and performing some linear operations. The gravitational potential can then be transformed back into real space, and differentiated to calculate the gravitational force on at the mesh points. The forces can then be interpolated, using the same interpolated technique, at the positions of each of the mass elements in the simulation.

All of the simulations considered in this thesis are based on the GADGET-3 code (last described in Springel et al., 2008) which uses a hybrid of the octree and particle-mesh methods. For shorter-range interactions the octree is used, and conversely the particle-mesh method is used for longer-range interactions.

2.3 Hydrodynamical Solvers

There are two main types of numerical methods for following the evolution of fluid flow, these are Eulerian and Lagrangian. Eulerian methods discretise a fixed volume of fluid and model the fluid properties at points on the regular mesh. The locations of the mesh cell are fixed in the Eulierian scheme. Conversely in Lagrangian schemes the fluid is divided into mass elements, typically referred to as particles, which store the fluid properties. In a Lagrangian scheme, the movement of the mass elements is explicitly tied to the fluid flow. There are many advantages and disadvantages to both methods. In the context of cosmological simulations the main advantages of the Langrangian scheme are that the local resolution of the simulation follows the mass flow, meaning that higher density regions are naturally resolved by more mass elements. It also advantageous to treat the fluid as particles, as this allows the fluid to easily be gravitationally coupled to the dark matter component, which is also generally modelled with particles. Conversely, the Eulerian technique is implicitly better at capturing shocks and instabilities, a common occurrence in galaxy formation.

The Eagle simulations used in this thesis use the Gadget-3 solver which uses a Lagrangian technique, namely smoothed particle hydrodynamics (SPH). In SPH, fluid elements are represented by particles about which their mass is distributed according to a kernel function. The Eagle simulations use the Hopkins (2013) formulation of pressure-entropy SPH, which defines the thermodynamic state of particles in terms of pressure and entropy and ensures that pressure varies smoothly across discontinuities. SPH is non-diffusive, therefore to model the mixing of different phases of gas and the transfer of heat between particles it implements the thermal conduction switch of Price (2008) and it also includes artificial viscosity following Cullen & Dehnen (2010) in order to capture shocks. This combination of numerical methods are generally known as ANARCHY (Schaye et al., 2015).

The Auriga simulations use Arepo which employs a semi-Lagrangian scheme. In the Arepo hydrodynamic solver the fluid is followed in an unstructured mesh con-

structed from a Voronoi tessellation of a set of mesh-generating points which then allow a finite-volume discretisation of the magneto-hydrodynamic equations. The mesh generating points can move with the fluid flow. Mesh simulations typically use a Riemann solver method to calculate the cell fluxes of all of the conserved quantities of the fluid. This moving mesh property reduces the flux between cells, thus reducing the advection errors that afflict fixed mesh codes. The use of the mesh eliminates the need for artificial viscosity to capture shocks, as is used in most SPH codes (including EAGLE).

2.4 Subgrid models

Hydrodynamical simulations of galaxy formation must model of processes such as gas cooling, star formation, supernovae and AGN feedback as discussed in Section 1.2. However, many of these processes occur on length and mass scales that are much lower can be resolved by modern simulations. For example, in the EAGLE simulations the mass of a baryonic element is of order $\sim 10^6$ $M_\odot$, thus it is not possible to include a complete, resolved model of stars (like the Sun) with masses that are a million times smaller than this. Therefore, these physics processes are included in the simulations via the inclusion of a sub-resolution model, which attempts to faithfully model the effects of these processes on much larger scales. Subgrid models are often based on analytical predictions, physical arguments or empirical laws obtained from observations. The subgrid models used in this thesis have a variety of free parameters which can be tuned to reproduce some properties of the real Universe.

Both the AURIGA and EAGLE galaxy formation models include a variety of sub-resolution baryonic physics relevant to galaxy formation such as radiative gas cooling (Wiersma et al., 2009), star formation (Schaye & Dalla Vecchia, 2008), metal enrichment (Wiersma et al., 2009), black-hole seeding, active galactic nuclei (AGN) feedback (Springel, 2005; Rosas-Guevara et al., 2015) and feedback from stellar evolution (Dalla Vecchia & Schaye, 2012). The subgrid physics model has several parameters which can be tuned to reproduce a subset of present-day observational

properties such as the stellar mass function, the size distribution of disc galaxies and the relationship between galaxy stellar mass and central black hole mass. It is important to note that, in general, the gas properties of the simulations are not tuned to match any observations and, as a result they are genuine predictions of the galaxy formation models. This section will describe three of the most important sub-resolution baryonic physics: gas cooling in Section 2.4.1, star formation and SNe feedback in Section 2.4.2 and finally, blackhole seeding, growth and AGN feedback in Section 2.4.3.

2.4.1 Cooling

Gas cooling is arguably the most important process in the formation of galaxies. As outlined in Section 1.2, gas which falls into massive dark matter halos must cool to form galaxies in the centre. Gas cooling is where gas dissipates its energy via radiative cooling.

The radiaitve cooling in most hydrodynamical gas simulations uses look up tables to go from gas with particular temperature and metallicity to a cooling rate. This use of look up tables significantly reduces the computational expense of performing these calculations on the fly. The radiative cooling in both Eagle and Auriga uses the publicly available CLOUDY model (Ferland et al., 2013), which includes both primordial and metal line cooling in the temperature range $10^4 - 10^8$ K. The contributions to cooling of 11 elements (H, He, C, N, O, Ne, Mg, Si, S, Ca and Fe) are tabulated as a function of hydrogen number density, temperature and redshift (Wiersma et al., 2009). The abundance of the 11 elements important to cooling are self-consistently evolved through the simulations, and are injected into the gas via metal enrichment from stellar evolution and supernovae. While Auriga also tracks the abundance of each element most important in cooling, the implementation of cooling is not undertaken on an element-by-element basis. This is because there is little difference in relative abundances from solar abundances, thus the computational overhead is not worthwhile. Instead, the metal-line cooling rates are based on the

rates of gas with solar composition and scaled linear with the metallicity of the gas. See Vogelsberger et al. (2013) for more detail on the cooling in Auriga.

In both simulations the cooling tables assume the gas is an optically thin plasma in collisional ionisation equilibrium. The cooling rates also assume the gas is photoionised and include a simple time-varying UV/X-ray background from galaxies and quasars. Eagle and Auriga use different UV/X-ray background models, but for the MW-mass galaxies studied in Chapter 4 the differences are not important.

2.4.2 Stellar formation and feedback

The prescription for energy injection from SNe feedback is critically important as SNe can deposit large amounts of thermal and kinetic energy into the gas immediately surrounding the galaxy. Observations show that the energy feedback from SNe can heat the gas to temperatures, $T \geq 10^7$ K, which is hot enough to contribute to the X-ray luminosity within the galactic halo (Strickland & Heckman, 2007). Observations suggest that this hot gas is also able to drive winds via conversion of thermal to kinetic energy, which can propagate to large radii enriching and heating material (Rupke, 2018). As it is not currently possible to resolve individual stars or SNe within large volume cosmological simulations; instead, a single stellar particle of mass, $\approx 10^6$ $M_\odot$, represents a population of stars. The simulations then require a prescription for energy deposition and metal enrichment from each star particle onto the surrounding gas which is tuned in order to reproduce a variety of observed galaxy properties.

Traditionally, hydrodynamical simulation codes have injected the energy from SNe events within a single stellar population (SSP), represented by a star particle, over a large mass of gas (Schaye & Dalla Vecchia, 2008; Creasey et al., 2011; Keller et al., 2014). For a standard stellar initial mass function (IMF) there is ≈ 1 supernova per 100 $M_\odot$ of initial stellar mass. Assuming the energy from SNe within this SSP is injected into a mass of gas equal to the initial stellar mass formed leads to high initial temperatures for the gas, $T \geq 10^7$ K. In the case where the same amount of energy

is distributed over a much larger mass of gas, the temperature increase experienced by the gas will be much lower, which reduces the cooling time. If the cooling time is significantly shorter than the sound-crossing time of the gas, the energy injection is no longer able to drive winds efficiently. Schaye & Dalla Vecchia (2008) showed that in this case, simulations are unable to reproduce observed star-formation rates and stellar masses of galaxies. There are several different SNe energy injection techniques that have been used to address this 'over-cooling' problem, including injecting energy in kinetic form, depositing the energy thermally while disabling radiative cooling for a short period and dumping the energy both thermally and kinetically (e.g. Navarro & White, 1993; Hernquist & Springel, 2003; Schaye & Dalla Vecchia, 2008).

In the Apostle simulations all the SNe energy from an SSP is injected in the form of thermal energy (Schaye et al., 2015). Rather than distributing the energy evenly over all of the neighbouring gas particles, the energy is injected into a small number of neighbours *stochastically* (Dalla Vecchia & Schaye, 2012). This method allows the energy per unit mass, which corresponds to the temperature change of a gas particle, to be defined. In these simulations each gas particle heated by SN feedback is always subject to the same temperature increase, $\Delta T_{\rm SN} = 10^{7.5}$ K.

The SNe feedback scheme in the Auriga simulations consists of an initially decoupled wind whose main free parameters are the energy available per unit mass of SNII and the wind velocity. The wind velocity scales with the 1-dimensional velocity dispersion of local dark matter particles. Qualitatively, SNe winds are modelled by 'wind particles' which are launched in an isotropic random direction carrying mass, energy, momentum and metals. Upon launch, the wind particles are decoupled from hydrodynamic forces and experience only gravity. The wind particles can recouple either when they reach a region of low-density gas (5% of the star-formation density threshold) or when they exceed a maximum travel time (0.025 of the Hubble time at launch). When the wind recouples, it deposits energy, momentum and metals into the gas cells it intersects.

2.4.3 Black holes and AGN feedback

The formation and growth of black holes is still very uncertain. Furthermore, the detailed evolution of their accretion discs occurs on mass and length scales well below the resolution of cosmological simulations. Therefore, these processes must also be treated with subgrid prescriptions. In both the EAGLE and AURIGA simulations black hole (BH) seeds are placed at the centre of Friends of Friends (FoF) groups with a mass greater than a critical value that do not already contain a BH. The rate of gas accretion by BHs is modelled using the local gas density, velocity and angular momentum, along with the mass of the BH. Both simulations apply techniques to ensure the BH remains at the centre of the halo as the resolution of the simulations are not sufficient to accurately resolve the dynamical friction. As the black holes accrete mass they are able to build up a reservoir of energy which can then be injected into the surrounding gas in form of AGN feedback.

In EAGLE as the BH accretes gas, it accumulates a reservoir of energy equal to the energy of the gas mass accreted multiplied by the radiative efficiency, which is taken to be 10%. When the BH has stored sufficient energy, it can stochastically increase the temperature of some of the neighbouring gas particles by a temperature of $\Delta T_{\rm AGN}$. In the standard EAGLE simulations, the surrounding gas particles are subject to a temperature change of $\Delta T_{\rm AGN} = 10^{8.5}$ K; however this can be varied. A lower temperature change means particles are heated more often, a (higher) temperature change, less often. As the change in temperature is fixed, the black holes must build up a sufficient amount of energy before they can inject energy.

The black holes in AURIGA model the feedback from the AGN to the surrounding gas with two modes, a quasar- and a radio-mode. As in EAGLE the energy injection rate from AGN feedback is proportional to the mass of gas accreted, but the feedback is injected in two modes. Feedback associated with the quasar mode is injected via a thermal energy increase, heating gas cells neighbouring the BH. In the radio mode, feedback stochastically heats bubbles of gas at randomly placed locations, with probability following an inverse square distance profile in the range of $(0.15-1)$ of the virial radius, around the black hole. The bubbles are a fixed size relative to

the virial radius of the halo. The AGN model used in the APOSTLE simulations in this work differs slightly from the reference model in Schaye et al. (2015). Namely, in this work the AGN model uses a viscosity which is hundred times lower than the reference model this reduces the accretion rate and growth of the black holes. This model is referred to as 'ViscLo' in Crain et al. (2015). In Section 4.9 we discuss the impacts of the different AGN models on our results.

2.5 Calculating mock observables

Cosmological hydrodynamical galaxy simulations generate an abundance of data which can be explicitly extracted and analysed. However, it is very difficult to compare some of these properties with the real Universe as they not directly observable. Instead, a powerful method is to generate mock observables directly from the simulations. We describe the calculation of X-ray emission Section 2.5.1, ion column densities in Section 2.5.2 and finally the dispersion measure (DM) in Section 2.5.3.

2.5.1 Computing the X-ray emission

The X-ray emission of galactic gas coronae is calculated in post-processing. The X-ray luminosity of each gas particle is calculated independently using the precomputed lookup tables from the Astrophysical Plasma Emission Code APEC 3.0.1 data (Smith et al., 2001; Foster et al., 2012). The data assumes that the gas is an optically thin plasma in collisional ionisation equilibrium. The total cooling rate is computed for individual elements as a function of photon energy. The total cooling rate per element is computed by integrating over a given range of photon energies, $0.5 - 2.0$ keV. We then calculate the total cooling rate by summing the overall contribution of each element,

$$\Lambda_{\rm X} = \sum_i X_i \Lambda_{{\rm X},i} \ , \tag{2.5.1}$$

where X_i is the ratio of the element abundance in the gas relative to the solar abundance, $\Lambda_{\mathrm{X},i}$ is the cooling rate of the gas in the X-ray band, $0.5 - 2.0$ keV (hereafter, soft X-ray), assuming solar abundances, and Λ_{X} is the total soft X-ray luminosity. We use the solar abundances of Anders & Grevesse (1989) to normalise the abundances in our simulations.

The summation in Eq. 2.5.1 is performed over nine elements: hydrogen, helium, carbon, nitrogen, oxygen, neon, magnesium, silicon and iron, which are independently tracked within the simulation. The total X-ray luminosity from the hot halo is the sum of the X-ray emission of all the particles within a given spatial region. This X-ray calculation does not include contributions from non-gaseous X-ray sources within galaxies, e.g. X-ray binaries. The effect of these sources is discussed when comparing to suitable datasets.

We calculate the projected coronal soft X-ray luminosity around a galaxy in the following way. We select all gas particles within a sphere of radius, R_{200}, centred on the centre-of-mass of the halo. The total X-ray emission is then calculated by summing the X-ray emission from all the gas particles within a 2D annulus through the sphere.

The APEC software, used to generate the X-ray luminosity emission tables, was not used to generate the emission tables used for calculating cooling rates within the simulations; instead, the simulations used tables generated by CLOUDY. This use of two different emission tables can lead to an error in the computations of X-ray luminosities. For example, if the APEC emission tables predict higher emissivity than CLOUDY, then the X-ray luminosity will be overpredicted since a self-consistent simulation using the APEC cooling tables would have less gas at the same density and temperature due to the faster cooling. This effect is not important for gas with long cooling times, but it may be significant for gas with shorter cooling times. We expect this to be a small effect in this work as the X-ray emission is dominated by hotter, slower cooling gas $\approx 10^6$ K.

In Fig. 2.1 we plot the cooling function from all ions assuming primordial abundance as well as metallicities $Z_\odot$, $0.1Z_\odot$ (Anders & Grevesse, 1989), as a function of tem-

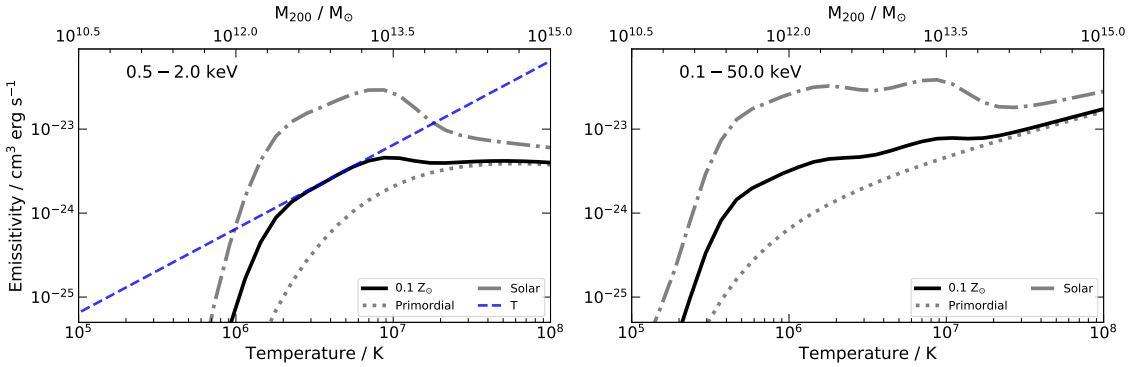

Figure 2.1: The black-solid, grey-dashed and grey-dotted lines show the cooling function in the $(0.5-2.0)$ keV (left) and $(0.1-50)$ keV (right) band from all ions, assuming a metallicity of $0.1Z_{\odot}$, $Z_{\odot}$ and the primordial value (Anders & Grevesse, 1989), as a function of temperature using the AtomDB v3.0.1 code. The approximation, $\Lambda \propto T$, to the soft X-ray cooling function is shown by the dashed-blue line for $Z = 0.1Z_{\odot}$.

perature using the AtomDB (v3.0.1) in the two energy bands $(0.1 - 50)$ keV and $(0.5-2.0)$ keV. We also show an approximation to the total soft X-ray cooling function for $Z = 0.1Z_{\odot}$. In general, we find that the behaviour of the cooling function in the $(0.5-2.0)$ keV energy band can be well described by a simple power law relation $\Lambda \propto T$ for $T \approx (10^6 - 10^7)$ K and $\Lambda = \text{const}$ for $T \approx (10^7 - 10^8)$ K.

These approximations do not adequately capture the rapid increase in the cooling function at a temperature of $T \approx 10^6$ K. They also do not appropriately model the flattening of the soft X-ray cooling function at temperatures above 10^7 K, which is due to a significant fraction of the photons having energies outside the selected range. In general, these inadequacies have little impact in the halo mass range, $10^{12}-10^{13.5}$ $M_{\odot}$, in which we apply these approximations. The right panel of Fig. 2.1 shows that a power law can describe well the cooling function in the $(0.1 - 50)$ keV band over an even broader range of halo mass; however, there is limited observational data in that energy band.

A variety of observational estimates of the metallicity of gaseous coronae have yielded values of $Z \approx 0.1Z_{\odot}$. This is consistent with the hot halo gas metallicity we find in the EAGLE simulations and in previous hydrodynamic simulations (e.g. Crain et al., 2010). It may be seen in Fig. 2.1 that the slope of the cooling function is largely independent of the metallicity which, however, has a larger effect on the

normalisation. Therefore the metallicity of the gaseous corona is unimportant, as long as it does not vary significantly with halo mass.

2.5.2 Ion number densities

We calculate column densities of several ionised species following Wijers et al. (2019). The total number of ions, N_{X_i}, of each species in a given mass of gas is given by,

$$N_{X_i} = \frac{m_X f_{X_i}}{m_Z}, \tag{2.5.2}$$

where m_X is the total mass of element X, f_{X_i} is the ionization fraction of the i^{th} ion, m_Z is the mass of an atom of element X and Z is the atomic number of the ionized element.

We calculate the ionisation fraction of each species using the lookup tables of Hummels et al. (2017). These are computed under the assumption of collisional ionisation equilibrium (CIE). They only consider radiation from the metagalactic UV background according to the model of Haardt & Madau (2012) in which the radiation field is only a function of redshift. The lookup tables are generated from a series of single-zone simulations with the photoionisation code, CLOUDY (Ferland et al., 2013) and the method used for the "grackle" chemistry and cooling library (Smith et al., 2016). The ion fractions are tabulated as a function of log temperature, log atomic hydrogen number density and redshift.

In both APOSTLE and AURIGA the masses of some elements are tracked within the code; these are hydrogen, helium, carbon, nitrogen, oxygen, neon, magnesium, silicon and iron. We calculate the number of species of each element from Eq. 2.5.2 with the total mass of each element as tracked by the code, and the calculated mass fraction of each species state. We can then make 2-dimensional column density maps of each species by smoothing the contribution from each gas particle onto a 2D grid with a two-dimensional SPH smoothing kernel. We make these 2D maps by projecting through each of the x, y and z axis. We then separate the 2D maps, which cover a region of (8×8) R_{200}, into 100 annuli with linearly spaced radii. In each annulus,

we have many lines-of-sight through the halo. We then take the column density at radius, r, to be the median column density calculated within the annulus that encloses the radius, r, for all three projected maps. We choose to use the median as it is more representative of a single random line-of-sight through a halo in the real universe. However, the mean value, which is often significantly higher, is also of interest as observed values can be biased by the detection thresholds of instruments.

Apostle and Auriga use different yield tables when calculating the fraction of different elements returned from SNIa to the ISM. These yield tables typically differ by $< 20\%$ for the species considered in this work. However, these difference are negligible in the results presented in Section 4.8.1, which span many orders of magnitude. It is possible to normalise these yield fractions in post-processing, but we choose to use the simulation tracked quantities are they are self-consistent with the gas cooling.

2.5.3 The dispersion measure

Fast radio bursts (FRBs) are bright pulses of radio emission with periods of order milliseconds, typically originating from extragalactic sources (see review by Cordes & Chatterjee, 2019). The first FRB, which was reported by Lorimer et al. (2007), was found in archival data from the 64 m Parkes radio telescope. By 2019, there were over 80 distinct FRB sources reported in the literature (see review by Petroff, 2017). In the next few years, these FRB catalogues will grow by orders of magnitude with current and future surveys detecting thousands of events per year (Connor et al., 2016).

As radiation from an FRB propagates through the intervening gas, the free electrons in the gas retard the radiation. As the retardation of the radiation is frequency dependent, this process disperses the FRB pulse, thus producing a measurable time delay between the highest and lowest radio frequencies of the pulse. The dispersion measure quantifies this time delay. The dispersion measure, from observations of the

photon arrival time as a function of frequency, is given by,

$$\int (1+z)\ n_e\ dr\ , \tag{2.5.3}$$

which provides an integral constraint on the free electron density, n_e, along the line-of-sight from the observer to the source, where dr is the path length in comoving coordinates. The free electron density and the radiation path in Eq. 2.5.3 are also in comoving units. The dispersion measure will include contributions from free electrons in the IGM (Zheng et al., 2014; Shull & Danforth, 2018), our galaxy, the Local Group, the galaxy hosting the FRB and baryons residing in other galactic haloes which intersect the sightline (McQuinn, 2014). As such, FRBs provide a possible way to investigate the presence of baryons that are difficult to observe with other methods.

In hydrodynamical simulations, we can calculate contributions to the dispersion measure from both the ISM and the hot halo of MW-like galaxies, and investigate the model dependence. The electron column density can be calculated for sightlines in a similar way to that described in Section 4.8.1 below. We calculate the number of free electrons for each gaseous particle or cell in the simulations by computing the number density of H II, He II and He III, which dominate the total electron density; these calculations again utilise the ion fraction lookup tables of Hummels et al. (2017).

Chapter 3

Origin of simulated X-ray coronae

3.1 Introduction

Several methods can be used to probe the hot gas surrounding galaxies, such as observations of the thermal Sunyaev-Zel'dovich (SZ) effect (Sunyaev & Zeldovich, 1970; Vanderlinde et al., 2010; Planck Collaboration et al., 2013; Anderson et al., 2015) and X-ray emission, on which we focus in this work. In the analytic model of White & Frenk (1991) the typical temperature of the gaseous atmosphere is $T > 10^6$ K in a halo of mass, 10^{12} $M_\odot$. Therefore, the atmosphere radiates as it cools through line-emission and continuum, with significant emission in the soft X-ray energy band, $0.5 - 2.0$ keV (see Putman et al., 2012, for a recent review).

The first attempts to detect soft X-ray emission from hot, gaseous, coronae around nearby, late-type galaxies were made with the *ROSAT* X-ray satellite, but no convincing evidence for it was found (Benson et al., 2000). These observations instead provided upper limits for the X-ray luminosity of the coronae, which were almost two orders of magnitude lower than the analytical predictions of White & Frenk (1991). The origin of the overestimate can be traced back to the assumption in that paper that the gas has an isothermal density profile whereas, as found by Crain et al. (2010) in the GIMIC cosmological hydrodynamics simulations, the gas is more diffuse due to the removal of low entropy gas by star formation and, most importantly

on galactic scales, energy injection from supernovae

Advances in X-ray detector sensitivity in the *XMM-Newton* and *Chandra* telescopes led to the first detections of diffuse X-ray emission around nearby, late-type galaxies (Strickland et al., 2004; Wang et al., 2005; Tüllmann et al., 2006; Li et al., 2007; Owen & Warwick, 2009; Sun et al., 2009). While detections of diffuse, X-ray coronae are now commonplace, a variety of studies have found that they appear as thick discs (Strickland et al., 2004), trace galactic outflows of Hα (Tüllmann et al., 2006), and have total luminosities that correlate strongly, and positively, with the recent star-formation rate (Li & Wang, 2013b). Highly star-forming galaxies, such as M82, also exhibit filamentary X-ray structures above, and below, the galactic plane (Strickland et al., 2004; Li & Wang, 2013a). These observations and inferred correlations suggest that the dominant source of the X-ray emission around local disc galaxies is gas heated by supernovae (SNe) feedback[1], rather than gas cooling from an accreted quasi-hydrostatic atmosphere. This interpretation, however, is in conflict with more recent deep *XMM-Newton* observations of NGC 6753 (Bogdán et al., 2017), NGC 1961 (Anderson et al., 2016) and NGC 891 (Hodges-Kluck et al., 2018). These data provide compelling evidence for the existence of hot, low-metallicity atmospheres of gas that are consistent with accretion from the IGM and subsequent shock-heating to the virial temperature of the halo. Nevertheless, the source of X-ray emission around late-type galaxies, like the Milky Way (MW) and M31, remains controversial.

A further important unknown is the mass fraction in hot atmospheres. In galaxy clusters, the halos are almost 'baryonically closed' (White et al., 1993; Vikhlinin et al., 2006; Pratt et al., 2009; Lin et al., 2012), such that their baryon-to-dark-matter mass ratios within the virial radius are approximately equal to the mean cosmic ratio, $f_b = \rho_b/\rho_m$, where ρ_b and ρ_m are the baryonic and total matter density of the universe, respectively. This ratio is taken to be 0.157 (Planck Collaboration et al., 2013). However, the baryon fractions of halos around L^* galaxies, appear to be much lower than this and thus a significant fraction of the baryons appear to be

[1]We follow the incorrect, but now common usage of the word "feedback" to refer to the energy emitted by supernovae or by AGN.

'missing' from the haloes (Bregman et al., 2018). In this chapter we also study the gas fraction of halos, $f_{\rm gas}$, which we define as the ratio of the mass of hot gas to halo mass, normalised by the mean cosmic baryon fraction, f_b. Galaxy halos also contain cold and warm, which is detectable in absorption studies of galaxies (Tumlinson et al., 2017), however in the halo mass range we focus on, hot gas dominates the total baryonic mass.

In this chapter, we use the large volume, cosmological hydrodynamical simulation suite EAGLE (Schaye et al., 2015; Crain et al., 2015; McAlpine et al., 2016) to probe the origin, mass and X-ray properties of the hot gaseous atmospheres surrounding present-day disc galaxies. We use the simulations to investigate the relative contributions of the accreted shocked-heated gas and winds heated by feedback to the X-ray luminosity, $L_{\rm X}$, of hot gas atmospheres. We then compare the soft X-ray scaling relations $L_{\rm X} - M_{\rm vir}$ and $L_{\rm X} - M_{\rm star}$ for a large sample of simulated disc galaxies with observational data over a wide range of halo masses, $(10^{11} - 10^{15})$ $\rm M_{\odot}$. We further examine the effect of the varying gas fraction of halos on the slope and the normalisation of the $L_{\rm X} - M_{\rm vir}$ relation.

The EAGLE simulations have previously been shown to reproduce a wide range of observations of real galaxies, such as low-redshift hydrogen abundances (Lagos et al., 2015; Bahé et al., 2016), evolution of galaxy stellar masses (Furlong et al., 2015) and sizes (Furlong et al., 2017), star-formation rates and colours (Trayford et al., 2015, 2017) along with black hole masses and AGN luminosities (Rosas-Guevara et al., 2016).

The chapter is structured as follows. In Section 3.2 we discuss the simulations, the selection of our simulated disc galaxy sample, and present analytic predictions for the $L_{\rm X}-M_{\rm vir}$ relation. In Section 3.3 we perform a baryon census of the EAGLE reference simulation. We then investigate the origin of the X-ray emission in Section 3.4.1 and attempt to understand how this depends on both the spatial region around the galaxy and the halo mass. In Section 3.4.4 we compare the results of the simulations to a range of observational data. We further investigate the effects of AGN feedback on the X-ray and gas properties of halos by comparing simulations with differing

AGN models. In Section 3.4.2 we investigate the $L_{\rm X} - M_{\rm vir}$ scaling relations in the EAGLE simulations and compare them to our analytical predictions. In Section 3.5 we discuss how to infer the gas fractions of halos from the measured $L_{\rm X} - M_{\rm vir}$ relation. Section 3.6 we introduce the "missing feedback" problem and use high cadence simulation outputs to identify the physical origin in the simulations, before concluding in Section 3.7.

3.2 Methods and background

3.2.1 Numerical simulations

We make use of the large volume cosmological hydrodynamical simulations, EAGLE (Evolution and Assembly of GaLaxies and their Environments, Schaye et al., 2015; Crain et al., 2015; McAlpine et al., 2016), to follow the evolution of galaxies and their gaseous atmospheres. The EAGLE simulations adopt a ΛCDM cosmology with the parameters of Planck Collaboration et al. (2013) listed in Table 1 of Schaye et al. (2015). The EAGLE simulations used in this thesis are briefly described in Chapter 2, and a more detailed description can be found in Schaye et al. (2015).

In this work, we use several of the EAGLE simulations, described in Table 3.1. We focus on the largest volume simulation, Ref-L100N1504, which uses the EAGLE reference subgrid physics model. This simulation is of a periodic cube of side length 100 cMpc, populated with $N = 1504^3$ collisionless dark matter particles and an equal number of baryonic particles. The impact of AGN feedback is investigated by using two variants of the reference simulation. In the NoAGN simulation the AGN feedback has been disabled, whereas, in the AGNdT9 simulation, the AGN feedback has been modified such that each feedback event leads to a temperature change of $\Delta T_{\rm AGN} = 10^9$ K. The remainder of the physical parameters, including mass resolution, remain the same. Further details of these different EAGLE simulations may be found in Crain et al. (2015).

Name units	N	Mass $M_\odot$	Box Size cMpc	Δ T_{AGN} K
Ref-L100N1504	1504^3	1.81×10^6	100	$10^{8.5}$
NoAGN-L050N0752	752^3	1.81×10^6	50	-
AGNdT9-L050N0752	752^3	1.81×10^6	50	$10^{9.0}$

Table 3.1: Parameters of the EAGLE simulations analysed in this work. The columns are the name of the simulation, the number of dark matter particles (which is initially equal to the number of gas particles), initial gas particle mass, the length of the side of the box, and the temperature change induced by AGN feedback, if AGN feedback is enabled. The runs are named such that the prefix, e.g., 'Ref' refers to the subgrid physics parameters followed by *LXXXNYYYY* where *XXX* is the side-length of the cube in Mpc and $YYYY^3$ is the number of dark matter particles.

3.2.2 Halo and galaxy identification

In this section we describe the procedure to identify galaxies in the EAGLE simulations at redshift, $z = 0$. We also describe the morphological criteria that we employ to select only galaxies with significant disc components.

Dark matter halos are identified using a Friends-of-Friends (FoF) algorithm with a linking length of 0.2 times the mean dark matter interparticle separation (Davis et al., 1985). The gas, stars and BHs are associated with the FoF group of their nearest dark matter particle if it belongs to a FoF group. The constituent self-bound substructures (subhalos) within a FoF group are identified using the SUBFIND algorithm applied to both dark matter and baryonic particles (Springel et al., 2001; Dolag et al., 2009).

In this work we focus on *centrals*, which are the central galaxies in a dark matter halo. These are identified as the most massive individual subhalos with a centre of mass lying within a 20 proper kpc (pkpc) radius of the centre-of-mass of the host FoF group. If no such subhalo exists within the FoF group, we discard the halo. We further require that galaxies be subhalos containing at least 500 star particles, in order to ensure we have a large sample of star particles to use for morphological classification.

We compute the spherical overdensity mass (Lacey & Cole, 1994) of each FoF halo

about the deepest particle within the potential of the halo. We define the halo radius to be the spherical radius within which the mean enclosed density is Δ times the critical density of the universe, ρ_c. We generally adopt $\Delta = 200$ to define virial quantities but we also use $\Delta = 500$ in some analyses to allow a more appropriate comparison to the observational data of Anderson et al. (2016).

3.2.3 Morphological and isolation selection

We characterise the morphology of galaxies by means of the $\kappa_{\rm rot}$ parameter introduced by Sales et al. (2012). The parameter is defined as,

$$\kappa_{\rm rot} = \frac{1}{K} \sum \frac{1}{2} m \left(\frac{j_{i,z}}{R_i} \right)^2 , \tag{3.2.1}$$

where K is the total kinetic energy of the stellar particles, m is the mass of each stellar particle, $j_{i,z}$ is the z-component of the specific angular momentum, R_i is the 2D projected radius from the z-axis and the sum is performed over all stellar particles within the galaxy. The galaxy is oriented such that the total angular momentum of all stellar particles within the galaxy lies along the z-axis. We consider all stellar particles within a spherical radius of 30 pkpc around the most bound stellar particle to be associated with the galaxy. In general $\kappa_{\rm rot} \approx 1$ for discs with perfect circular motions, whereas $\kappa_{\rm rot} \approx 1/3$ for non-rotating systems. A visual inspection of the stellar projections, both edge- and face-on, of galaxies in Sales et al. (2012) suggests that $\kappa_{\rm rot} \geq 0.50$ corresponds to galaxies that exhibit clear disc morphology.

We also apply an isolation criterion to the sample of disc galaxies analysed. We only select galaxies in halos which do not intersect a sphere of radius, $3R_{200}$, spanned by any of their neighbouring halos. These galaxies are undesirable as their X-ray emission is often dominated by the hot gas associated with their (more) massive neighbours.

We can increase the stringency of the disc criterion by increasing the required threshold value of $\kappa_{\rm rot}$, but in this work, we define disc galaxies to be those with $\kappa_{\rm rot} \geq 0.50$; this results in a sample of $\approx$ 5000 disc galaxies in the fiducial simulation, Ref-

L100N1504. Increasing $\kappa_{\rm rot}$ further reduces the size of our sample significantly, but does not change our main results; decreasing the value leads to the selection of a large number of galaxies that have no observable disc component in projection, e.g. elliptical and irregular galaxies which would not be appropriate for comparison with most of the observational samples considered here.

Galaxies with halo mass, $\geq 10^{12.5}$ M$_\odot$, are not subject to any morphological criterion. This is because very few halos of this mass host disc galaxies in EAGLE and the primary observational data to which we compare in this mass range makes no selection for disc galaxies.

3.2.4 $L_{\rm X} - M_{\rm vir}$ relation

For gas in hydrostatic equilibrium in a dark matter halo, $L_{\rm X} \propto M_{\rm vir}^{\alpha}$. If the bolometric X-ray emission is dominated by thermal bremsstrahlung radiation, halos have a constant gas fraction, and the gas density profiles are self-similar, then the slope of the scaling relation has the classical value, $\alpha = 4/3$ (Kaiser, 1986; Sarazin, 1986). However, in the halo mass and energy range considered in this work, the first two of these assumptions are not valid.

We can derive the scaling relation in the halo mass range, $10^{12.0} - 10^{13.5}$ M$_\odot$, and energy band, $0.5 - 2.0$ keV, following the work of Böhringer et al. (2012):

$$L_{\rm X} \propto f_{\rm gas}^2 \Lambda(T_{\rm vir}) M_{\rm vir} \ , \tag{3.2.2}$$

where $f_{\rm gas}$ is the gas fraction of the halo normalised by the cosmic baryon to total mass ratio; $\Lambda(T_{\rm vir})$ is the cooling function of the gas as a function of the virial temperature, $T_{\rm vir}$; and $M_{\rm vir}$ is the virial mass [2] In the halo mass range, $10^{11.5} - 10^{13.5}$ M$_\odot$, the cooling rate, $\Lambda_{\rm X}$, is approximately proportional to the temperature of the gas, as demonstrated in Section 2.5.1. As the virial temperature scales as $T_{\rm vir} \propto M_{\rm vir}^{2/3}$, then $\Lambda \propto M_{\rm vir}^{2/3}$. In the case when the baryon fraction can be expressed

[2] We use the term "virial mass" to refer to both M_{200} and M_{500} but the distinction should be clear in the appropriate context. These quantities scale proportionally and agree to within 10%.

as a power law, $f_{\rm gas} \propto M_{\rm vir}^{\beta}$, Eq. 3.2.2 simplifies to,

$$\begin{aligned} L_{\rm X} &\propto M_{\rm vir}^{\alpha} \\ &\propto f_{\rm gas}^{2} M_{\rm vir}^{5/3} \\ &\propto M_{\rm vir}^{2\beta} M_{\rm vir}^{5/3} \propto M_{\rm vir}^{5/3+2\beta} \ . \end{aligned} \tag{3.2.3}$$

This derivation assumes that the halo gas is at the virial temperature of the halo and that the gas density profiles are self-similar as a function of halo mass. We explore the validity of these assumptions in Section 3.4.3. It is often common to consider the X-ray luminosity as a function of stellar mass, e.g. $L_{\rm X} \propto M_{\rm star}^{\alpha^*}$.

When the gas fraction is constant as a function of halo mass, the slope of the $L_{\rm X} - M_{\rm vir}$ relation is $\alpha = 5/3$. The increased steepness, compared to the classical self-similar prediction, $\alpha = 4/3$, is due to the scaling of the cooling function in this halo mass range and energy band considered. It is also clear from Eq. 3.2.3 that an increase in the halo gas fraction, $f_{\rm gas}$, with increasing halo mass, will result in a steeper slope for the $L_{\rm X} - M_{\rm vir}$ relation.

3.3 Baryon census

The baryon fraction of our sample of disc galaxies is shown in Fig. 3.1 as a function of halo mass. Here, we plot the baryon fraction of stars, cold gas ($T \leq 5 \times 10^5$ K), hot gas ($T > 5 \times 10^5$ K) and total baryons. The distinction between hot and cold gas is motivated in Section 2.5.1, where we show the X-ray cooling function as a function of gas temperature. In general, gas below a temperature of 5×10^5 K has negligible X-ray emission in the energy band range, $0.5 - 2.0$ keV, on which we focus in this work.

Fig. 3.1 demonstrates that the baryon content of low-mass halos, $\rm M_{200} < 10^{12}$ $\rm M_{\odot}$, is dominated by stars and cold gas. The total baryon fraction within these halos is much lower than the mean cosmic baryon-to-dark matter ratio. This low baryon fraction is the consequence of the efficient feedback which heats gas and can eject it to distances well beyond the virial radius of the halo (Schaller et al., 2015b; Mitchell

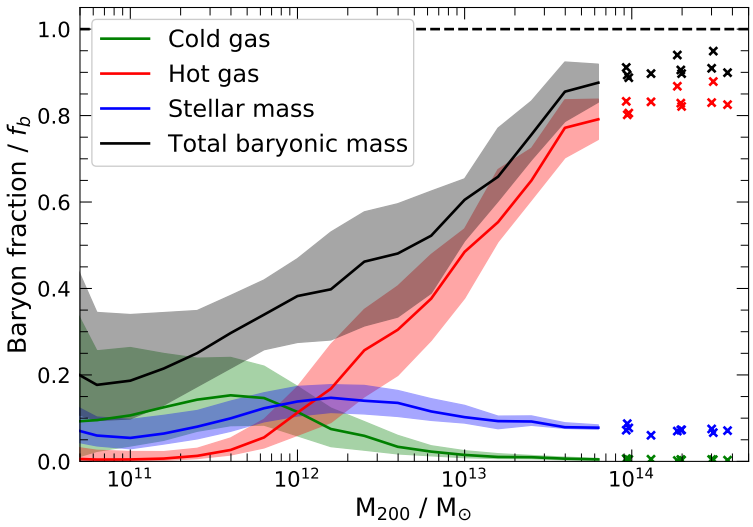

Figure 3.1: The baryon fraction of a sample of disc galaxies, selected from the EAGLE $(100\ \mathrm{Mpc})^3$ reference model, Ref-L100N1504, as a function of the halo mass at redshift $z = 0$. The values are normalised to the mean baryon fraction of the universe, f_b. The lines show the median, in mass bins of 0.20 dex, of the baryon fraction of stars, cold gas ($T < 5 \times 10^5$ K), hot gas ($T > 5 \times 10^5$ K) and all baryonic particles in green, blue, red and black respectively. In bins with less than five objects, we show the results as individual crosses. The shaded bands enclose the 15th and 85th percentiles.

et al., 2019). In low mass halos we see a negligible contribution of mass from hot gas. This is not surprising since even if these halos hosted gaseous halos of accreted gas, their typical temperature would be $\leq 5 \times 10^5$ K, which we classify as cold gas. Since our sample of galaxies was selected to be isolated, dynamical interactions, such as stripping, should not affect the baryon content of the halos.

As the halo mass increases above a critical mass, $\mathrm{M}_{200} \approx 10^{12}\ \mathrm{M}_\odot$, we find a rapid increase in the contribution of hot gas and in the total baryon fraction. The increase in the amount of hot gas is due to the virial temperature of the halos increasing to a value that exceeds the threshold for our definition of hot gas, 5×10^5 K. The increase in total baryon fraction is likely due to the deepening of the gravitational potential well of the halo, which increases its ability to retain gas heated by feedback. As the halo mass increases further, to $\approx 3 \times 10^{12}\ \mathrm{M}_\odot$ and above, the hot gas becomes the predominant mass component within the halo. The cooling time of the accreted gas is now so long that, after shock-heating, the gas forms a hot, quasi-hydrostatic

atmosphere at (approximately) the virial temperature of the halo (Larson, 1974; White & Rees, 1978; White & Frenk, 1991).

In the EAGLE simulations, the feedback efficiencies of SN and AGN, which regulate the stellar mass and halo baryon fractions, cannot be predicted from first principles. As discussed in Section 3.2, adjustable parameters are calibrated to match observed present-day galaxy properties, such as the galaxy stellar mass function. The simulations also broadly reproduce the stellar-to-halo mass relationship inferred from abundance matching (Behroozi et al., 2013; Moster et al., 2013). However, EAGLE slightly underpredicts the stellar mass at low halo mass and slightly overpredicts it at high stellar mass (see Fig. 8 of Schaye et al., 2015). In contrast to the galaxy stellar mass function, the baryon fraction of halos are direct, non-calibrated predictions of the subgrid physics model.

Unfortunately, the gas fractions in real halos, at a given halo or stellar mass, are uncertain. Previous studies of hot gas in the Milky Way have suggested that the mass of hot gas within the virial radius ranges between $(2-13)\times10^{10}$ $M_\odot$ (Nicastro et al., 2016), with various other estimates falling within this large range (Gupta et al., 2012; Faerman et al., 2017; Bregman et al., 2018). These constraints suggest that hot gas can account for a fraction between $(10-100)\%$ of the baryon budget of the MW. In higher mass objects, e.g. clusters, the baryon fractions are better constrained and the hot gas makes up between $(70-100)\%$ of the total baryon budget (Vikhlinin et al., 2006; Pratt et al., 2009; Lin et al., 2012). The results of Fig. 3.1 are consistent with current observational constraints.

3.4 The X-ray luminosity

Fig. 3.1 shows that galaxies in halos of mass $\geq 10^{12}$ $M_\odot$ in the EAGLE simulations are surrounded by hot gaseous coronae. While these gaseous atmospheres make up the majority of the hot gas mass in the halo, it is not clear whether they are the primary source of X-ray emission in these halos. Winds driven by feedback may dominate the X-ray emission as they are typically very hot, dense and metal-rich.

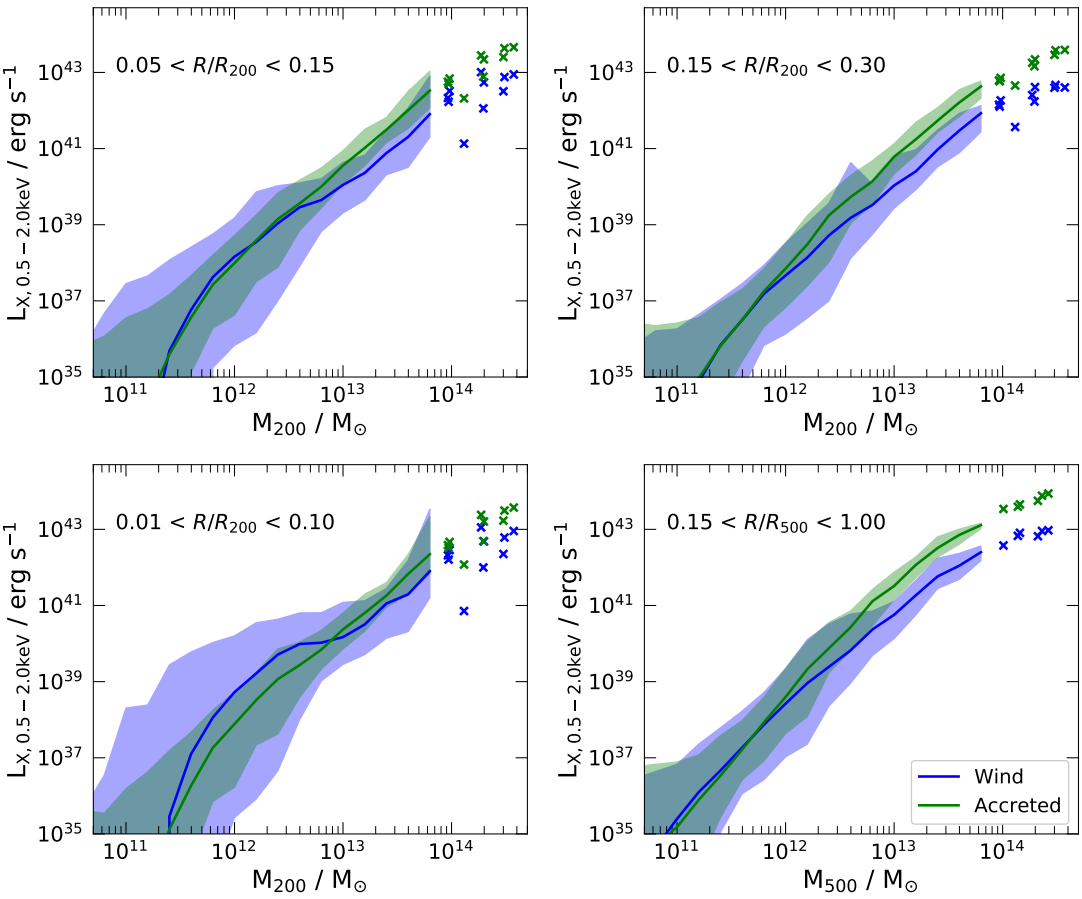

Figure 3.2: The soft X-ray luminosity, 0.5-2.0 keV, within different annuli around the galactic centre at $z = 0$ for a sample simulated disc galaxies in the EAGLE simulation, Ref-L100N1504, as a function of the halo mass. The top left, top right, bottom left and bottom right show the X-ray luminosity in the annuli $0.05 < r/R_{200} < 0.15$, $0.15 < r/R_{200} < 0.30$, $0.01 < r/R_{200} < 0.10$ and $0.15 < r/R_{500} < 1.00$, respectively. In all panels the simulated median X-ray luminosity is calculated for both accreted gas (green) and wind (blue) in halo mass bins of 0.20 dex and shown with the solid line. The luminosities of halos in bins sampled by fewer than five galaxies are shown individually. The shaded bands enclose the 15th and 85th percentiles within the same mass bins. The halo mass in each panel is taken to be M_{500}, except for the lower-left panel where we use M_{200}, to provide the best comparison to the respective observations in Section 3.4.

Therefore, we must first identify the origin of the dominant X-ray emitting gas before meaningful comparisons can be made between simulated and observed X-ray halo luminosities.

3.4.1 The origin of the X-ray emission

We analyse the contribution of wind and accreted gas to the total X-ray emission by considering the history of every gas particle within the virial radius of the halos. This gas can be classified into two categories: interstellar medium (ISM) and circumgalactic medium (CGM). The ISM is typically the high-density star-forming gas within the galaxy, whereas the CGM is the surrounding halo gas. In the EAGLE simulations, the ISM is usually defined as gas with a physical atomic number density, $n_H > 0.1$ cm^{-3}, while all other gas within the halo is considered to be part of the CGM.

The typical definition of "wind" is gas that has been ejected from the ISM into the CGM or beyond. We, therefore, distinguish "wind" from "accreted" gas particles according to their ISM and halo accretion histories. Specifically, we compare the time since the particle was last classified as ISM, $t_{\rm ISM}$, to the time since the particle was most recently accreted into any FoF halo, $t_{\rm accretion}$. We calculate $t_{\rm accretion}$ using high-cadence (240 equally-spaced outputs from when the age of the universe is 1 Gyr to 13.85 Gyr) simulation outputs to calculate the time when each gas particle was most recently *not* associated with a FoF group, $t_{\rm accretion}$. The $t_{\rm ISM}$ is tracked by the simulation code which stores the most recent time, if ever, when a gas particle was at an atomic number density higher than the threshold for star formation, $n_{\rm H} \approx 0.1$ cm^{-3}.

The case $t_{\rm ISM} > t_{\rm accretion}$ indicates that a gas particle was accreted by the present-day halo *after* it was last in the ISM of a galaxy. This suggests the gas particle was within the ISM of a galaxy at an earlier time and was then ejected from that halo before joining the CGM of a progenitor of the present-day halo. This gas, in the context of the present-day host halo, represents *accretion*. By contrast, $t_{\rm ISM} < t_{\rm accretion}$ indicates

the gas particle has been in the ISM of the galaxy since it was last accreted into a progenitor of the present-day halo. This gas was accreted, cooled and joined the ISM before being ejected, probably as a result of feedback, into the CGM. We, therefore, classify these particles as *wind*.

In Fig. 3.2 we plot the coronal soft X-ray luminosity within several 2D annuli for a sample of disc galaxies selected from the Ref-L100N1504 simulation, as a function of the halo mass. These annuli are chosen as they allow a direct comparison with observations which we present in Section 3.4.4. We show the X-ray luminosity contribution from gas particles classified as *accretion* and *wind* separately, in green and blue, respectively.

The largest contribution from wind is seen in the bottom-left panel of Fig. 3.2 which shows the central region of the halo. In this annulus, the X-ray emission from wind can be up to two orders of magnitude more luminous than emission from accreted gas, with the median X-ray emission from wind about an order of magnitude more luminous than from accreted gas for halos of mass $\leq 10^{13}$ $\mathrm{M}_{\odot}$. However, above this mass, the median X-ray emission from accreted gas is typically more luminous, but there is still significant scatter likely reflecting different recent star-formation rates. The *wind* contributes disproportionately to the X-ray luminosity compared to its contribution to the gas mass, which is not shown. This is because the gas defined as *wind* is consistently hotter, more metal-rich and denser than accreted gas (Crain et al., 2010). The upper percentile of the X-ray emission from *wind* in the bottom-left panel of Fig. 3.2 shows that the $L_{\mathrm{X}} - M_{\mathrm{halo}}$ relationship flattens at low halo masses, reflecting that the X-ray emission is less dependent on halo mass and more dependent on the recent star formation rate. This reflects the increase in X-ray luminosity in these halos, $M_{\mathrm{vir}} \leq 10^{13}$ $\mathrm{M}_{\odot}$, whereas there is no increase in the median, total X-ray luminosity of higher mass halos, $M_{\mathrm{vir}} \geq 10^{13}$ $\mathrm{M}_{\odot}$, due to *wind* in any of the annuli considered. In the lowest mass halos, $\mathrm{M}_{200} \leq 10^{12}$ $\mathrm{M}_{\odot}$, the $L_{\mathrm{X}} - M_{\mathrm{halo}}$ relation steepens again as below this halo mass there is very little accreted gas sufficiently hot to produce soft X-rays. Therefore, the X-ray emission drops rapidly with decreasing halo mass for low mass halos. In these same halos the

recent star formation rates are not converged in the reference simulation, increasing (decreasing) the resolution of the simulation increases (decreases) the star formation rate. As the X-ray luminosity in these halos is dominated by wind (see Fig.3.2), this means the X-ray luminosity may not be converged in these halos. Therefore, the X-ray luminosity predictions for these low mass halos should be used with caution. In more massive halos, $M_{200} \geq 10^{12}$ $M_{\odot}$ both the recent star formation rate, and X-ray luminosity, are well converged with varied resolution.

In radial regions further out, we see a reduction in the contribution of X-ray luminosity from *wind* at a given halo mass. This reduction happens because feedback processes, which generate winds, are concentrated in the central regions of the halo. In the upper- and lower-right panels of Fig. 3.2, where the inner region is excised, we see that the X-ray emission from *wind* in lower mass halos, $M_{\rm vir} \leq 10^{12}$ $M_{\odot}$, is of the same order as the total X-ray emission within the halo. However, for higher mass halos, the median X-ray emission from accreted material is significantly more luminous than *wind*. As the halo mass increases further, the fraction of the X-ray emission produced by accreted gas converges to $\approx 100\%$ at a halo mass of $\approx 10^{13}$ $M_{\odot}$. These outer annuli are therefore ideal for probing quasi-hydrostatic, accreted halos without pollution from the X-ray luminous, metal-rich wind. It should be noted, however, that the X-ray surface brightness is much lower in the outer regions, and thus difficult to observe around individual galaxies. Nevertheless, Oppenheimer et al. (2020b) argue that 4-year eROSITA observations should be able to detect X-ray emission out to ≈ 200 kpc for stacked data around halos of mass, $\geq 10^{12}$ $M_{\odot}$.

We note that the X-ray emission from diffuse gas which we classify as *wind* in the EAGLE simulations may not be representative of the X-ray emission around real highly star-forming galaxies. This X-ray emission is the result of a subgrid feedback model which injects thermal energy directly into gas particles. The direct heating of gas particles within the ISM of a galaxy, by both AGN and SNe feedback, leads to star particles of mass, $M \approx 10^6$ $M_{\odot}$, with high-metallicities, $Z \approx$ $Z_{\odot}$, high densities $n_{\rm H} \geq 0.1$ cm^{-3} and temperatures exceeding 10^7 K. The feedback model is, of course, just an approximation and its realism can only be established by comparison with

observations, such as those in Section 3.4.4 below.

Interactions between wind and accreted gas complicate the identification of the origin of X-ray emission. In halos of mass $\sim 10^{12}$ $M_\odot$ we expect that the accreted gas is shock-heated to the virial temperature White & Frenk (1991). However, in some cases, there could be additional shocks caused by wind-halo interaction, whereby hot outflows heat the gas in the CGM. As a result energy injected by supernovae may be emitted by particles which we have classified as accreted. This can lead to an overestimation of the energy emitted by accreted gas. This effect will be largest in lower mass halos for two reasons. The first is that the velocity at which the ejected gas encounters the infalling gas is larger in small mass haloes. Secondly, in small halos, the X-ray emission produced by wind and accreted gas appear to be comparable, whereas in massive halos, accreted gas dominates the total X-ray emission.

In summary, we find that a large fraction of the X-ray emission in the central region, $R < 0.10R_{\rm vir}$, of halos of $M_{\rm vir} \leq 10^{13}$ $M_\odot$ is produced by *wind*, which is the direct result of feedback processes associated with stellar evolution and AGN. However, when the central region is excised, the gas classified as *accretion* becomes the predominant source of X-ray emission in halos of mass $\geq 10^{12}$ $M_\odot$. This shows that accreted X-ray emitting coronae do exist around halos of mass $M_{\rm vir} \geq 10^{12}$, as predicted by White & Frenk (1991), at least within the EAGLE hydrodynamical simulations.

3.4.2 The X-ray scaling relations

The coronal soft X-ray luminosity in 2D annuli for our sample of disc galaxies selected from the reference EAGLE simulation is shown in Figs. 3.3 and 3.4 as a function of halo and stellar mass respectively. These annuli are the same as those considered in Fig. 3.2. In Figs. 3.3 and 3.4 we also plot observational data from Bogdán et al. (2015), Li et al. (2017) (bottom-left panel) and Anderson et al. (2015) (bottom-right panel).

The general trend in Figs. 3.3 and 3.4 is that the X-ray luminosity increases with

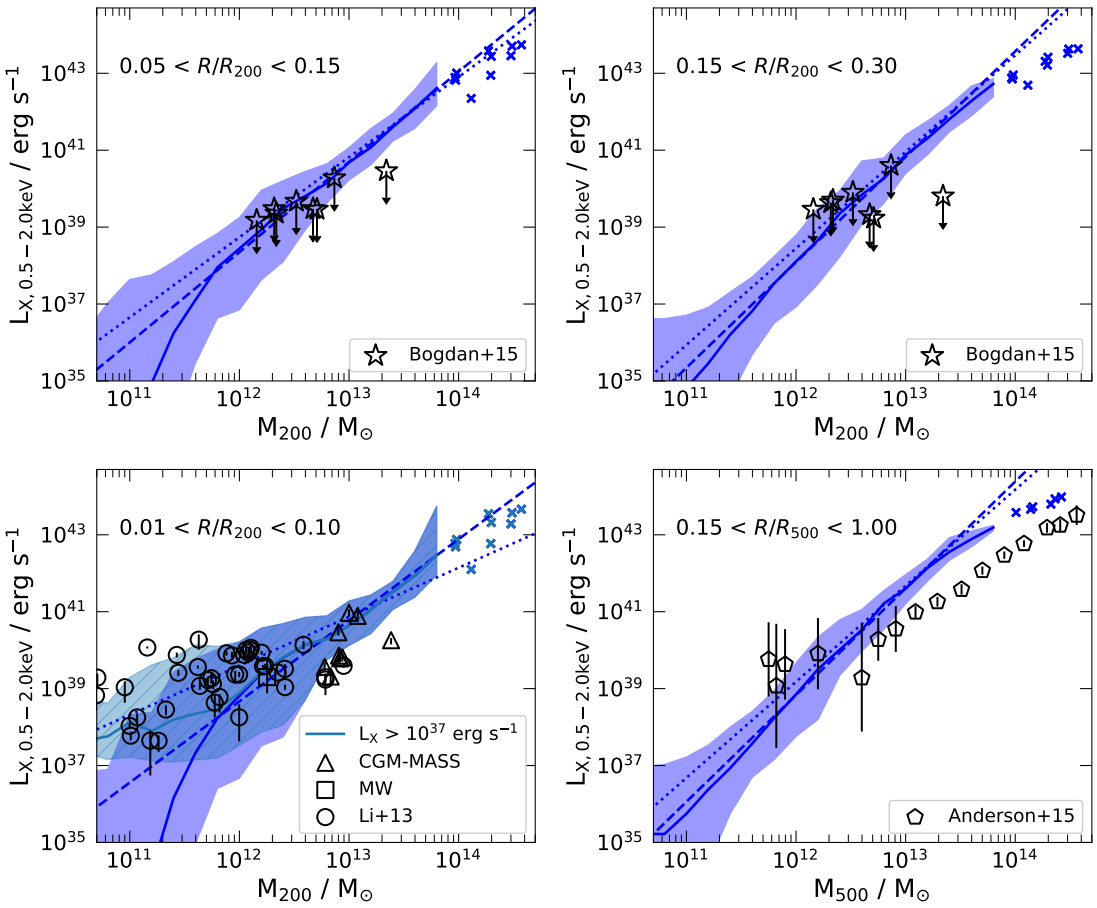

Figure 3.3: The soft X-ray luminosity, 0.5-2.0 keV, within different annuli around the galactic centre at $z = 0$ for a sample of simulated disc galaxies in the EAGLE simulation, Ref-L100N1504, as a function of halo mass. The top-left, top-right, bottom-left and bottom-right panels show the X-ray luminosity in the annuli $0.05 < r/R_{200} < 0.15$, $0.15 < r/R_{200} < 0.30$, $0.01 < r/R_{200} < 0.10$ and $0.15 < r/R_{500} < 1.00$, respectively. These regions are chosen to allow appropriate comparisons with the observational results of Bogdán et al. (2015) (top panels), Li et al. (2017) (bottom left) and Anderson et al. (2015) (bottom right) which are shown as the black data points with errorbars. In all panels the simulated median X-ray luminosity is calculated in halo mass bins of 0.20 dex. The luminosities of halos in bins sampled by fewer than five galaxies are shown individually. The shaded bands enclose the 15th and 85th percentiles within the same mass bins. The dashed (dotted) lines show the best-fit to median (mean) X-ray luminosity in the mass range $10^{11.5} < M_{\rm vir}/\ {\rm M}_\odot < 10^{13.5}$. The teal region in the lower-left panel shows the same sample with all galaxies of X-ray luminosity below 10^{37} ergs^{-1} excluded. The halo mass in each panel is taken to be M_{200}, except for the lower-right panel where we use M_{500}, to provide the best comparison to the respective observations.

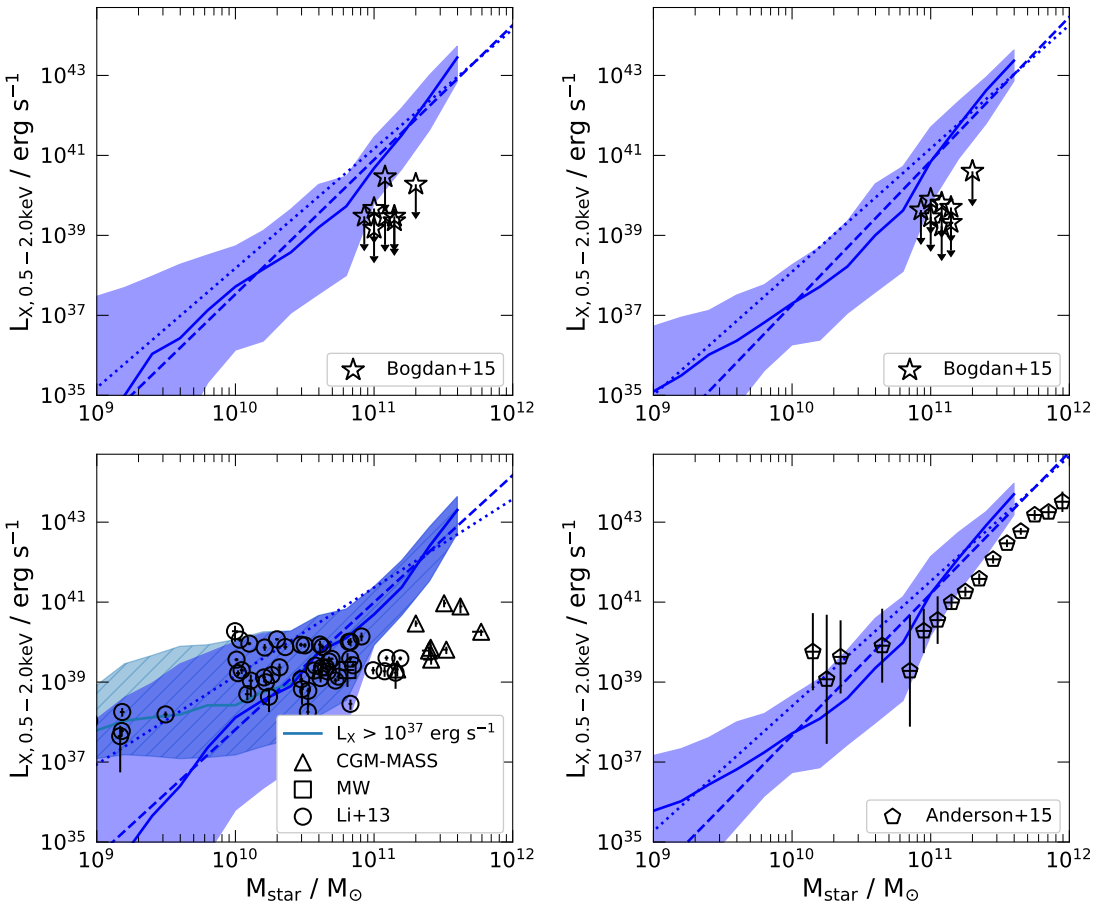

Figure 3.4: The same as Fig. 3.3, but with the X-ray luminosity plotted as a function of the *stellar* mass of the central galaxy. The stellar mass is defined to be the total mass of stars within a 3D sphere of radius 30 pkpc. The dashed (dotted) lines show the best-fit to median (mean) X-ray luminosity in the mass range $10^{9.5} < M_{\rm star}/\ {\rm M}_\odot < 10^{11.5}$. The teal region in the lower-left panel shows the sample with all galaxies of X-ray luminosities below 10^{37} ergs^{-1} excluded.

both halo and stellar mass. We can also see that the scatter in X-ray luminosity, at either a fixed halo or stellar mass, increases with decreasing mass. The larger scatter at low mass may be interpreted as the result of the greater importance of non-gravitationally heated gas, which is concentrated around the central regions and not directly related to the halo mass. As the halo mass increases, the scatter in the X-ray luminosity decreases, reflecting the increasing importance of gravitational heating on the X-ray luminosity.

As we can see in Fig. 3.3 the $L_{\rm X} - M_{\rm vir}$ relationship is fairly well described by a single

power law over approximately three orders of magnitude in halo mass. We plot the best-fit line to the relation in all panels of the figure using linear regression on the logarithm of the median of the X-ray luminosity as a function of the logarithm of the median halo mass. We find the exponent of the scaling relation, $L_X \propto M_{\rm vir}^{\alpha}$, for the median X-ray luminosity to be $\alpha = 2.2 \pm 0.1, 2.6 \pm 0.1, 2.1 \pm 0.1, 2.8 \pm 0.1$ in the halo mass range, $(10^{11.5} - 10^{13.5})$ $M_{\odot}$, for the upper-left, upper-right, lower-left and lower-right panels, respectively. Repeating this process with a best fit to the mean X-ray luminosity gives $\alpha = 1.8 \pm 0.1, 2.4 \pm 0.1, 1.3 \pm 0.1, 2.5 \pm 0.1$ in the same mass range for the upper-left, upper-right, lower-left and lower-right panels, respectively. We apply the same methodology to the $L_{\rm X} - M_{\rm star}$ relation, shown in Fig. 3.4, in the stellar-mass range $(10^{9} - 10^{11})$ $M_{\odot}$ and find the exponent of the relation to be, $\alpha^{*} = 3.4 \pm 0.1, 3.5 \pm 0.2, 3.2 \pm 0.1, 3.5 \pm 0.2$ for the median X-ray luminosity in the upper-left, upper-right, lower-left and lower-right panels, respectively. These slopes reduce to $\alpha^{*} = 2.7 \pm 0.2, 3.2 \pm 0.2, 2.2 \pm 0.2, 3.2 \pm 0.2$ in the same mass range for the mean X-ray luminosity, respectively.

The $L_{\rm X} - M_{\rm vir}$ and $L_{\rm X} - M_{\rm star}$ scaling relations are systemically flatter in the two left panels of Figs. 3.3 and 3.4 which probe the inner region of the halo. We also see that the difference in the slope of the scaling relations, $L_{\rm X} - M_{\rm vir}$ and $L_{\rm X} - M_{\rm star}$ between the best fit to the median and the best fit to the mean X-ray luminosity is much larger in these two panels.

The origin of the flatter slope, and the discrepancy between the mean and median X-ray luminosity over a small range of halo mass, is due to the enhanced X-ray emission in low mass halos, $\sim (10^{11} - 10^{13})$ $M_{\odot}$ in the inner region compared to the outer region. The increased X-ray luminosity within the central regions is caused by feedback, as shown in Fig. 3.2. However, not all low-mass galaxies have recent star formation. Thus, we see a scatter of up to four orders of magnitude in the X-ray luminosity in these halos. Therefore, a small sample of highly star-forming, X-ray luminous galaxies are able significantly to increase the mean X-ray luminosity, while having a smaller impact on the median X-ray luminosity, at a fixed halo mass. As the median X-ray luminosity is less affected by feedback from recent star formation, we

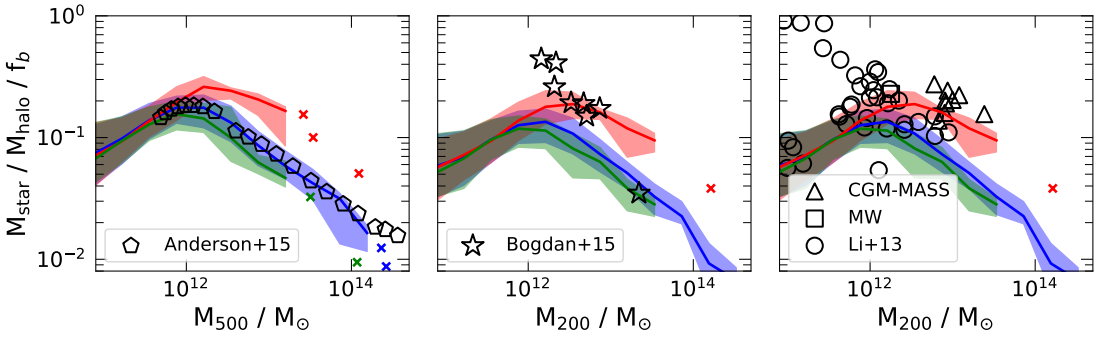

Figure 3.5: The stellar-to-halo mass ratio, normalised by the mean universal baryon fraction, f_b, as a function of both M_{500} (left panel) and M_{200} (central and right panels). Results from three different EAGLE simulations, Ref-L100N1504 (blue), NoAGN-L050N0752 (red) and AGNdT9-L050N0752 (green), are shown as medians in halo mass bins of 0.20 dex. When there are fewer than five objects in a bin, we plot the results of individual galaxies. We also show the 20th to 80th percentiles of the distribution as shaded regions. The observational results of Anderson et al. (2015) (left), Bogdán et al. (2015) (center) and Li et al. (2017) (right) are plotted.

focus on the median X-ray luminosity in the remainder of this chapter. In the outer regions, displayed in the two right panels of Fig. 3.3, we find that the slope of the scaling relation, $L_{\rm X} - M_{\rm vir}$, is steeper than the analytical prediction for self-similar gaseous halos, $\alpha = 4/3$, presented by Kaiser (1986) and Sarazin (1986) and the 1.8 value inferred from the observations of Anderson et al. (2015). We investigate the origin of the steeper slope of the $L_{\rm X} - M_{\rm vir}$ scaling relation in Section 3.4.5.

Stellar-halo mass relationship

In Fig. 3.5 we plot the stellar-to-halo mass ratio normalised by the mean universal baryon fraction, f_b, as a function of M_{500} (left panel) and M_{200} (central and right panels). The results from three different EAGLE simulations, Ref-L100N1504, NoAGN-L050N0752 and AGNdT9-L050N0752, are shown. We also plot the observational data of Anderson et al. (2015) (left), Bogdán et al. (2015) (center) and Li et al. (2017) (right). We define the stellar mass as the total mass of stars within a fixed spherical aperture of radius 30 pkpc. This aperture is chosen as Schaye et al. (2015) found that it yields stellar masses similar to those inferred from the Petrosian-r band aperture often used in observational studies.

The two EAGLE simulations, Ref-L100N1504 and AGNdT9-L050N0752, have a consistent stellar-to-halo mass relation which, moreover, agrees with the results of Moster et al. (2013) from abundance matching (Schaye et al., 2015). However, the NoAGN-L050N0752 simulation overpredicts the stellar-mass in galaxies of $\geq 10^{12}$ $M_{\odot}$. The stellar-halo mass relation of the two main simulations, Ref-L100N1504 and AGNdT9-L050N0752, broadly agree with the observations of Anderson et al. (2015) and Bogdán et al. (2015). However, the sample of Li et al. (2017) contains a population of low mass halos with very high stellar masses which are not found in the EAGLE simulations.

The stellar-dominated galaxies at low halo masses of Li et al. (2017) are inconsistent with the abundance matching predictions of Moster et al. (2013). The cause of this could be an incorrect inference of the halo mass from the measured rotation velocities. The uncertainty in the halo masses complicates the interpretation of the observational $L_{\rm X} - M_{\rm vir}$ relation.

3.4.3 Hot gas self-similarity

The radial profiles of the gas density estimated from all of the galaxies in the EAGLE Ref-L100N1504 simulated in the halo mass range, $10^{12} - 10^{13.5}$ $M_{\odot}$, are shown in Fig. 3.6. The profiles are normalised by the individual baryon-to-dark-matter ratio within each halo. We see that the normalised gas density profiles in the central region vary significantly as a function of halo mass. However, in the outer regions, the gas density profiles exhibit self-similarity across two orders of magnitude of halo mass. This self-similarity also appears to be present in the GIMIC simulations (Crain et al., 2009) as may be seen in the top-left panel of fig 8 of Crain et al. (2010). While the slopes of the gas density profiles are clearly self-similar in Crain et al. (2010), the normalisation increases with halo mass due to the increasing gas fraction in high-mass halos.

In the central regions, the normalised gas density, at a fixed radius, is much higher in lower mass halos. This likely reflects the differing impact of feedback in these

halos. In lower mass halos AGN feedback and, in some cases, SNe feedback, is able to eject gas to the virial radius and beyond. This will lower the total gas fraction of the halo, but if the process takes place over a long timescale, the density profile should remain unaffected. In more massive halos, winds driven by AGN are unlikely to leave the halo, and thus the net result is that gas is transported outwards. This process acts to increase the density at large radii while decreasing it at small radii.

The self-similarity of the hot gas profiles in the outer regions of the halo validates a key assumption in the derivation of Eq. 3.2.2. The observed self-similarity reflects the fact that the gravitational forces are dominated by the dark matter distribution, which has previously been shown to be well converged for different subgrid physics models (Schaye et al., 2015). As such, when appropriately normalised by their individual gas fractions, the gas radial density profiles in the radial range, $(0.15 - 1.00)\ R_{500}$, agree in both trend and normalisation. This is also expected from Fig. 3.2 in which we showed that the X-ray emission in this radial range (and the mass fraction which is not shown) are dominated by accreted gas. Although the gas density profiles in the EAGLE simulations display self-similarity, it is not clear whether this behaviour will be also be present in other cosmological hydrodynamical simulations or, indeed, in the real universe. Interesting future work might assess how well these results hold across other simulations with different subgrid models and parameters.

3.4.4 Comparison to observations

We now calculate the coronal X-ray luminosity from the simulated galaxies in a way that allows a fair comparison to observations, that is, within the same annulus and energy range. However, there are still limitations in the direct comparison of simulated and observed X-ray luminosities. For example, when calculating the X-ray emission in an annulus, we only include gas within a sphere of the virial radius. However, in real observations, the line-of-sight X-ray emission may be contaminated by non-gaseous X-ray sources such as X-ray binaries in the galaxy, or unrelated background and foreground objects. A fraction of the coronal X-ray emission in

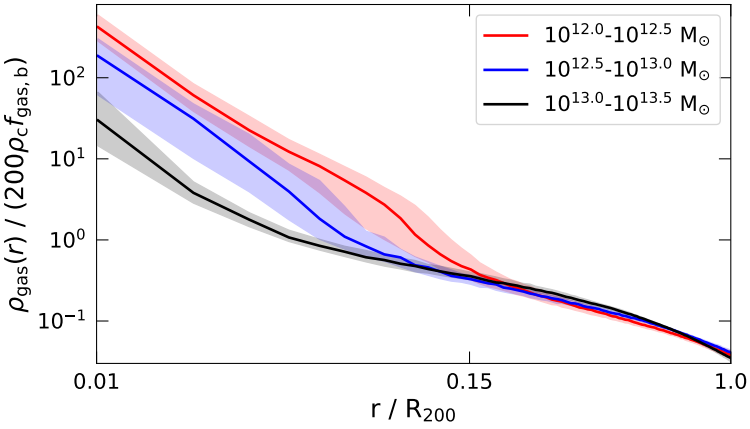

Figure 3.6: Three-dimensional, spherically averaged radial density profiles of the gas within halos of disc galaxies in the EAGLE Ref-L100N1504 simulation. We show the median gas density profile in halos in mass bins of: $10^{12} - 10^{12.5}$ $M_\odot$ (red), $10^{12.5} - 10^{13.0}$ $M_\odot$ (blue) and $10^{13} - 10^{13.5}$ $M_\odot$ (black). The density profiles are normalised by 200 times the critical mass density of the universe, the cosmic baryon-to-dark matter ratio and the gas fraction of each halo. The bands enclose the 30th and 70th percentiles.

the real universe may be absorbed, particularly at lower energies. These effects are not considered when calculating the X-ray emission from simulated galaxies. As our analysis of the simulations is not instrument-limited, we include galaxies with X-ray luminosities well below the current detection threshold. The simulations thus contain more low luminosity objects than observational samples, but we account for that in the comparison with the data.

In the top two panels of Fig. 3.3 and Fig. 3.4 we compare the simulations to the data presented by Bogdán et al. (2015), who used Chandra to search for soft X-ray emission around eight normal spiral galaxies. No statistically significant diffuse soft X-ray emission was detected around any of these galaxies. We therefore use the inferred 3σ upper limits for our comparison. As these observations excise the central regions, any contamination unresolved X-ray point sources should be small.

The upper limits derived from the observations of Bogdán et al. (2015) generally overlap with the 15th to 85th percentiles predicted by EAGLE. However, these upper limits Bogdán et al. (2015) are consistently lower than the mean and median X-ray luminosity found in the simulations. Therefore, there does appear to be some

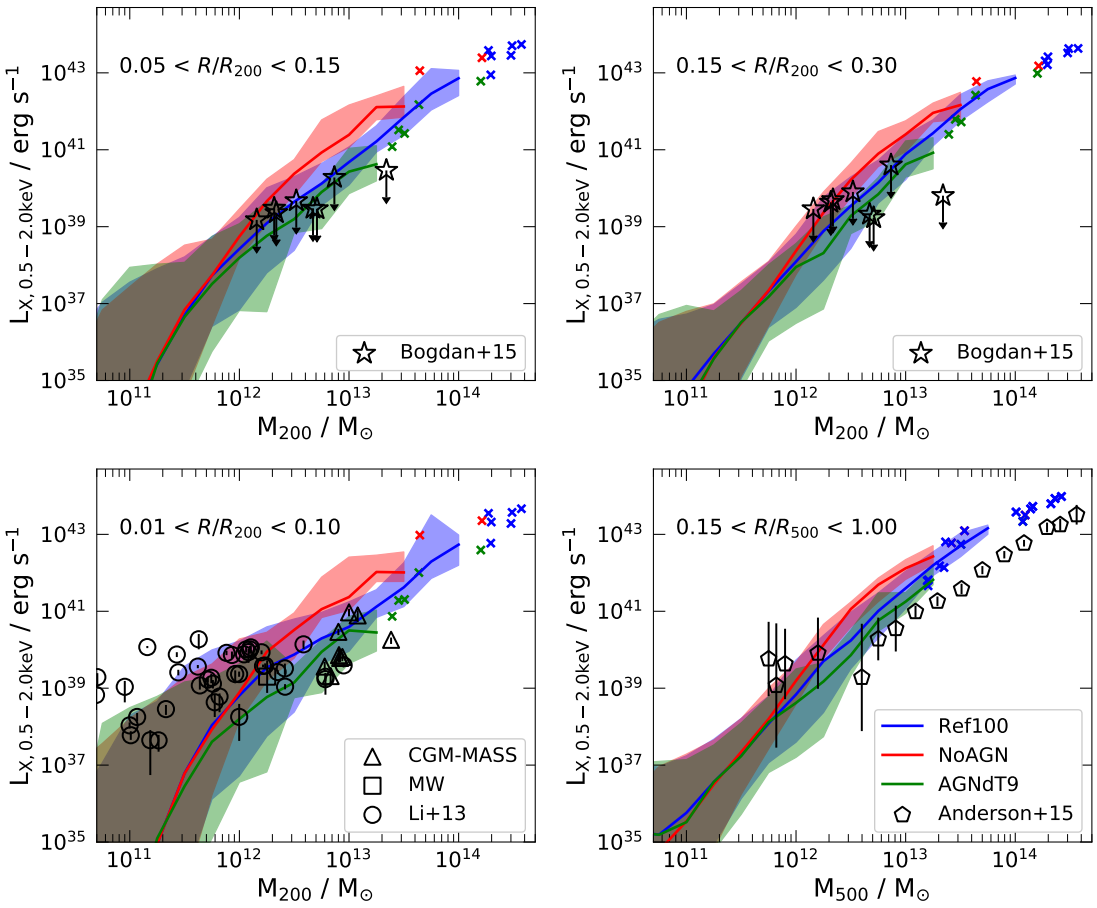

Figure 3.7: The same as Fig. 3.3, but showing the X-ray luminosity for three different samples of discs galaxies taken from the EAGLE simulations Ref-L100N1034 (blue), NoAGN-L050N0752 (red), AGNdT9-L050N0752 (green). This comparison shows the impact of varying the AGN feedback model on the X-ray luminosity to halo mass relationship.

evidence that the simulations are slightly, but significantly overpredicting the X-ray emission at large luminosities. However, the X-ray luminosities as a function of stellar mass in the simulations are significantly higher than the observational limits, as may be seen in Fig. 3.4. The reason for the discrepancy between the results at fixed halo and at fixed stellar mass could be due to two reasons. The first is that the stellar-to-halo mass relationship in the EAGLE simulations could be incorrect. However, abundance matching suggests that the EAGLE relation agrees well with the data (Schaye et al., 2015). Secondly, it could be that the halo or stellar masses inferred for the real galaxies is incorrect. The stellar masses in Bogdán et al. (2015)

are estimated from K-band luminosities in the 2MASS survey, while the halo masses are estimated from the circular velocity of gas in the disc, which is then converted to a halo mass following Navarro et al. (1997). In Section 3.4.2, we compare the stellar-to-halo mass relation of these observations with results from the EAGLE simulation. In particular, the central panel of Fig. 3.5 compares the stellar baryon fraction as a function of halo mass in three different EAGLE simulations to the observational estimates of Bogdán et al. (2015). These observations imply that the stellar mass accounts for between 15% and 50% of the baryon budget of the halos. However, constraints from abundance matching suggest that this value should be closer to 10% (Moster et al., 2013). This is indicative of an overestimated stellar mass, or an underestimated halo mass. As the stellar mass is more directly inferred than the halo mass, we assume that it is the halo masses that are underestimated.

As the X-ray emission is calculated in a halo mass dependent aperture, $(0.05 - 0.15)\ R_{500}$, this can lead to an incorrect value for the X-ray luminosity. Since the X-ray emission is typically centrally peaked; an underestimated halo mass implies that the central region excised would be too small, leading to higher X-ray luminosities. Thus, if the assumed halo masses are indeed too small, the data points on the upper-left panel of Fig. 3.3 should be moved down (as more central emission should be excised) and to the right (towards higher halo masses), increasing the discrepancy with the EAGLE simulations. The same data points would remain at the same stellar mass, but may also decrease in X-ray luminosity in Fig. 3.4.

Fig. 3.2 shows that, at least within the simulations, the observations of Bogdán et al. (2015) probe the transition between *wind* and *accretion* dominated X-ray emission. If the Bogdán et al. (2015) halo masses are underestimated, their data will shift towards the *accretion*-dominated regime. The overestimated X-ray emission in the simulations could then reflect excessive hot gas baryon fractions, or incorrect thermodynamic properties for the gas.

In the bottom left panel of Figs. 3.3 and 3.4 we compare the predictions from the EAGLE simulations to observations of massive, isolated spiral galaxies homogeneously reanalysed by Li et al. (2017). This sample includes the detections of NGC 1961

(Bogdán et al., 2013; Anderson et al., 2016) and NGC 6753 (Bogdán et al., 2013), which are referred to as "massive spirals". The CGM-MASS sample of Li et al. (2017) and a measurement of the Milky Way X-ray luminosity from Snowden et al. (1997) are also included alongside the original sample of inclined disc galaxies presented by Li & Wang (2013a) and Li et al. (2014). These observations use Chandra and XMM-Newton to probe the inner regions of nearby halos.

We first consider the X-ray luminosity as a function of halo mass from the innermost region. In this regime the observations are consistent, in both the overall trend and scatter, with the simulated galaxies within the halo mass range $(10^{11} - 10^{13})$ $M_\odot$. The agreement is particularly good when we exclude all simulated galaxies with X-ray luminosities below 10^{37} ergs^{-1}, as shown by the teal region in Figs. 3.3 and 3.4. This luminosity cut is consistent with the observational limits of the data. For the highest mass halos the simulations appear to overestimate the X-ray luminosity; however, this is a tentative result given the small size of the observational sample. The simulations also reproduce the trend of the observed $L_{\rm X} - M_{\rm star}$ relation in this innermost annulus. In the lower-left panel of Fig. 3.4 we see that below a stellar mass of $\approx 10^{11}$ $M_\odot$ the simulations are consistent with the observations, particularly once we exclude halos of luminosity below 10^{37} ergs^{-1}.

Fig. 3.2 shows that the dominant source of X-ray emission in the innermost region in the EAGLE simulations is hot winds produced by feedback. We therefore suggest that the observations of Li et al. (2017) are probing SNe-heated hot gas, rather than the innermost region of a hot accreted halo.

Finally, the bottom right panel of Fig. 3.3 compares our simulations to the stacked X-ray observations of Anderson et al. (2015), which consist of a sample of approximately 250000 "locally brightest galaxies" from the Sloan Digital Sky Survey. A more detailed description of the selection criteria is given in Planck Collaboration et al. (2013) but, in summary, galaxies are selected if they are brighter than a threshold in extinction-corrected Petrosian r-magnitude band while also being the brightest object within a 1 Mpc projected radius. These selection criteria were chosen in an attempt to select a population of 'central' galaxies. Our sample of simulated galaxies

is subject to a conceptually similar selection process, in that we also choose isolated galaxies. The X-ray emission from the real galaxies is stacked in bins of stellar mass, and these stellar masses are converted into halo masses. It should be noted that for this sample an overdensity of $\Delta = 500$ is used to define the halo mass; to facilitate a fair comparison we also compute this mass for our simulated halos.

In the regime of MW-mass halos we find that the X-ray luminosities in the EAGLE simulations are in good agreement with the observations at both fixed halo and stellar mass. However, above this mass, the slopes of the $L_{\rm X} - M_{\rm vir}$ and $L_{\rm X} - M_{\rm star}$ relations in the simulations are steeper than for the real galaxies. The overprediction of the X-ray luminosity in the simulation peaks at a halo mass of $\sim 3 \times 10^{13}$ M$_\odot$ and then decreases to around a factor of three for the most massive halos, $\sim 10^{14}$ M$_\odot$. Wang et al. (2016) recalibrated the estimated halo masses of the Anderson et al. (2015) sample using weak lensing data. Wang et al. (2016) suggest that the halo masses from Anderson et al. (2015) are slightly too large, with an almost constant overestimation of between $0.05 - 0.10$ dex (see Fig. 10, right panel of Wang et al. (2016)). Thus, using the $L_{\rm X} - M_{\rm vir}$ slope of 1.9 for the Anderson et al. (2015) data we predict that correcting the halo masses would increase the X-ray luminosity, at a given halo mass, by a factor of approximately $\sim 1.2 - 1.5$. Furthermore, a decrease in the inferred halo mass would decrease the virial radius, and therefore decrease the size of the excised central region. This would increase the X-ray emission, as emission is centrally peaked. We expect that these effects may change the results by up to a factor of two when combined. Given the large dynamic range of the data, this correction does not significantly reduce the tension between the EAGLE simulations and observations.

3.4.5 Effects of AGN

In this section we use the three EAGLE simulations, Ref-L100N1034, NoAGN-L050N0752 and AGNdT9-L050N0752, to investigate the effects of varying the implementation of AGN feedback on the $L_{\rm X} - M_{\rm vir}$ relationship. The three simulations were introduced in Section 3.2. We repeat the sample selection process outlined in

Section 3.2.3 independently in each simulation. The X-ray luminosity as a function of halo mass in the three simulations is displayed in Fig. 3.7 for the same spatial regions, and compared to the same observational data as in Fig. 3.3.

In all four regions we see that the X-ray luminosity in lower mass halos, $\leq 10^{12}$ $M_{\odot}$, is unchanged by the variation of the AGN feedback implementation. In the EAGLE galaxy formation model AGN have little effect on galactic properties below this critical mass (Schaye et al., 2015; Rosas-Guevara et al., 2016; Bower et al., 2017a; Davies et al., 2019). Observationally, it is also known that galaxies of stellar mass below $\sim 10^{10}$ $M_{\odot}$, which corresponds to a halo mass of $\sim 10^{12}$ $M_{\odot}$, seldom host powerful AGN (Kauffmann et al., 2003). Above this halo mass we see a general trend across all the spatial annuli: halos with no-AGN feedback have higher X-ray luminosities. The differences in the X-ray luminosity in simulations with and without AGN peak in the $(10^{12} - 10^{13})$ $M_{\odot}$ mass range. At higher masses, $\sim 10^{14}$ $M_{\odot}$, the results from all the simulations appear to converge. However, this is a tentative result as the two $(50 \text{ Mpc})^3$ simulations have a small number of haloes in this mass range.

The AGNdT9-L050N0752 simulation has a modified AGN feedback model in which the change in temperature, $\Delta T_{\rm AGN}$, due to AGN feedback is increased to 10^9 K. In this simulation we see that the X-ray luminosity at fixed halo mass in the range, $(10^{12} - 10^{13})$ $M_{\odot}$, is lower than in both the reference and no-AGN models. The decrease in luminosity, which is typically about 0.5 dex, improves the agreement with the observations in all spatial regions. This indicates that the AGN feedback in the reference model is under efficient. Schaye et al. (2015) also found that the modified AGN feedback in AGNdT9-L050N0752 improves the agreement between simulated and observed X-ray emission for some of the most massive objects, $M_{500} \geq 10^{13}$ $M_{\odot}$. Further to this, Correa et al. (2018) found an upturn in the ratio of the cooling radius to the virial radius of high mass halos, $\geq 10^{13}$ $M_{\odot}$, within the EAGLE reference simulation. This upturn has also been attributed to under efficient AGN feedback in high-mass halos. The increase in the cooling radius can account for the significant overprediction of the X-ray luminosity in the inner regions of high-mass halos (as

seen in the two left panels of Fig. 3.3).

In the EAGLE model, the main effect of AGN feedback is to eject gas beyond the virial radius of the halo, as we show in Section 3.5. This decreases the total hot gas mass and thus gas density in the halo, thus decreasing the X-ray luminosity at fixed halo mass. AGN feedback can also decrease the SFR in the galaxy, which would reduce the X-ray emission from wind in the innermost regions. These results are consistent with those of Bogdán et al. (2015) who analysed a sample of spiral galaxies in the ILLUSTRIS simulations. Their "textbook" ILLUSTRIS spiral galaxies undershoot the observed X-ray emission, a fact that Bogdán et al. (2015) attributed to over-efficient radio-mode AGN feedback which acts to reduce the baryon fraction. However, the Bogdán et al. (2015) X-ray calculation follows Navarro et al. (1995) which assumes primordial gas fractions and a power-law fit to the cooling function. A more exact calculation of the X-ray luminosities in the ILLUSTRIS simulations would likely yield higher X-ray luminosities.

It is also interesting to note that the FIRE simulations analysed in van de Voort et al. (2016) do not include AGN feedback and recover the observed X-ray emission in $(10^{12} - 10^{13})$ $\mathrm{M}_{\odot}$ more convincingly than the EAGLE reference model. The reason for the improved agreement in this case may the implementation of stellar feedback which, in the FIRE simulations, can drive efficient winds, even in high mass halos. It is clear from Fig. 2 in van de Voort et al. (2016) that the hot gas baryon fraction within their halos is $\sim 0.25 f_b$ at a halo mass of $\sim 10^{13}$ $\mathrm{M}_{\odot}$, which is lower than that found in any of the EAGLE simulations we are considering.

3.5 Estimating the gas fractions from the $L_{\rm X} - M_{\rm vir}$ relation

In Section 3.2.4 we showed that the dependence of the baryon fraction on halo mass is encoded in the $L_{\rm X} - M_{\rm vir}$ relation. An increase in baryon fraction with halo mass increases the slope of the relation and vice versa. If a power law can describe the

Name	$L_{\rm X} - M_{500}$ α	Predicted $f_{\rm gas} - M_{500}$ β	Empirical $f_{\rm gas} - M_{500}$ β
Ref-L100N1504	2.68 ± 0.10	0.51 ± 0.05	0.58 ± 0.02
NoAGN-L050N0752	1.98 ± 0.16	0.16 ± 0.08	0.18 ± 0.05
AGNdT9-L050N0752	2.64 ± 0.05	0.48 ± 0.03	0.44 ± 0.10

Table 3.2: Best-fit exponents of the $L_{\rm X} - M_{\rm vir}$ and $f_{\rm gas} - M_{\rm vir}$ relationships in the EAGLE simulations. The exponents are calculated in the halo mass range $10^{12.5} - 10^{13.5}$ $\rm M_\odot$. The columns give the name of the simulation, the exponent of the $L_{\rm X} - M_{\rm vir}$ relation, the predicted exponent of the $f_{\rm gas} - M_{\rm vir}$ relation and the exponent of the $f_{\rm gas} - M_{\rm vir}$ relation. The relations are fit within the halo mass range, $10^{12.5} - 10^{13.5}$ $\rm M_\odot$.

gas fraction as a function of halo mass, then Eq. 3.2.3 can be used to calculate the halo mass dependency of the gas fraction from the logarithmic slope of the $L_{\rm X} - M_{\rm vir}$ relation. We evaluate this technique using the X-ray luminosity, halo masses and gas fractions of our three EAGLE simulations, Ref-L100N1034, NoAGN-L050N0752 and AGNdT9-L050N0752. The variations in AGN feedback lead to noticeable differences in baryon fraction and its dependence on halo mass for halos of $M_{\rm vir} \geq 10^{12}$ $\rm M_\odot$.

In the left-hand panel of Fig. 3.8 we plot the coronal soft X-ray luminosity, in mass bins of 0.20 dex, within an annulus, $0.15 < R/R_{500} < 1.00$. The X-ray luminosity is plotted as a function of halo mass, as in Fig. 3.3, focusing on the mass range of interest, $\rm M_{200} \geq 10^{12}$ $\rm M_\odot$, where significant gaseous halos are present (see Fig. 3.1). The right panel shows the median gas fraction within the same annulus as a function of halo mass, M_{500}. As in Section 3.4.2, we fit straight-lines to the logarithm of both the median X-ray luminosity and the median gas fraction plotted against the logarithm of the halo mass. We fit both of these properties in the halo mass range, $10^{12.5} - 10^{13.5}$ $\rm M_\odot$, and tabulate the best-fit parameters in Table 3.2. The mass range we fit in is different from that in Section 3.4.2 and thus the slopes are slightly different.

We now use the slope of the $L_{\rm X} - M_{\rm vir}$ relation to estimate the scaling of $f_{\rm gas}$ with $M_{\rm vir}$. According to Eq. 3.2.3, $f_{\rm gas} \propto M_{\rm vir}^{\beta}$ with $\beta = (\alpha_{\rm vir} - 5/3)/2$ (where $\alpha_{\rm vir}$ is defined through $L_{\rm X} \propto M_{\rm vir}^{\alpha_{\rm vir}}$). We can calculate this scaling directly in the simulations, as it is the slope of the best-fit line shown in the right-hand panel of Fig. 3.8. We tabulate

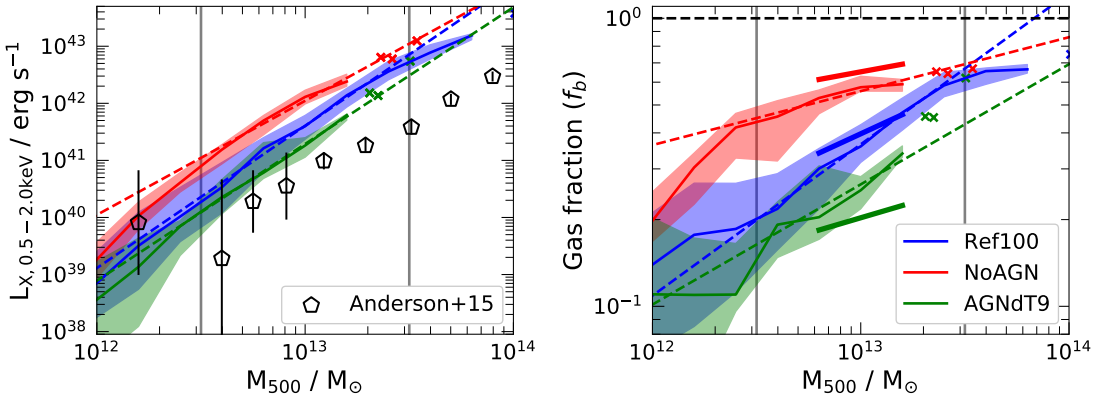

Figure 3.8: The coronal soft X-ray luminosity (left) and gas mass fraction (right) as a function of halo mass, M_{500}. In both panels we only consider gas within the 3D virial radius, R_{500}, and within the annulus $0.15 < R/R_{500} < 1.00$. The solid curves and shaded bands show the median and 15th to 85th percentiles in mass bins of 0.20 dex respectively. In bins that would enclose less than five objects we plot individual galaxies. The Ref-L100N1034, NoAGN-L050N0752 and AGNdT9-L050N752 are shown by the green, blue and red curves respectively. We also add best-fit lines in both panels, which are shown with dashed lines. The model parameters of the best fits are shown in Table 3.2. The black vertical lines show the range of halo mass over which the best-fit is calculated. The thick solid line segments in the right panel show the predicted slopes for the $f_{gas} - M_{vir}$ estimated from the slopes of the $L_X - M_{500}$ relation in the left panel, following Eq. 3.2.3.

α_{vir}, the predicted value of β and the empirical value of β from the simulations in Table 3.2. The $1-\sigma$ errors of the best-fit parameters, calculated from the covariance of the Jacobian, are also included.

As Table 3.2 shows, the measured values of the logarithmic slopes of the $f_{gas} - M_{vir}$ relation in all three simulations agree well with our predictions from Section 3.4.2, within 1.3σ. The steepening of the $L_X - M_{vir}$ above a slope of 5/3 is accounted for by the variation of the gas fraction as a function of halo mass. This demonstrates that the X-ray emission is adequately described by Eq. 3.2.3 and that the variation of the gas fraction makes an important and measurable contribution to the logarithmic slope of the $L_X - M_{vir}$ relation. In particular, we can distinguish between simulations with different AGN implementations by the slope of the corresponding $L_X - M_{vir}$ relation. In principle, this same methodology can be applied to the real universe to understand how the gaseous baryon fraction varies, from MW-mass halos to galaxy

clusters.

We show that the $L_{\rm X} - M_{\rm vir}$ relation is strongly dependent on the $f_{\rm gas} - M_{\rm vir}$ trend within the EAGLE simulations in Fig. 3.8. Furthermore, we also see that the normalisation and scatter of the gaseous baryon fractions are also observable in the observed X-ray luminosity. At fixed halo mass, we see that the most luminous halos are found in the NoAGN-L050N0752 simulation. This increased X-ray luminosity is due to the lack of AGN feedback which leads to an increased gas fraction within the virial radius.

The $L_{\rm X} - M_{\rm vir}$ relation flattens significantly at large halo mass, $\geq 10^{13.5}$ M$_\odot$. This is caused by both a flattening of the soft X-ray cooling function with temperature (see Section 2.5.1) and by the near-constant gas fraction in high mass halos. These effects should combine to produce an $L_{\rm X} - M_{\rm vir}$ relation where $L_{\rm X} \propto M_{\rm vir}$ for halos of mass $\gg 10^{13.5}$ M$_\odot$ within the soft X-ray energy band. However, since the simulations analysed here have no objects in this mass range, we cannot test the validity of this prediction.

The data of Anderson et al. (2015) are consistent with a shallow $L_{\rm X} - M_{\rm vir}$ scaling relation, with $\alpha_{\rm vir} \approx 1.8$, in the halo mass range $M_{500} \geq 10^{12}$ M$_\odot$. Anderson et al. (2015) attributed the increase from the logarithmic slope of 4/3 predicted by Kaiser (1986) and Sarazin (1986) to the effects of non-gravitational heating from AGN. They suggested that "self-regulated" AGN feedback should increase the X-ray luminosity of higher mass halos. In their picture, thermal instabilities due to radiative cooling in the hot halo result in high BH accretion rates, which cause energy build-up and subsequent feedback that heats the gas in the central region. This process repeats cyclically. However, in the EAGLE simulations, we find the opposite to be true. Table 3.2 shows that the shallowest slope of the $L_{\rm X} - M_{\rm vir}$ relation occurs in the NoAGN-L050N0752 simulation. AGN feedback in the other two simulations significantly increases the logarithmic slope of the $L_{\rm X} - M_{\rm vir}$ relation. We suggest that the primary effect of AGN feedback is to *decrease* the X-ray emission, at fixed halo mass, particularly in lower mass halos of $M_{200} \approx (10^{12} - 10^{13})$ M$_\odot$. This is due to the ejective nature of AGN feedback which reduces both the mass and the density

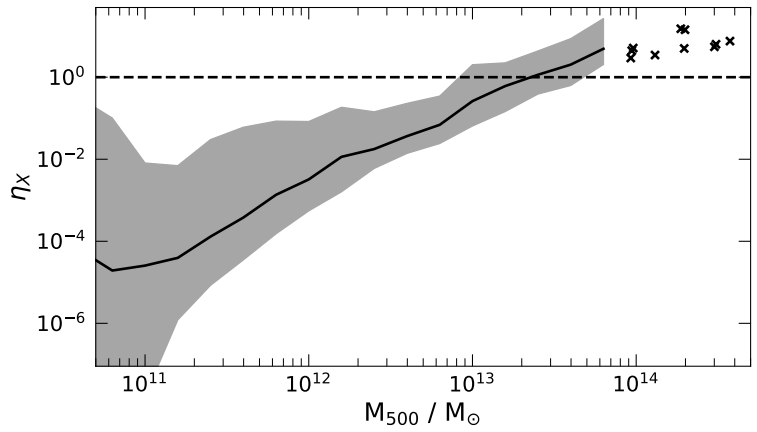

Figure 3.9: The X-ray coupling efficiency, η_X, as a function of halo mass in the EAGLE reference simulation for a sample of isolated disc galaxies. The X-ray coupling efficiency is defined as the ratio of the observed X-ray luminosity to the rate of energy input due to SNe, $L_{\rm X}/\dot{E}_{\rm SN}$. The power injected by SNe, $\dot{E}_{\rm SN}$, can be calculated in the simulations from the mean star formation rate in the last 250 Myr and the mean energy injected per unit of initial stellar mass formed. The black line shows the median X-ray coupling efficiency, in halo mass bins of 0.20 dex, where the X-ray luminosity has been calculated from all the gas within the virial radius. The shaded bands enclose the 15th and 85th percentiles.

of the X-ray emitting gas.

A reinterpretation of the data of Anderson et al. (2015), shown in the left panel of Fig. 3.8, in the context of Eq. 3.2.3 suggests that the halo gas fraction is approximately independent of halo mass, $\beta \approx 0.1$. When comparing the simulation results with measurements derived from stacked observational data, it is more appropriate to compare to the mean of the simulated data rather than the median. We showed in Section 3.4.2 that the slope of the $L_{\rm X} - M_{\rm vir}$ relation decreases by approximately 0.3 when fit to the mean, rather than the median, X-ray luminosity in the annulus $0.15 < R/R_{500} < 1.00$. This suggests that the low value of β, which we inferred from the Anderson et al. (2015) results could be higher, $\beta \approx 0.25$. This result is more consistent with the gas fraction variation in the NoAGN EAGLE simulation which predicts the MW hot halo hosts approximately $(30 - 40)\%$ of the total halo baryon budget.

In summary, in the EAGLE simulations, we find that the steepening of the $L_{\rm X} - M_{\rm vir}$ relation above 5/3 is due to the variation of the halo gas fraction with halo mass.

Table 3.2 demonstrates that the slope of the $f_{\rm gas} - M_{\rm vir}$ relation can be robustly and precisely extracted from observations of the $L_{\rm X} - M_{\rm vir}$ relation in the halo mass range $10^{12} - 10^{13.5}$ $\rm M_{\odot}$. This same methodology can be applied to the real universe to constrain the gas fraction of halos. As the $f_{\rm gas} - M_{\rm vir}$ relation is strongly affected by AGN feedback, these constraints will provide insight on the scale and extent of AGN driven winds.

3.6 Missing feedback problem

The inner region of the hot X-ray-emitting coronae around disc galaxies is the site of a complex interplay between the accreted, quasi-hydrostatic halo and the hot, metal-enriched winds driven by SNe feedback within the ISM (Putman et al., 2012). However, X-ray observations of the inner regions of star-forming disc galaxies typically find relatively low X-ray luminosities (Li & Wang, 2013a). The observed X-ray luminosities can be compared with the rate of energy input into galaxies from SNe feedback. The coupling efficiency, η_X, is defined as the ratio of the observed X-ray luminosity to the rate of energy input from SNe which can be calculated from the inferred recent star formation rate, $\eta_X = L_{\rm X}/\dot{E}_{\rm SN}$. In real observations, the mean value of this coupling efficiency has been found to be very small, approximately $\eta_X \approx 0.004$ (Li & Wang, 2013b), and thus the energy input by SNe is said to be "missing". The apparent low X-ray luminosity is sometimes referred to as the "missing feedback" problem (e.g. Wang, 2010).

The fate of SNe-heated gas falls into one of three categories:

1. **halo ejection:** hot gas is rapidly blown out of the galactic halo and joins the intergalactic medium;

2. **galaxy ejection:** hot gas is ejected from the galaxy but remains within the virial radius of the halo;

3. **galactic fountain:** outflowing gas cools rapidly and infalls back into the ISM of the galaxy.

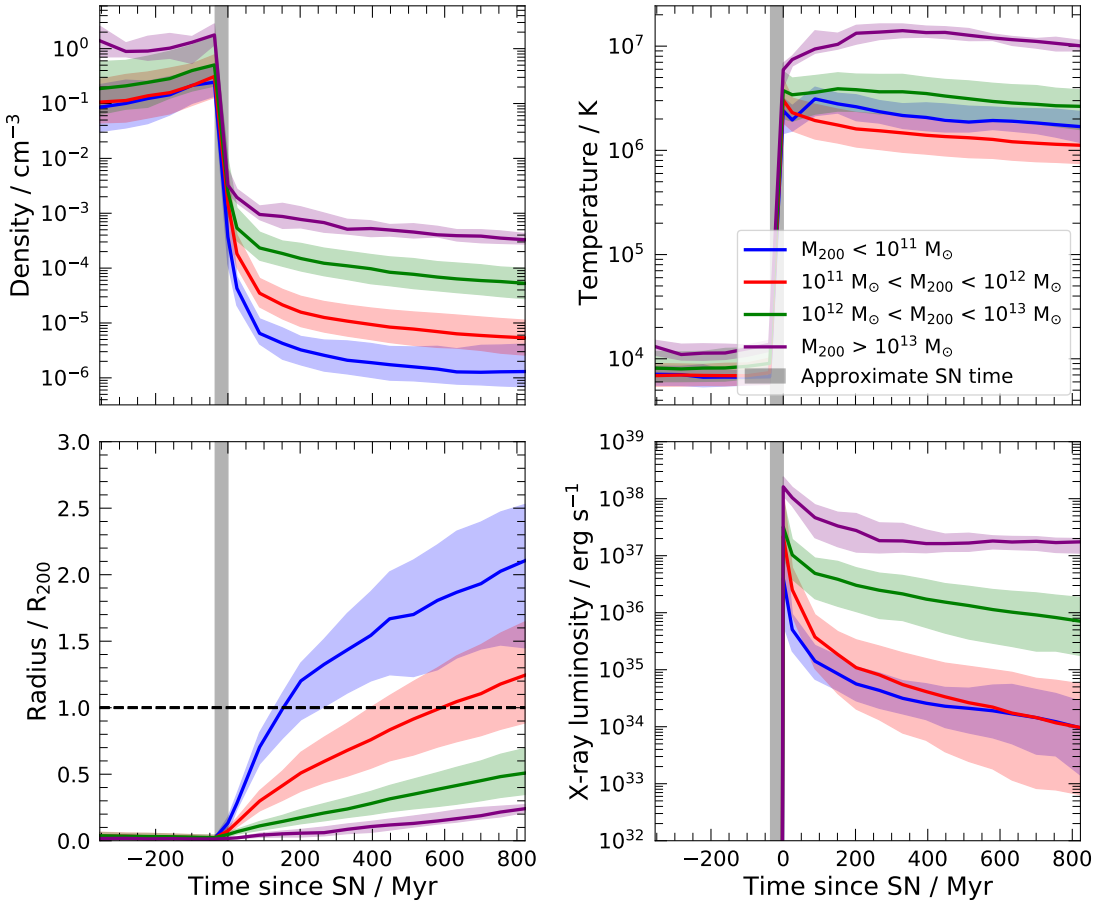

Figure 3.10: The properties of gas particles within the halo virial radius of disc galaxies in the EAGLE reference simulation, which have been subject to direct SNe energy feedback within the last 25 Myr of $z = 0.1$. The particles are separated into categories based on the $z = 0$ virial mass, M_{200}, of the host halo. We show the median property, at each time output, for all particles in halo mass ranges: $M_{200} < 10^{11}$ M$_\odot$, $10^{11} < M_{200}/$ M$_\odot < 10^{12}$, $10^{12} < M_{200}/$ M$_\odot < 10^{13}$ and $M_{200} > 10^{13}$ M$_\odot$, shown by the blue, red, green and purple lines respectively. The median atomic number density, temperature, radius and X-ray luminosity, of each particle are show in the upper-left, upper-right, bottom-left and bottom-right panels respectively. The shaded regions enclose the 20th and 80th percentiles.

The low X-ray luminosity observed within the central regions of star-forming galaxies can be used to distinguish amongst these three possibilities. For example, in the case of an efficient galactic fountain, it is expected that there will be significant X-ray emission concentrated around the central regions of the halo. These X-rays will be emitted by hot, dense gas as it cools and falls back into the galaxy. The other two scenarios will lead to hot gas moving outwards through the galactic halo and thus reducing in density. These halos will have much less X-ray emission, for the same SFR, as less energy is radiated due to the lower density.

The value of the X-ray coupling efficiency in the EAGLE reference simulation is shown in Fig. 3.9 for a sample of isolated disc galaxies. We calculate the X-ray luminosity for all gas particles within a sphere of radius, R_{200}, centred on the centre of mass of the halo. The rate of energy injection by SNe, $\dot{E}_{\rm SN}$, is known in the EAGLE simulations: the subgrid model assumes that, on average, 8.73×10^{15} erg g^{-1} of energy is injected per unit of initial stellar mass formed. This can be combined with the mean star formation within the last 250 Myr to calculate the mean energy injection rate.

Fig. 3.9 shows that, typically, the X-ray coupling efficiency increases with halo mass. This is consistent with the work of Li & Wang (2013b) who suggest that halos with more gas in their central regions are able to retain more of the gas heated by feedback and thus be more X-ray luminous at a given SFR. The correlation between halo mass and X-ray coupling efficiency is consistent with the results of Fig. 3.3 which shows that in very low mass halos there is a very rapid increase in the X-ray luminosity with halo mass. As we can see in Fig. 3.2, low mass halos of $\rm M_{200} \leq 10^{11.5}$ $\rm M_{\odot}$, are *wind*-dominated and therefore the X-ray emission from them is powered by SNe. In these halos, there is a positive correlation between SFR and halo mass. As the X-ray coupling efficiency is also proportional to the halo mass, this results in a steep relationship between X-ray luminosity and halo mass for low mass halos.

We now attempt to understand the origin of the varying X-ray coupling efficiency in the EAGLE simulations. We start by selecting all gas particles within the virial radius of disc galaxies in the EAGLE reference simulation that have been subject

to direct SNe heating within the last 25 Myr at $z = 0.1$. We then use a series of high-cadence outputs from the simulations to track several properties of the selected particles as a function of time, starting approximately 300 Myr before the feedback event, until ≈ 800 Myr after. The particles are then separated into four $z = 0$ host halo mass bins: $M_{200} < 10^{11}$ M$_\odot$, $10^{11} < M_{200}/\text{ M}_\odot < 10^{12}$, $10^{12} < M_{200}/\text{ M}_\odot < 10^{13}$ and $M_{200} > 10^{13}$ M$_\odot$. We plot the median atomic number density, temperature, radius and X-ray luminosity of each particle in each halo mass bin at every output. These are shown in the upper-left, upper-right, bottom-left and bottom-right panels of Fig. 3.10 respectively. The shaded regions show the bands that enclose the 20th and 80th percentiles.

In Fig. 3.10 we see that prior to the feedback event, the majority of the gas is dense (≈ 0.1 cm^{-3}), cold ($\approx 10^4$ K) and near the centre of the halo. This is consistent with being the ISM of the central galaxy. In the output immediately after the feedback event, the gas undergoes an almost instantaneous temperature increase to approximately 10^7 K, which is lower than the peak temperature of $10^{7.5}$ K imposed by SNe feedback. This suggests that the initial cooling rate must be very high and, as a result, the maximum temperature is poorly sampled. In the 25 Myr after the feedback event, the median temperature of the SNe-heated gas, in all but the most massive halos, declines to $\approx (1-3) \times 10^6$ K. As the gas evolves further, the median temperature stabilises; this is likely because the density has decreased and thus, the radiative cooling efficiency has also decreased. As the density and temperature stabilise, the X-ray luminosity reaches an approximately constant value that correlates with halo mass. In the most massive halos, $\geq 10^{13}$ M$_\odot$, the post-SNe temperature of the gas is approximately a constant value of 10^7 K. This high temperature is likely the result of the feedback-heated gas approaching thermal equilibrium as it mixes with the surrounding hot halo gas.

The 3D physical distance from the centre of the galaxy, normalised by the virial radius of the host halo, is plotted in the bottom-left panel of Fig. 3.10 as a function of time since the feedback event. In the lowest mass halos, $M_{200} < 10^{11}$ M$_\odot$, the median gas particle subject to feedback leaves the virial radius of the halo in less than

200 Myr. On the other hand, in the more massive halos, $10^{12} < M_{200}/\ \mathrm{M}_{\odot} < 10^{13}$, the median particle is still within the inner half of the virial radius after 500 Myr. In lower mass halos, the density drops more rapidly. These effects combine to compound the "missing feedback" problem in low mass halos, as seen in Fig. 3.9. It is also likely that these effects are not independent, e.g. leaving the halo more rapidly will result in faster decreasing densities.

Fundamentally, the EAGLE simulations predict that the so-called "missing feedback" is associated with outflowing material. Therefore we predict that halos with galactic fountains should have much higher X-ray coupling efficiencies. Future observations might be able to distinguish between efficient galactic fountains, as in the Auriga simulations (Grand et al., 2019), and the more outflowing, baryon-deficient halos produced in the EAGLE simulations.

3.7 Discussion and Conclusions

The presence of hot accreted X-ray luminous gaseous atmospheres in quasi-hydrostatic equilibrium around late-type galaxies in halos of mass $\geq 10^{12}$ $\mathrm{M}_{\odot}$ is a fundamental prediction of galaxy formation models within ΛCDM (White & Frenk, 1991). After numerous failed searches for diffuse X-ray emission from these galaxies over the years, detections were finally forthcoming in the early 2000s, as discussed in the Introduction. However, these detections have often been attributed to hot, outflowing winds driven by feedback in the ISM of the galaxy rather than by accreted coronae. We have used the large-volume, cosmological hydrodynamics EAGLE simulations to investigate the origin and properties of the hot, X-ray emitting gas around disc galaxies. Although our focus has been on emission from individual $\sim L^{\star}$ galaxies, we have also briefly considered more and less massive galaxies, particularly when discussing scaling relations. Our main results are as follows:

- The EAGLE simulations predict that MW-mass halos are baryon deficient relative to the mean baryon faction (see Fig. 3.1). Specifically, they contain

only $\approx 40\%$ of the mean cosmic baryon fraction within their halo virial radius. About half of the baryons are present as a hot ($T > 10^{5.5}$ K) gaseous halo. This baryon deficiency is attributed to feedback which can drive halo-wide winds. In more massive haloes, $M_{\rm vir} \geq 5 \times 10^{13}$ M$_\odot$, the baryon fraction approaches the cosmic mean.

- The central halo X-ray emission in the EAGLE simulations is dominated by winds triggered by SNe feedback. The X-ray emission in the outer regions is generally produced by an accreted, quasi-hydrostatic hot gaseous halo (see Fig. 3.2). Excising the inner $0.10R_{\rm vir}$ of the halo is sufficient to remove the majority of the hot gas heated by SNe feedback in halos of mass $\geq 10^{12}$ M$_\odot$, thus allowing us to probe the emission from hot, accreted atmospheres predicted in the analytic galaxy formation framework proposed by White & Rees (1978) and, for ΛCDM, by White & Frenk (1991).

- The EAGLE simulations reproduce the observed general trend of X-ray luminosity with halo mass; however, the simulations typically overpredict the X-ray luminosity in the outer regions of haloes of mass $M_{\rm vir} \geq 2 \times 10^{12}$ M$_\odot$ (see Fig. 3.3). The origin of the excess emission appears to be too high a gas fraction. Varying the parameters of AGN feedback to make it more expulsive, as in the AGNdT9-L050N0752 simulation, can improve the agreement with the observed X-ray luminosities. In the inner regions, where winds dominate the X-ray luminosity, the EAGLE simulations reproduce both the trend and scatter of the observed $L_{\rm X} - M_{\rm vir}$ relation.

- We predict that any steepening of the logarithmic slope of the $L_{\rm X} - M_{\rm vir}$ relation, above the self-similar value, $\alpha = 5/3$, is due to a varying hot gas fraction with halo mass. We show that the logarithmic slope of the power-law relationship between gas baryon fraction and halo mass can be inferred from the $L_{\rm X} - M_{\rm vir}$ relation using an analytical relation we derived, Eq. 3.2.3. This relation holds across several EAGLE simulations which employ different AGN feedback prescriptions. The same methodology can be applied to future X-ray

observations to constrain the slope, normalisation and scatter of the halo gas fraction as a function of halo mass.

- We identify the physical origin of the so-called "missing feedback" around low-mass, star-forming galaxies. The EAGLE simulations suggest that much of the energy injected by SNe feedback is lost as hot gas is ejected from the halo into the low-density IGM (see Fig. 3.10). Hot winds, driven by SNe feedback, can leave low mass halos of mass, $\approx 10^{11}$ $M_{\odot}$, in a timescale of ≈ 100 Myr. By contrast, in higher-mass halos, which have a more gas-rich central region, the outflowing gas is trapped at a higher density where it can radiate a larger fraction of the injected energy. This leads to a sharp increase in X-ray luminosity as a function of halo mass within the central regions.

Chapter 4

Apostle-Auriga: a comparison

4.1 Introduction

As described in Chapter 2 the inclusion of sub-resolution models is critical to reproduce realistic galaxy populations in modern hydrodynamical simulations. While the inclusion of subgrid models in simulations is universal, there is no standard implementation, particularly for feedback from both SNe and AGN. The complexity of baryon physics, together with limited resolution, makes it impossible to include feedback *ab initio* from individual massive stars, SNe or AGN in representative cosmological simulations. Instead, simulations rely on 'subgrid' prescriptions of feedback, that is, physically motivated models whose parameters may be calibrated by reference to observational data. Thus, even though the physical processes responsible for stellar winds, SNe and AGN feedback are not resolved, it is hoped that their effects on large scales can be faithfully reproduced.

Fundamentally, the SNe subgrid model describes how SNe energy from a single star particle, which typically represents a simple stellar population (SSP), is distributed to neighbouring gas elements. Energy can be injected into either a single gas resolution element, or into many, as kinetic (Navarro & White, 1993; Dalla Vecchia & Schaye, 2012) or thermal (Dalla Vecchia & Schaye, 2012; Schaye et al., 2015) energy, or both (Springel & Hernquist, 2003; Vogelsberger et al., 2014). There are subtleties

within these different models such as the amount of energy available per mass of stars formed, thermal losses, the ratio of thermal to kinetic energy injection, the decoupling of hydrodynamics to disable cooling and more. Similar considerations apply to AGN feedback (see Smith et al. 2018 for an in-depth review).

In modern simulations the free parameters of the SNe and AGN subgrid models are tuned to reproduce a selection of properties of real galaxies. Gas properties are rarely included in this calibration and are often taken as model predictions that can be compared with observational data. Large-scale gas properties such as cosmic accretion into haloes and onto galaxies have been studied extensively (e.g. Kereš et al., 2005; Brooks et al., 2009; Oppenheimer et al., 2010; Hafen et al., 2019; Hou et al., 2019). These analyses illustrate how the injection of gas and metals by feedback complicates the baryon cycle within the circumgalactic medium (CGM) of galaxies, affecting gas inflow rates onto galaxies by both reducing the rate of first-time gaseous infall (van de Voort et al., 2011a; Nelson et al., 2015) and by recycling previously ejected winds (Oppenheimer et al., 2010). However, the sensitivity of these processes to the details of the subgrid model or the spatial scale at which they are significant is uncertain (van de Voort et al., 2011b).

Differences in hydrodynamical solvers introduce further uncertainty in the cosmological baryon cycle (Sijacki et al., 2012; Kereš et al., 2012; Vogelsberger et al., 2012; Torrey et al., 2012; Bird et al., 2013; Nelson et al., 2013). In general, it appears that hot gas in moving-mesh simulations cools more efficiently than in particle-based simulations; therefore, two simulations with the same subgrid model but different hydrodynamical solvers can have different gas properties. We do not investigate the effects of different hydrodynamical solvers in this thesis, although we consider the implications in light of our results. As we suspect, these differences turn out to be secondary to those introduced by the subgrid models (Hayward et al., 2014; Schaller et al., 2015a; Hopkins et al., 2018).

In this chapter, we focus on the effects of different implementations of SNe feedback on the Local Group baryon cycle. We compare the (untuned) emergent baryon cycle in the Apostle and Auriga simulations of two Local Group-like volumes (Sawala

et al., 2016; Fattahi et al., 2016). The two simulations use the same gravity solver and initial conditions but have different subgrid galaxy formation models, with, in particular, very different approaches to SNe and AGN feedback. The Auriga simulations use hydrodynamically decoupled wind particles that are launched isotropically and, upon recoupling, inject both thermal and kinetic energy into the surrounding gas. In Apostle, SNe energy is injected as a 'thermal dump' which heats a small number of neighbouring gas elements to a predefined temperature.

Despite the large differences in the subgrid model, which extends beyond the implementation of SNe feedback, both of these galaxy formation models produce galaxies at the present day that match many observed properties. Furthermore, both models have been demonstrated to be give a good match to properties of the galaxy population as a whole. The Apostle model is a modified version of the EAGLE reference model (Schaye et al., 2015; Crain et al., 2015). However, it has 'weaker' AGN (due to slower black hole accretion and growth) and is used at an order of magnitude higher mass resolution than in the calibration runs (Crain et al., 2015). This difference in resolution is significant, as the EAGLE model is very resolution-dependent. The Auriga model has not been explicitly used in large cosmological simulations; however, it is based on the model used in the Illustris simulations (Vogelsberger et al., 2013, 2014; Torrey et al., 2014), and is similar to that in IllustrisTNG (Nelson et al., 2018) and FABLE (Henden et al., 2018).

The baryon cycle around galaxies, focussing on the CGM, has previously been studied in hydrodynamic simulations using particle tracking techniques similar to those in this thesis using both 'zoom' simulations (Nelson et al., 2013; Ford et al., 2014; Christensen et al., 2018; Suresh et al., 2019; Sokołowska et al., 2018; Tollet et al., 2019; Hafen et al., 2019, 2020) and large volume cosmological simulations (Nelson et al., 2019; Wright et al., 2020; Borrow et al., 2020; Mitchell et al., 2020b,a; Mitchell & Schaye, 2021a,b). In general, the different simulations agree that the CGM of the MW is dominated by cosmological gas accretion on first infall; however, the FIRE simulations (Hafen et al., 2019) predict much higher baryon fractions than EAGLE (Wright et al., 2020; Mitchell et al., 2020b) due to AGN feedback in EAGLE. This

Table 4.1: Simulation parameters at $z = 0$. The columns are: 1) halo name in the form, AP-XX-YY-Apostle/Auriga, where XX and YY identify the volume and the halo, respectively; 2) halo virial mass; 3) halo radius; 4) baryon fraction within R_{200}; 5) stellar mass within 30 kpc; 6) the $\kappa_{\rm rot}$ rotation parameter; 7) radial scale-length; 8) bulge effective radius; 9) Sersic index of the bulge; 10) Black hole mass

	Dark matter		Baryons						
Halo name	$\frac{M_{200}}{[10^{12}{\rm M}_\odot]}$	$\frac{R_{200}}{[{\rm kpc}]}$	$f_{\rm b}$	$\frac{M_*}{[10^{10}{\rm M}_\odot]}$	$\kappa_{\rm rot}$	$\frac{R_{\rm d}}{[{\rm kpc}]}$	$\frac{R_{\rm eff}}{[{\rm kpc}]}$	n	$\frac{M_{\rm BH}}{[M_\odot]}$
AP-S5-N1-Apostle	0.91	199	0.53	2.03	0.58	3.31	1.00	1.02	$10^{6.37}$
AP-S5-N1-Auriga	0.99	205	0.89	5.89	0.66	1.87	0.55	1.04	$10^{8.11}$
AP-S5-N2-Apostle	0.79	190	0.64	1.60	0.54	3.21	0.91	1.06	$10^{6.27}$
AP-S5-N2-Auriga	0.80	191	0.88	3.95	0.64	2.15	0.49	1.07	$10^{7.59}$
AP-V1-N1-Apostle	1.64	242	0.82	4.49	0.58	3.93	1.05	0.99	$10^{6.81}$
AP-V1-N1-Auriga	1.64	242	0.86	10.51	0.59	7.62	0.68	0.73	$10^{7.96}$
AP-V1-N2-Apostle	1.02	207	0.59	1.62	0.26	3.51	1.21	1.06	$10^{6.38}$
AP-V1-N2-Auriga	1.12	213	0.99	3.77	0.68	3.74	0.89	0.92	$10^{7.36}$

chapter builds on this foundation and compares the results between two different simulations, thus attempting to understand the results' model dependence.

This chapter is structured as follows. In Section 4.2 we introduce our sample of simulated haloes and describe the stellar properties of the central galaxies, including morphology, surface density and stellar-mass to halo-mass (SMHM) relation. In Section 4.3 we describe how the particles are tracked and matched between the two simulations using the same initial conditions. We then present our results, starting with a baryon census around our Local Group analogues in Section 4.5, and a particle-by-particle analysis of the 'missing baryons' at $z = 0$ in Section 4.6. In Section 4.7, we attempt to understand how differences in the subgrid models lead to very different baryon cycles on scales up to $\sim$ 1Mpc. We present predicted observables in Section 4.8, and discuss the prospects of constraining the subgrid implementation of SNe feedback from current and future observational datasets. Finally, in Section 4.9 we discuss the implications of our results, including several caveats, and summarize our conclusions.

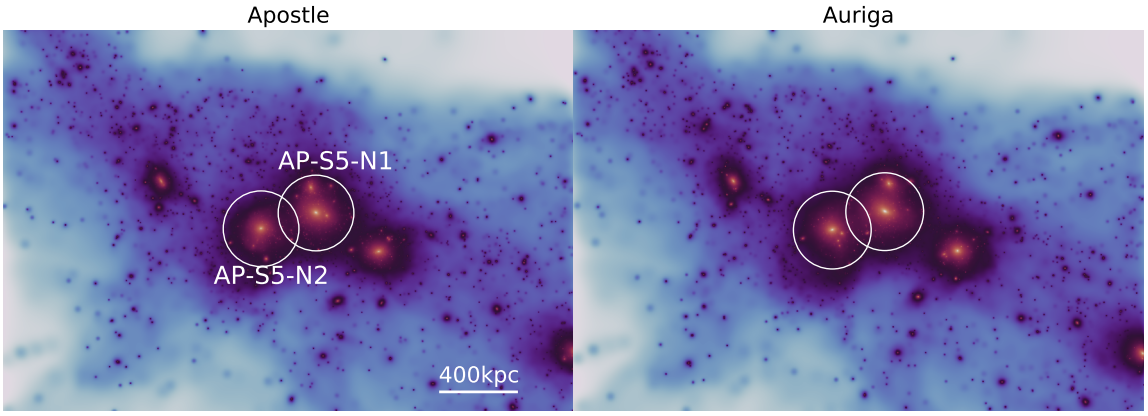

Figure 4.1: Present-day mass-weighted density projection of the dark matter for the AP-S5 volume in both APOSTLE (left) and AURIGA (right). The projected rectangle has dimensions of $(3 \times 2 \times 3)$ Mpc in the x, y and z directions, respectively, centered on the centre of the mass of the two primary haloes. The white circles illustrate R_{200} for these two haloes. The two main haloes do not overlap in 3D space but they do in this particular x-y 2D projection.

4.2 The sample

We focus on ΛCDM hydrodynamical simulations of two Local Group-like volumes. Each is a zoom simulation of a region of radius $2 - 3$ Mpc that contains a pair of large haloes with virial masses in the range 5×10^{11} $M_\odot$ to 2.5×10^{12} $M_\odot$[1]. We refer to the four haloes, split across two volumes, as AP-XX-NY, where XX =S5, V1 specifies which of the two volumes the halo is in, and $Y = 1, 2$ identifies the two primary haloes. AP-V1 and AP-S5 correspond to AP-1 and AP-11 in the original APOSTLE simulations described in Sawala et al. (2016) and Fattahi et al. (2016). The volumes were selected to match some of the dynamical constraints of the Local Group. The two primary haloes are required to have present-day physical separations of ≈ 800 kpc and radial velocities in the range $(0 - 250)$ km s^{-1}. The volumes are also required to have no additional haloes of mass equal to, or greater than, the least massive of the pair within a radius 2.5 Mpc of the pair midpoint. More details about the selection criteria may be found in Fattahi et al. (2016).

[1]We define the virial quantities, R_{200} and M_{200}, according to the spherical overdensity mass (Lacey & Cole, 1994) of each halo centred around the most bound particle within the halo. R_{200} is the radius within which the mean enclosed density, $\Delta = 200$ times the critical density of the universe.

The 'zoom-in' initial conditions (ICs) were created using second-order Lagrangian perturbation theory implemented within IC_GEN (Jenkins, 2010). These ICs have initial gas (dark matter) particle masses of $1.2(5.9)\times10^5$ $M_\odot$, and maximum softening lengths of 307 pc. This resolution level corresponds exactly to the L2 resolution in Sawala et al. (2016) and Fattahi et al. (2016), and is similar to the level 4 resolution in Grand et al. (2017).

AP-XX-YY-Apostle are the APOSTLE simulations which were run using a highly modified version of the GADGET-3 code (Springel, 2005). The fluid properties are calculated with the particle-based smoothed particle hydrodynamics (SPH) technique (Lucy, 1977; Gingold & Monaghan, 1977). The APOSTLE simulations adopted a pressure-entropy formulation of SPH (Hopkins, 2013), with artificial viscosity and conduction switches (Price, 2008; Cullen & Dehnen, 2010) which, when combined, are known as ANARCHY (Schaye et al., 2015). This set up is the same as that in the EAGLE simulations.

The AURIGA simulations, AP-XX-YY-Auriga, were performed with the magneto-hydrodynamics code AREPO (Springel, 2010). The gas is followed in an unstructured mesh constructed from a Voronoi tessellation of a set of mesh-generating points which then allow a finite-volume discretisation of the magneto-hydrodynamic equations. The mesh generating points can move with the fluid flow. This moving mesh property reduces the flux between cells, thus reducing the advection errors that afflict fixed mesh codes. For a detailed description we refer the reader to Springel (2010) and Grand et al. (2017).

The AURIGA simulations follow the amplification of cosmic magnetic fields from a minute primordial seed field. The magnetic fields are dynamically coupled to the gas through magnetic pressure. Pillepich et al. (2017) demonstrates that the stellar mass to halo mass (SMHM) relation is sensitive to the inclusion of magnetic fields, particularly for haloes of $M_{200} \geq 10^{12}$ $M_\odot$. However, this is not important in this thesis as both galaxy formation models are calibrated to reproduce realistic $L^\star$ galaxies.

While the general method of calculating the physical fluid properties in the two

simulations is different, there are some similarities. Both numerical schemes have the property that resolution follows mass, namely, high-density regions are resolved with more cells or particles. Also, both APOSTLE and AURIGA have the same method for calculating gravitational forces: a standard TreePM method (Springel, 2005). This is a hybrid technique that uses a Fast Fourier Transform method for long-range forces, and a hierarchical octree algorithm for short-range forces, both with adaptive timestepping.

The initial conditions are chosen to produce present-day Milky Way (MW) and M31 analogues. As both the AURIGA and APOSTLE simulations share exactly the same initial conditions, we expect several properties of the simulations to be similar. Specifically, the dark matter properties should be consistent in both simulations. Furthermore, as both simulations tune the subgrid models to recover real galaxy properties, we expect some stellar properties to be similar, but less so than the dark matter properties.

Dark matter haloes are identified using a Friends-of-Friends (FoF) algorithm (Davis et al., 1985). The constituent self-bound substructures (subhaloes) within a FoF group are identified using the SUBFIND algorithm applied to both dark matter and baryonic particles (Springel et al., 2001; Dolag et al., 2009).

Table 4.1 lists properties of the two primary haloes in both volumes. We see that the baryonic properties of the four haloes in the two simulations differ somewhat, with up to a factor of two difference in the stellar mass. We also tabulate the baryon fraction, $f_{\rm b}$, in each halo, which we define as the ratio of baryonic to total mass normalised by the mean cosmic baryon fraction, $\Omega_{\rm b}/\Omega_{\rm m} \sim 0.167$, within $\rm R_{200}$. We find that the baryon fraction in the APOSTLE simulations is systematically lower than in their AURIGA counterparts. The virial properties of the haloes are all consistent, however, with small differences in virial mass and radius which are due to the different halo baryon fractions.

Fig. 4.1 shows a dark matter projection of the AP-S5 volume in both APOSTLE and AURIGA. A visual inspection shows that the dark matter distribution of the two haloes, and their local environment, are almost identical in the two simulations.

There is some variation in the location of satellite galaxies and nearby dwarf galaxies; this is likely due to the different baryonic properties and the stochastic nature of n-body simulations.

In Fig. 4.2 we plot the SMHM relation for the four primary haloes in the two simulation volumes, APOSTLE and AURIGA, alongside the inferred relation from abundance matching (Behroozi et al., 2013). We also include several resolved lower mass field 'central'[2] haloes from both APOSTLE and AURIGA to give an indication of the SMHM over a broader mass range. We define the stellar masses as the total stellar mass within an aperture of 30 kpc. The stellar masses of the AURIGA galaxies are consistently larger than those of the APOSTLE galaxies, at a given halo mass, over the entire range of halo masses. As both APOSTLE and AURIGA model the same volume, the differences are not due to sample variance. However, these are only single realisations of the model, and most galaxy formation models incorporate highly stochastic processes; thus re-running these simulations may produce somewhat different results (Genel et al., 2019; Keller et al., 2019; Davies et al., 2021).

Despite using a modified and higher resolution version of the EAGLE galaxy formation model, the four APOSTLE haloes in this thesis are similar to their EAGLE counterparts. The four APOSTLE haloes, which have a halo mass $\sim 10^{12}$ $M_\odot$, have a stellar mass range, $M_* \sim (1-5) \times 10^{10}$ $M_\odot$. This is in agreement with the EAGLE reference simulations which predict a range of $(0.5-5) \times 10^{10}$ $M_\odot$ (see Figure 7 of Matthee et al. 2017). The black hole mass of the four APOSTLE haloes is approximately a few $\sim 10^6$ $M_\odot$, which is very similar to those of the EAGLE reference simulation with the same stellar/halo mass (see Figure 10 of Schaye et al. 2015). However, the APOSTLE haloes in this study are considerably more baryon rich than those found in the EAGLE reference simulation. This predicts 15th and 85th percentiles for the halo baryon fraction of $f_\mathrm{b} \sim 0.3-0.45$, for halo masses of $\sim 10^{12}$ $M_\odot$ (see Figure 1 of Kelly et al. 2021). The lowest baryon fraction of the APOSTLE haloes presented in Table 1 is $f_\mathrm{b} = 0.53$. The reason for the larger baryon fraction in APOSTLE is likely two-fold. First, the APOSTLE simulations use the 'ViscLo' subgrid

[2]'Central' refers to the most massive subhalo with a FoF (Davis et al., 1985) group.

physics parameters, which are identical to the EAGLE reference parameters except for a lower viscosity for the BH's subgrid accretion. Thus, the APOSTLE black holes will accrete at a lower rate than EAGLE black holes. Secondly, the EAGLE simulations were calibrated at a lower resolution. Using a similar model with higher mass resolution can make the stellar feedback more efficient which can reduce gas accretion onto the BH, stalling its growth and reducing AGN feedback. Oppenheimer et al. (2020b) demonstrated that sudden black hole growth, and AGN feedback, can reduce the baryon fraction around MW-mass haloes.

We also briefly analyse the stellar surface density profiles of the four primary haloes at the present day. We fit the surface density profiles with a combination of an exponential profile of scale radius, $R_{\rm D}$, and a Sersic profile of the form $\exp(R/R_{\rm eff})^n$ (Sérsic, 1963). The values of the best-fit parameters, $R_{\rm D}$, $R_{\rm eff}$ and n, are given in Table 4.1. The fit parameters of the models are consistent with the isolated MW-mass galaxies, the original AURIGA haloes, presented in Grand et al. (2017). Furthermore, the stellar surface density at the solar radius is a few times ~ 10 M$_\odot$ pc^{-2} in all of the haloes which is consistent with estimates for the Milky Way (Flynn et al., 2006). The surface density profiles, and best fit models, can be seen in Fig. 4.4. The galaxy stellar surface density profiles are similar in most cases in the two simulations, albeit with a systematically higher surface density in the case of AURIGA.

We also calculate the $\kappa_{\rm rot}$ rotation parameter for each galaxy, a measure of the fraction of kinetic energy in organized rotation, which correlates with morphology (Sales et al., 2012). The quantity $\kappa_{\rm rot}$ is defined such that $\kappa_{\rm rot} \approx 1$ for discs with perfect circular motions and $\kappa_{\rm rot} \approx 1/3$ for systems with an isotropic velocity dispersion. Thus, a large $\kappa_{\rm rot}$ indicates a disc galaxy, whereas a lower value indicates an elliptical galaxy. $\kappa_{\rm rot}$ requires a definition of the z-axis which we take to be the direction of the total angular momentum of all stars within 30 kpc of the centre of the galaxy. The large values of $\kappa_{\rm rot}$ in Table 4.1 are consistent with a visual inspection of Fig. 4.3, which shows face-on and edge-on stellar projections of the four primary haloes. In Fig. 4.3 we see that most of the galaxies appear to be 'disky' in projection, with the exception of AP-V1-N2-Apostle, which has a low $\kappa_{\rm rot}$.

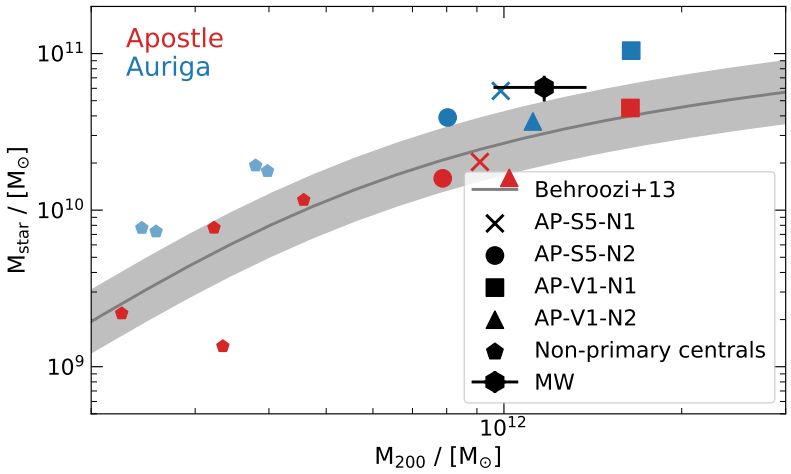

Figure 4.2: The stellar-mass-to-halo-mass relation in the APOSTLE (red) and AURIGA (blue) simulations. The four different symbols (cross, circle, square and triangle) differentiate the four different primary haloes. The smaller blue and red pentagons show the SMHM relation for 'central' field galaxies in the APOSTLE and AURIGA simulations respectively. The black solid line and grey shaded region are the results of Behroozi et al. (2013) with an estimated scatter of ±0.2 dex. We also show as a black hexagon with errorbars the estimate for the Milky Way halo mass by Callingham et al. (2019) and of the stellar mass by Licquia & Newman (2015)

In general, the AURIGA simulations exhibit more recognisable morphological features, spiral arms and distinct bar components (AP-S5-N2, AP-V1-N1 and AP-V1-N2). The APOSTLE simulations produce smoother looking discs, with little morphological evidence of either a bar or spiral arms. It is unclear what causes these morphological differences, but they could be due to different effective spatial resolutions in the two simulations. In SPH simulations, the smoothing length determines the spatial resolution, and the ratio of the smoothing length to the mean inter-particle separation is usually a free parameter taken to be ~ 1.3 (Price, 2012). Whereas in moving mesh simulations, the cells have a spatial radius of approximately ~ 0.5 the mean cell separation. Thus moving mesh simulations typically have a $\sim 1.3/0.5 \sim 2.4$ times better spatial resolution at the same mass resolution[3].

Fig. 4.4 shows stellar surface density profiles, for stellar mass within ±5 kpc of the mid plane in the vertical direction, for all simulations at $z = 0$. The profiles are

[3]By the same mass resolution, we mean that the cell mass in a moving mesh simulation is equal to the particle mass in an SPH simulation, as in this thesis.

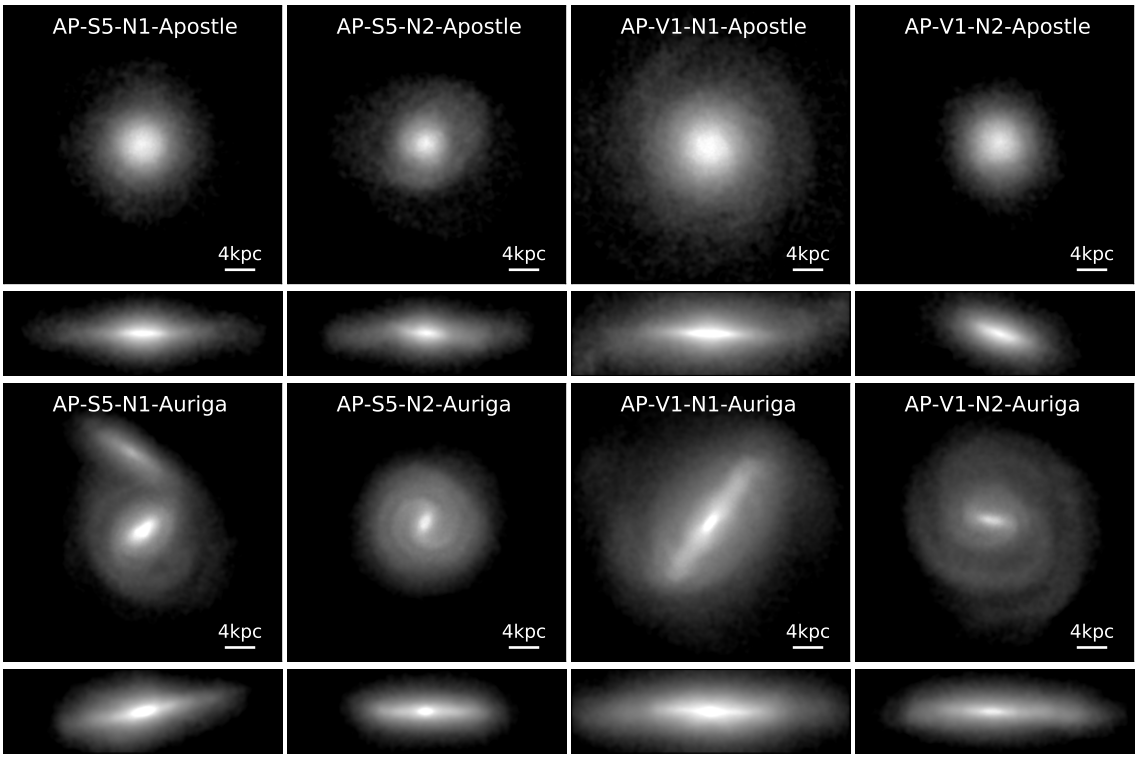

Figure 4.3: Mass-weighted face-on (top) and edge-on (bottom) projections of the stars in the four haloes in the APOSTLE and AURIGA simulations at $z = 0$

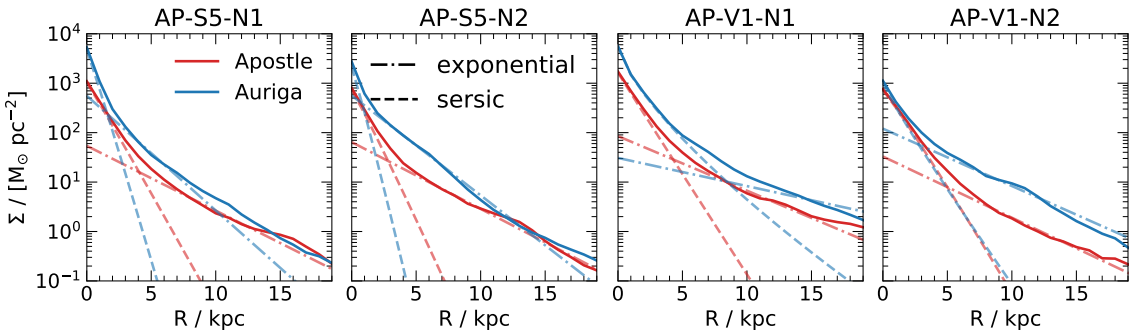

Figure 4.4: The radial stellar surface density profiles of the four primary haloes. The surface densities are calculated using all the stellar particles within a physical height of ± 5 kpc from the galactic plane; these are shown as solid lines. The radial profiles are simultaneously fit with a Sersic (dashed) and exponential (dashed-dotted) profile using a non-linear least-squares method. Results for the APOSTLE and AURIGA simulations are shown in red and blue respectively. The best-fit parameters may be found in Table 4.1.

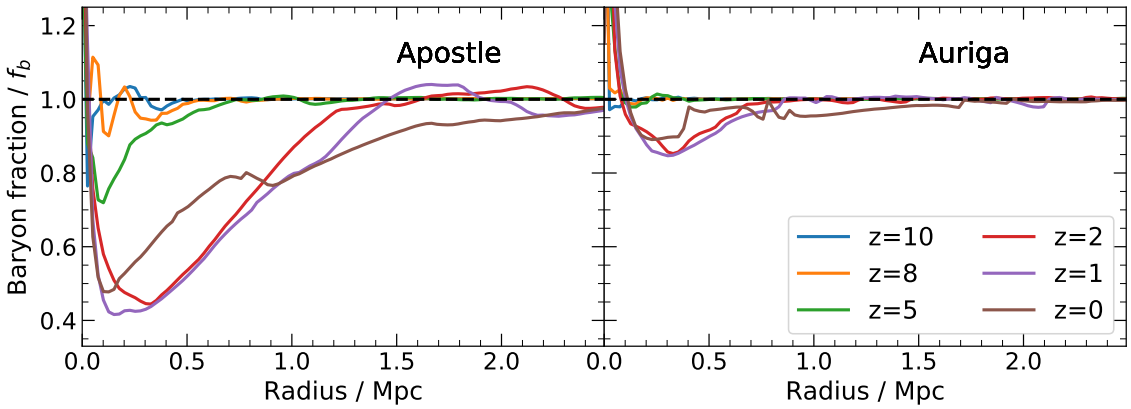

Figure 4.5: The baryon fraction within a sphere centred around the primary halo, AP-S5-N1, as a function of the sphere radius. The baryon fraction is calculated within 100 spheres with a linearly increasing radius in the range $0 - 2.5$ Mpc (co-moving). We repeat the process at six redshifts, $z = 0,\ 1,\ 2,\ 5,\ 8$ and 10, which are shown by the brown, purple, red, green, orange and blue solid lines, respectively. The left panel shows the results in APOSTLE and the right panel in AURIGA. The baryon fraction is normalised by the mean baryonic-to-dark matter ratio, f_b, in the universe. The dashed black line indicates a baryonically closed system.

simultaneously fit with a linear sum of an exponential profile of scale radius, $R_{\rm D}$, and a Sersic profile of the form $\exp(R/R_{\rm eff})^n$ (Sérsic, 1963). The best fit values are calculated using the least squares method to logarithm density profile.

4.3 Methods

4.4 Tracer particles and particle matching

The quasi-Lagrangian technique of AREPO allows mass to advect between gas cells so each cell may not represent the same material over the course of the simulation. The AURIGA simulations, however, include Lagrangian Monte Carlo tracer particles (Genel et al., 2013; DeFelippis et al., 2017) which enable us to track the evolutionary history of individual gas mass elements in a way that allows direct comparison to SPH gas particles in APOSTLE. The Monte Carlo tracer particles have been shown to reproduce the density field in various tests, including cosmological simulations, accurately (Genel et al., 2013).

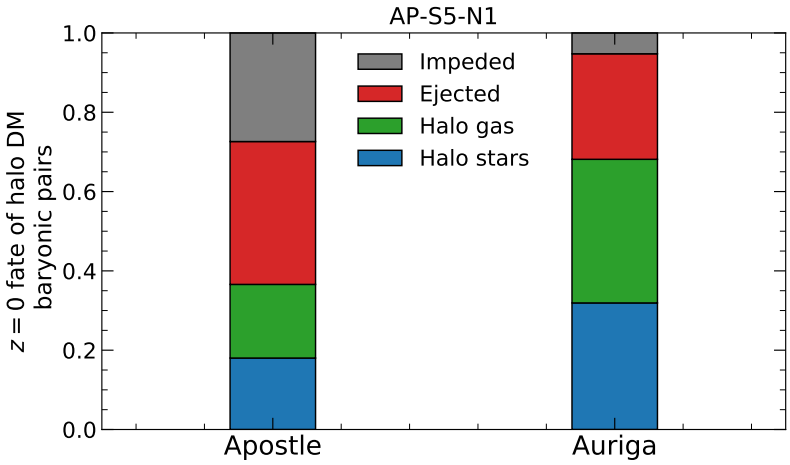

Figure 4.6: The present-day fate of the baryonic counterparts of the dark matter particles within R_{200} of the primary halo AP-S5-N1 in Apostle and Auriga. The halo stars, halo gas, ejected gas and impeded gas are shown by blue, green, red and grey bars, respectively. See the text for a detailed description of these categories.

In Auriga, a single tracer particle is attached to each gas cell at the beginning of the simulation. As the simulation proceeds, tracer particles can transfer across cell boundaries with a probability given by the ratio of the outward-moving mass flux across a face and the mass of the cell. This allows the tracer particles to emulate the evolution of a Lagrangian gas element. The tracer particles do not carry any physical properties. Instead, they inherit the properties of the baryonic element to which they are attached at any given time. The tracer particles introduce a Poisson noise due to their probabilistic evolution. However, as we use several million tracer particles, this noise is insignificant.

A combination of identical initial conditions and the tracer particles in Auriga allows us to perform a detailed comparison between the two simulations on the scales of individual baryonic mass-elements. In the Apostle simulations, each dark matter particle in the initial conditions is assigned a gas particle at the start of the simulation. This represents the baryonic mass from the same Lagrangian region as the associated dark matter particle. Likewise, the dark matter particles within Auriga are assigned tracer particles. Both the tracer particles in Auriga, and the gas particles in Apostle, are assigned permanent, unique ID's dependent on their parent dark matter particle. The unique ID assigned to each particle facilitates

direct comparison of the same baryonic mass elements between the two simulations.

4.5 Baryon evolution

As we have shown in Section 4.2, APOSTLE and AURIGA produce galaxies in MW-mass haloes that have roughly similar morphologies, stellar masses and stellar mass distributions. However, as the simulations are calibrated to reproduce a number of stellar properties of the observed galaxy population, these similarities are not too surprising. In this section we explore the effects of the two different hydrodynamical schemes and feedback implementations on the *untuned* baryon properties. In particular, we investigate the baryon fraction around the two pairs of MW and M31 analogues and how this evolves with both radius and time.

In Fig. 4.5 we investigate the baryon fraction within a sphere centred on the main progenitors of the AP-S5-N1 simulations, as a function of radius at six different redshifts. Even though both simulations follow the assembly of the same dark matter halo, the baryon fraction within a sphere of radius ≈ 500 kpc (comoving) begins to differ significantly between $z = 8$ and $z = 5$. By $z = 2$ the APOSTLE model has developed a baryon deficiency of $\geq 10\%$ within a radius of ≥ 1 Mpc (comoving), extending to ≈ 2 Mpc at the present day. We refer to this is the Local Group baryon deficiency. By contrast, in the AURIGA simulations the baryon fraction is within 10% of unity for radii ≥ 0.5 Mpc (comoving) at all redshifts. Furthermore, the minimum baryon fraction within a sphere around the primary AURIGA galaxy is $\approx 80\%$, approximately twice that of its APOSTLE counterpart.

In Table 4.1 the baryon fraction of AP-V1-N1-Apostle is similar ($\sim 0.85\Omega_{\rm b}/\Omega_{\rm m}$) to that of the AURIGA counterpart. However, the baryon fraction of this galaxy at $z = 1$ was $\sim 0.5\Omega_{\rm b}/\Omega_{\rm m}$, almost a factor of two lower than in AURIGA. Furthermore, the baryon fraction within a radius of ~ 1 Mpc is $\sim 30\%$ lower than in AURIGA. Thus, even the most baryon rich halo in APOSTLE is still baryon poor compared to the same halo in AURIGA. The differences in the baryon fraction of the haloes in the local region, out to ~ 1 Mpc, around AP-S5-N1 are representative of the sample.

Thus, while we focus on the individual halo AP-S5-N1 for illustration, the general results are valid for all haloes in our sample.

In both APOSTLE and AURIGA the halo baryon deficiency peaks at around $z = 1-2$, which is consistent with the observed peak in the star formation rate in the real universe (Madau & Dickinson, 2014). However, the amplitude, spatial extent and scale of the baryon deficiency in APOSTLE, compared to AURIGA, is striking. This difference is particularly remarkable given that the primary galaxies are relatively similar.

AGN feedback is often thought to be the cause of low baryon fractions in MW-mass, and more massive haloes in cosmological hydrodynamical simulations (Bower et al., 2017a; Nelson et al., 2018; Davies et al., 2019). Nevertheless, we see from Fig. 4.5 that the decrease in baryon fraction in APOSTLE sets in at high redshift when the halo masses, and thus the black hole masses, are much lower. These results thus imply a different driver for the low baryon fractions at early times. While these haloes are already baryon deficient early in their evolution, the addition of AGN feedback can further decrease the baryon fraction. As described, the AGN feedback in APOSTLE is weaker than that found in EAGLE, which can explain why the APOSTLE haloes are almost twice as baryon rich as those in the EAGLE reference model.

Although the two simulations predict very different local baryon fractions, both within the halo and beyond, it is difficult to ascertain which of these models is the more *realistic*. In practice, it is very difficult to infer the baryon fractions of real galaxies. For external galaxies these are typically derived from X-ray emission using surface brightness maps to infer a gas density profile. These inferences also require information about the temperature and metallicity profiles, which are difficult to measure accurately with current instruments (Bregman et al., 2018).

In the Milky Way, the baryonic mass in stars, cold and mildly photoionised gas and dust is estimated to be 0.65×10^{11} $\mathrm{M}_\odot$ (McMillan, 2011). The total mass of the halo, which is dominated by dark matter, is estimated to be $(1.17 \pm 0.15) \times 10^{12}$ $\mathrm{M}_\odot$ (Callingham et al., 2019). Assuming a universal baryon fraction of $\Omega_\mathrm{b}/\Omega_\mathrm{m} \approx 0.157$ (Planck Collaboration et al., 2013) implies that $0.8{\times}10^{11}$ $\mathrm{M}_\odot$ of the MW's baryons are

unaccounted for. There is strong evidence that some fraction of these unaccounted baryons resides in a hot gaseous corona surrounding massive haloes; however, the total mass remains uncertain. An accurate estimate of the mass of the MW hot halo requires knowledge of the gas density profile as a function of radius. While the column density distribution of electrons is constrained in the direction towards the LMC (Anderson & Bregman, 2010), there is a degeneracy between the normalisation and the slope of the electron density profile (Bregman et al., 2018). Assuming a flat density profile (e.g. Gupta et al., 2012, 2014; Faerman et al., 2017), the MW appears to be 'baryonically closed'. However, for faster declining density profiles (see Miller & Bregman, 2015; Li & Bregman, 2017), the gaseous halo out to R_{200} contains only half of the unaccounted baryons. Therefore, the predictions of Fig. 4.5 for both Apostle and Auriga are consistent with observations given the uncertainties.

4.6 The missing halo baryons

In this section we carry out a detailed analysis, on a particle-by-particle basis, of the differences in the present-day baryon contents of the Apostle and Auriga Local Group analogues. As we described in Section 4.4, each dark matter particle is assigned a gas particle, or a tracer particle, which shares the same Lagrangian region in the initial conditions. In the absence of baryonic physics, these particles would evolve purely under gravity and would thus end up in the same halo as their dark matter counterparts. We refer to these as 'predestined' particles. However, hydrodynamics and feedback will significantly alter their fate.

We start our analysis by identifying all the dark matter particles present in each of the primary haloes at $z = 0$. We then identify the baryonic companions of these dark matter halo particles and categorise their $z = 0$ state, as illustrated in Fig. 4.6, classifying them into the following four categories:

- **Halo gas:** gas particles within R_{200} of the primary halo
- **Halo stars:** star particles within R_{200} of the primary halo

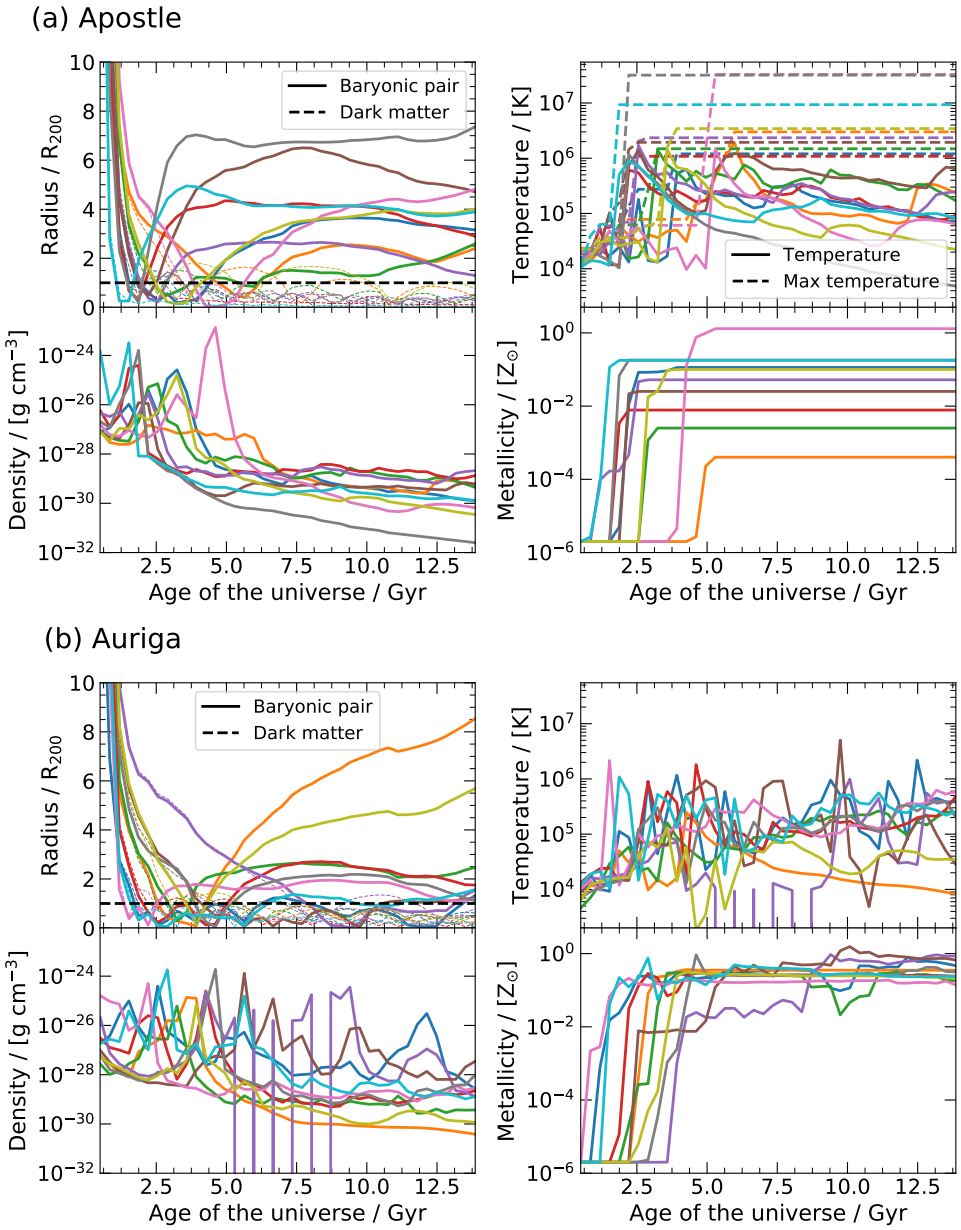

Figure 4.7: The evolution of 10 randomly selected halo baryonic tracer particles classified as 'ejected' from an (a) Apostle and (b) Auriga halo. For both (a) and (b), the top-left, top-right, bottom-left, and bottom-right panels show the radius from halo centre, mean temperature, density and metallicity as a function of time. The particle properties are sampled at 60 snapshots linearly spaced as a function of the age of the universe. The radius is given in units of $R_{200}(z)$. The top-left panel also includes the radial position of the dark matter counterpart of each baryon particle; these are illustrated with a dashed line of the same colour. In the bottom-right panel, which shows the metallicity, there are several lines which lie on top of one another and thus are not visible. The same random particle is identified in each panel by the same coloured line.

- **Ejected gas:** gas particles which are outside R_{200} at $z = 0$ but had closest approach radii smaller than R_{200} at a previous redshift
- **Impeded gas:** gas particles which are outside R_{200} at $z = 0$ and had closest approach radii larger than R_{200} at all previous redshifts.

It is important to note that Fig. 4.6 does not include baryons in the present-day halo if the dark matter counterpart is not in the halo. These baryons make a negligible contribution to the halo baryon mass.

There are several important differences in Fig. 4.6 between APOSTLE and AURIGA. About 35% of the baryonic pairs of the $z = 0$ dark matter halo particles lie inside the primary halo of the APOSTLE simulation, whereas in the AURIGA simulations approximately 70% of the baryon counterparts are within R_{200}. The baryons that lie within the halo are split between stars and gas in a roughly 1 : 1 ratio in both simulations.

While the fate of the retained baryon counterparts is similar in the two simulations, the evolution of the absent baryons is considerably different. In APOSTLE we find that almost half of the baryon counterparts which are missing *never entered the halo*, whereas in AURIGA almost $\approx 90\%$ of the absent baryons entered the halo before being ejected, presumably by SNe or AGN feedback.

4.6.1 Ejected gas

In Fig. 4.7 (a) and (b) we show the evolution of 10 randomly selected 'predestined' halo baryons which have been classified as 'ejected'. The particles are sampled at 60 snapshots linearly spaced as a function of the age of the universe, corresponding to a temporal resolution of ≈ 200 Myr.

In both simulations we see that the radial trajectories of both the gas and paired dark matter particles are generally very similar at early times. As the dark matter and baryon counterparts get closer to the main halo, their paths deviate and there is a tendency for gas accretion to be delayed relative to dark matter.

Following accretion into the halo, the trajectory of the gas begins to differ significantly from that of the dark matter. This deviation is caused by hydrodynamical forces which determine the subsequent evolution of the baryons. Most of the baryonic particles sampled in Fig. 4.7 (a) and (b) reach a high density upon accretion and increase their metallicity. This behaviour is consistent with halo gas that has cooled, been accreted onto the central galaxy and later ejected.

Focusing first on APOSTLE, Fig. 4.7 (a), we see that most of the randomly selected 'ejected' particles were ejected over 6 Gyr ago. In general, these particles reach a maximum radius, and near-constant, separation of $\approx (3-8)\mathrm{R}_{200}$ very quickly. At the present day, this corresponds to a physical distance of $\approx (500-1500)$ kpc and is consistent with the conclusions of Section 4.5 which reveals a baryon deficient Local Group on scales of up to 2 Mpc. There also appears to be a general trend in that the earlier the gas ejection, the greater its radial separation from the primary galaxy.

Fig. 4.7 (a) shows that prior to being ejected, most of the APOSTLE gas was cold but then underwent a sudden temperature increase, with maximum temperatures regularly exceeding 10^7 K. The ejection of the gas from the halo rapidly follows the temperature increase. This process most likely proceeds as follows: the cold gas is part of the galaxy's ISM; some of it is heated to a temperature $T \geq 10^7$ K either directly by SNe feedback or indirectly by interaction with a SNe-heated particle. The hot gas then gains energy and is accelerated to a velocity that exceeds the escape velocity of the halo. This gas can then escape beyond R_{200} and join the low-density IGM where it remains until the present day. It is interesting that much of the ejected gas does not have a maximum temperature, $T = 10^{7.5}$ K. This indicates that this gas was not directly heated by SNe but rather by interactions with SNe-heated gas. There is also little evidence of the effect of AGN feedback, which heats gas particles to even higher temperatures. However, these results are likely sensitive to the exact subgrid parameters chosen.

In Fig. 4.7 (b) we see that the evolution of both baryons and dark matter is similar in AURIGA and APOSTLE before ejection. However, in AURIGA, the ejected gas typically reaches a maximum radial distance of $\sim 3\mathrm{R}_{200}$ before turning back and

falling into the halo by the present day. Thus, the 'ejected' gas in AURIGA likely has a shorter recycling timescale than the gas in APOSTLE, much of which never reenters the halo. However, gas that was ejected at early times and re-accreted is not, by definition, included in Fig. 4.7 (b). Short recycling times in AURIGA were first reported by Grand et al. (2019) who show the model gives rise to efficient galactic fountains within the inner ~ 30 kpc, with median recycling times of ~ 500 Myr in MW-mass haloes.

4.6.2 Impeded gas

We now analyse the evolution of ten randomly selected 'predestined', baryonic particles which have *never* entered the primary halo. These are plotted in Fig. 4.8 (a) and (b) for APOSTLE and AURIGA, respectively. In Fig. 4.8(a) we see that about half the randomly-selected particles in APOSTLE make their initial approach at redshift, $z \sim 2-3$. As the dark matter particles are accreted into the halo, their baryon counterparts start being impeded at a radius $\sim 4\mathrm{R}_{200}$. The subsequent fate of these particles can differ substantially. About half of them remain at a distance $\geq 3\mathrm{R}_{200}$ until the present day, whereas the other half continue to approach the primary halo and are almost accreted by $z = 0$.

The (maximum) temperature of the 'predestined' impeded particles in APOSTLE is shown in the top-right panel of Fig. 4.8 (a). The overall temperature evolution of all impeded particles is quantitatively similar. Initially, the gas is at low temperature, $\approx 10^4$ K, but as it approaches the halo, it is subject to an almost instantaneous temperature rise to $\approx 10^6$ K. Since the maximum temperature of the gas is always well below $10^{7.5}$ K, this rise is not the result of direct SNe or AGN heating. Furthermore, before closest approach, these gas particles also have low density and metallicity, with one or two exceptions. These properties are consistent with pristine gas within the IGM, thus confirming that direct feedback did not heat these particles.

In Fig. 4.8 (b) we see that the accretion time of the dark matter counterparts of the ten randomly selected impeded baryons in AURIGA is recent, within the last

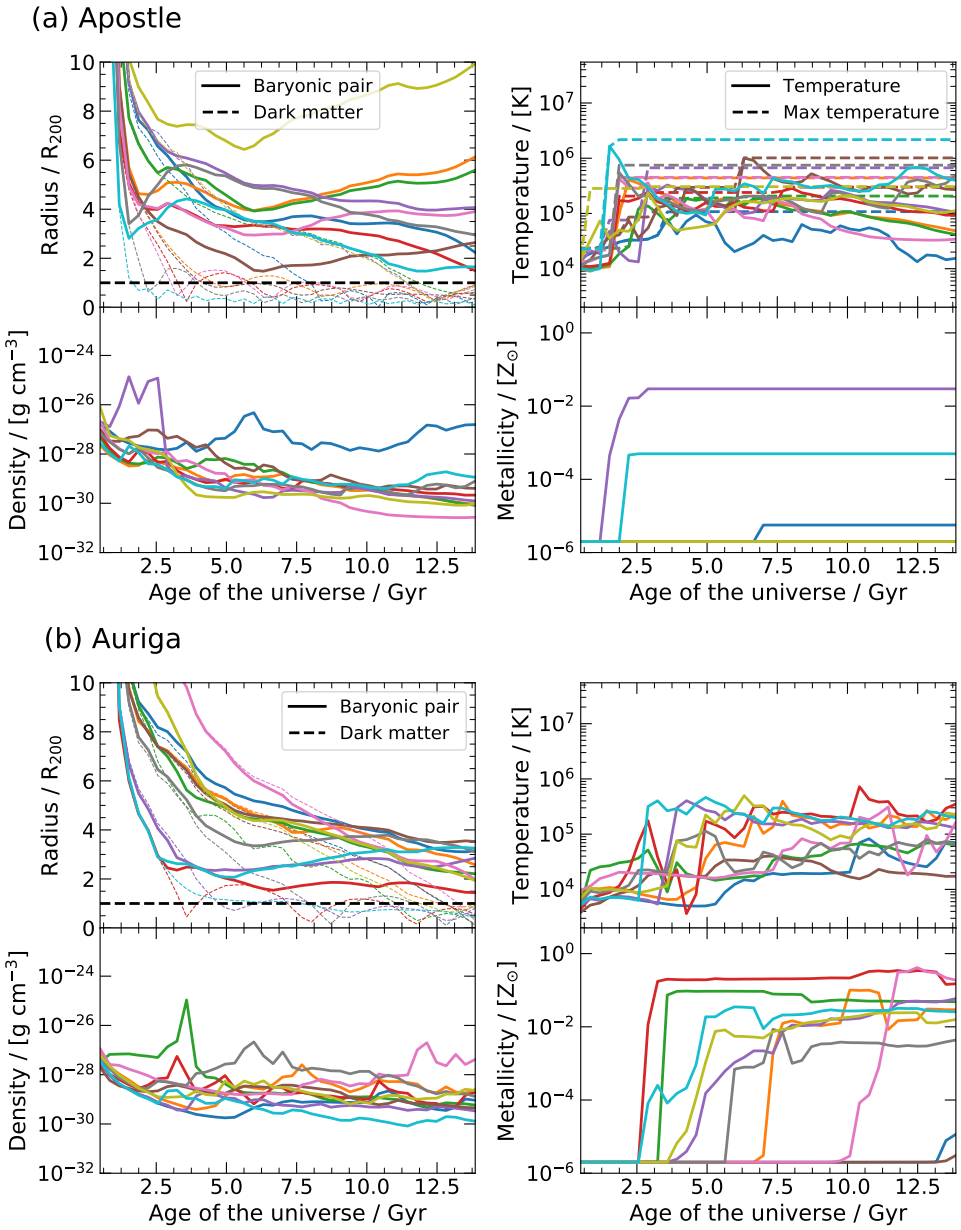

Figure 4.8: The evolution of 10 randomly selected halo baryonic tracer particles classified as 'impeded' from an (a) Apostle and (b) Auriga halo. For both (a) and (b), the top-left, top-right, bottom-left, and bottom-right panels show the radius from halo centre, temperature, density and metallicity as a function of time. The particle properties are sampled at 60 snapshots linearly spaced as a function of the age of the universe. The radius is normalised to the (time-dependent) R_{200}. The top-left panel also includes the radial position of the dark matter counterpart of each baryon particle; these are illustrated with a dashed line of the same colour. In the bottom-right panel, which shows the metallicity, there are several lines which lie on top of one another and thus are not visible. As with Fig. 4.7 the same random particle is identified in each panel by the same coloured line.

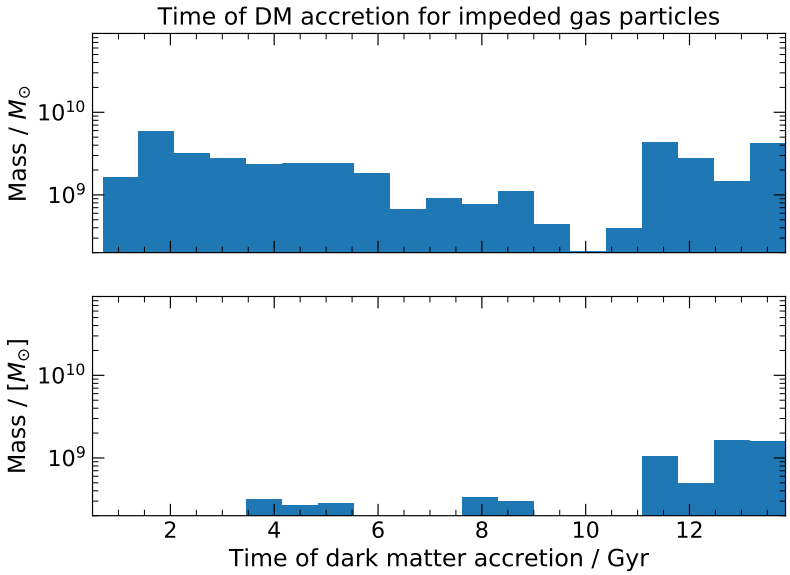

Figure 4.9: Mass-weighted histogram of the age of the universe at the time of accretion of the dark matter particles associated with 'predestined' baryon particles that have been *impeded*. The top panel shows results for the AP-S5-N1 halo in APOSTLE and the bottom panel for AURIGA. This shows that cosmic gas accretion is significantly impeded at all times in APOSTLE, whereas AURIGA only impedes cosmic gas accretion, relative to dark matter accretion, at late times.

$\approx$ 4 Gyr, for most particles. In APOSTLE we saw that before closest approach, the baryon particles were relatively unenriched, cold and at low density showing no sign of interaction with nearby galaxies. However, as seen in the bottom right panel of Fig. 4.8 (b), much of the impeded gas in AURIGA is enriched; this suggests the cause of the impediment could be interactions with other nearby galaxies at earlier times. The impeded gas could have been accreted by these galaxies or have interacted with their winds.

In Fig. 4.9 we show the mass-weighted distribution of first accretion times of all dark matter particles associated with 'predestined' baryon particles classified as 'impeded'. The APOSTLE simulations have a weakly bimodal distribution: the dark matter associated with impeded gas was accreted either at early or at late times. In the AURIGA simulations the late accreted population dominates.

The presence of hot quasi-hydrostatic haloes can impede gas accretion at late times. Haloes of mass $\gtrapprox 10^{12}$ $M_\odot$ have massive hot gaseous coronae. These gaseous haloes, which often extend beyond R_{200}, can exert pressure on the accreting gas and thus

delay its accretion. The accretion of the collisionless dark matter is, of course, not impeded. The process impeding gas accretion at early times and late time in APOSTLE is likely to be similar. However, the progenitors of the present-day primary haloes are not massive enough at high redshift to support massive atmospheres of primordial gas to explain the observed scale of suppressed accretion so most of the gaseous atmosphere must be gas that was reheated and ejected.

The explanation is provided in Fig. 4.14 which shows temperature projections of the AP-S5-N1 halo at four times between $z = 3.5$ and $z = 2$ in both APOSTLE and AURIGA. We overlay the positions of sixteen randomly selected baryon/dark matter pairs chosen so that they were 'impeded' at early times in APOSTLE. The same pairs, originating from the same Lagrangian region in AURIGA, are also overlaid. The blue circles show the x, y positions of the dark matter and the white circles those of the baryons. The white dotted line connects the baryon/dark matter pairs to help visualise the differences in the evolution of the two species.

We see that in APOSTLE the MW progenitors are encased in a hot, $\approx 10^6$ K, corona of gas that occupies a volume of radius twice as large as that of the AURIGA counterparts. This gas halo consists of a mixture of accreting primordial gas and hot outflowing winds fuelled by feedback from the central galaxy. As shown in Fig. 4.7, gas particles in the ISM can be heated by SNe feedback, generating a hot, outflowing wind that can reach distances of up to $4\mathrm{R}_{200}$ in less than 1 Gyr. This outflowing gas interacts with the accreting gas, applying an outward force sufficient to delay or prevent accretion. This leads to large amounts of 'predestined' gas 'impeded' from accreting at early times in APOSTLE (as seen in Fig. 4.6). The overlaid particles in Fig. 4.14 succinctly demonstrate this process.

In contrast, the AURIGA haloes have hot gaseous components that barely extend beyond R_{200} and do not evolve in time significantly. As the hot component in AURIGA is less massive and cooler than in APOSTLE, the dark matter/baryon pairs evolve similarly until they reach $\sim 1.5\mathrm{R}_{200}$. At radii $\leq 1.5\mathrm{R}_{200}$ gas accretion is delayed relative to the dark matter by hydrodynamical forces. However, it appears less than 5% of gas is completely prevented from accretion.

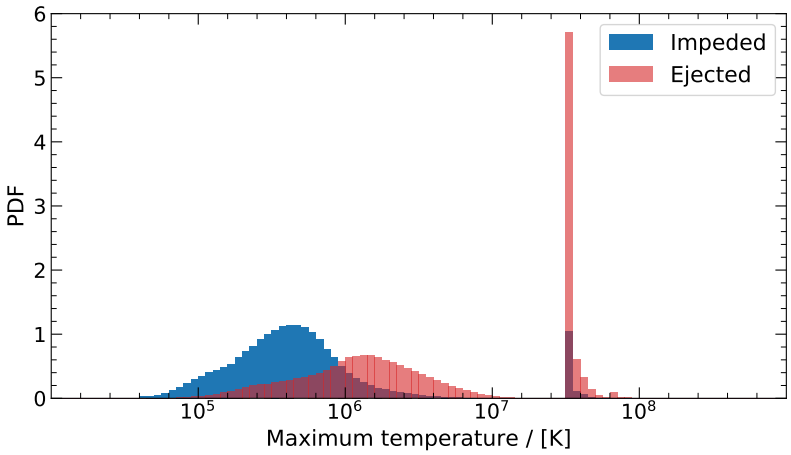

Figure 4.10: A normalized histogram of the logarithmic maximum historical temperature of all the ejected (red) and impeded (blue) gas particles identified in the AP-S5-N1 halo of the Apostle simulation. The maximum temperature is the highest temperature recorded throughout the entire simulation. We do not show the maximum temperature for the tracer particles in Auriga as the tracer particles do not store this information.

4.6.3 Quantitative sample properties

This section quantifies various statistics of the entire ejected and impeded gas populations in the Apostle and Auriga simulations of AP-S5-N1. It is worth reminding the reader that ejected and impeded gas populations are much smaller in Auriga than Apostle. In Fig. 4.10 we show the maximum temperature ever achieved by both ejected and impeded gas particles in the Apostle simulations. We start by analysing the ejected particles where we find that $\approx 35\%$ of the gas has a maximum temperature above $10^{7.5}$ K indicating direct heating by feedback. This shows that most of the ejected gas was not directly heated but rather entrained by a wind. We also note that $\approx 0.03\%$ of the ejected gas was heated to temperatures $10^{8.5}$ K, again suggesting AGN feedback only has a negligible effect in this halo. The median maximum temperature of the impeded gas is $\approx 10^{5.6}$ K which is consistent with the findings of Fig 4.8 in which we suggest most of the impeded gas, in Apostle, is cold before being heated almost instantaneously to $\approx 10^6$ K as it approaches the halo. Unfortunately, this analysis can not be repeated for the Auriga simulations as the simulations do not track the maximum temperature.

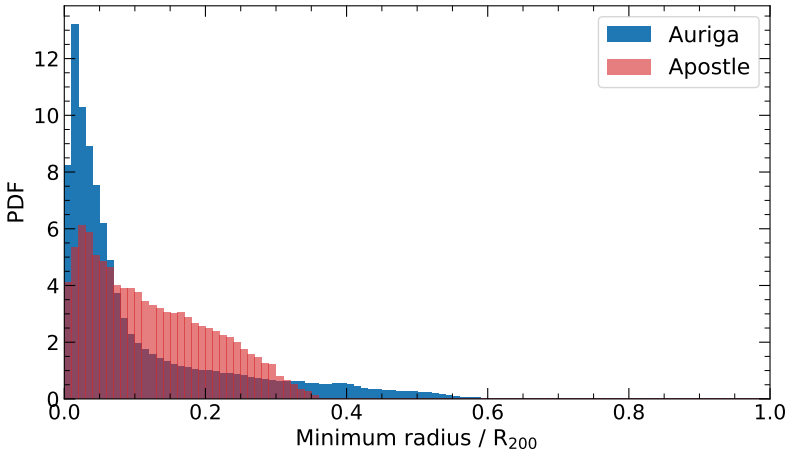

Figure 4.11: A normalized histogram of the minimum recorded galactocentric radius of all the ejected gas particles identified in the AP-S5-N1 volume of both Apostle (red) and Auriga (blue).

In Fig. 4.11 we show the minimum radius of ejected gas particles in both Apostle and Auriga prior to ejection. In Auriga, we find that over 85% of the ejected gas particles resided at a minimum radius $\leq 0.15R_{200}$, suggesting that these particles were ejected from ISM of the galaxy. In Apostle, we find only 65% of the ejected gas particles came from within $\leq 0.15R_{200}$. This again suggests that most of the ejected gas from Apostle comes from the ISM. Combining this with the result that SNe directly heated $\approx 35\%$ of the ejected gas suggests that half of the entrained gas comes from the ISM, and half comes from the CGM in Apostle.

Fig. 4.12 shows the radius of both ejected and impeded gas particles, at the present-day, in both Apostle and Auriga. We see that almost 70% of the ejected gas in Auriga resides within a radius of $\leq 2R_{200}$ at the present day. In contrast, only 30% of the Apostle ejected gas resides within this radius. This is in agreement with the results of the randomly selected particles in Fig. 4.7 and demonstrates the significant difference in the fate of the ejected gas between the two simulations. The results of the impeded gas are similar. In the Auriga, which has a lot less impeded gas, we see that 75% of the impeded gas is within $3R_{200}$, and a considerable portion of this has been nearby galaxy. Again, the Apostle shows a much more extended distribution of impeded gas with only 35% of the impeded gas within $3R_{200}$ at the present day. This supports the results of Fig. 4.8 which shows the same results for a

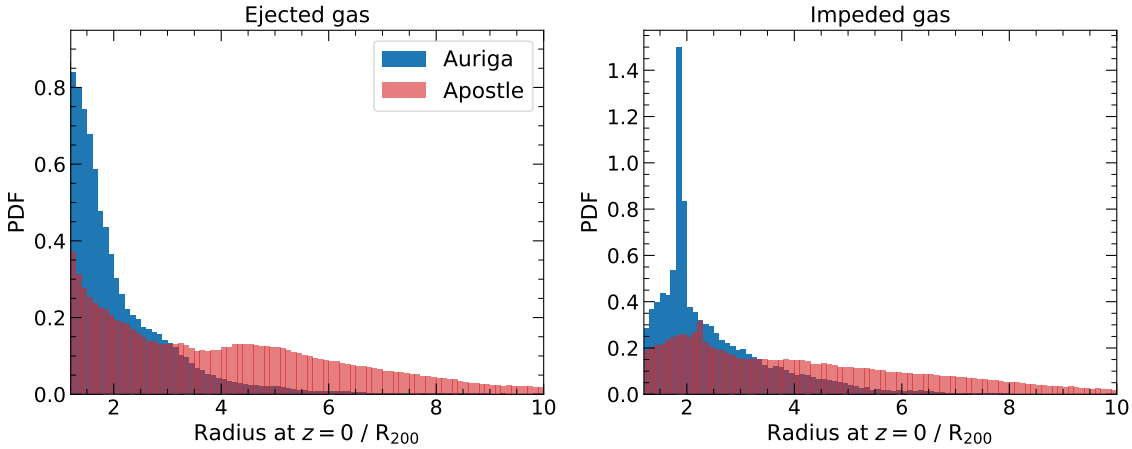

Figure 4.12: A normalized histogram of the present-day, $z = 0$, galactocentric radius of all the ejected (left) and impeded (right) gas particles identified in the AP-S5-N1 volume of both Apostle (red) and Auriga (blue).

small random sample of particles.

Finally, we look at the present-day metallicity of all the ejected and impeded gas particles, in both Apostle and Auriga, in Fig. 4.13. We first describe the metallicity of the ejected gas. In Auriga $\approx 80\%$ of the ejected particles have a metallicity of ≥ 0.1 $Z_\odot$. In Apostle, only $\approx 60\%$ of the ejected particles have a metallicity of ≥ 0.1 $Z_\odot$. Both of these results are consistent with the fraction of ejected particles with a minimum radius $\leq 0.15R_{200}$. These results suggest that the mass loading factor in Apostle is likely higher than in Auriga. The impeded gas in Apostle is almost entirely pristine with over 70% of the gas having a metallicity $\leq 10^{-5}$ $Z_\odot$. Conversely, 30% of the impeded gas in Auriga has a metallicity above ≥ 0.1 $Z_\odot$. It appears that much of the impeded gas in Auriga has directly interacted with a nearby galaxy, or the wind of a nearby galaxy, causing metal enrichment. The results of Fig. 4.8 suggest that a significant fraction of the impeded gas in Auriga may have been stripped from progenitors of the main halo, explaining their enrichment.

To conclude, the results of Figs. 4.10-4.13 demonstrate that the randomly selected particles presented in Sections 4.6.1 and 4.6.2 are in fact representative of the whole sample of ejected and impeded particles.

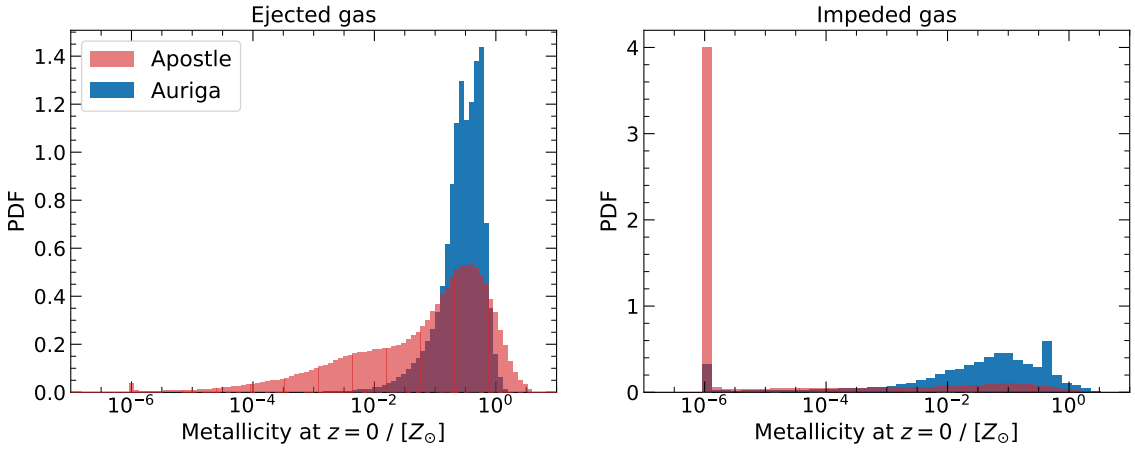

Figure 4.13: A normalized histogram of the present-day, $z = 0$, logarithmic metallicity of all the ejected (left) and impeded (right) gas particles identified in the AP-S5-N1 volume of both Apostle (red) and Auriga (blue). We set the minimum metallicity to be 10^{-6} $Z_\odot$ to ensure inclusion in the histogram.

4.6.4 The fate of impeded and ejected baryons

Fig. 4.15 shows the projected dark matter and gas density of both 'ejected' and 'impeded' baryons that were 'predestined' to end up in the primary halo but are missing. In the Apostle simulations, the present-day distribution of these missing baryons is different for the 'impeded' and 'ejected' components. The impeded gas appears to be elongated roughly along the x-axis which, as can be seen in the projected dark matter distribution, traces a local filament. By contrast, the ejected gas tends to be elongated along the y-axis, that is, perpendicular to the filament.

The reason for this apparent difference in the different distributions of impeded and ejected gas may be because the impeded gas flows towards the halo along the filament and would have been accreted by the halo had the pressure of the hot halo not impeded it. Thus, it remains in the filament, centred around the halo. The ejected material, on the other hand, finds the path of least resistance, which is perpendicular to the filament: along the filament direction the wind encounters relatively high density gas while in the perpendicular direction, the density and pressure of the surrounding medium drop rapidly. As a result, gas ejected perpendicular to the filament can reach larger radii, giving rise to the apparent elongated distribution seen in Fig. 4.15. However, Fig. 4.15 is not sufficient to prove this process happens,

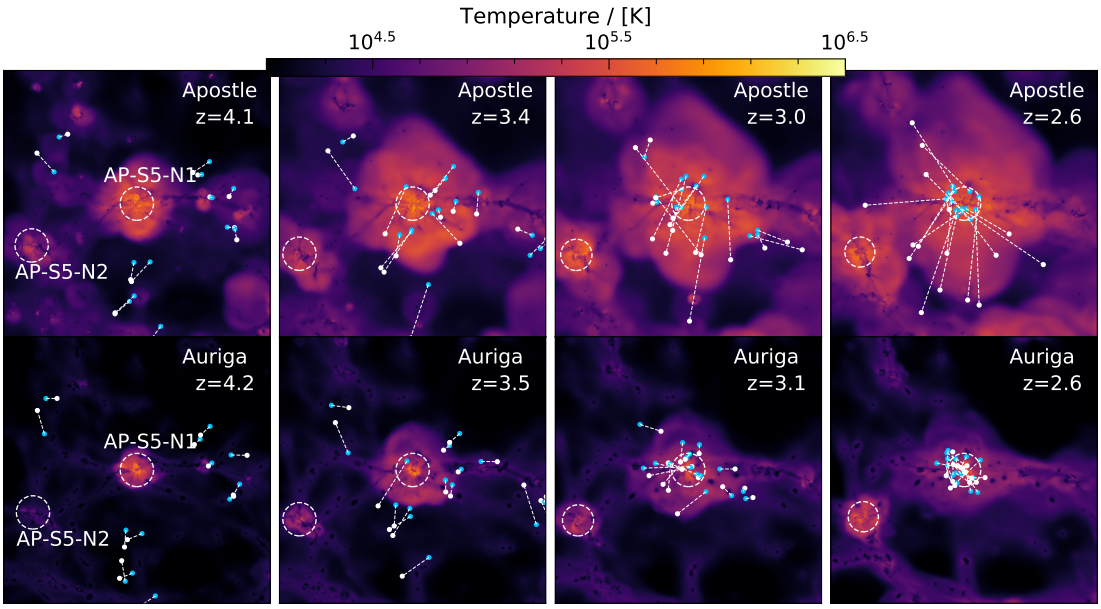

Figure 4.14: Mass-weighted temperature projections through a region of size ($16 \times 16 \times 24$) R_{200} centred on the location of the progenitor of the primary galaxy in AP-S5-N1 at four redshifts, $z \sim 4, 3.5, 3, 2.5$. Results are shown for both Apostle (top row) and Auriga (bottom row). The white and blue circles show the positions of sixteen randomly selected baryon-dark matter counterparts which are 'impeded' at early times in Apostle. The same counterparts, originating from the same Lagrangian region, are shown in Auriga. The white dotted lines connect the baryon/dark matter counterparts. The white dashed circles identifies the R_{200} of the two main haloes.

analysis of the surface density profiles along and perpendicular to the filament could quantitatively demonstrate this effect.

An interesting detail in Fig. 4.15 is the transfer of baryons between the M31 and MW analogues. This is due primarily to the effect of gas ejection from both galaxies which can cause cross-contamination. This process is an example of halo gas transfer, (see Borrow et al., 2020) and indicates that the proximity of M31 may have influenced the evolution of the MW, although the amounts of gas transferred are very small.

While the two simulations predict very different morphologies for the ejected baryons, these differences are likely undetectable in the real universe because of the low density of ejected material.

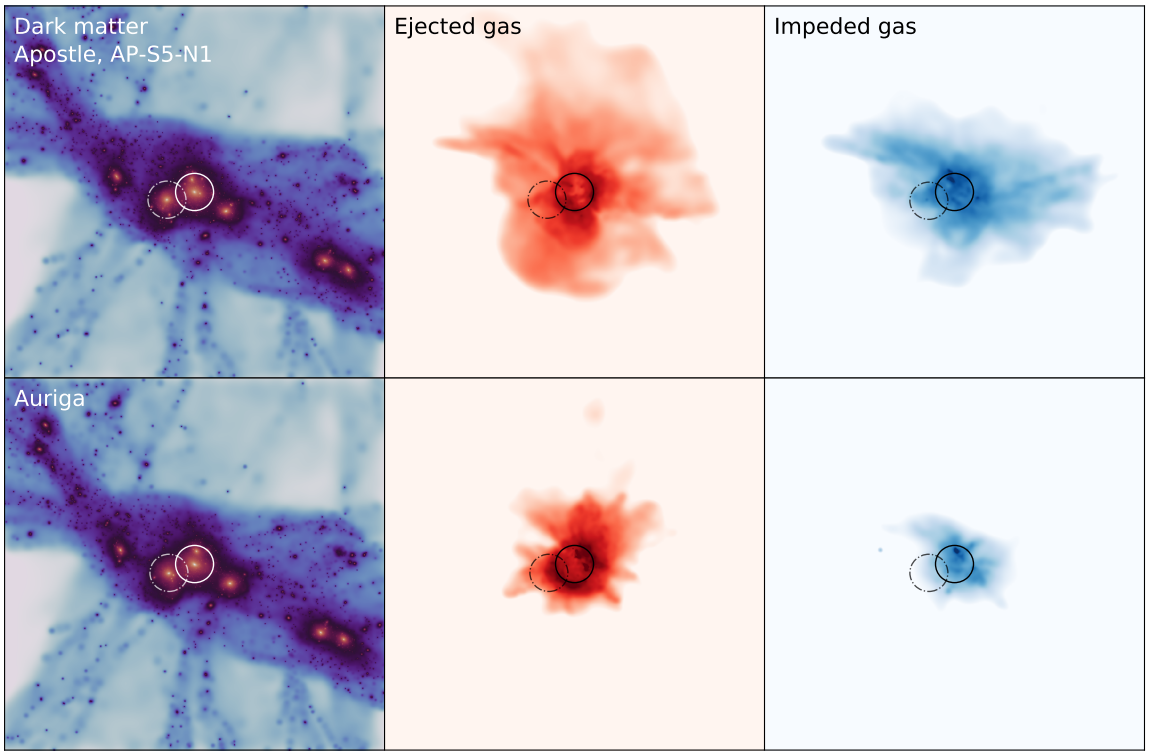

Figure 4.15: The $z = 0$ projected density of dark matter (left), ejected baryons (center) and impeded baryons (right) for the AP-S5-N1 halo in both Apostle (top) and Auriga (bottom). The projected cuboid has dimensions of $20 \times 20 \times 8$ R_{200} in the x, y and z directions, respectively. The solid white/black circles indicate R_{200} of the halo AP-S5-N1 and the dashed-dotted circles that of AP-S5-N2.

4.7 Understanding the differences

In Fig. 4.16 we show histograms of the gas density and temperature weighted by mass, metal mass and radial velocity for both Apostle and Auriga at four redshifts. All gas particles/cells within a sphere of radius 3 R_{200} around the centre of the primary halo of AP-S5-N1 are included. As in Section 4.5, we focus on this particular example but our general results are valid for all haloes in our sample.

We can see in the figure the gas responsible for impeding accretion in Apostle at $z = 2 - 3$: it is hot, $\geq 10^6$ K, low density, $\sim 10^{-4}$ cm^{-3}, slightly metal-enriched and outflowing with a mean radial velocity exceeding 100 km s^{-1} relative to the centre of mass of the halo. This gas component is visible from $z = 3$ until $z = 1$. In Auriga gas with similar temperature and density is less enriched and is not outflowing. There is some hot enriched gas with large outflow velocities at all redshifts, but this gas

appears to cool and mix with inflowing material as there is no evidence of less dense and slightly cooler outflows.

At higher redshift, the majority of the metals in Fig. 4.16(b) reside in hot, diffuse gas. As shown by Fig. 4.16 (c) this material is outflowing. Interestingly, we do not see any evidence of a significant cooler metal component developing until about $z = 1 - 2$. When this cooler metal component appears, it is radially inflowing, suggesting the recycling of earlier outflows.

In Auriga we first see a population of metal-enriched gas that is both hot and dense at approximately $z = 3$. By $z = 2$, this enriched gas appears to have cooled and increased in density. This is inferred from distribution of metals. These features suggest the presence of galactic fountains even at high-redshift. The Auriga haloes also contain a component of very dense gas, $n_{\rm H} \geq 10^{-2}$ cm^{-3}, with temperature ranging between $T \approx 10^4 - 10^7$ K. This is a further indication of efficient galactic fountains: the high densities lead to short cooling times, of order ~ 200 Myr, and, for this substantial amount of gas to be present, it must be continuously replenished by the heating of dense gas by feedback.

The differences in the nature of outflows in Apostle and Auriga could be due to differences in the SNe subgrid models. The Apostle SNe feedback model specifies the temperature increase of gas particles. In this model, SNe energy is effectively saved up and released in concentrated form stochastically. This technique means that gas is heated to higher temperatures less frequently, thus preventing the over-cooling problem (Dalla Vecchia & Schaye, 2012). Whereas in Auriga, the energy injected per unit mass of SNII is fixed. This difference in the model causes gas in Apostle to reach higher temperatures post-SNe feedback.

The total cooling efficiency of moderately enriched gas has a local minimum around a temperature of 10^7 K and increases quite steeply both with increasing and decreasing temperature (see e.g. Fig. 9 of Baugh, 2006). Thus, a post-feedback temperature lower than 10^7 K leads to both a higher cooling rate and lower thermal energy. When these effects are combined, the cooling time can be reduced by an order of magnitude or more. The lower post-feedback temperature in Auriga could allow

SNe-heated gas to radiate a significant fraction of the injected energy on a timescale of order several hundred million years. This reduced cooling time would facilitate short recycling times for gas in AURIGA and prevent the build up of a hot, SNe-fueled atmosphere at high redshift.

In APOSTLE, by contrast, feedback heats the gas to $10^{7.5}$ K, and thus radiative cooling is relatively inefficient. Fig. 3.10 shows the density and temperature of gas particles 500 Myr before and after SNe heating in the EAGLE reference simulation. That figure shows that gas particles that experience SNe feedback decrease their density by over two orders of magnitude within $\leq$ 20 Myr of being heated. This expansion prevents efficient radiative cooling and also makes the gas buoyant so that it is accelerated out through the halo (Bower et al., 2017b).

Fig. 4.17 shows a mass-weighted projection of the radial velocity of the gas in AP-S5-N1 for both APOSTLE (top row) and AURIGA (bottom row) at five redshifts, $z \sim 0,\ 1,\ 2,\ 3,\ 4$. It is clear from these projections that rapid outflowing material extends well beyond the halo, reaching distances of $\sim 4\mathrm{R}_{200}$ at $z = 4$ in APOSTLE. These strong, halo-wide outflows are readily visible until $z = 1$. By contrast, in AURIGA the mass-weighted radial velocity of the outflows is much slower, and their spatial extent is smaller. These radial velocity projections indicate that APOSTLE haloes experience strong outflows with high covering fractions. A high outflow velocity, combined with a large covering fraction, can impede cosmological gas accretion on the scale of the entire halo. By contrast, in AURIGA we see less extended outflows because a significant fraction of the SNe-heated material cools and is efficiently recycled near the centre of the halo. van de Voort et al. (2021) shows that the magnetic fields, included in the AURIGA simulations, can reduce the outflow velocities of gas around the central galaxies. This extra pressure from magnetic fields in AURIGA could be contributing to the reduced gas ejection from the halo compared to that found in APOSTLE.

Another factor that can vary the velocity and spatial extent of outflows is the potential depth. In Fig. 4.18 we show the approximate circular velocity profiles as a function of radius in the four primary haloes in both APOSTLE and AURIGA at

$z = 0$. These approximate circular velocity profiles are calculated from the total enclosed mass assuming spherical symmetry. We see that in the inner 50 kpc the circular velocity is systematically higher in Auriga, by up to as much as ~ 100 kms^{-1}. This difference is because the Apostle model is much more efficient at driving winds from the central galaxy, propagating out to scales exceeding the virial radius (Mitchell et al., 2020b). This process reduces the density in the inner region, thus reducing the escape velocity and making future gas ejection more efficient. Whereas in Auriga the opposite happens, as wind is inefficient at removing gas from the central region, the central density increases, thus deepening the potential well.

As described in Section 4.2, the gas dynamics in Auriga are followed with a moving-mesh technique. Several studies have investigated the differences between moving-mesh and particle-based hydrodynamics techniques in the context of galaxy formation simulations (Sijacki et al., 2012; Kereš et al., 2012; Vogelsberger et al., 2012; Torrey et al., 2012; Bird et al., 2013; Nelson et al., 2013). A general result from these studies is that gas in moving-mesh simulations cools more efficiently than in their particle-based counterparts. The cooling efficiency of hot gas is artificially suppressed in particle-based simulations by spurious viscous heating and the viscous damping of SPH noise on small scales. Furthermore, moving-mesh simulations model energy dissipation more realistically by allowing cascading to smaller spatial scales and higher densities (Nelson et al., 2013). As we mentioned earlier, we expect these difference to be subdominant to the large differences in the subgrid models between Apostle and Auriga.

4.8 Observational tests

We have shown in Sections 4.5 and 4.6 that the Apostle and Auriga simulations predict very different baryon cycles around our MW and M31 analogues. We now turn to the observable signatures of strong outflows in Apostle and galactic fountains in Auriga. We present mock observations of absorber column densities and dispersion measure around our MW and M31 analogues. We aim to construct

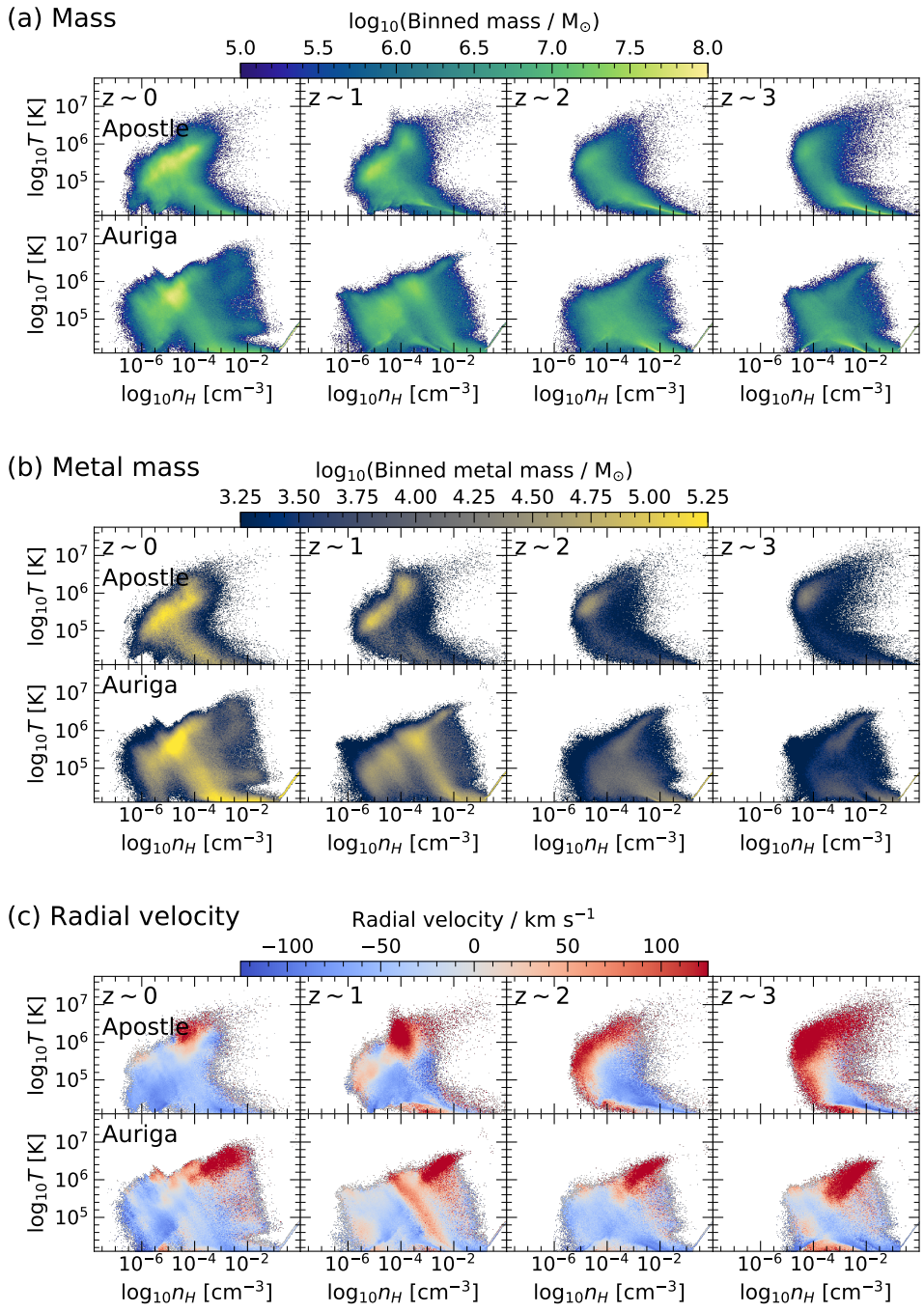

Figure 4.16: Gas density-temperature diagrams for a primary halo, AP-S5-N1, in both APOSTLE (top row) and AURIGA (bottom row). The histograms are coloured according to (a) mass, (b) metal mass and (c) mass-weighted radial velocity. They include all gas with temperature $T > 10^4$ K that is within radius, $r < 3\mathrm{R}_{200}$, of the primary halo. The four columns show the gas distributions at four redshifts, $z \sim 0,\ 1,\ 2,\ 3$, from left to right, respectively. The histograms are generated with 300 logarithmically spaced bins in the density range, $10^{-8} - 1$ cm^{-3}, and temperature range, $10^{3.5} - 10^{7.5}$ K.

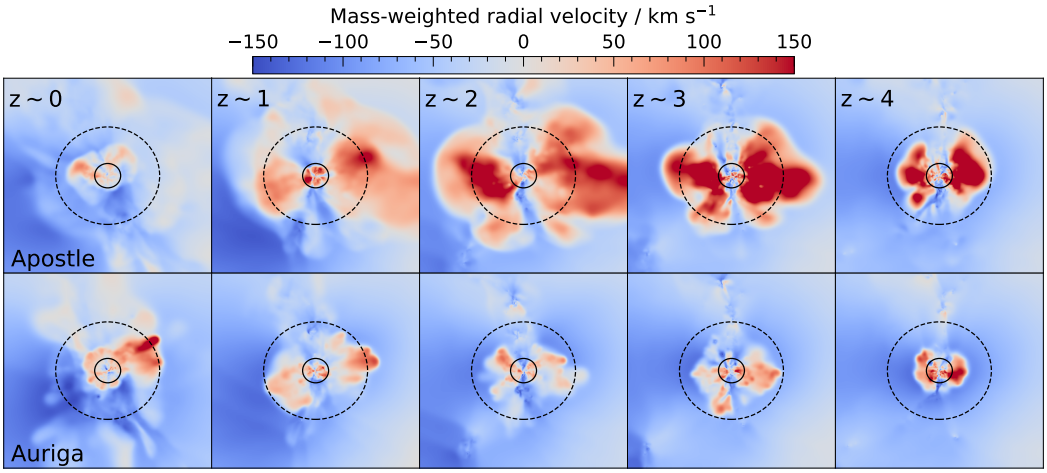

Figure 4.17: Mass-weighted projection of the radial gas velocity for AP-S5-N1 in both Apostle (top row) and Auriga (bottom row) at five redshifts, $z \sim 0,\ 1,\ 2,\ 3,\ 4$, from left to right, respectively. The region of these projections has size $(16 \times 16 \times 2)$ R_{200} in the x, y and z directions, respectively, where the z-axis is into the page. The solid black circle indicates R_{200} and the dashed back curve $4 \times R_{200}$.

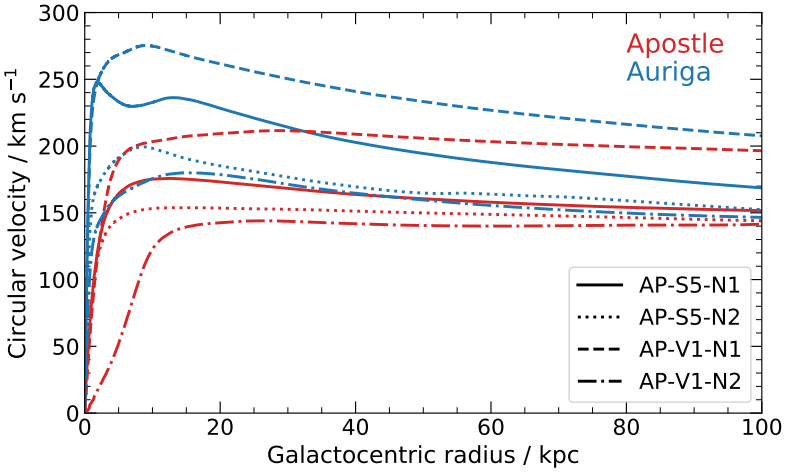

Figure 4.18: The approximate circular velocity of the four primary haloes in both Apostle and Auriga at $z = 0$. The circular velocity, $V_{\rm circ}$, at radius r is calculated from the total enclosed mass, $M(< r)$, assuming spherical symmetry $V_{\rm circ}^2 = GM(< r)/r$ where G is the gravitational constant. The Apostle and Auriga simulations are shown in red and blue, respectively.

mappings between the physical state of the baryons and real observables and, in particular, to identify observables that may be sensitive to the differences in the gas properties seen in the APOSTLE and AURIGA simulations.

4.8.1 Column densities

We show, in Fig. 4.19, the regions of the density-temperature plane where different species are relatively abundant. The contours enclose regions where each species contributes 10 per cent of the maximum ion fraction of the respective element in collisional ionisation equilibrium at $z = 1$. We show these contours as they highlight regions of the density-temperature phase space where each species is likely to be detected. This analysis is similar to Wijers et al. (2020) which analysed lower resolution, large volume cosmological simulations using the EAGLE galaxy formation model.

The species that probe the hottest gas, at $T \geq 10^6$ K, are typically O VII O VIII and Mg X. However, there is a degeneracy as these ionisation states are also plentiful in lower temperature, lower density gas. In the absence of other observables, it is difficult to distinguish whether detection of these ions is from a low density or a high density region. However, given that, in practice, the detection of these lines requires a moderately high column density, it is likely that any detection will be from gas at high density and, thus, high temperature. We also see in the figure that Ne VI, Ne VIII and O VI probe a cooler component, at $T \leq 10^6$ K. This transition temperature, $T = 10^6$ K, is a significant threshold as it has the potential to distinguish hydrostatic gas at the virial temperature of MW-mass haloes from hotter gas heated by feedback energy.

The species O VII and O VIII are well suited for identifying very hot outflows. Unfortunately, these ions are challenging to observe in the real universe because the wavelengths of their lines are so short, $\sim$ 20 Å. These highly ionized stages of oxygen, the most abundant metal, have transitions that are detectable in X-rays. However, even modern X-ray instruments do not have the required resolution or

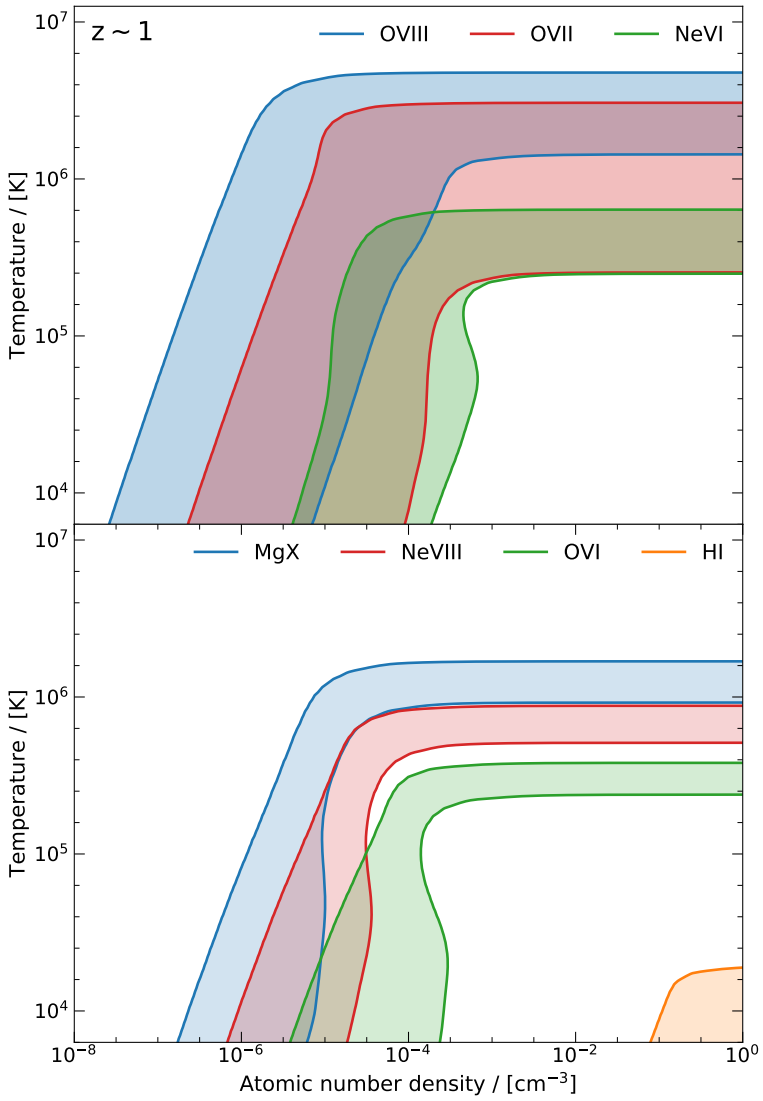

Figure 4.19: Temperatures and densities at which different metal species occur at $z = 1$. The ion fractions are calculated from the lookup tables of Hummels et al. (2017), assuming only radiation from the metagalactic UV background according to the model of Haardt & Madau (2012). These lookup tables are computed under the assumption of collisional ionisation equilibrium (CIE). The contours for each of the indicated species are at 10 per cent of the maximum ion fraction. The top panel shows Ne VI (green), O VII (red) and O VIII (blue) and the bottom panel H I (orange), O VI (green), Ne VIII (red) and Mg X (blue).

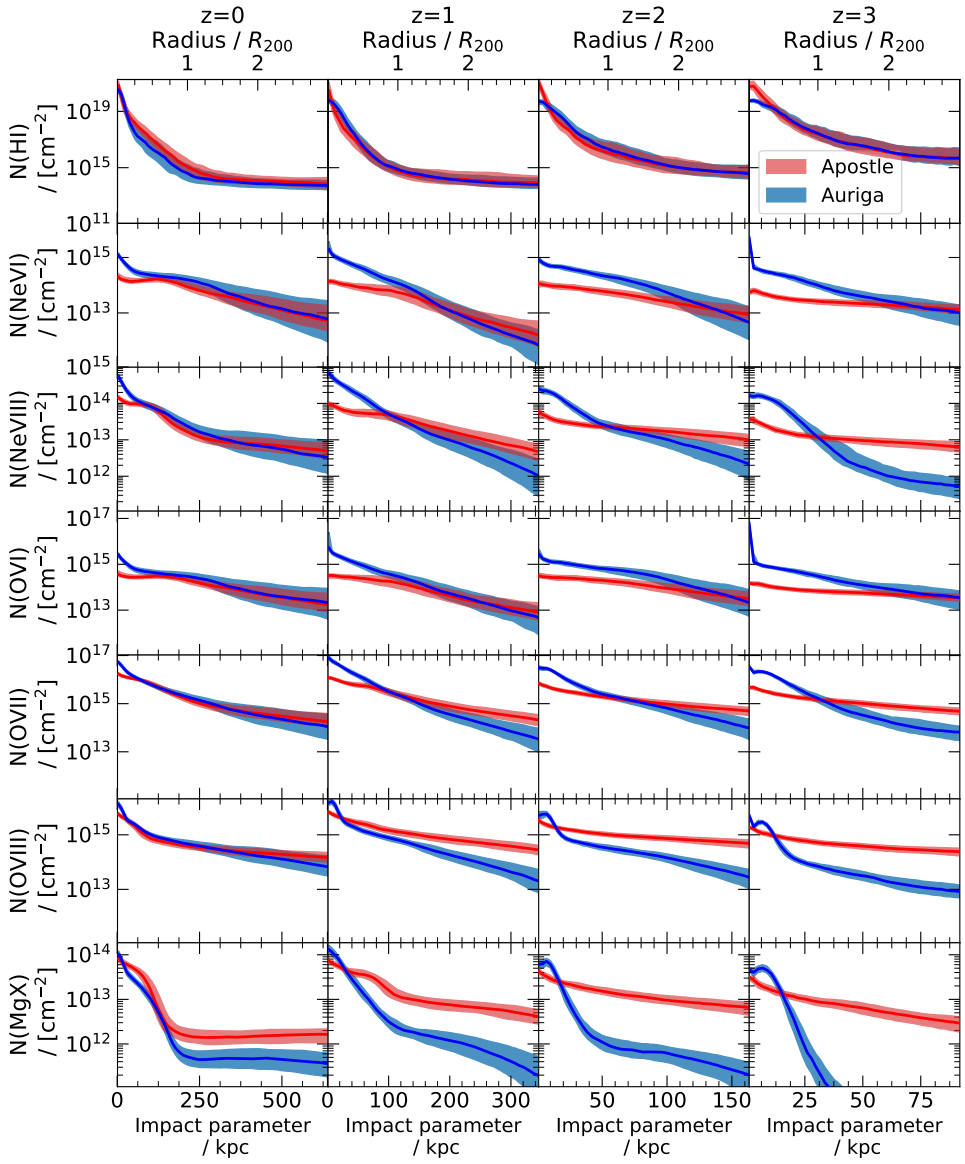

Figure 4.20: Atomic column number densities of several species as a function of impact parameter from the centre of the primary halo in both the Apostle (red) and Auriga (blue) simulations, out to $3R_{200}$ at four redshifts $z \sim 0,\ 1,\ 2,\ 3$ from left to right, respectively. From top to bottom, the rows show results for H I, Ne VI, Ne VIII, O VI, O VII, O VIII and Mg X, respectively. The column density at a fixed radius, r, for each halo is calculated by taking the median column density of many sightlines through a small annulus. We also compute the lower and upper quartiles of the column density in each annulus. The solid lines are the mean of the median column density, at each radius, for all four haloes. The shaded regions illustrate the range between the mean of the lower and upper quartiles for all of the haloes. We choose to use the median and quartiles as these are more comparable to a single random line-of-sight through a halo in the real universe. The results are binned by impact parameter, and the mean virial radius is used to show the approximate impact parameter as a function of R_{200} for all four haloes on the same plot.

sensitivity. Ne VI, Ne VIII Mg X and O VI probe a similar, but typically cooler component of gas, but have much longer transition wavelengths, e.g. 558 Å, 770 Å, 610 Å and 1032 Å, respectively. These are readily detectable with UV instruments and represent good probes of hot, collisionally ionized gas, easier to detect than than their X-ray counterparts, O VII and O VIII.

We now consider each of the ions considered in Fig. 4.20, one at a time. We begin with the column density profile of H I shown in the top row of Fig. 4.20. In general, the H I column density profile is similar at all redshifts in both simulations. The profile is centrally peaked and falls off rapidly, typically decreasing by about 4 orders of magnitude within the first 100 kpc, where it flattens to a near constant number density of 10^{15} cm^{-2}.

Between $z = 3$ and $z = 1$, the mean and scatter of the H I column density at fixed impact parameter agree well in both APOSTLE and AURIGA. However, at $z = 0$, there is a slight systematic offset in APOSTLE where the H I column densities are about a factor of five higher than in AURIGA. The offset diminishes in both the centre, < 30 kpc, and beyond R_{200}. The similarity of the H I distributions in both simulations is not surprising. In particular, we see in Fig. 4.16 that the distribution of gas at high densities and low temperatures, where H I typically occurs, is very similar in the two (see Fig. 4.19).

The second, third and fourth rows from the top of Fig. 4.20 show the column density profiles of O VI, Ne VI and Ne VIII, respectively. We discuss the distributions of these ions collectively, as they have similar general trends and typically probe gas at the same density and temperature, as demonstrated in Fig. 4.19. O VI, Ne VI and Ne VIII probe progressively hotter populations of dense gas, increasing from $10^{5.5}$ K up to 10^6 K. Ne VI typically probes a broader range of temperatures, ~ 0.4 dex, compared to ~ 0.2 dex for O VI and Ne VIII.

At $z = 0$, the column densities of O VI, Ne VI and Ne VIII in AURIGA are higher than in APOSTLE at all radii, but the difference is maximal at the centre of the halo. Outside the central region, beyond ~ 30 kpc, the differences in column density are fairly small, typically a factor of two or less. Although the mean column density

differs at a given impact parameter, the range of column densities for the whole sample typically overlaps. The differences, however, can be substantial at higher redshift, $z \geq 1$. In Fig. 4.20 we see a general behaviour in the O VI, Ne VI and Ne VIII profiles in both APOSTLE and AURIGA. In APOSTLE, the column density distributions are relatively flat, typically decreasing by only an order of magnitude over a radial range $3R_{200}$. In contrast, in AURIGA, the central column densities are typically higher and decrease much faster, dropping by over four orders of magnitude over the same radial range.

The differences in the column density profiles of O VI, Ne VI and Ne VIII at $z \geq 1$ in APOSTLE and AURIGA are most notable in both the innermost and outermost regions. In AURIGA, the column densities of these ions are higher in the centre ($r < 50$ kpc), where they can be up to a hundred times higher than in APOSTLE. However, as the column densities in AURIGA decrease so rapidly with increasing radius, the column densities in APOSTLE end up being much higher in the outermost regions, ~ 150 kpc. In particular, the column densities of these ions in the outer regions of APOSTLE are up to three orders of magnitude higher than in AURIGA. We also note that the column density variance at fixed impact parameter is much larger in AURIGA than in APOSTLE, particularly in the outer regions.

The ions O VII, O VIII and Mg X probe some of the hottest gas surrounding our galaxies. O VII and O VIII probe a broad range of hot gas, $T \sim 10^{5.5} - 10^{6.5}$ K, and $T \sim 10^{6} - 10^{6.5}$ K, respectively. Mg X probes gas in a narrower temperature range, $T \sim 10^{6} - 10^{6.25}$ K. These three ions, O VII, O VIII and Mg X, are shown in the fifth, sixth and seventh rows from the top of Fig. 4.20. As with the other ions, we find fairly good agreement between APOSTLE and AURIGA at $z = 0$, with a considerable systematic offset for Mg X. Remarkably, the column densities of O VII and O VIII agree to within 10% beyond the inner 10 kpc. Both APOSTLE and AURIGA predict relatively flat column densities as a function of impact parameter for both O VII and O VIII. The predictions for Mg X differ slightly. The column density of Mg X drops rapidly beyond radius ~ 200 kpc and flattens to a near-constant value of $\sim 10^{12}$ cm^{-2} in both simulations. While the general shape of the profiles are similar

in both simulations, the column density in APOSTLE is typically a factor of $2-5$ higher than in AURIGA.

At $z \geq 1$, O VII, O VIII and Mg X follow a similar trend as O VI, Ne VI and Ne VIII. In the central regions, the column densities in AURIGA are either higher (O VII) or approximately equal to those in APOSTLE. Further out, the column densities are much higher in APOSTLE. This difference is due to the steeply declining column densities in AURIGA and the much flatter profiles in APOSTLE. The differences in O VII, O VIII and Mg X between APOSTLE and AURIGA are most prominent at $z = 3$. Mg X is the most extreme case. In AURIGA it is only present within 40 kpc of the halo centre, whereas in APOSTLE there are still very high Mg X column densities out to 150 kpc and even beyond.

At the present day, the column densities of all the ions considered in Fig. 4.20 are broadly consistent in the two simulations within the halo-to-halo scatter. The main exception occurs in the central regions (≤ 30 kpc), where the AURIGA haloes typically have a peak in column density that can be up to a factor of ten higher than in APOSTLE. These larger column densities at the centres of AURIGA haloes could be a signature of galactic fountains, which is where enriched, hot outflows recycle within a small central region. The other notable exception is the larger Mg X column density in APOSTLE, at all radii, but particularly in the outermost regions. This enhancement likely reflects the presence of more hot, $T \geq 10^6$ K, enriched gas at large radii in APOSTLE arising from the larger spatial extent of the hot outflowing material in this case.

We find a consistent trend among all the ions considered in Fig. 4.20 for $z \geq 1$, with the exception of H I. This trend consists of higher column densities in the innermost regions of the AURIGA simulations, which then decline with impact parameter more rapidly than in APOSTLE. The important offshoot is that the APOSTLE haloes have significantly higher column densities at large radii, ≥ 100 kpc, with the differences increasing with redshift.

The large column densities of Ne VI, Ne VIII, O VII, O VIII and Mg X in the outer regions of the APOSTLE simulations at $z \sim 1-3$ are a strong signature of hot,

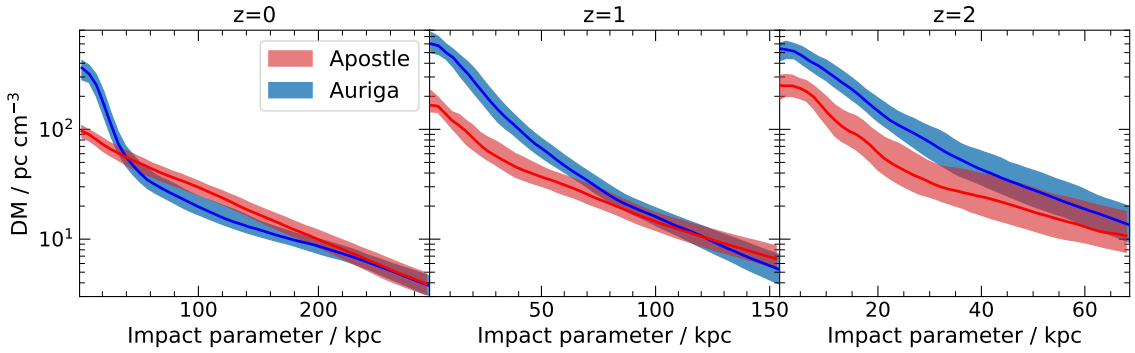

Figure 4.21: The dispersion measure of all four haloes in Apostle and Auriga at three redshifts, $z \sim 0,\ 1,\ 2$ from left to right, respectively. The dispersion measure, at fixed radius, r, for each halo is calculated by taking the median dispersion measure of many sightlines through a small annulus of depth R_{200}. We also compute the lower and upper quartiles of the dispersion measure in each annulus. The solid line shows the mean of the median dispersion measure, at each radius, for all four haloes. The shaded region illustrates the range between the mean of the lower and upper quartiles for all the haloes. The dispersion measure at higher redshift is calculated in the frame of the halo at that redshift, not from an observer at the present day.

accretion-impeding outflows. A visual inspection of the evolving temperature projections in Fig. 4.14 demonstrates that hot gas, $T \sim 10^6$ K, in Apostle extends to radii of order $\geq 4\mathrm{R}_{200}$ by $z = 3$. By contrast, the Auriga galaxies develop a much cooler, $T \leq 10^{5.5}$, halo of gas which does not extend beyond $2\mathrm{R}_{200}$. This hot gas distribution in Auriga produces column densities that drop rapidly at $\mathrm{R}_{200} \sim 50$ kpc at $z = 3$ and then drop even further beyond $3\mathrm{R}_{200} \approx 150$ kpc.

The peak in the column densities of Ne VI, Ne VIII, O VI, O VII and O VIII at the centre of the Auriga haloes can be readily understood by reference to the density-temperature histograms in Fig. 4.16. Panels (a) and (b) show that there is a population of very dense gas, $n_{\mathrm{H}} \geq 10^{-2}$ cm^{-3}, with temperatures ranging between $T \approx 10^4 - 10^7$ K. As described in Section 4.7, this gas component appears to be a product of a galactic fountain. The high density of the gas leads to very short cooling times, $\sim$ 200 Myr, so for such a massive gas component to be present it must be continuously replenished by the heating of dense gas. This gas is heated to $T \geq 10^6$ K where it cools at almost constant density before rejoining the ISM of the central galaxy. Therefore, the centrally-concentrated peak in ion column densities in Auriga appears to be a strong signature of galactic fountains.

In summary, we find that the APOSTLE simulations produce almost flat column density profiles for ions which probe hot gas, out to radii of $\sim 3\mathrm{R}_{200}$ between $z = 0{-}3$. These flat density profiles are produced by hot, outflowing gas driven by SNe within the central galaxy. In contrast, the AURIGA simulations predict rapidly declining column densities with radius as the SNe driven outflows are unable to eject large amounts of hot gas to such large radii. Instead, the AURIGA simulations generate galactic fountains where dense gas is heated to high temperatures, $T \approx 10^7$ K, and then cools at a high, almost constant, density. This fountain produces an observable central peak in the column densities of Ne VI, Ne VIII, O VI, O VII and O VIII which is not present in APOSTLE.

4.8.2 Dispersion measure

The dispersion measure is a measure of the free electron column density along a sightline and, potentially, one of the most useful metrics of the baryon content of the Local Group. As discussed in Section 2.5.3, CHIME is predicted to detect between 2 and 40 FRBs day^{-1} over the whole sky (Connor et al., 2016). The hot halo of M31 makes a significant contribution to the dispersion measure of FRBs when their emission passes through the halo with an impact parameter of $\leq$ 150 kpc; this corresponds to an angle of approximately 11° on the sky, assuming that M31 is $\sim$ 770 kpc away from the MW. Therefore, M31 covers approximately $\sim$ 400 deg^2, or $\sim$ 1% of the sky. This implies that the CHIME survey should expect to detect roughly between 10 and 150 FRB's per year behind the M31 halo. These can be compared with sightlines adjacent to M31. If the foreground contribution from the MW is uniform, or at least smooth over a narrow range of viewing angles, and the FRB population has the same redshift distribution over this range, the differences in these dispersion measures will be a direct reflection of the properties of the plasma in M31. The contribution of M31 to the dispersion measure can then be used to infer the amount of hot gas present in M31 and, thus, to constrain its baryon fraction.

In this section we compute the dispersion measure from several thousand random sightlines through the four primary MW-like haloes at three redshifts, $z = 0,\ 1,\ 2$.

The electron column density is calculated for parallel sightlines as described in Section 4.8.1. These are projected directly through $2 \times R_{200}$ of the primary halo at varying impact parameters. The dispersion measure at a given radius of each halo is calculated by taking the median of many sightlines in a small annulus. We project through the x, y and z axes and combine the results. Additionally we compute the lower and upper quartiles in each annulus.

The dispersion measure profiles in Fig. 4.21 represent idealized observations of M31 from Earth, with contributions from the MW and material beyond M31 removed (i.e. the IGM and other distant haloes). In practice, we expect the contribution from halo gas in M31 to be large, and thus to be readily detectable when compared with sightlines that do not pass through M31. Although they are not realistic mocks of observations from Earth, the results in Fig. 4.21 provide some insight into how the dispersion measure of a halo varies with impact parameter and redshift, and thus may help interpret observational data. Later in this section, we discuss how future work could improve the realism of the simulated profiles and how they could be used to exploit the constraining power of future observations.

With current data it is only possible to make direct measurements of today's dispersion measure around M31 and other Local Group galaxies. We do, however, include results from higher redshifts in Fig. 4.21 to understand how the dispersion measure evolves and to give insight on the possible background contributions to observations. (The dispersion measure at higher redshift is calculated in the frame of the halo at that redshift, not from an observer at the present day.)

At the present day, both simulations predict a similar trend, with the dispersion measure being highest in the central regions and declining with increasing impact parameter. At $z = 0$, the dispersion measure typically drops from a peak value of $\geq 10^2$ pc cm^{-3} in the centre of the halo to ~ 1 pc cm^{-3} at R_{200}, and continues to fall beyond this radius (not shown in the figure). Beyond the inner 50 kpc, APOSTLE and AURIGA predict similar profiles. The main difference occurs in the centre of the halo. In APOSTLE the dispersion measure decreases with impact parameter at an almost constant rate. In AURIGA there is a peak at the very centre which drops

rapidly out to 50 kpc. Beyond that, both the slope and amplitude of the profiles in the two simulations are approximately equal.

The peak in the dispersion measure in the inner regions of Auriga is also present at higher redshifts. At $z \geq 1$ a similar peak, but of lower amplitude, also appears in the Apostle simulations. The peak at the centre of the Auriga haloes at all redshifts coincides with the peak in the column densities of the ions that trace the warm-hot gas within the CGM (see Fig. 4.20) Thus, the origin of this large dispersion measure is plausibly the same as that of the ions. Feedback produces hot, metal-enriched, centrally-concentrated gas which is dense. This gas then cools, at an almost constant density, before rejoining the ISM. The electron mass will trace the gas mass in Fig. 4.16 (a). It is the hot gas of atomic density ≥ 0.001 cm^{-3} in Auriga that produces the centrally concentrated dispersion measure peak. This gas is not present in Apostle at $z = 0$ and, as a result, the profile is much flatter near the centre.

At higher redshift, Auriga predicts a higher dispersion measure throughout the halo. This behaviour is similar to that of the column densities of Ne VI, Ne VIII, O VI and O VII in the central regions seen in Fig. 4.20, which typically probe gas at temperature $\sim 10^{5.5}$ K. The difference in baryon mass in the haloes of Apostle and Auriga drives the difference in the amplitude of the dispersion measure profiles.

At lower redshift, the baryon fraction of the Auriga haloes is still a factor of two higher than the Apostle counterparts. However, the dispersion measure in two simulations tends to agree reasonably well outside of the central region, ≥ 50 kpc. Inside the central region, the Auriga haloes boast a significantly higher dispersion measure, thus indicating that the extra baryonic mass in Auriga, at present-day, is centrally concentrated. Efficient galactic fountains in Auriga can continuously produce centrally concentrated hot gas.

In summary, the dispersion measure is a measure of the amount of ionised gas along the line-of-sight and is strongly sensitive to the distribution of hot gas around MW-mass haloes, which is mostly ionised. The similar dispersion measure profiles in the outer regions of Apostle and Auriga at $z = 0$ imply that the haloes in the two simulations have similar amounts of hot gas in this region, despite having

large differences in baryon fraction. This is possible as the extra baryons present in Auriga are centrally concentrated due to the galactic fountains, which leads to a large central peak in the dispersion measure profile in Auriga.

We predict that future surveys of dispersion measure inferred from FRBs should be able to identify or exclude the existence of a galactic fountain in either the MW or M31, through analysis of dispersion measure variation with impact parameter within the central regions. We also expect that the background, e.g. the contributions from the IGM and other intervening haloes at higher redshift, should be larger if there are hot, spatially extended outflows at high redshift, such as those found in Apostle. It may also be possible to identify the presence of a hot galactic fountain by direct observation of X-ray emission (Oppenheimer et al., 2020a).

In this analysis, we did not include material which is part of the ISM. When calculating the free electron density we discarded gaseous material with an atomic number density ≥ 0.1 cm^{-1} or a temperature $\leq 10^4$ K. Gas in this regime is not modelled explicitly in the simulations, however the distribution and morphology of the cold gas is in reasonable agreement with observations (Marinacci et al., 2017). The dispersion measure profiles in the innermost regions may well be higher than predicted in this thesis due to dispersion by ISM gas. However, predictions for the ISM suggest that it contributes only ≤ 50 pc cm^{-3} (Lorimer et al., 2007); thus the central regions should be dominated by contributions from halo gas.

Finally, we stress that realistic mock catalogues will be needed to interpret future data. Constructing these will require combining high-resolution Local Group simulations such as those presented here with large-volume cosmological simulations to determine the expected background.

4.8.3 Comparing to current observations

In this section we compare our preliminary mock observations of the column densities of Ne viii for our sample of four MW-mass haloes with current observations. The COS-Halos survey (Tumlinson et al., 2013) and CASBaH survey (Burchett et al.,

2019) are absorption line studies of galaxies in the UV. They typically cover the redshift range $0.05 < z < 1.5$ and provide information on column densities and covering fractions of H I, Ne VIII and O VI. Burchett et al. (2019) collated a statistical sample of Ne VIII CGM absorbers. This sample includes 29 CGM systems in the redshift range $z = 0.5 - 1.5$, with a median redshift, $z = 0.68$, stellar masses in the range $10^{9.5} - 10^{11.5}$ $M_\odot$ and impact parameters within 450 kpc of the central galaxy.

In Fig. 4.22 we compare the column density of Ne VIII, as in Fig. 4.20, at $z = 0.5$ for both APOSTLE and AURIGA, with observational data, including both the detections (solid black circles) and non-detections (empty triangles) of Burchett et al. (2019). The highest inferred column density of Ne VIII is 14.98 ± 0.09 cm^{-2} at an impact parameter of 69 kpc and redshift, $z = 0.93$. The central galaxy of this system has an estimated stellar mass of $10^{11.2}$ $M_\odot$, slightly larger than our simulated galaxies. This high observed column density is larger than found in any of the predictions of APOSTLE and AURIGA, as seen in the figure. However, column densities this high are not uncommon at lower impact parameters in AURIGA.

The column densities at slightly larger radii, $100 - 200$ kpc, are consistent with the predictions of both simulations, with almost all of the observational detections in this range overlapping the results from our simulations within the uncertainties. In the outer regions, the observations are dominated by upper limits which are higher than, and thus consistent with the inferred column densities in the simulations.

The observations follow the general trend that the inner regions are dominated by detections of $\approx 10^{14}$ cm^{-2}, whereas the outer regions are mostly upper limits between $\approx 10^{13.5} - 10^{14}$ cm^{-2}. This is suggestive of a Ne VIII column density profile which typically declines by ≥ 0.5 dex between an impact parameter of 150 kpc and 300 kpc. This is also seen in both APOSTLE and AURIGA. APOSTLE better recovers the (approximately) flat distribution of Ne VIII detections; however, AURIGA agrees better with the higher central column densities. In any case, the model preferences are driven by two data points, the ones with the lowest and highest impact parameters. Therefore the model choice is subjective, and there is no clear preference towards either APOSTLE or AURIGA.

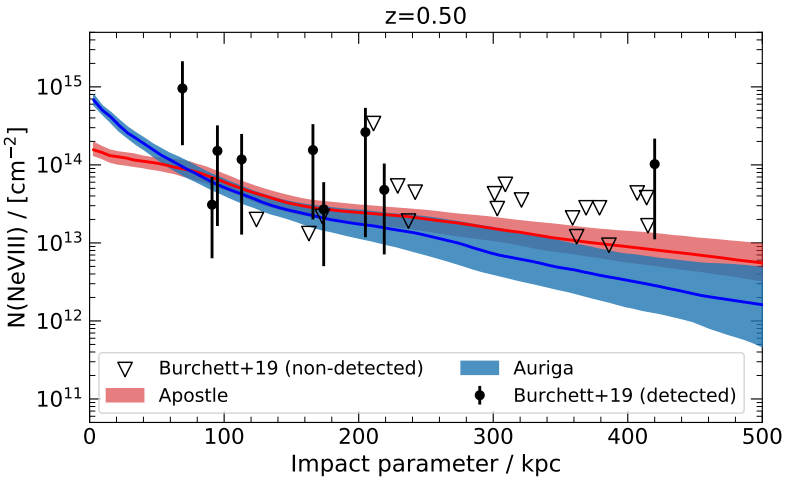

Figure 4.22: The atomic column number density of Ne VIII as a function of impact parameter from the centre of the primary halo in both the APOSTLE (red) and AURIGA (blue) simulations out to 500 kpc at $z = 0.5$. The column density at a fixed radius, r, for a single halo is calculated by taking the median column density of many sightlines through a small annulus. We also compute the lower and upper quartiles of the column density in each annulus. The solid line shows the mean of the median column density, at each radius, for all four haloes. The shaded region illustrates the range between the mean of the lower, and upper quartiles, for all of the haloes sampled. We also include the observational detections (solid black circles) and non-detections (empty triangles) of Burchett et al. (2019).

4.9 Discussion and Conclusions

The two simulations that we have analysed in this work have been shown to reproduce many galaxy observables even though they involve different galaxy formation models and hydrodynamical schemes. In particular the large-volume EAGLE simulations, which are similar APOSTLE simulations, reproduce the galaxy stellar mass function (Schaye et al., 2015), the evolution of galaxy masses (Furlong et al., 2015), sizes (Furlong et al., 2017) and colours (Trayford et al., 2015). Similarly, large volume simulations with a similar model to AURIGA have successfully reproduced the scaling relations and evolution of galaxy sizes (Genel et al., 2018), the formation of realistic disc galaxies (Pillepich et al., 2018), the gas-phase mass-metallicity relation (Torrey et al., 2019) and the diversity of kinematic properties observed in the MW-type galaxies (Lovell et al., 2018).

In this work, we have analysed the emergent baryon cycle around two Local Group-

like volumes centred around a pair of haloes similar to those of the MW and M31. We investigated how the baryon cycle differed when using the different subgrid models of the APOSTLE and AURIGA simulations. While these models are similar, they have significantly different implementations of SNe and AGN feedback. APOSTLE injects all the energy from SNe in the form of a thermal energy 'dump', whereas AURIGA uses hydrodynamically decoupled 'wind' particles that carry mass, energy, momentum and metals away from the ISM to lower density regions of the galactic halo.

In Section 4.5, we explored the effects of the different feedback implementations on baryonic evolution, particularly the baryon fraction, in and around the two primary haloes as a function of time. We found the minimum baryon fraction within a sphere around a primary APOSTLE galaxy to be $\approx 40\%$ of the cosmic baryon budget, which is approximately half the value found in AURIGA. Furthermore, the APOSTLE simulations exhibit a baryon deficiency of $\geq 10\%$ within a radius ≥ 1 Mpc (comoving) of the halo, extending to ≈ 2 Mpc at the present day. Thus, in APOSTLE, the Local Group is a baryon deficient environment. Conversely, in the AURIGA simulations the baryon fraction is within 5% of unity at all radii ≥ 0.5 Mpc (comoving), and at all redshifts. This difference in the baryon evolution is remarkable given that both simulations use the exact same initial conditions and produce central galaxies with relatively similar stellar properties. This is consistent with the findings of Mitchell & Schaye (2021b) which show the gas mass, and thus density, of the CGM are more sensitive to the baryon cycle than is the case for the properties of the central galaxy.

In Section 4.6 we conducted a census of all the baryons expected to lie within R_{200} at the present day due to gravitational forces alone (which we called 'predestined'). In APOSTLE we found that $\sim 35\%$ of the baryonic counterparts of the $z = 0$ dark matter halo particles inhabit the primary halo, whereas in AURIGA approximately 70% do. Furthermore, in APOSTLE we found that almost half of the baryon counterparts of dark matter particles that are missing *never entered the halo*: they are 'impeded'. By contrast, in AURIGA almost 90% of the absent baryons entered the halo before being ejected.

We also found that the physical extent of ejected and impeded baryons, in both APOSTLE and AURIGA is such that there is baryonic mixing between the two primary haloes. This baryonic mass transfer, shown in Fig. 4.15, indicates that the presence of M31 may influence the evolution of the MW and vice versa (see Borrow et al., 2020).

The large 'impeded' gas component in APOSTLE is produced by halo-scale fast outflows with high covering fractions. The AURIGA simulations do not produce sufficiently large outflows to impede accretion significantly. However, SNe feedback in both, APOSTLE and AURIGA inject a similar amount of energy per unit mass into the surrounding gas. Thus, the different fates of the energetic gas must result from the method of injecting the energy, or the subsequent evolution of the gas (followed with two different hydrodynamical scheme.). We strongly suspect that it is the former that is responsible for the different outcomes, however, at later times, it is likely that there are effects from AGN feedback too.

This differences in the SNe subgrid prescriptions in APOSTLE and AURIGA result in the post-SNe temperature of the gas in APOSTLE being much higher that in AURIGA and, crucially, greater than 10^7 K. Thus, in APOSTLE radiative cooling is inefficient and the gas expands adiabatically. This expansion produces hot, low-density parcels of gas which are buoyant and accelerate outwards through the halo (Bower et al., 2017b). Conversely, in AURIGA the lower post-SNe temperature makes radiatively cooling more efficient and the gas cools rapidly, at almost constant density, and recycles on a short timescale.

To summarise, we have found that the processes that regulate the rate of star formation in a MW-mass galaxy can be classified into two broad categories: ejective and preventative. The AURIGA simulations are dominated by ejective feedback with relatively short recycling times, regulating star formation without significantly reducing the halo baryon fraction. However, in APOSTLE feedback at high redshift ejects a large mass of gas beyond R_{200}. This gas has such a large covering fraction and outward pressure that it can suppress the cosmological accretion of gas. These findings are consistent with the results from the large volume EAGLE simulations

(Mitchell et al., 2019, 2020a) and the NIHAO simulations (Tollet et al., 2019) which all identify reduced cosmic gas accretion rates due to feedback processes. Wright et al. (2020) also show that outflows from AGN feedback are able to decrease the solid angle available for cosmological gas accretion, thus also suppressing further accretion. The FIRE simulations (Muratov et al., 2015) present some evidence that bursts of star formation at high redshift can suppress gas accretion into the *inner* halo; however, it is not clear if this suppression extends to R_{200} or low redshift. The FIRE simulations also produce (almost) baryonically closed MW-mass haloes (Hafen et al., 2019), thus more closely resembling those in Auriga, than Apostle. These results highlight a fundamental difference in the outcome of the feedback processes in various subgrid implementations.

A caveat is that the stellar mass of the central galaxies in Apostle is typically a factor of two lower than in Auriga. In principle, we could 'tune' the feedback parameters in Apostle to produce more massive galaxies in 10^{12} $M_\odot$ haloes and still end up with baryon-deficient haloes due to preventative feedback. Schaller et al. (2015a) demonstrates that the 'weak SNe' EAGLE variant can produce MW-mass haloes with stellar masses consistent with the Auriga galaxies, albeit with weaker feedback than used in Auriga. Furthermore, Wright et al. (2020) show that the rate of gas accretion at R_{200} for the same 'weak SNe' simulation differs from the EAGLE reference model used in this work by less than 20%. Thus, the EAGLE 'weak SNe' simulation produces Auriga-mass galaxies, while still suppressing cosmological gas accretion as shown in this work.

While we suspect SNe feedback as the leading cause of differences in the baryon cycle around our simulated galaxies, there are other differences in the two simulations that could contribute. Namely, both simulations use different hydrodynamical solvers; however Schaller et al. (2015a) and Hopkins et al. (2018) have demonstrated that the treatment of feedback is more significant in determining the outcome of simulations of this kind than the details of the hydrodynamics solver. Apostle and Auriga also use different implementations of AGN feedback. We find that the effect of AGN on the baryon cycles analysed in this work is subdominant; however, previous studies

show they can still have a significant effect on the CGM and even the central galaxy. While van de Voort et al. (2021) show the total gas mass within the virial radius of a MW-mass halo simulated with the Auriga model both with and without AGN feedback differs by only a few percent, the inclusion of AGN feedback decreases the $z = 0$ stellar mass by $\sim 30\%$. More recently, Irodotou et al. (2021) explicitly showed that the quasar and radio modes of the Auriga AGN feedback model suppress star formation in the inner and outer parts of the galaxy through ejective and preventative feedback, respectively (see also Figure 17 of Grand et al. 2017). Davies et al. (2020) show that AGN feedback can significantly reduce the baryon fractions of haloes of mass $\sim 10^{12}$ $M_\odot$. They show that the baryon fraction, at fixed halo mass, shows a strong anti-correlation with the black hole mass. Oppenheimer et al. (2020b) also demonstrate that AGN feedback can significantly reduce the baryon fraction of MW-mass haloes to very low values, particularly those with black holes of mass $\geq 10^7$ $M_\odot$.

As previously described, the Apostle simulations use a modified version of the EAGLE reference model in which the AGN feedback is effectively weaker. At the same time the higher gas mass resolution in Apostle can make the stellar feedback more efficient. As a result, the present-day black hole masses in the Apostle haloes are all $\leq 10^{6.8}$ $M_\odot$. This means the baryon cycle in these haloes is dominated by stellar feedback.

In Section 4.8 we investigated the observable signatures of strong, accretion-impeding outflows in Apostle and efficient galactic fountains in Auriga. We concluded that the Apostle simulations produce almost flat column density profiles of ions which probe hot gas –Ne VI, Ne VIII, O VI, O VII, O VIII and Mg X– out to radii $\sim 3R_{200}$ between $z = 0-3$. These flat profiles are a signature of hot, outflowing gas driven by SNe within the central galaxy. In contrast, the Auriga simulations predict rapidly declining column densities with radius, as the SNe driven outflows are unable to eject large amounts of hot gas to such large radii. We attempted to constrain the two subgrid models by comparing to the data on Ne VIII presented by Burchett et al. (2019). Unfortunately, these data are not constraining due to the small number of

detections at very small and very large impact parameters.

We also investigated the dispersion measure, which probes the integrated free electron density along the line-of-sight. We found that the main difference between the dispersion measure profiles in Auriga and Apostle is also at the very centre. In Auriga, there is a peak at impact parameter ≤ 50 kpc, not found in Apostle. The dispersion measure is a promising observational diagnostic of the evolution of baryons around galaxies. A combination of high-resolution Local Group analogues, like those presented in this work, and large-volume cosmological simulations would facilitate the production of more realistic mock catalogues of FRBs. Large cosmological volumes allow modelling random sightlines out to the typical FRB redshifts, $z \sim 2$. These background contributions can be added to predictions from Local Group analogues to make realistic mocks of what would be seen from the Earth when looking, for example, in the direction of M31. These can be compared with real sightlines in the direction of M31 and just adjacent to it. As future surveys should detect hundreds of FRBs per year behind M31, these observations should be able to constrain models and shed light on the dominant processes involved in the galactic baryon cycle.

To conclude, we find that ejective and preventative feedback work in tandem to reduce the amount of gas within haloes in the Apostle galaxy formation model. In Auriga, MW-mass galactic haloes are almost 'baryonically closed', as ejective feedback beyond R_{200} typically re-accretes and does not significantly impede further cosmic gas accretion. These results are consistent with the analysis of Wright et al. (2020) which found that baryonic feedback plays two roles in regulating the evolution of haloes by both directly removing gas from haloes, and suppressing gas inflow to haloes. Future observations of FRBs and CGM ion absorption should provide valuable data to compare and constrain different galaxy formation models. Dwarf galaxies may also provide a suitable laboratory for studying the baryon cycle. In particular, Fig. 4.2 shows there are significant differences in the stellar-mass/halo-mass relation of lower mass galaxies in the two models; these differences carry over into the baryon fraction of these objects. It is also likely that the size of the heated

gas coronae around haloes within the Local Group will affect the number of star-free dark matter haloes, which are even less massive than dwarf galaxies, in the local environment (Benítez-Llambay et al., 2017; Sykes et al., 2019).

Chapter 5

The Halo Basis Expansion Technique

5.1 Introduction

The large dynamic mass range of cosmological structure formation makes it difficult to run simulations of galaxy formation. The mass of haloes in the Universe ranges from approximately 10^{-5} $M_\odot$ to 10^{15} $M_\odot$ (Wang et al., 2020). Thus, to perform a single cosmological simulation, with a fixed mass resolution, that can well resolve all of these structures would require at least $\sim 10^{20}$ mass elements. Assuming a modest amount of memory per mass element of order $\gg 40$ bytes (Springel, 2005) would require at least a zettabyte of memory. Therefore studying the interaction of low mass haloes in the immediate environment of massive haloes requires novel techniques.

Galactic haloes have been extensively approximated using analytic, spherically symmetric density profiles. These density profiles usually come in the form of a double-power law and can include the time evolution of the halo in their free parameters. These models were first suggested by Dubinski & Carlberg (1991) and, more famously, by Navarro et al. (1997). While these spherically symmetric, power-law models are widely successful in reproducing the observed averaged density profiles of

dark matter haloes, they should be considered zeroth-order approximations. Cosmological simulations of structure formation in the Universe have thoroughly demonstrated that dark matter haloes can have a complex structure and cannot be wholly described by a spherically symmetric density function. There is also observational evidence of this structure; for example, the recent modelling of stellar streams in the Milky Way halo has demonstrated the non-spherical gravitational effects of the Large Magellanic Cloud (Erkal et al., 2019).

Lowing et al. (2011) demonstrated that the self-consistent field (SCF) method could be used to study the time-evolution of galaxy haloes. The SCF is compelling to study dark matter haloes as it can couple the zeroth-order spherically symmetric power-law models with non-spherical deviations, thus faithfully including deviations from spherical symmetry. The method was originally introduced by Ostriker & Mark (1968) for studying the equilibrium structure of rapidly rotating stars. It has also been used to study problems in galactic stability (Clutton-Brock, 1972; Fridman et al., 1984), and to evolve collisionless stellar systems (Hernquist & Ostriker, 1992). The basic idea of the SCF method is that the density and potential of a system can be expressed using a complete biorthogonal basis series expansion (BSE). This series expansion can be used with a finite number of terms to approximate the real density and potential. The work of Lowing et al. (2011) advanced the SCF technique and applied it in a novel way to provide computationally efficient descriptions of the structure of haloes in dark matter simulations followed through time. Lowing et al. (2011) demonstrated that this technique could be used to approximate very expensive n-body halo simulations and then replay them at will, at a much lower computational cost. This allows the study of the evolving environment of the haloes, with the possibility of inserting new objects into the replayed simulations and evolving them as if present in the original simulation. For example, we can insert subhaloes that are below the resolution of the original simulation and evolve them with the full complexity of the evolving potential in a cosmological environment. The inserted objects are generally considered mass-less because they have no impact on the approximated background potential, but they can be self-gravitating if required.

In recent years the SCF method has undergone even further development, focusing on increasing the accuracy of the technique for modelling dark matter haloes in a cosmological setting. Sanders et al. (2020) addressed the issue that cosmological haloes participate in the large-scale Hubble flow and therefore must include forces on the haloes from external forces. These external forces are caused by larger-scale structures and the buffeting of accretion events (they can also be artificially introduced, as we will see later). Sanders et al. (2020) also investigated the choice of basis expansion set and compared the Hernquist-Ostriker biorthogonal basis set with other families of biorthogonal basis expansions, which contain free parameters that can be tuned to match the zeroth-order profile of the distribution being approximated (Vasiliev, 2013; Lilley et al., 2018a,b).

There is a wide range of future potential applications for the SCF method in the context of halo evolution. The SCF method allows us to analytically approximate the gravitational potential of haloes, taken from n-body simulations. We can then use these approximations to investigate the evolution of new objects within the halo of interest as if they had been present in the original simulation. For example, this method enables the study of tidal stripping of low-mass satellite galaxies within the context of massive haloes, without the cost of re-simulating the parent halo at the mass resolution of the satellite. We do this by inserting a high-resolution particle model of a satellite galaxy into an analytic approximation of the parent halo and evolving through time. We can calculate the forces on the satellite galaxy at any point in space and time from the BSE approximation without re-simulating the parent halo's evolution. The BSE method also allows us to control the parameters of the approximated halo. For example, by modifying the BSE approximation's coefficients, we can investigate the effects of tidal stripping as a function of the infall parameters, the disc properties, or even the parent halo concentration. This technique allows us to focus our computational resources on objects of interest while also including the environmental effects of the halo. In Section 5.6 we describe further developments to the BSE, including modelling hydrodynamical effects.

As this thesis focuses on the properties of the halo surrounding MW-like galaxies, we

explore how the SCF method can be used to study the infall, and tidal evolution, of satellite galaxies into more massive haloes, including the effects from galactic discs and hydrodynamical pressures on the halo. This chapter is structured as follows. In Section 5.2 we start by introducing the SCF method and describe how it can be used to model galactic haloes extracted from n-body simulations. We also include a discussion on the computational complexity of the method. In Section 5.3 we then validate the method, and implementation, using some idealised tests generated from known analytic density profiles. In Section 5.4 we demonstrate the accuracy of the method in a similar way to that of Sanders et al. (2020) and identify some of the limitations of the method. In Section 5.5 we describe a novel method to include a thin, time-dependent galactic disc in the BSE method. We also suggest a method to include massive subhaloes in the expansion more accurately. Finally, in Section 5.6 we summarise our main findings and explore possible future works which could introduce a hydrodynamically modelled hot halo.

5.2 Theory and implementation

This section recapitulates the method of using a basis set expansion to approximate the density profiles of dark matter haloes extracted from n-body cosmological simulations. The method can be very efficient when the lowest order terms are able to match the spherically-averaged density profile of a cosmological dark-matter halo. The deviations from this spherical model can then be described by the addition of higher-order terms in the basis set. The following derivation follows Hernquist & Ostriker (1992) and more recently, Lowing (2011). The derivation presented in this work is motivated for two reasons. Firstly we provide an expanded derivation with more explicit steps than previously presented, and secondly, we correct some mistakes present in Lowing (2011). This section first describes the BSE method introduced by Lowing et al. (2011) before introducing further developments from Sanders et al. (2020) in Sections 5.2.4 and Sections 5.2.5. Finally, in Section 5.2.6 we present a computational complexity analysis of the technique.

We start by considering the density and potential in the form of series expansion. The basis expansion of both the density and potential is performed in spherical polar coordinates in the frame of the halo. We describe the definition of the frame of the halo in greater detail in Section 5.4.1. The spherical polar coordinates are r the radial distance from the centre of the halo, θ the polar angle and ϕ the azimuthal angle. In these coordinates the basis expansion is as follows,

$$\rho(\mathbf{r}) = \rho(r, \theta, \phi) = \sum_{nlm} A_{nlm} \rho_{nlm}(r, \theta, \phi) \tag{5.2.1}$$

$$\Phi(\mathbf{r}) = \Phi(r, \theta, \phi) = \sum_{nlm} A_{nlm} \Phi_{nlm}(r, \theta, \phi) \tag{5.2.2}$$

where $\rho_{nlm}(r, \theta, \phi)$ and $\Phi_{nlm}(r, \theta, \phi)$ are the basis functions and A_{nlm} are the coefficients. The basis functions, and coefficients, are labelled by the indices n, l and m. A biorthogonal series satisfies the biorthogonality property,

$$\int \rho(\mathbf{r})_{nlm} \Phi_{n'l'm'}(\mathbf{r}) \, d\mathbf{V} = \delta_{nn'} \delta_{ll'} \delta_{mm'} \ . \tag{5.2.3}$$

The biorthogonality property ensures that each coefficient only depends on a single potential basis function and that there are no contributions from other basis functions. The density, ρ_{nlm}, and potential, Φ_{nlm}, must also satisfy the Poisson equation,

$$\nabla^2 \Phi_{nlm}(\mathbf{r}) = 4\pi G \rho_{nlm}(\mathbf{r}) \ . \tag{5.2.4}$$

In Section 5.2.1 we will describe the biorthogonal basis set used in this thesis and describe how the coefficients can be calculated from particles in an n-body simulation.

5.2.1 Hernquist-Ostriker Basis Set Expansion

There are many choices of basis sets which satisfy the constraints of both Eq. 5.2.3 and Eq. 5.2.4. Some of the first basis expansions were found by Clutton-Brock (1972) and Hernquist & Ostriker (1992) who identified biorthogonal expansions where the lowest order terms are that of the Plummer sphere (Plummer, 1911) and Hernquist

sphere (Hernquist & Ostriker, 1992), respectively. More recently Lilley et al. (2018b) identified a novel set of analytic biorthogonal expansions based with a lowest order model, $\rho \propto r^{1/\alpha-2}$ and $\rho \propto r^{-3-1/(2\alpha)}$, for small and large radii, respectively. The basis set family of Lilley et al. (2018b) is extremely powerful as for $\alpha \approx 1$ the lowest order density profile behaves very similarly to that of the Navarro-Frenk-White (NFW) profile (Navarro et al., 1997). Cosmological n-body simulations have demonstrated that dark matter haloes have a density profile with a universal shape, which the NFW profile can well describe for haloes ranging over twenty orders of magnitude in mass (Wang et al., 2020).

This thesis uses the halo expansion basis set described by Hernquist & Ostriker (1992) due to its simplicity and ease of implementation. Sanders et al. (2020) also demonstrated that despite the greater flexibility of the basis set family introduced by Lilley et al. (2018b), there are no significant improvements over the Hernquist & Ostriker (1992) expansion for dark matter haloes when using more than a few terms in the expansion.

We split the radial and spherical dependence of the series expansion in Eqs. 5.2.1 and 5.2.2,

$$\rho(\mathbf{r}) = \rho(r,\theta,\phi) = \sum_{n=0}^{\infty}\sum_{l=0}^{\infty}\sum_{m=-l}^{l} A_{nlm}\rho_{nl}(r)Y_{lm}(\theta,\phi) \tag{5.2.5}$$

$$\Phi(\mathbf{r}) = \Phi(r,\theta,\phi) = \sum_{n=0}^{\infty}\sum_{l=0}^{\infty}\sum_{m=-l}^{l} A_{nlm}\Phi_{nl}(r)Y_{lm}(\theta,\phi) \tag{5.2.6}$$

where $Y_{lm}(\theta,\phi)$ are the spherical harmonics, and $\rho_{nl}(r)$ and $\Phi_{nl}(r)$ are purely radial terms. In this thesis we use the following definition of the spherical harmonics, Y_{lm},

$$Y_{lm}(\theta,\phi) = \sqrt{\frac{2l+1}{4\pi}\frac{(l-m)!}{(l+m)!}}P_l^m(\cos\theta)e^{im\phi} \ . \tag{5.2.7}$$

The real part of the spherical harmonics, $\mathrm{Re(Y_{lm})}$, can be written as,

$$\mathrm{Re}(\mathrm{Y_{lm}}) = \begin{cases} \sqrt{\frac{2l+1}{4\pi}\frac{(l-|m|)!}{(l+|m|)!}} P_l^{|m|}(\cos\theta)\sin(|m|\phi), & m < 0 \\ \sqrt{\frac{2l+1}{4\pi}\frac{(l-m)!}{(l+m)!}} P_l^{m}(\cos\theta)\cos(m\phi), & m \geq 0 \end{cases} \tag{5.2.8}$$

where $P_l^m(\theta)$ are the associated Legendre polynomials.

Using the Hernquist & Ostriker (1992) basis set, the zeroth order term radial terms are,

$$\rho_{000} = \frac{1}{2\pi}\frac{1}{r}\frac{1}{(1+r)^3} \tag{5.2.9}$$

$$\Phi_{000} = \frac{-1}{1+r} \tag{5.2.10}$$

for the density and potential, respectively, where Newton's constant, $G = 1$. The radial dependence, r, is usually expressed as $r = r'/R_s$ where r' is the the physical radius, and R_s is a 'scale radius'. The scale radius sets the physical scale where the density profile transitions from behaving as $\rho \propto r^{-1}$ (small r) and $\rho \propto r^{-4}$ (large r). The behaviour of the zeroth order radial term is similar to that of the NFW profile, however the NFW profile is slightly shallower for large radii. At large radii the NFW profile bevaves as $\rho \propto r^{-3}$. The general terms in the Hernquist & Ostriker (1992) expansion are,

$$\rho_{nl}(r) = \frac{K_{nl}}{2\pi}\frac{r^l}{r(1+r)^{(2l+3)}} C_n^{(2l+3/2)}\sqrt{4\pi} \tag{5.2.11}$$

$$\Phi_{nl}(r) = -\frac{r^l}{(1+r)^{2l+1}} C_n^{(2l+3/2)}\sqrt{4\pi} \tag{5.2.12}$$

where $\zeta = (r-1)/(r+1)$ and transforms the radial dependency from $r \in [0, \infty)$ to $\zeta \in [-1, 1)$, and $C_n^{(2l+3/2)}(\zeta)$ are the ultra-spherical polynomials. The terms, K_{nl} are,

$$K_{nl} = \frac{1}{2}n(n+4l+3) + (l+1)(2l+1)\ . \tag{5.2.13}$$

these can be used to express the density and potential basis expansions as purely real quantities,

$$\Phi(\mathbf{r}) = \sum_{n=0}^{\infty}\sum_{l=0}^{\infty}\sum_{m=0}^{l} N_{lm}(\cos\theta)\Phi_{nl}(r)[S_{nlm}\cos(m\phi) + T_{nlm}\sin(m\phi)] \tag{5.2.14}$$

$$\rho(\mathbf{r}) = \sum_{n=0}^{\infty}\sum_{l=0}^{\infty}\sum_{m=0}^{l} N_{lm}(\cos\theta)\rho_{nl}(r)[S_{nlm}\cos(m\phi) + T_{nlm}\sin(m\phi)] \tag{5.2.15}$$

where S_{nlm} and T_{nlm} are the BSE coefficients, and we have combined the contributions of positive and negative m into a single summation $N_{lm}(\cos\theta)$ are the normalised associated Legendre polynomials,

$$N_{lm}(\cos\theta) = \sqrt{\frac{2l+1}{4\pi}\frac{(l-m)!}{(l+m)!}}P_l^m(\cos\theta)\ , \tag{5.2.16}$$

where the ϕ dependence has been explicitly included in Eqs. 5.2.14 and 5.2.15. Following the derivation from Hernquist & Ostriker (1992), the final full set of potential and density basis functions are found to be

$$\rho(r,\theta)_{nlm} = \rho_{nl}(r)N_{lm}(\cos\theta)\ , \tag{5.2.17}$$

$$\Phi(r,\theta)_{nlm} = \Phi_{nl}(r)N_{lm}(\cos\theta)\ . \tag{5.2.18}$$

In order to express a density field using the basis expansion set we must calculate the value of the coefficients, S_{nlm} and T_{nlm} in Eqs. 5.2.14 and 5.2.15. By calculating the potential coefficients from the underlying particle distribution, we can construct the BSE approximation of the potential. These coefficients can then be used to replay the evolution of the (approximate) potential of the original simulation but at a much lower cost. We will describe how to calculate the coefficients of the BSE from a particle distribution, like those in Lagrangian n-body cosmological simulations described in Chapter 2. In a particle distribution, the particle density is described as,

$$\rho(\mathbf{r}) = \rho(r,\theta,\phi) = \sum_k \frac{m_k}{r_k^2 sin\theta_k}\delta(r-r_k)\delta(\theta-\theta_k)\delta(\phi-\phi_k)\ , \tag{5.2.19}$$

where m_k is the particle mass, and r_k, θ_k, ϕ_k are the polar coordinates of the k-th particle. The density is evaluated by summing over all of the particles in the

distribution. Lowing et al. (2011) and Sanders et al. (2020) typically consider the halo particles as those within a spherical region with a radius a few times the virial radius of the halo.

The coefficients T_{nlm} (S_{nlm}) can be calculated by multiplying both sides of Eq. 5.2.15 by $[N_{lm}(\cos\theta)\Phi_{nl}(r)\cos(m\phi)]$ (or $[N_{lm}(\cos\theta)\Phi_{nl}(r)\sin(m\phi)]$ for S_{nlm}) and integrating over all space. These coefficients can be calculated at any time, by using the particle masses and distribution in Eq. 5.2.19 at that time. We start with the LHS of Eq. 5.2.15,

$$\begin{aligned}
&\int \rho(r,\theta,\phi,t) \times [N_{lm}(\cos\theta)\Phi_{nl}(r)\cos(m\phi)]\ d\mathbf{V} \\
&= \int \sum_k \Big(\frac{m_k}{r_k^2 sin\theta_k}\delta(r-r_k)\delta(\theta-\theta_k)\delta(\phi-\phi_k)\Big) N_{lm}(\cos\theta)\Phi_{nl}(r)\cos(m\phi)\ d\mathbf{V} \\
&= \sum_k m_k N_{lm}(\cos\theta_k)\Phi_{nl}(r_k)\cos(m\phi_k)\ .
\end{aligned} \tag{5.2.20}$$

The volume integral, $d\mathbf{V}$, is equal to $d\mathbf{V} = r^2\sin\theta dr d\theta d\phi$. Now, moving onto the RHS of Eq. 5.2.15,

$$\begin{aligned}
&\int \text{RHS} \times [N_{lm}(\cos\theta)\Phi_{nl}(r)\cos(m\phi)]\ d\mathbf{V} \\
&= \int \sum_{l'=0}^{\infty}\sum_{m'=0}^{l'}\sum_{n'=0}^{\infty} N_{l'm'}(\cos\theta)\rho_{n'l'}(r)[S_{n'l'm'}\cos(m'\phi) + T_{n'l'm'}\sin(m'\phi)] \\
&\qquad N_{lm}(\cos\theta)\Phi_{nl}(r)\cos(m\phi)\ d\mathbf{V} \\
&= \int\int\int \sum_{l'=0}^{\infty}\sum_{m'=0}^{l'}\sum_{n'=0}^{\infty} N_{l'm'}(\cos\theta)\rho_{n'l'}(r)[S_{n'l'm'}\cos(m'\phi) + T_{n'l'm'}\sin(m'\phi)] \\
&\qquad N_{lm}(\cos\theta)\Phi_{nl}(r)\cos(m\phi)\ r^2 dr d(\cos\theta) d\phi.
\end{aligned} \tag{5.2.21}$$

We can separate the terms of Eq. 5.2.21 into those which only depend on r, θ and ϕ. We can then simplify each of the components, independently. We start with the θ component of Eq. 5.2.21,

$$\sum_{l'=0}^{\infty}\sum_{m'=0}^{l'}\int N_{l'm'}(\cos\theta)N_{lm}(\cos\theta)\ d(\cos\theta) = \sum_{l'=0}^{\infty}\sum_{m'=0}^{l'}\frac{\delta_{l'l}\delta_{m'm}}{2\pi} = \frac{1}{2\pi}\ . \tag{5.2.22}$$

This allows the reduction of Eq. 5.2.21 to,

$$\begin{aligned}&\int \text{RHS}\times[N_{lm}(\cos\theta)\Phi_{nl}(r)\cos(m\phi)]\ d\mathbf{V}\\ &=\frac{1}{2\pi}\int\int\sum_{n'=0}^{\infty}\rho_{n'l}(r)[S_{n'lm}\cos(m\phi)+T_{n'lm}\sin(m\phi)]\Phi_{nl}(r)\cos(m\phi)\ r^2drd\phi.\end{aligned} \tag{5.2.23}$$

Then the radial component of Eq. 5.2.21,

$$\sum_{n'=0}^{\infty}\int\rho_{n'l}(r)\Phi_{nl}(r)\ r^2dr = \sum_{n'=0}^{\infty}\delta_{n'n}I_{nl} = I_{nl} \tag{5.2.24}$$

where I_{nl} is,

$$I_{nl} = -K_{nl}\frac{4\pi}{2^{8l+6}}\frac{\Gamma(n+4l+3)}{n!(n+2l+3/2)[\Gamma(2l+3/2)]^2} \tag{5.2.25}$$

This allows further reduction of Eq. 5.2.21 to,

$$\begin{aligned}&\int \text{RHS}\times[N_{lm}(\cos\theta)\Phi_{nl}(r)\cos(m\phi)]\ d\mathbf{V}\\ &=\frac{1}{2\pi}\int I_{nl}[S_{nlm}\cos(m\phi)+T_{nlm}\sin(m\phi)]\cos(m\phi)\ d\phi.\end{aligned} \tag{5.2.26}$$

We can then use $\int\cos(m\phi)\sin(m\phi)\ d\phi = 0$ and $\int\cos(m\phi)\cos(m\phi)\ d\phi = (1+\delta_{m0})\pi$, where m is an integer. Simplifying the RHS of Eq. 5.2.15 leads to,

$$\sum_k m_kN_{lm}(\cos\theta_k)\Phi_{nl}(r_k)\cos(m\phi_k) = \frac{1}{2\pi}I_{nl}S_{nlm}(1+\delta_{m0})\pi\ , \tag{5.2.27}$$

which can be re-arranged to yield S_{nlm},

$$S_{nlm} = (2-\delta_{m0})A_{nl}\sum_k m_kN_{lm}(\cos\theta_k)\Phi_{nl}(r_k)\cos(m\phi_k)\ , \tag{5.2.28}$$

where $A_{nl} = 1/I_{nl}$. The same process can be repeated to calculate the coefficients T_{nlm} by multiplying by $[N_{lm}(\cos\theta)\Phi_{nl}(r)\sin(m\phi)]$, yielding,

$$T_{nlm} = (2 - \delta_{m0})A_{nl}\sum_k m_k N_{lm}(\cos\theta_k)\Phi_{nl}(r_k)\sin(m\phi_k) \ . \tag{5.2.29}$$

Eqs. 5.2.28 and 5.2.29 can then be used to calculate the coefficients, with a single sum over all of the particles in the region of interest.

5.2.2 Calculating the density, potential and acceleration

Both the radial and spherical harmonic basis sets are complete, so when summed from zero to infinity (over both n, l and m) the expansion converges to the exact distribution, although the convergence can be non-uniform. In practice, a good approximation to the original distribution can be achieved by truncating the series to a finite number of terms,

$$\Phi(\mathbf{r},t) = \sum_{n=0}^{n_{\max}}\sum_{l=0}^{l_{\max}}\sum_{m=0}^{l} N_{lm}(\cos\theta)\Phi_{nl}(r)[S_{nlm}\cos(m\phi) + T_{nlm}\sin(m\phi)] \tag{5.2.30}$$

$$\rho(\mathbf{r},t) = \sum_{n=0}^{n_{\max}}\sum_{l=0}^{l_{\max}}\sum_{m=0}^{l} N_{lm}(\cos\theta)\rho_{nl}(r)[S_{nlm}\cos(m\phi) + T_{nlm}\sin(m\phi)] \ , \tag{5.2.31}$$

where $n_{\max}$ and $l_{\max}$ are typically of order ~ 10. The accelerations can be calculated by taking the gradient of the potential, Eq. 5.2.30,

$$\begin{aligned} a_r(r,\theta,\phi) = -\sum_{n=0}^{n_{\max}}\sum_{l=0}^{l_{\max}}\sum_{m=0}^{l} N_{lm}(\cos\theta)\frac{d}{dr}\Phi_{nl}(r) \\ [S_{nlm}\cos(m\phi) + T_{nlm}\sin(m\phi)] \ , \end{aligned} \tag{5.2.32}$$

$$\begin{aligned} a_\theta(r,\theta,\phi) = -\frac{1}{r}\sum_{n=0}^{n_{\max}}\sum_{l=0}^{l_{\max}}\sum_{m=0}^{l} \frac{dN_{lm}(\cos\theta)}{d\theta}\Phi_{nl}(r) \\ [S_{nlm}\cos(m\phi) + T_{nlm}\sin(m\phi)] \ , \end{aligned} \tag{5.2.33}$$

$$a_\phi(r,\theta,\phi) = -\frac{1}{r}\sum_{n=0}^{n_{\max}}\sum_{l=0}^{l_{\rm lmax}}\sum_{m=0}^{l}\frac{mN_{lm}(\cos\theta)}{\sin\theta}\Phi_{nl}(r) \\ [T_{nlm}\cos(m\phi) - S_{nlm}\sin(m\phi)] \ , \tag{5.2.34}$$

The computed coefficients can then be used to evaluate Eq. 5.2.31, Eq. 5.2.30 or Eqs. 5.2.32-5.2.34, thus calculating the density, potential or acceleration, respectively, at any point in space.

5.2.3 Time dependence

The time dependence of the BSE can be introduced by considering a time dependent version of the particle density profile given by Eq. 5.2.19,

$$\rho(\mathbf{r},t) = \rho(r,\theta,\phi,t) = \sum_k \frac{m_{k,t}}{r_{k,t}^2 sin\theta_{k,t}}\delta(r-r_{k,t})\delta(\theta-\theta_{k,t})\delta(\phi-\phi_{k,t}) \ , \tag{5.2.35}$$

where mass and polar coordinates are defined for each particle, k, at time t. In general, the particle mass in dark matter only simulations is constant and time-independent. However, most baryonic cosmological simulations allow the stellar- and gas-particle masses to vary with time. Propagating this time-dependent density profile through the derivations in Section 5.2.1 leads to the time-dependent BSE coefficients,

$$S_{nlm}(t) = (2-\delta_{m0})A_{nl}\sum_k m_{k,t}N_{lm}(\cos\theta_{k,t})\Phi_{nl}(r_{k,t})\cos(m\phi_{k,t}) \ , \tag{5.2.36}$$

$$T_{nlm}(t) = (2-\delta_{m0})A_{nl}\sum_k m_{k,t}N_{lm}(\cos\theta_{k,t})\Phi_{nl}(r_{k,t})\sin(m\phi_{k,t}) \ . \tag{5.2.37}$$

Cosmological simulations generally output the particle properties at pre-defined times; these are usually referred to as snapshots. The particle properties in each snapshot can be used to calculate the BSE coefficients at the time of each of the snapshots. The coefficients can then be interpolated at any time within the range spanned by these snapshots. In this thesis, we use a simple linear interpolation scheme.

Sanders et al. (2020) demonstrated that the sampling period of the snapshots needs to be relatively small to ensure that haloes can be accurately reproduced at any point in time. In particular, they show the accuracy of the reproduction of test particle orbits begin to deteriorate significantly when the snapshot interval exceeds ~ 0.1 Gyr. However, this threshold is likely to be sensitive to the scale at which the coefficients of the BSE vary and thus depends on the evolution of the halo and the choice of basis set.

5.2.4 Inertial correction

In this section, and Section 5.2.5 we now introduce more recent developments to the BSE technique for following halo evolution presented by Sanders et al. (2020). The inertial correction accounts for the forces on the system due to the fact that the centre of the halo is a non-inertial frame of reference. The inclusion of this inertial correction is crucial in ensuring that the basis expansion technique, solved in the frame of the halo, accurately reproduces the forces found in cosmological simulations.

The comoving coordinate of the center of the halo frame can be expressed as $\boldsymbol{x} = \boldsymbol{r}/a$, where a is the cosmological scale factor and r is the physical position of the halo centre. We aim to calculate the peculiar velocity, which is the velocity of the halo without the Hubble flow, $\boldsymbol{u} = \dot{\boldsymbol{r}} - H\boldsymbol{r} = \dot{\boldsymbol{x}}a$, where $H = \dot{a}/a$ and is the time-dependent Hubble parameter. Following this, the acceleration of the halo reference frame can then be calculated from $\dot{\boldsymbol{u}}$. Therefore, we find the total force on a test particle, within the reference frame of the halo, is given by

$$\mathbf{F}(\mathbf{r}, t) = -\boldsymbol{\nabla}\phi(\mathbf{r}, t) - \dot{\boldsymbol{u}} \ , \tag{5.2.38}$$

where $\phi(\mathbf{r}, t)$ is the potential, which can be calculated from Eq. 5.2.30. This inertial force was not included in the work of Lowing et al. (2011), however Sanders et al. (2020) has since highlighted the importance of including this term. Sanders et al. (2020) demonstrate that without the second term in Eq. 5.2.38, $\dot{\boldsymbol{u}}$, the method fails to

accurately reproduce the orbits of test particles when compared with cosmological n-body simulations. The inclusion of inertial correction is most important in the outer region of the halo, where the gravitational forces from the halo are weaker.

5.2.5 Truncation correction

We have extracted the density distribution from cosmological simulations by sampling the particles from an n-body simulation. However, due to computational resources it is not advisable to include every particle within the entire cosmological volume. As previously described, we typically only sample particles that are within a spherical region of radius, r_p. This technique produces the following density profile,

$$\rho(r,\theta,\phi) = \begin{cases} \sum_k \frac{m_k}{r_k^2 sin\theta_k}\delta(r-r_k)\delta(\theta-\theta_k)\delta(\phi-\phi_k) & r < r_p \\ 0 & r > r_p \end{cases} \tag{5.2.39}$$

where the truncation radius has inadvertently introduced a discontinuity in the density profile $r = r_p$, beyond which the density is zero. An alternative approximation to the density profile is,

$$\rho(r,\theta,\phi) = \begin{cases} \sum_k \frac{m_k}{r_k^2 sin\theta_k}\delta(r-r_k)\delta(\theta-\theta_k)\delta(\phi-\phi_k) & r < r_p \\ C\rho_{000}(r,\theta) & r > r_p \end{cases} \tag{5.2.40}$$

which includes the lowest order radial term, Eq. 5.2.17, beyond the truncation radius. The parameter C is a normalisation constant, which can be calculated in various ways. One possibility is to choose C such that density at $r_p + \epsilon$ matches the spherically averaged density of the particle distribution at radius, $r = r_p - \epsilon$, where ϵ is a small perturbation. This reduces the discontinuity at the truncation radius. However, there can still be smaller discontinuities present around the truncation radius. Alternatively, C can be chosen to ensure that the total mass within some radius, $r \gg r_p$, is the same as that found in the original cosmological simulation. When using the density distribution in Eq. 5.2.40 the RHS of Eq. 5.2.20 gains an extra term,

$$\begin{aligned}&\int \rho(\mathbf{r},t) \times [N_{lm}(\cos\theta)\Phi_{nl}(r)\cos(m\phi)]\ d\mathbf{V} \\ &= \sum_k m_k N_{lm}(\cos\theta_k)\Phi_{nl}(r_k)\cos(m\phi_k) + I^{\text{corr}}_{nlm}\end{aligned} \tag{5.2.41}$$

where the extra term is $I^{\text{corr}}_{nlm} = C\int_{r_p}^{\infty}\rho_{000}(r,\theta)N_{lm}(\cos\theta)\Phi_{nl}(r)\cos(m\phi)\ d\mathbf{V}$. Propagating this extra term through the derivation presented in Section 5.2 leads to the corrected coefficients, S^{corr}_{nlm},

$$S^{\text{corr}}_{nlm} = (2-\delta_{m0})A_{nl}\Big(\sum_k m_k N_{lm}(\cos\theta_k)\Phi_{nl}(r_k)\cos(m\phi_k) + I^{\text{corr}}_{nlm}\Big)\ . \tag{5.2.42}$$

Using the definition of $\rho_{000}(r,\theta,\phi)$ in the Hernquist-Ostriker BSE, we can compute the value of the extra term in the truncation corrected coefficients, S^{corr}_{nlm}. Substituting in Eq. 5.2.9 into the integral for I^{corr}_{nlm} yields,

$$I^{\text{corr}}_{nlm} = C\int_{r_p}^{\infty}\Big(\frac{1}{2\pi}\frac{1}{r(1+r)^3}C_0^{3/2}(\zeta)\sqrt{4\pi}N_{00}(\cos\theta)\Big)N_{lm}(\cos\theta)\Phi_{nl}(r)\cos(m\phi)\ d\mathbf{V}\ . \tag{5.2.43}$$

We can again seperate the integral of Eq. 5.2.43 into separate components depending on only r, θ and ϕ. Starting with θ-component of Eq. 5.2.43

$$\int N_{lm}(\cos\theta)N_{00}(\cos\theta)\ d(\cos\theta) = \frac{1}{2\pi}\delta_{l0}\delta_{m0}\ , \tag{5.2.44}$$

and then the ϕ-component, $\int\cos(m\phi)d\phi = 2\pi$ when $m=0$, which reduces Eq. 5.2.43 to,

$$
\begin{aligned}
I_{nlm}^{\text{corr}} &= \delta_{l0}\delta_{m0} C \frac{\sqrt{4\pi}}{2\pi} \int_{r_p}^{\infty} \frac{1}{r(1+r)^3} C_m^{3/2}(\zeta) \Phi_{nl}(r) r^2 \, dr \\
I_{nlm}^{\text{corr}} &= C \frac{\sqrt{4\pi}}{2\pi} \int_{r_p}^{\infty} \frac{1}{r(1+r)^3} C_0^{3/2}(\zeta) \Phi_{n0}(r) r^2 \, dr \\
I_{nlm}^{\text{corr}} &= C \frac{\sqrt{4\pi}}{2\pi} \int_{r_p}^{\infty} \frac{1}{r(1+r)^3} C_0^{3/2}(\zeta) \left(\frac{-\sqrt{4\pi}}{(1+r)} C_n^{3/2}(\zeta) \right) r^2 \, dr \\
&= -C \frac{4\pi}{2\pi} \int_{r_p}^{\infty} \frac{1}{r(1+r)^4} C_0^{3/2}(\zeta) C_n^{3/2}(\zeta) r^2 \, dr \\
&= -2C \int_{r_p}^{\infty} \frac{r}{(1+r)^4} C_n^{3/2}(\zeta) \, dr
\end{aligned}
\tag{5.2.45}
$$

The correction in Eq. 5.2.45 only needs to be applied to the S_{nlm} coefficients. When repeating the process above for the T_{nlm} coefficients, we initially multiply through by $[N_{lm}(\cos\theta)\Phi_{nl}(r)\sin(m\phi)]$. When solving the for the ϕ component we find that $\int \sin(m\phi) d\phi = 0$ and thus, there are no contributions to T_{nlm} coefficients. In fact, the correction only needs to be applied to S_{n00} coefficients, as both l and m must be zero due to the delta functions in Eq. 5.2.44. Therefore, the truncated corrected BSE coefficient, S_{n00}^{corr}, can be written as combination of the uncorrected coefficient, S_{n00}, with an additional term,

$$
S_{n00}^{\text{corr}} = S_{n00} - 2CA_{n0} \int_{r_p}^{\infty} \frac{r}{(1+r)^4} C_n^{3/2}(\zeta) \, dr \; . \tag{5.2.46}
$$

The inclusion of the truncation correction, which extends the particle density from a finite region onto an infinite region, can be particularly important in the outer regions, $r \geq r_p$. The standard use of the BSE on the density profile, which has a discontinuity at $r = r_p$, can result in large spikes of negative density at large radii. These spikes are produced by higher-order expansion terms in the BSE. They are analogous to the Gibbs phenomenon, which occurs when a finite number of terms in a Fourier series is used to resolve a jump discontinuity.

Alternatively, the effects of the artificial spikes in negative density due to the discontinuity in the density function can be reduced by increasing the truncation radius

such that it is a lot larger than the region of interest. This ensures that spurious density artefacts occur beyond the region of interest, thus substantially limiting their effect. However, as this technique includes a larger volume, it also includes more particles when calculating the coefficients. This increases the computational cost of calculating the coefficients, as the calculation of the coefficients scales linearly with the number of particles.

5.2.6 Performance considerations

There are two cases where the performance of the basis expansion technique must be considered. The first is during the initial calculation of the coefficients, which in this thesis are extracted from n-body cosmological simulations. The second is when using the coefficients to calculate the forces at many locations and times to evolve the orbits of point masses through the approximated potential.

We start by exploring the computational complexity of calculating the coefficients using big-O notation (Bachman, 1894). The coefficients of the BSE are calculated using Eq. 5.2.27, which, for a single coefficient, requires a sum over all of the particles in the region of interest. This process must then be repeated for all of the coefficients. The leading order number of coefficients is equal to $n_{\max} \times l_{\max} \times l_{\max}$. Therefore, we find that the computational complexity of calculating the coefficients from the n-body simulation is $O(n_{\text{particles}} n_{\max} l_{\max}^2)$ where $n_{\text{particles}}$ is the total number of particles in the region of interest. Previous works often using a fixed relation to relate $n_{\max}$ and $l_{\max}$ with Sanders et al. (2020) suggesting the a relation of $n_{\max} \sim 2l_{\max} + 2$.

One of the choices when calculating the coefficients for the BSE is to decide the ordering of the sums. Namely, is it more efficient to calculate the contribution of a single particle to every coefficient or the contribution from every particle to a single coefficient? This question is challenging to answer as it can depend on various circumstances, including, but not limited to, the choice of basis expansion series and hardware available. In the Herquinst-Ostriker basis expansion, we use the spherical harmonics, which contain the associated Legendre polynomials, $P_{lm}(\cos\theta_k)$. These

associated Legendre polynomials are typically calculated using a recursion relation where the polynomial at one point can be expressed by neighbouring Legendre Polynomials at the same point. Thus, for this component of the expansion, it is much more efficient to calculate the contribution of an individual particle to all of the coefficients up to $n_{\rm max}$ and $l_{\rm max}$ before moving onto the next particle. Furthermore, this approach also lends itself to an efficient parallelisation strategy. This ordering of the calculation allows the particles to be split into independent groups of roughly equal size. The contribution to the coefficients can be calculated independently for each of the particle groups, and the final coefficients can be calculated by summing the partial coefficients produced by each of the groups. This is an example of an embarrassingly parallel problem with no dependency (and therefore no need for communication) between the parallel particle groups except at the very end of the calculation, where the results must be summed to produce the total coefficients.

We now consider the computational complexity of calculating the force from the previously calculated coefficients as described in Eqs. 5.2.32-5.2.34. The complexity is the same as for calculating the coefficients, $O(n_{\rm evaluations} n_{\rm max} l_{\rm max}^2)$ where the number of particles is replaced by the number of times the force must be evaluated, $n_{\rm evaluations}$. For high-resolution satellites, the number of $n_{\rm evaluations}$ will be equal to the number of particles in the subhalo. However, it is likely that this will not be the dominant calculation. For a massive infalling satellite, we must also calculate the self-gravity between the particles within the satellite. At worst, the self-gravity will scale with $O(n_{\rm particles}^2)$ where $n_{\rm particles}$ is the number of particles in the satellite. As discussed in Chapter 2 the self-gravity scaling can be reduced. However, these approximations are not always accurate when applied within an individual subhalo. The complexity of the BSE force could be reduced for a simulation with a large number of particles by calculating the force at fixed points on a grid. These forces can then be interpolated from the grid to the positions of the particles. However, this interpolation will decrease the accuracy of the forces and potentially have a significant impact on the accuracy of the tidal forces.

5.3 Idealised tests

This section describes some basic, idealised tests using the SCF technique to model static, analytic density profiles. In Section 5.3.1 we will attempt to model a system of particles sampled from a Hernquist profile, using the Herquinst-Ostriker BSE and compare the computed coefficients with the analytic predictions. In Section 5.3.2 we will extend the idealised tests to model a random realisation of an NFW halo and investigate the choice of the scale length. The BSE methods are implemented by the in-house python library, `pyHEX`, which is based on a C++ library produced in the preparation of Lowing et al. (2011). The examples in this section are also included in the python library in the form of integration tests to continuously validate the software's accuracy throughout development.

5.3.1 Hernquist Model

We start by demonstrating the success of the method to re-produce some artificial, random realisations of isolated density profiles which are generated from a specified analytic model. We start with a Hernquist profile, which is of the form,

$$\rho(r) = \frac{M}{2\pi}\frac{1}{r}\frac{1}{(r+1)^3} \tag{5.3.1}$$

where r is scaled by the characteristic scale length of the system, a, and M is the system's total mass. We start by generating a particle realisation of this system, using $500,000$ particles of the same mass. The modelled system has a total mass, 10^{12} $M_\odot$ and a scale length of 30 kpc. In the left panel of Fig. 5.1 we attempt to model this realisation with a BSE with a single radial term. This toy model allows us to validate that the BSE can accurately reproduce the analytic model when the correct scale length is used. In this example, the scalelength of the zeroth-order term is not measured from the underlying particle distribution. Instead, we trial fixed values shown in Fig. 5.1. We try the true scale length of the particle distribution, alongside two values which are ten times smaller and ten times larger. The coefficients of

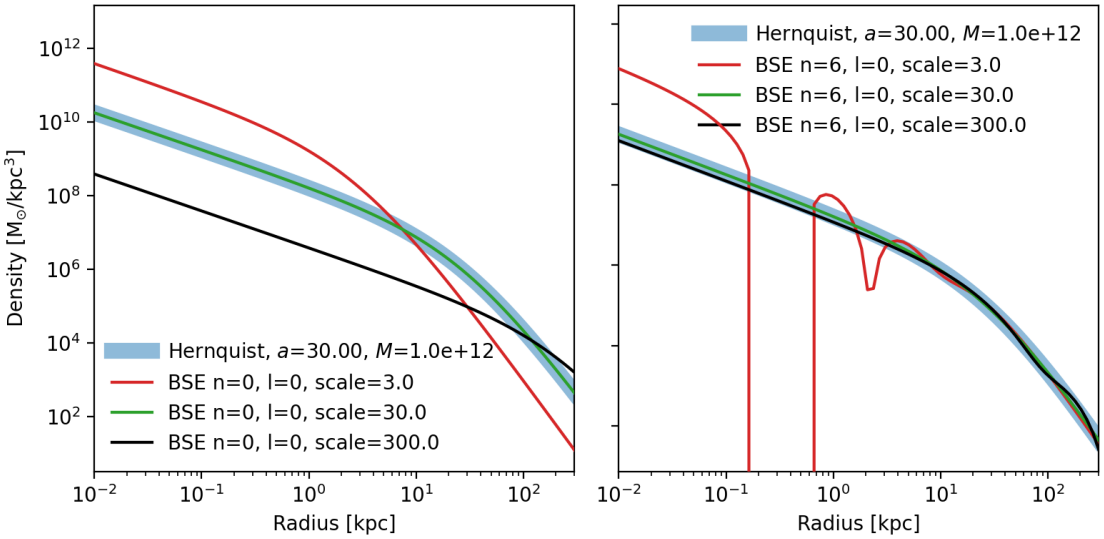

Figure 5.1: Left: The thick blue line shows the analytic density of a Hernquist profile with total mass, 10^{12} $M_\odot$, and a scale length of 30 kpc. The red, green and black lines show a single term approximation to the analytic Hernquist profile using a single term of the Herquinst-Ostriker BSE with scale lengths $3, 30, 300$ kpc, respectively. The right panel shows the same results. However, the BSE fits shown now use 7 radial terms, but still, no azimuthal terms, as we are approximating a spherically symmetric system.

the BSE are calculated from the particle distribution assuming these three fixed scale lengths. In the left panel of Fig. 5.1 it is clear that when an incorrect scale length is used, with a single term, the expansion does a poor job of reproducing the analytic model. However, the BSE reproduces the analytic model (almost) perfectly with the correct scale length. This is expected, as the zeroth-order radial term of the Hernquist-Ostriker BSE is the Hernquist sphere (see Eq. 5.2.9). Furthermore, comparison of Eq. 5.2.9 and Eq. 5.3.1 shows that the coefficient of the first radial term should be equal to $M/\sqrt{4\pi}$. The calculated coefficient differs from the analytic prediction by less than 0.03%, which is a remarkably accurate reproduction given that we are not fitting to the analytic density but rather a particle distribution realisation of the profile.

In the right panel of Fig. 5.1 we show the BSE fit to the same analytic Hernquist model, however it now uses seven radial terms (in this thesis, an $n_{\rm max} = 6$ includes 7 terms, $n = 0, ..., 6$). In this case, we see that both the expansion that uses the

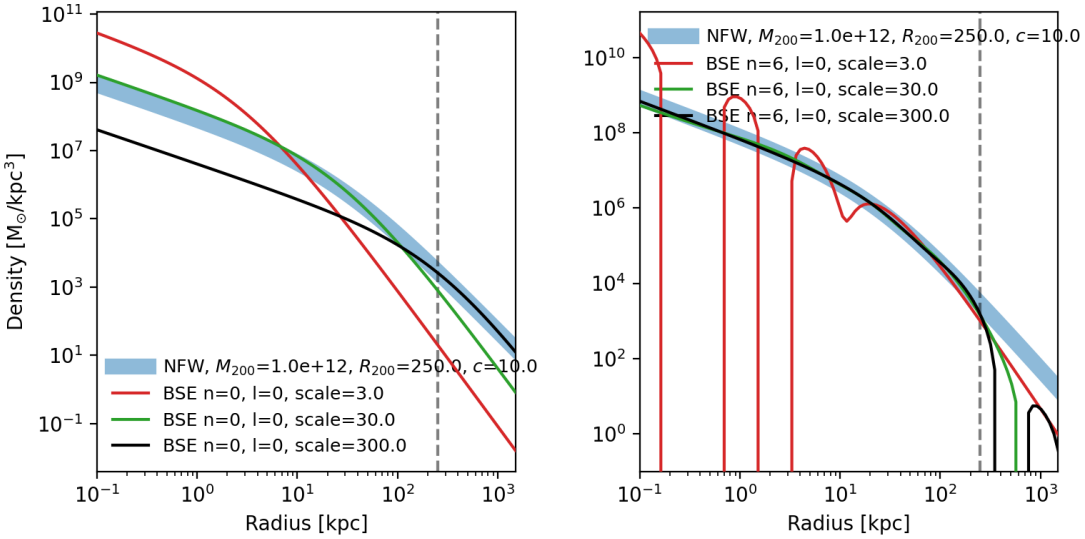

Figure 5.2: Similar Fig. 5.1, however the analytic profile being approximated is an NFW profile with parameters $M_{200} = 10^{12}$ $M_\odot$, $R_{200} = 250$ kpc and a concentration parameter, $c = 10$. The red, green and black lines shows a single term approximation to the analytic Hernquist profile using a the Herquinst-Ostriker BSE with scale lengths $3, 30, 300$ kpc, respectively.

correct scale length, 30 kpc, and the expansion that uses a much larger scale length, 300 kpc, can describe the modelled density distribution well. However, the expansion that uses a scale length an order of magnitude smaller than the true value produces a significantly worse fit to the density profile. These results are consistent with those of Lowing et al. (2011) who found that with a moderate amount of radial terms, the fit of the density profile is largely insensitive to the scale length, as long as it exceeds a threshold value. They found the threshold value to be ≈ 30 kpc for their MW-mass haloes extracted from cosmological n-body simulations.

5.3.2 NFW Model

The NFW halo has been shown to universally well describe the density profiles of galactic haloes, taken from n-body simulations, spanning ≈ 20 orders of magnitude in mass (Navarro et al., 1997; Wang et al., 2020). Thus, for the BSE to be useful in a cosmological setting, it must efficiently (i.e. with a small number of terms) accurately reproduce the NFW profile.

In this section we start with an idealised NFW halo of virial mass, $M_{200} = 10^{12}$ $M_{\odot}$, $R_{200} = 250$ kpc and a concentration parameter, $c = 10$. This NFW halo is then realised with a distribution of particles of equal mass, extending out to a radius of R_{200}. We show the BSE fits to the test NFW halo in Fig 5.2. The results are very similar to those of the Hernquist test in Section 5.3.1. The left panel of Fig 5.2 shows the BSE fit to the NFW density, using a single radial term and three different scale lengths. The best fit occurs when the scale length of the BSE is approximately equal to the R_{200}/c. However, as with the Hernquist profile, when more radial terms are considered, the fit using a larger scale length can also accurately reproduce the observed density profile. BSE's using a scale length that is a lot smaller than the true scale length leads to a poor fit, particularly in the innermost region, $r < 10$ kpc. These results are consistent with those of Lowing et al. (2011).

As seen in the right panel of both Figs. 5.1 and 5.2 artefacts can appear in the density profile in the outer region, e.g. beyond the cut off radius of the particles. This is due to the problem described in Section 5.2.5, where a discontinuity in the density profile leads to large spikes of negative and positive density. However, for both the Hernquist and NFW tests, these erroneous densities generally occur beyond the truncation radius. As such, we follow Lowing et al. (2011) and ignore the truncation correction and instead, we ensure that the truncation radius is larger than the radius of interest to minimise the discontinuity effects.

5.4 Cosmological tests

In this section, we apply the BSE expansion to a time-evolving MW-mass halo which has been extracted from a 'zoom in' cosmological simulation. We quantify the accuracy of the BSE by comparing the orbits of a sample of particles from the real cosmological simulation with predictions from orbits integrated using the BSE of the potential. We use the error measure introduced by Sanders et al. (2020) to quantify the difference between the predicted and original particle trajectories.

The halo used in this thesis is taken from the original sample of Auriga haloes

introduced by Grand et al. (2017). This is a sample of thirty 'zoom in' simulations of MW-mass, $0.5-2\times10^{12}$ $M_\odot$ haloes with the AURIGA galaxy formation model and the AREPO magnetohydrodynamics code. This suite of simulations is very similar to the AURIGA simulations described in Chapter 2. However, they follow relative 'isolated haloes' (rather than LG-like regions), are performed at a higher mass resolution and use slightly different cosmological parameters.

In this thesis we study AURIGA halo 16, Au16, from the original AURIGA sample (Grand et al., 2017). This isolated halo is evolved from high-redshift to the present day, with a dark matter particle mass of $\sim 3 \times 10^5$ $M_\odot$ and a mean gas cell mass of $\sim 5 \times 10^4$ $M_\odot$. The adopted cosmological parameters are $\Omega_m = 0.307$, $\Omega_b = 0.04825$, $\Omega_\Lambda = 0.693$ and a Hubble parameter of $h = 0.6777$ taken from Planck Collaboration et al. (2014). The initial conditions for the halo were identified in large volume simulations and the halo was selected as it is both MW-mass and relatively 'isolated' at the present day.

In this thesis, we study both the dark matter only and full magnetohydrodynamic simulation of the Au16 halo. At present day the halo has a virial mass of $M_{200} = 1.50 \times 10^{12}$ $M_\odot$, and in the full baryonic simulation produces a large disc galaxy with a total stellar-mass $\sim 5 \times 10^{10}$ $M_\odot$. The central galaxy of the Au16 halo is shown in Fig. 5.3. It has several well defined spiral arms, which are very blue, indicating the presence of young stars and, therefore, ongoing star formation. For a more in-depth description of the halo and simulation suite, we refer the reader to Grand et al. (2017).

In this section, we will use the Au16 halo as a test case to explore the BSE in a full cosmological environment. In Section 5.4.1 we discuss the definition of the halo frame of reference and explain why the choice of reference frame can impact the quality of the reproduced halo. In Sections 5.4.2 and 5.4.3 we show the results of the BSE approximation to Au16 halo, for both the dark matter only and full baryonic simulation. We then explore the accuracy of the method by attempting to reproduce the orbits of individual particles and comparing the results with those presented by Lowing et al. (2011) and Sanders et al. (2020).

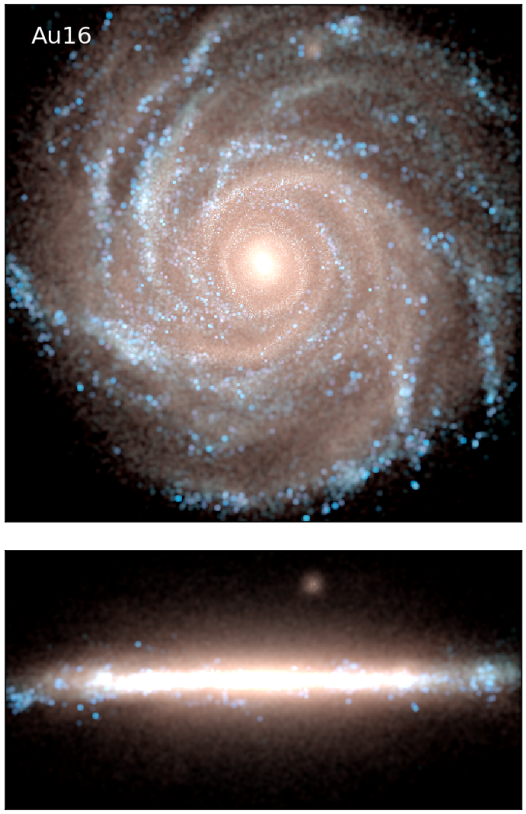

Figure 5.3: The face-on and edge-on projected stellar density at $z = 0$ for full baryonic simulations Au16. The images are synthesised from a projection of the K-, B- and U -band luminosity of stars, which are shown by the red, green and blue colour channels, in logarithmic intervals, respectively. Younger (older) star particles are therefore represented by bluer (redder) colours.

5.4.1 Halo property definitions

Accurate identification of the centre of the modelled halo is essential when using the Herquinst-Ostriker spherical BSE as the method is most efficient when representing a spherically symmetric distribution with some non-spherical deviations. Thus, choosing a reference frame that differs from the potential minimum can lead to poor reproductions of the halo. However, choosing the exact potential minimum of the halo can lead to a very noisy trajectory. This noise is amplified in the acceleration, the double derivative of the position, which is required as we use a non-inertial frame.

Previous implementations of the BSE method used to study cosmological haloes have used two different methods to identify the halo reference frame and subsequent

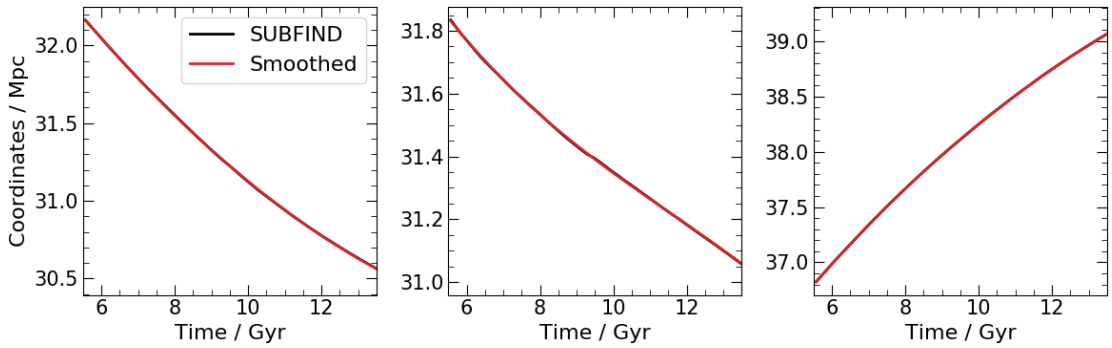

Figure 5.4: The centre of the primary halo of the AURIGA Au16 (DMO) simulation, in the simulation box frame, as a function of time. The coordinates in the x-, y-, and z-axes are shown in the three panels from left to the right, respectively. The centre of the halo is taken to be the centre of the potential as reported by SUBFIND. We also include a smoothed spline approximation to the halo centre.

trajectory. A natural choice for the centre of the halo would be to take the potential minimum of either the main subhalo of interest or the group taken from a halo finder such as SUBFIND (Springel et al., 2001; Dolag et al., 2009), or ROCKSTAR (Behroozi et al., 2012). These definitions typically calculate the virial radius and then calculate the potential minimum within the virial radius. However, this method is susceptible to sudden variation as large subhaloes are accreted and enter the virial radius of the halo. Therefore Lowing et al. (2011) proposed an alternative method of defining the halo centre by calculating the centre of mass of the particles in the inner 5% of the virial radius (again centred around the most bound particle). This definition is directly motivated to reduce the effects of accretion events and produce a smoother trajectory. However, this definition of the halo centre can still be easily displaced by interactions with subhaloes that have a pericentre that passes within the central region. Sanders et al. (2020) proposed a different method to achieve a smoothed trajectory. They still make use of a halo finder, in this case, Rockstar, which reports the halo centre through time. To reduce the noise on the halo trajectory, they construct a smooth approximate trajectory that follows the halo through time.

In this thesis, we smooth the trajectory of the halo centre as suggested by Sanders et al. (2020). We start with an initial halo trajectory by using the potential minimum as reported by the halo finder, SUBFIND. This trajectory is then approximated with

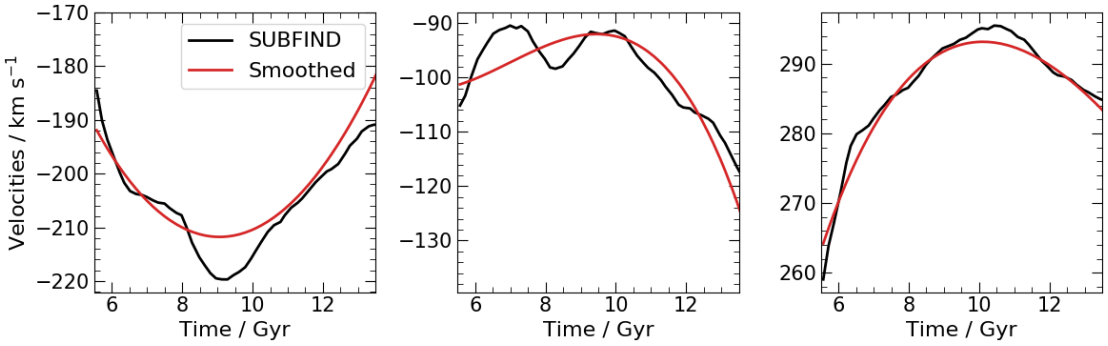

Figure 5.5: Similar to Fig. 5.4 but for the peculiar velocity of the primary halo in the AURIGA Au16 (DMO) simulation as reported by SUBFIND. We also show a smooth approximation (red line) to the peculiar velocity calculated from the derivative of the smoothed halo trajectory shown in Fig 5.4.

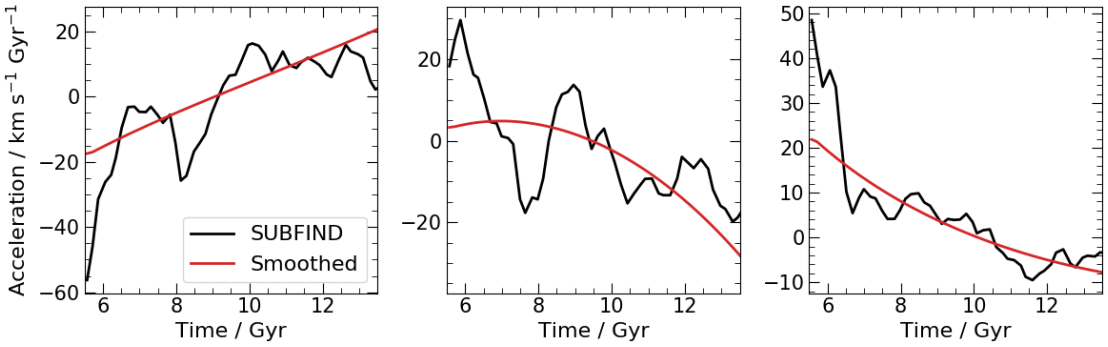

Figure 5.6: Similar to Fig. 5.4 but for the peculiar acceleration of the primary halo in the AURIGA Au16 (DMO). The SUBFIND value is calculated by taking the first derivative of the peculiar velocities reported by the halo finder. We also show a smooth approximation (red line) to the peculiar acceleration calculated from the second derivative of the smoothed halo trajectory shown in Fig 5.4.

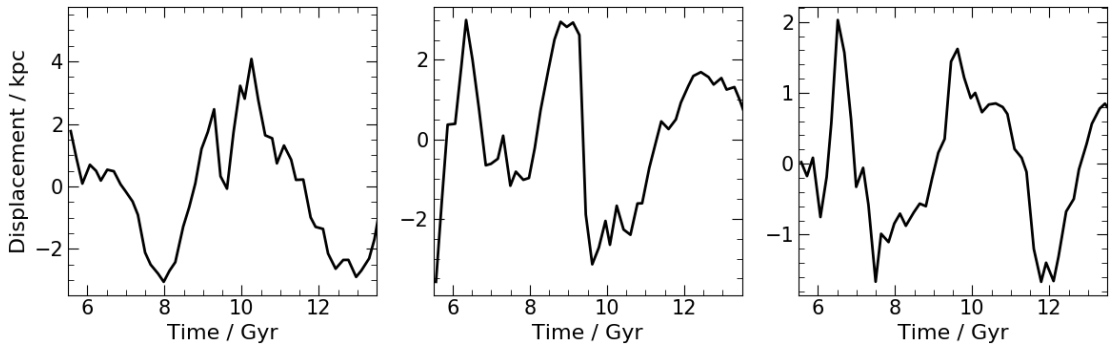

Figure 5.7: The distance between the centre of the primary halo of the AURIGA Au16 (DMO) simulation, as reported by the potential minimum in SUBFIND, and the smooth approximation shown in Fig. 5.4. The distance for each the x, y and z components are shown in the three panels from left to right, respectively.

a smooth spline as shown in Fig. 5.4. This smoothed trajectory leads to much smoother peculiar velocities and accelerations than are calculated directly from the halo finder. The difference between the original halo and smoothed halo trajectory can be seen in Fig. 5.7. In general, the smoothed trajectory lies within $\sim$ 4 kpc of the potential minimum calculated by SUBFIND which, as previously described, is important to ensure the BSE can accurately reproduce the original halo with a small number of terms in the expansion.

The use of the smoothed trajectory ensures that the peculiar velocity and acceleration of the halo are also smooth, as shown in Figs. 5.5 and 5.6. A smooth peculiar velocity, and more importantly, a smoothed peculiar acceleration, ensures that the linear interpolation of the peculiar acceleration is also accurate. Furthermore, this smoothed trajectory generally results in a smaller peculiar acceleration, thus reducing the impact of the inertial forces. The peculiar velocity, and acceleration, are calculated from the original trajectory using numerical differentiation between successive snapshots. The smoothed peculiar velocity, and acceleration, are calculated by analytical differentiating the smoothed trajectory.

The results of the Figs. 5.4-5.7 show the results for the Au16 dark matter only (DMO) halo. However, the results are generally the same for the MHD simulation. The introduction of baryons does not appear to affect the overall trajectory of the halo. Throughout this chapter, we use the smoothed trajectory to reconstruct the

evolution of the halo with the BSE method.

5.4.2 Modelled halo

This section introduces the BSE approximation to both the DMO and MHD simulations of the Au16 halo. We compare the spherically averaged density profile from the simulations with the reconstruction from the BSE. In the BSE approximation of Au16 halo, in both the DMO and full MHD simulation, we select all of the particles within a region of radius, $3R_{200}$. We calculate the basis expansion in physical coordinates, with a scale length of 30 kpc and using the Herquinst-Ostriker basis set.

In Fig. 5.8 we show the radially-averaged density profiles of the Au16 DMO halo at $z = 0$ along with reconstructions using the BSE. We show several BSE reconstructions with an increasing number of terms in the expansion. The first construction uses a single, spherically symmetric radial term representing the Hernquist profile. This zeroth-order approximation provides a reasonably good fit but underestimates the density in both the inner and outer regions. This is expected with the Herquinst-Ostriker basis set as the zeroth-order term differs from the NFW-profile, and we the chosen scale length may differ from the true scale length of the halo. Increasing the number of terms improves the fit significantly within the truncation radius. Beyond the truncation radius of the particle distribution, the addition of higher-order terms leads to the previously described Gibbs effect, which causes density artefacts (which are visible in the right panel of Fig. 5.8). However, these artefacts occur beyond the region of interest and are thus not significant. As such, we do not use the truncation correction derived in Section 5.2.5.

We also attempt to fit the radial density profile of the Au16 MHD simulation in Fig. 5.8 using the BSE technique. In general, we find that the fit is poorer than that found for the DMO simulation. The zeroth-order term of the BSE cannot capture the slope in the inner region, which differs from the DMO simulation due to an increased central density—increasing the number of terms in the expansion to $n_{\max} = 14$ and $l_{\max} = 6$ increases the quality of the fit and is able to capture the increased density

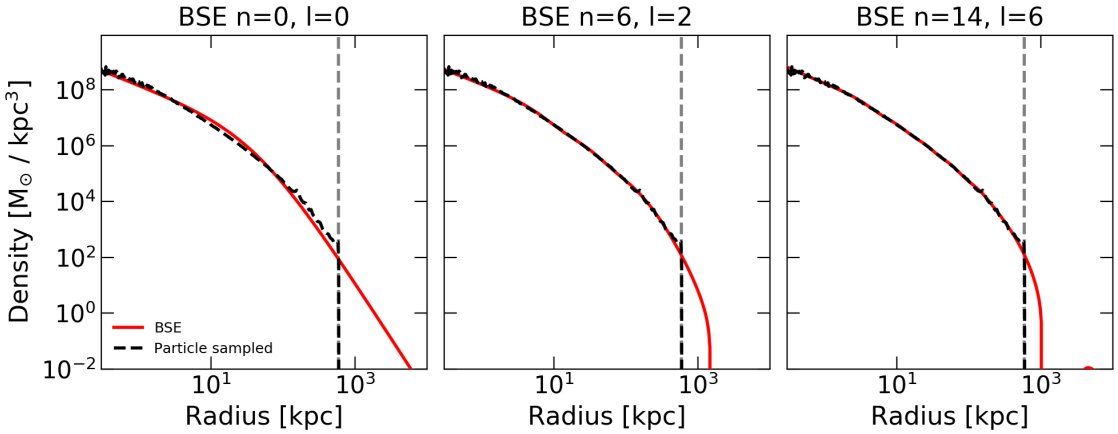

Figure 5.8: Radially-averaged density profiles of the halo at $z = 0$ along with reconstructions using the BSE. The reconstructions are shown with the red solid line. The three panels, from left to right, panels show successively more detailed reconstructions, using $n_{\max} = l_{\max} = 0$ (a single term), $n_{\max} = 6$ and $l_{\max} = 2$ and, finally, $n_{\max} = 14$ and $l_{\max} = 6$. The black dashed line shows the density as sampled from the particle distribution. The vertical grey dashed line shows the spherical truncation radius beyond which the density is assumed to be zero. Some of the small spikes in the density profile are due to substructure in the halo.

in the innermost region. In the MHD simulation, shown in Fig. 5.9, there is also a more noticeable spike in the spherically-averaged density profile at a radius of approximately ~ 150 kpc due to the presence of a massive subhalo. The BSE does not reproduce this spike, and it is unclear whether the BSE accurately captures the density of subhalo from analysis of the radial density profile alone.

In Fig. 5.10 we show the projected density through the DMO Au16 halo at the present day, for both the particle distribution and the BSE reconstruction. The density projection for the particles is calculated using the typical smoothed particle scattering technique as described in Price (2007) and Borrow & Kelly (2021). The density projection of the BSE is calculated by numerical integration of Eq. 5.2.31 over the z-axis of the simulation.

The left column of the density projections in Fig. 5.10 shows density projections through the particle distribution. The middle column shows the density projection through BSE approximated density field with a different number of terms in the expansion on each row. The right column shows the difference between the projected and actual density, normalized by the actual density. The top two rows, which show

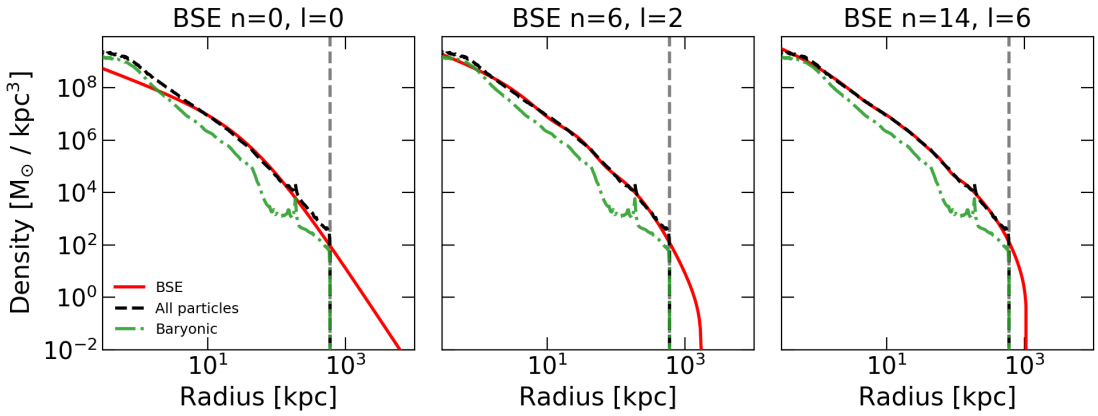

Figure 5.9: The same as Fig. 5.8 but for the MHD simulation. We show the total density sampled from the particles with the dashed black line. We also include the density of the baryons (stars and gas), as shown by the dashed-dotted green line.

the basis expansion using only a handful of terms, cannot accurately capture the nearby satellite. They also cannot capture some of the asymmetries in the innermost regions of the halo and systematically mispredict the density beyond the virial radius. As the number of terms in the expansion increases to $n_{\rm max} = 14$ and $l_{\rm max} = 6$, the BSE begins to capture the bulk behaviour of the density quite well, with less visible systematic errors. The reconstructions on the bottom two rows also begin to include an overdensity that is associated with the nearby massive satellite. However, the BSE reconstruction also includes several repeating over and under densities at the same radius of the subhalo. The pattern of these under and overdensities match those of the highest order spherical harmonic terms included in the expansion. These artefacts are likely the result of truncating the expansion abruptly.

In Fig. 5.11 we show the same density projection as Fig. 5.10; however, all of the particles associated with the massive subhalo have been removed. We then re-fit the basis expansion to the remaining particle distribution. We see that the spherical harmonic artefacts are no longer present in this case. Furthermore, the difference between the true and the reconstructed projected density profiles is also reduced. There are, however, very small isolated regions where the BSE under-estimates the projected density. The small spots of underdense regions are caused by small subhaloes in the original distribution, which are not captured by the BSE with the finite

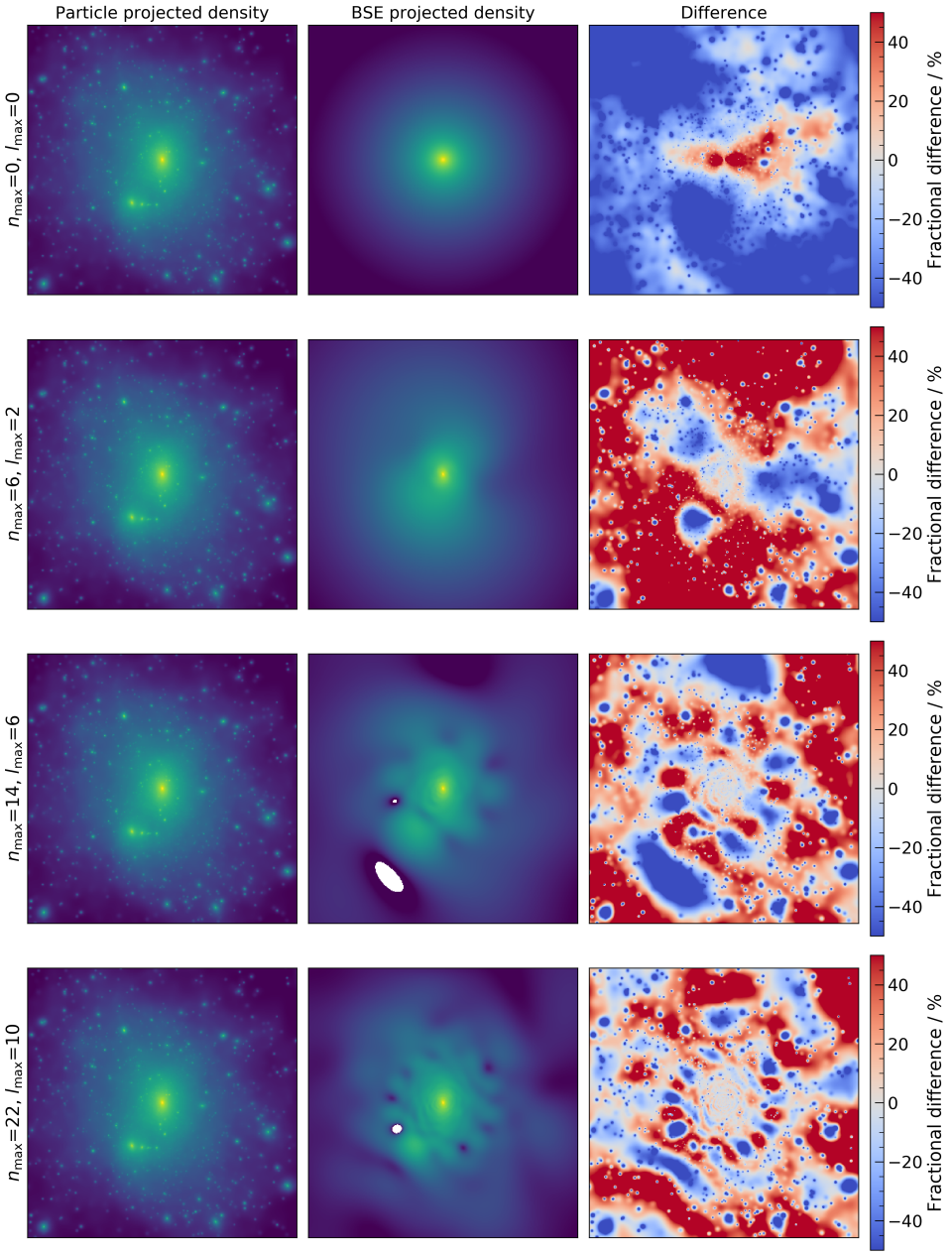

Figure 5.10: The projected mass density of the Au16 dark matter only halo, at the present day, through a region of $300 \times 300 \times 300$ kpc/h. The left column shows the projected particle density, the central column shows the projected BSE density with an increasing number of terms on each row, and the right column shows the difference between the particle density and the BSE density. The rows show the increasing number of terms in the BSE from $n_{\max} = l_{\max} = 0$ (a single term), $(n_{\max}, l_{\max}) = 6, 2$, $(n_{\max}, l_{\max}) = 14, 6$, and $(n_{\max}, l_{\max}) = 22, 10$, from top to bottom, respectively. A saturated red (blue) colour in the error column indicates a projected density error of 50% (−50%), paler colours indicate a lower percentage error. The graduated colour bar quantifies the fractional difference in the density profiles. The white dashed circle highlights the virial radius of the halo.

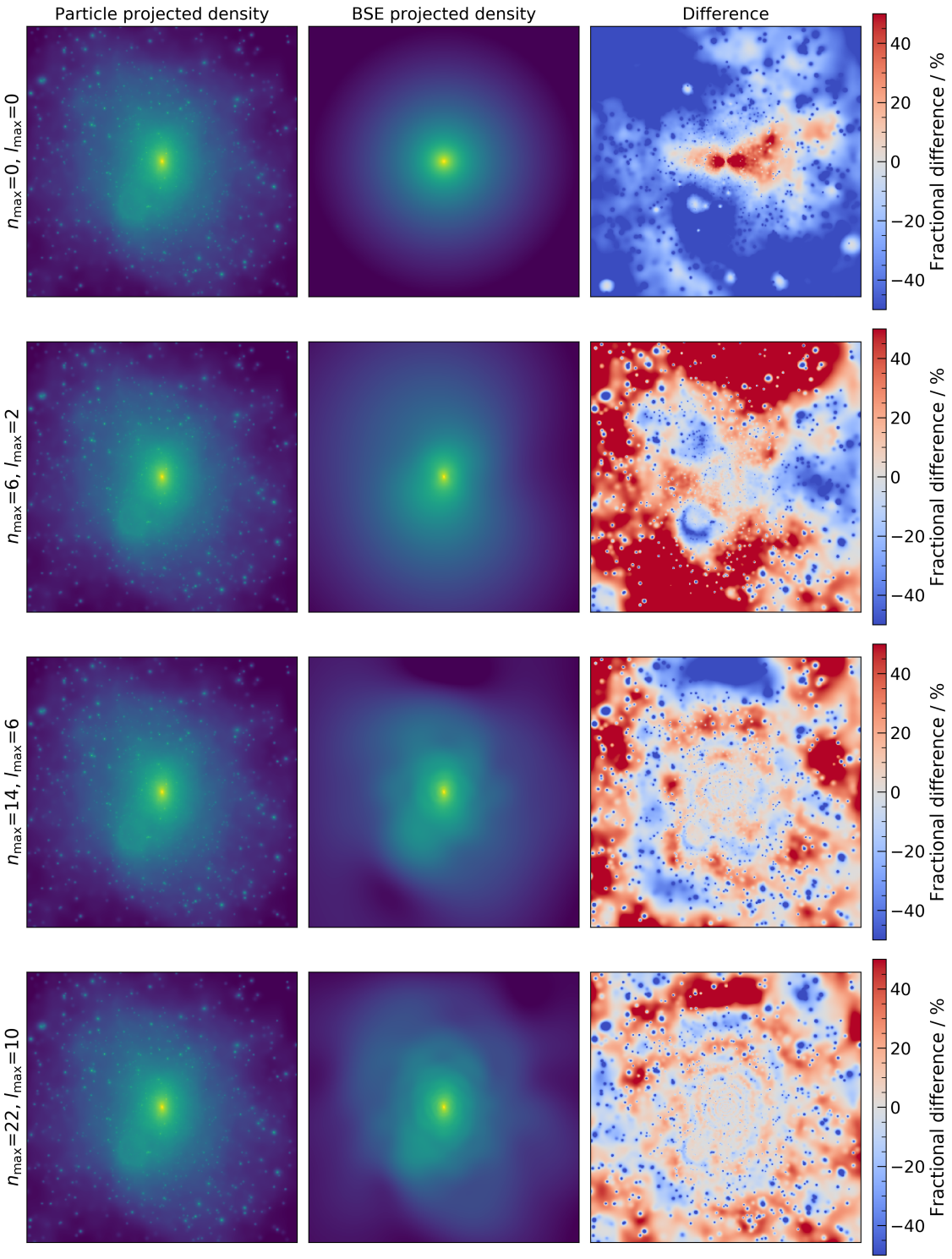

Figure 5.11: The same as Fig. 5.10 but with the particles associated with the most massive subhalo removed from the particle distribution and BSE approximation.

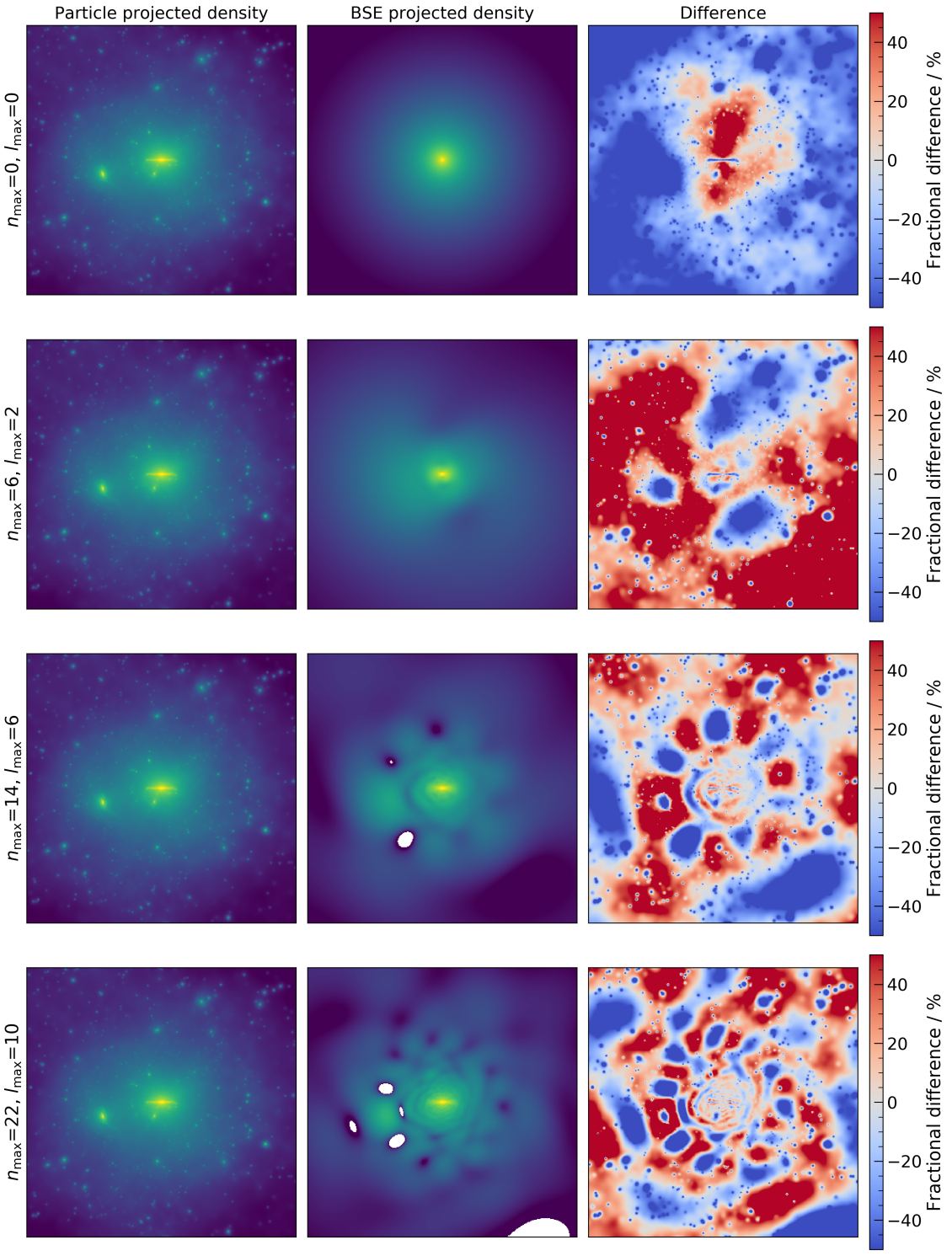

Figure 5.12: The same as Fig. 5.10 but for the MHD simulation of the Au16 halo. The density projection includes contributions from stars and gas alongside the dark matter.

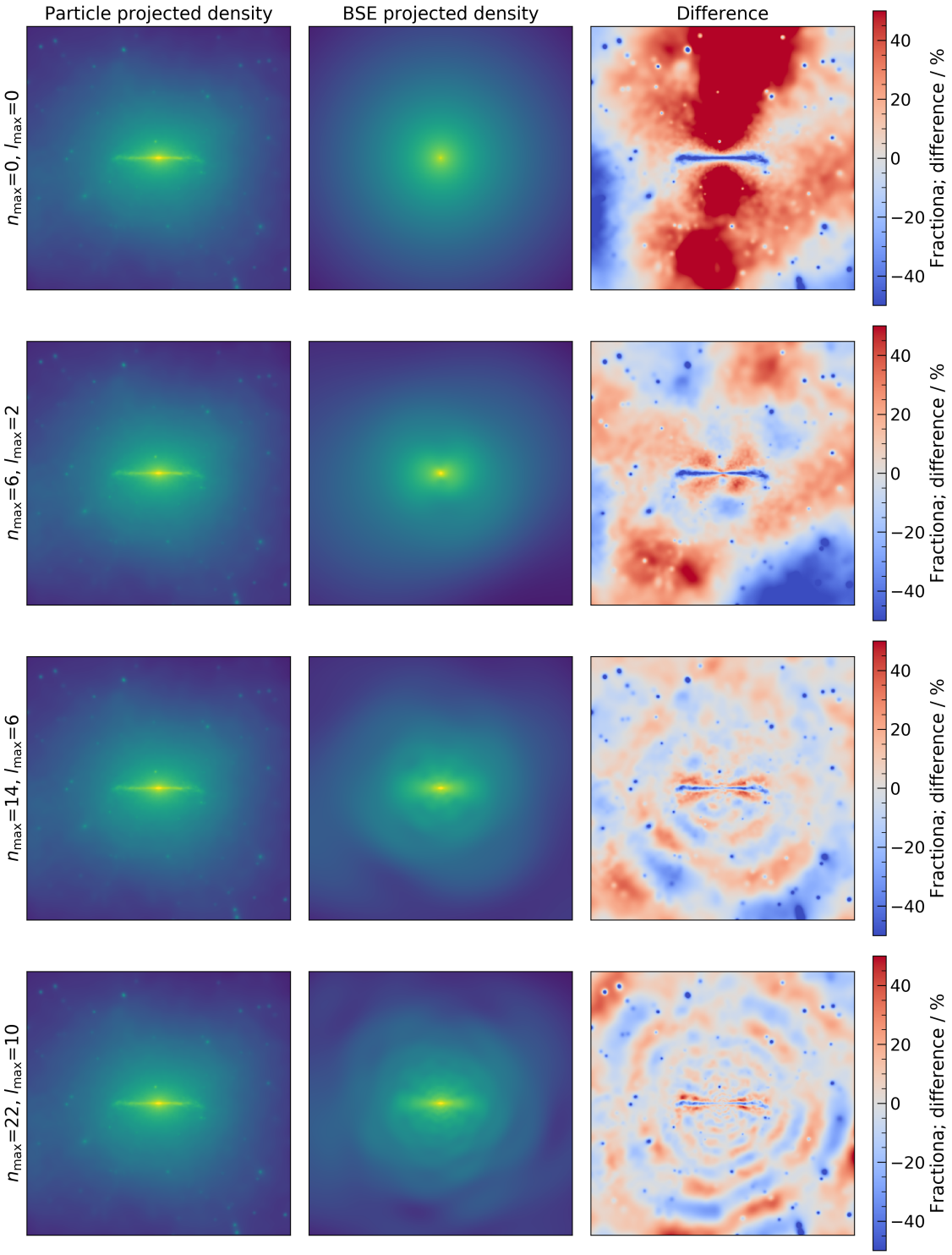

Figure 5.13: The same as Fig. 5.12 but now showing a zoomed in region, $100 \times 100 \times 100$ kpc/h and like Fig. 5.11 the particles associated with the most massive subhalo have been removed from the particle distribution and BSE approximation.

number of terms used in this thesis.

The spherical harmonic artefacts in the DMO Au16 projected density profile could be reduced by either including more angular terms or decreasing the weighting of the higher-order terms. However, even with these changes, the Herquinst-Ostriker BSE will still struggle to reproduce the density distribution of a displaced subhalo as the lower order radial terms are most efficient at modelling density profiles which decrease with increasing radius from the centre of the expansion.

In Fig. 5.12 we show the same density projection, but for the MHD simulation of the Au16 halo, which also contains stars and gas. This simulation has a massive disc component at the present day. In this zoom out projection, we see that the fit using a small number of terms completely neglects the disc component, thus underestimating the density. The BSE also over-estimates the density directly above and below the disc; this could be because these regions have a lower density than predicted by the zeroth-order symmetric profile. As the number of terms increases, the BSE reproduces the disc-like component. In the bottom row of Fig. 5.12, it is clear the BSE has been able to produce a disc-like structure, which appears to match that in the simulations fairly well. There are, however, still density artefacts due to the presence of the massive, displaced subhalo. Alongside these, there are also more visible radial bands of over and under densities, which are likely due to truncating the radial terms without a decreasing weighting for higher-order terms. These radial bands are likely more present in the MHD simulation as the higher-order radial terms have a larger contribution due to the disc.

We also show a zoomed-in projection of the reconstructed density profile of the MHD Au16 halo in Fig. 5.13. As with Fig. 5.12, we see that the BSE is able to capture the presence of the disc surprisingly well. The BSE can accurately imitate the radial and vertical extent of the disc. The disc in the MHD simulation has a very high density in the centre, which drops off rapidly above and below the plane. Most disc models use an exponential function to model the density profile above and below the disc plane. The BSE cannot fully capture this rapid decrease in density over such a small spatial scale. The BSE, therefore, underestimates the density of the disc towards the

centre and overestimates the density further out.

As the BSE appears to reconstruct the disc relatively well in Fig. 5.13, it can likely capture the gravitational effects of the disc reasonably well, particularly for points at large radii. However, given that the BSE reproduces a smeared version of the actual disc, it is unlikely that the BSE can accurately reproduce the correct tidal forces; thus, any models of satellite infall in the reconstructed potential will likely underestimate the effects of tidal stripping and disruption.

In summary, we find that the Herquinst-Ostriker BSE is able to accurately reproduce the density profile of a MW-mass halo extracted from a high-resolution cosmological simulation. Moreover, the full MHD simulation of the halo, which includes baryonic material and processes, is still well reproduced by the BSE with a small number of terms, $n_{\rm max} \approx 14$ and $l_{\rm max} = 6$. However, we identify two significant challenges to the BSE technique. First, the BSE method fails to accurately model a massive satellite near but displaced from the centre of the halo. Secondly, the BSE method fails to capture the thin disc found in the MHD simulation accurately. In general, the BSE method reproduces a smeared version of the true disc. In Section 5.5 we propose further developments to the BSE method, which would overcome these limitations without incurring a significant computational expense.

5.4.3 Particle orbits

We have shown that the spherically averaged density profile of both the DMO and baryonic haloes of an MW-mass halo can be well reproduced with Herquinst-Ostriker BSE. However, we have also found that the BSE technique fails to accurately reconstruct the true density field in the presence of massive, displaced satellites. We now investigate the accuracy of reproduced orbits of particles integrated over a few billion years.

A random sample of test particles is selected from the original n-body simulation. Particles within the simulation that are within the virial radius of the Au16 halo at both $z = 0$ and $z = 1$ are identified. We repeat this process for both the DMO and

MHD Au16 haloes; however, we start by describing the DMO halo first. These particles are then shuffled, and one hundred thousand of them are randomly selected to be used to test the orbit reconstruction using the BSE. We then take the initial positions and velocities of this sample of particles and transform them into the reference frame of the halo. The particles can then be evolved using forces calculated from the BSE and the inertial correction forces following Eq. 5.2.38. We then compare the orbits of these test particles using the BSE with the original particle trajectories from the n-body simulation. We use the BSE and halo reference frame for the Au16 halo described in sections 5.4.1 and 5.4.2.

In Figs. 5.14 and 5.15 we show orbits of six random particles which have a maximum galactocentric radius of less than 80 kpc. These particles are selected from the previously described random sample and evolved through the density field of the Herquinst-Ostriker BSE, with $n_{\max} = 30$ and $l_{\max} = 14$, for the DMO Au16 halo. We also include the trajectories of these particles in the cosmological n-body simulation.

Figs. 5.14 and 5.15 show the orbits of the same six particles, however starting the orbital integration at an age of the universe of $t \sim 9$ Gyr and ~ 6 Gyr, respectively. For Fig. 5.14, where the orbits are integrated from $t \sim 9$ Gyr we find that galactocentric radius as a function of time is very well reproduced in the BSE expansion. Furthermore, the projections of the trajectories in the cartesian axes also accurately trace those in the n-body simulation. Fig. 5.15, where the particle orbits are evolved from $t \sim 6$ Gyr, shows similar results to Fig. 5.14, however at late times the error on the galactocentric radius can be much larger. These errors tend to be most apparent at late times. Therefore, they could be because the orbits are integrated for a longer time and thus accumulate more error. However, some of the orbits, notably rows 2 and 3, appear to diverge from the true orbits quite early into their integration. This could be because the BSE approximation is less accurate at earlier times.

Figs. 5.16 and 5.17 show another sample of six randomly selected particles which are taken from the initial sample but are now constrained to have a maximum galactocentric radius which is greater than 150 kpc. This allows investigation of the orbit reconstruction of particles with longer orbital periods and apocenters close to the

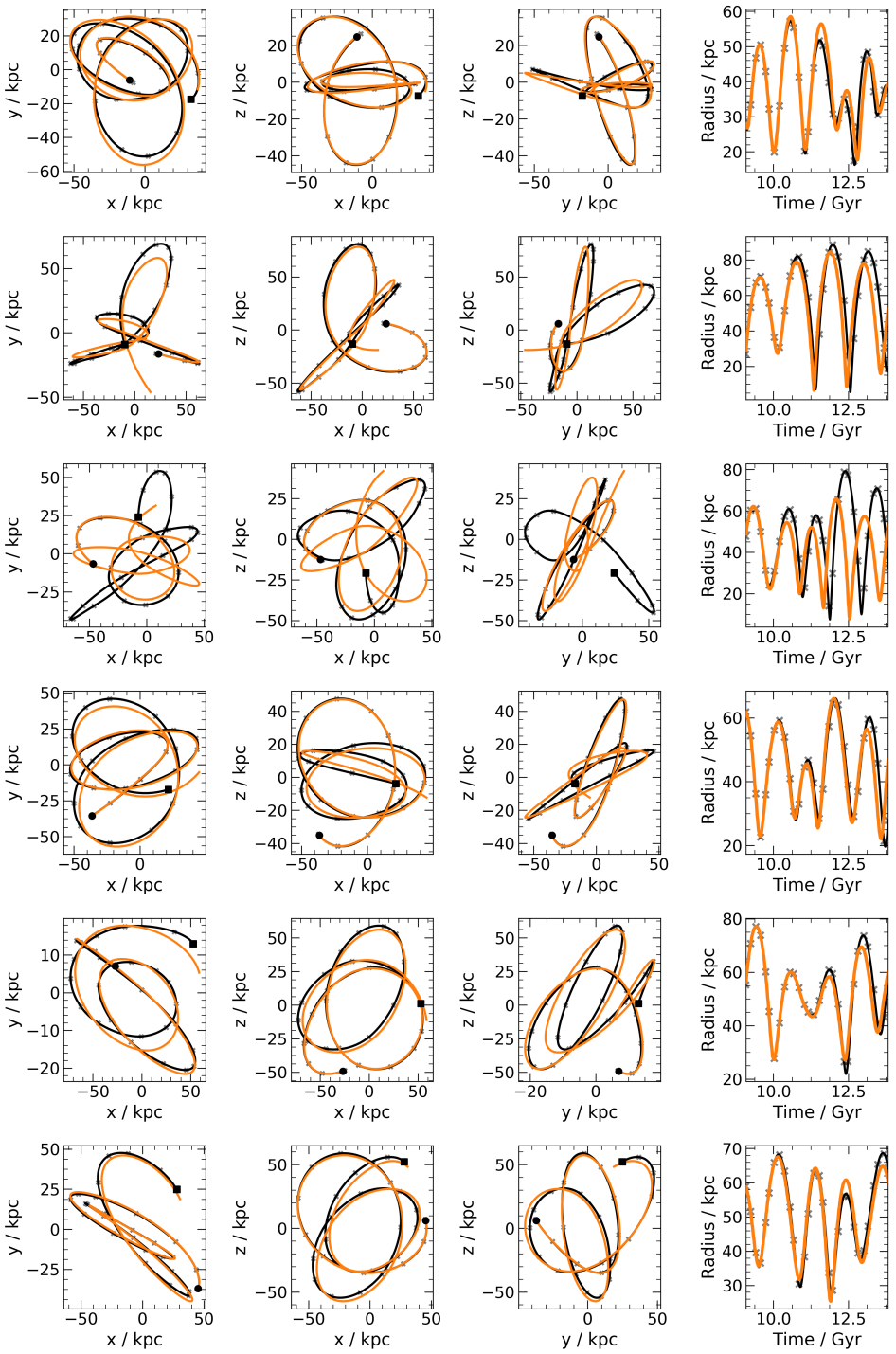

Figure 5.14: Examples of reconstructed orbits (orange) compared to the original trajectories of particles in the simulation (black lines), for the Herquinst-Ostriker BSE with $n_{\max} = 30$ and $l_{\max} = 14$. Each shows a single particle, with the first three columns showing its projections on three Cartesian axes, and the last column shows the time evolution of the galactocentric radius. These particles are evolved from ~ 9 Gyr to ~ 13.8 Gyr and are randomly selected from a sample of particles with a maximum galactocentric radius less than 80 kpc.

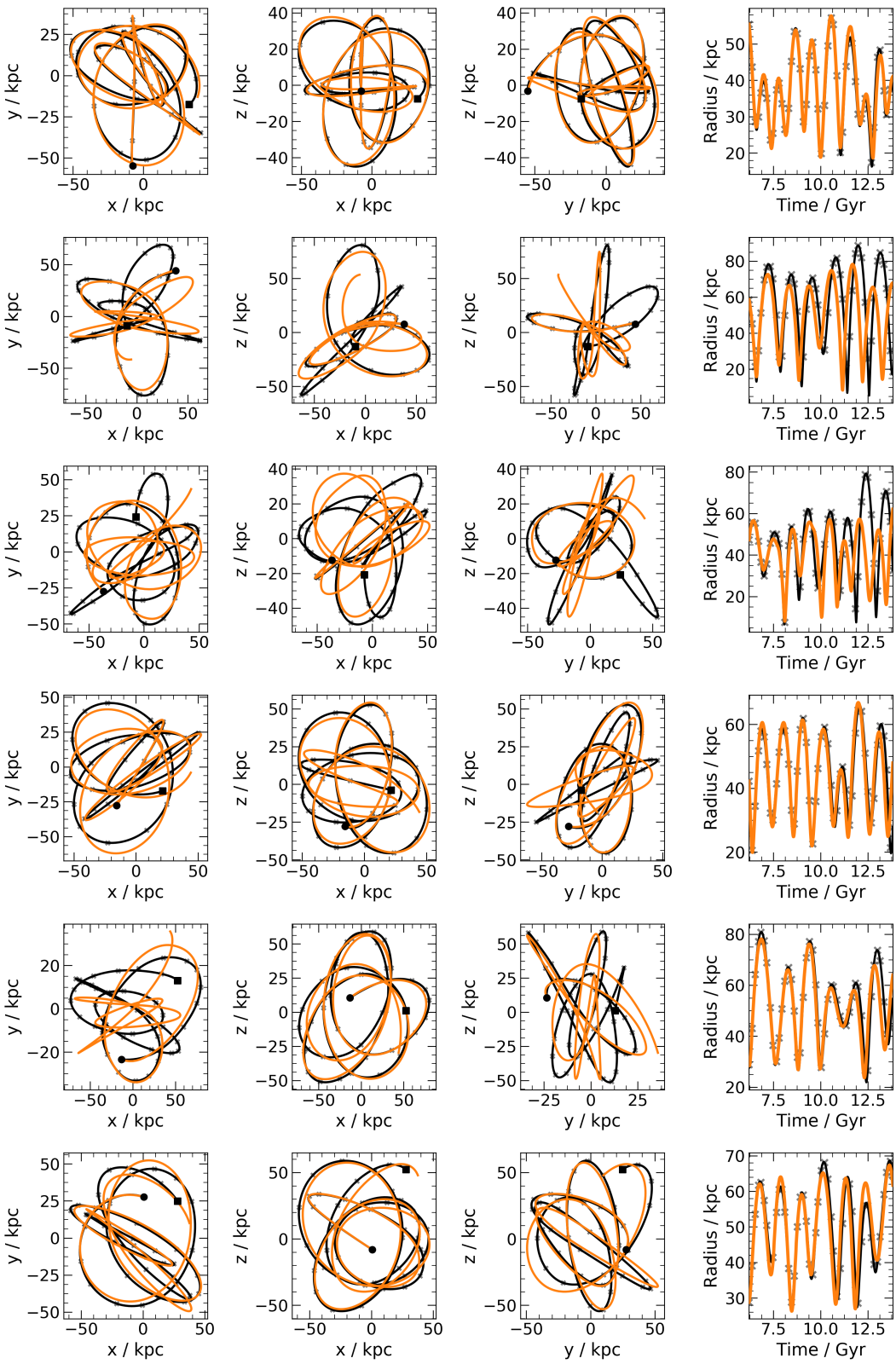

Figure 5.15: The same as Fig. 5.14, however the same particles are evolved from ~ 6 Gyr to ~ 13.8 Gyr.

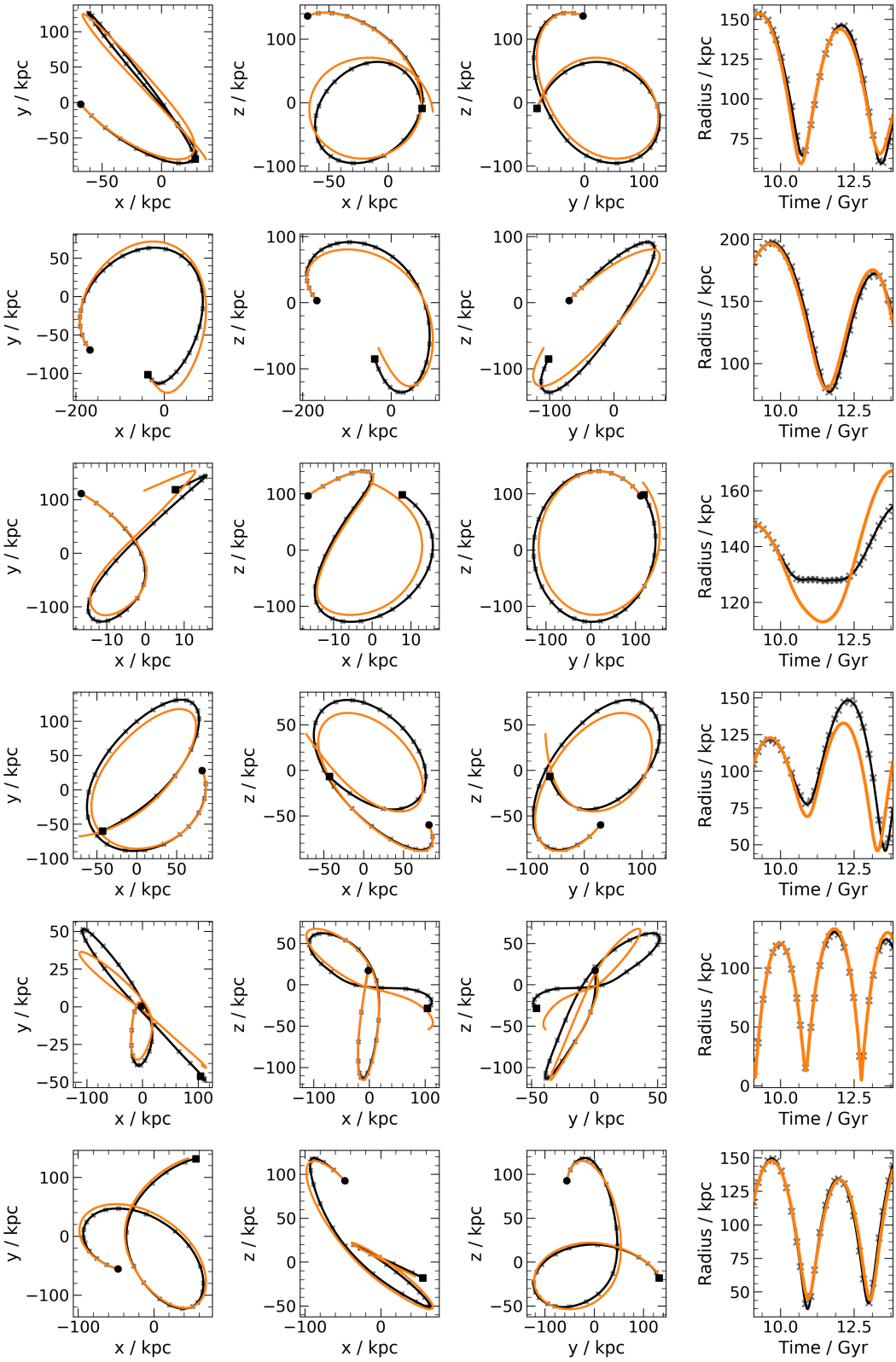

Figure 5.16: The same as Fig. 5.14; however, these particles were randomly selected from a sample of particles with a maximum galactocentric radius larger than 150 kpc.

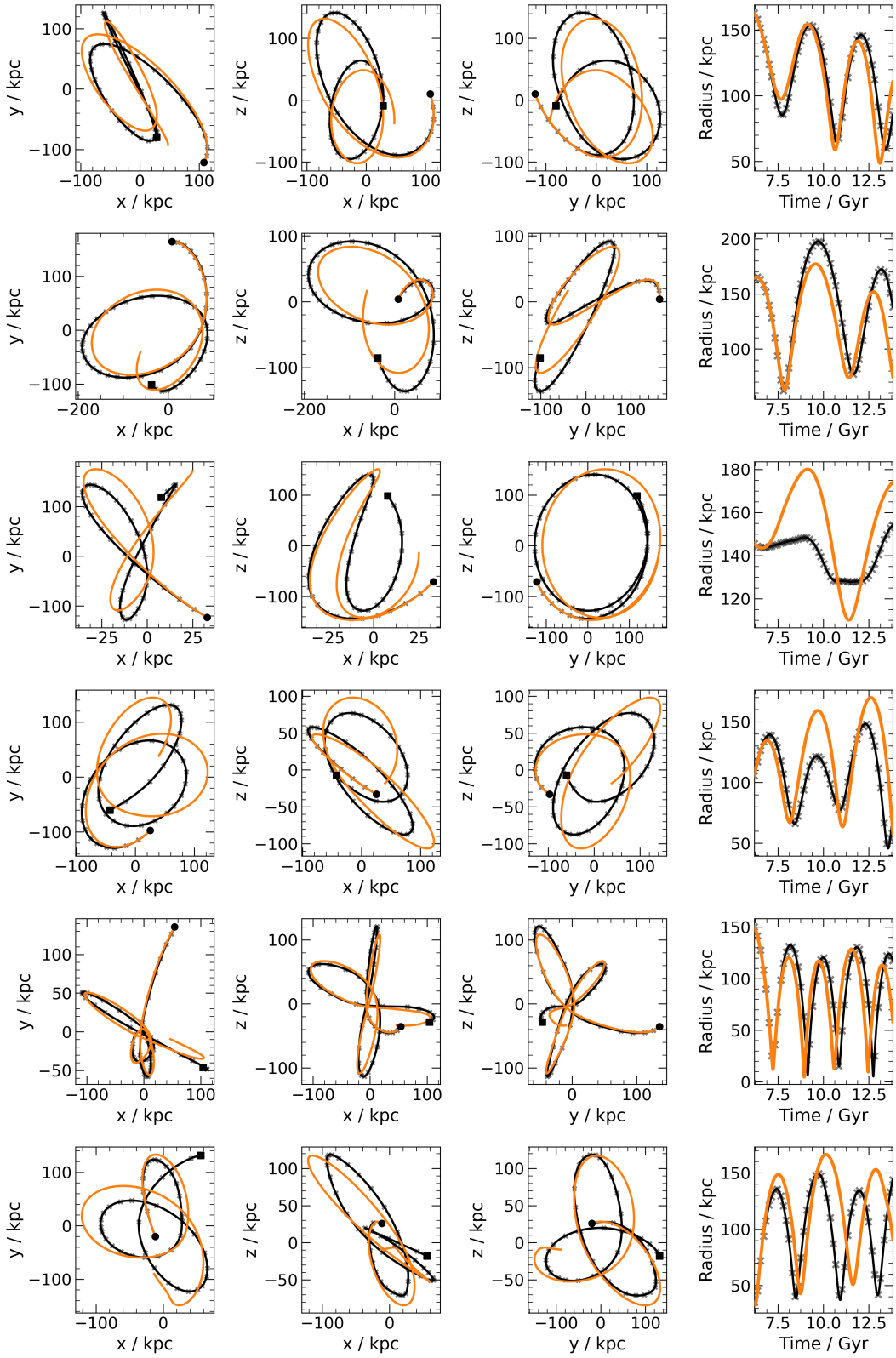

Figure 5.17: The same as Fig. 5.16, however these particles are evolved from ~ 6 Gyr to ~ 13.8 Gyr.

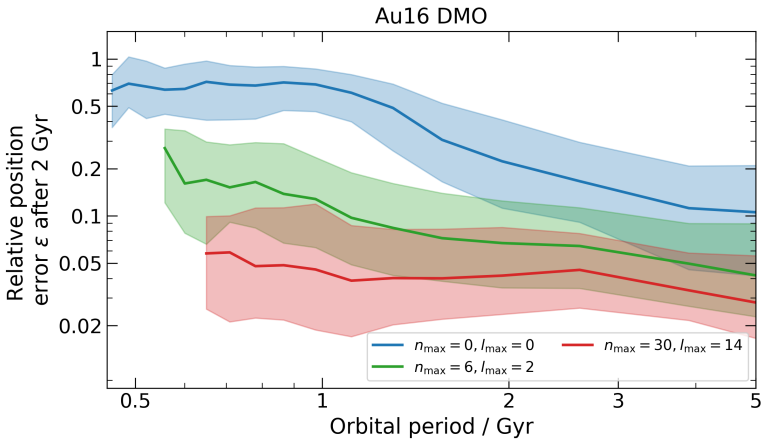

Figure 5.18: Median and $\pm 1\sigma$ envelope of the relative position error after 2 Gyr as a function of the orbital period for a sample of 100000 particles in the DMO Au16 halo. These particles are evolved starting from $t \sim 9$ Gyr and evolved for 2 Gyr of evolution before we calculate the relative positional error. We show three sets of results corresponding to BSE with different $n_{\rm max}$ and $l_{\rm max}$. The results are shown for $n_{\rm max} = l_{\rm max} = 0$ (blue), $n_{\rm max} = 6$ and $l_{\rm max} = 2$ (green) and, finally, $n_{\rm max} = 30$ and $l_{\rm max} = 14$ (red).

virial radius. In Fig. 5.16 we show reconstructed orbits starting at the age of the universe of ~ 9 Gyr. The radii of these orbits are generally well produced at all times. The deviation from the n-body simulation appears after the particles have passed through the first pericentre.

In Fig. 5.17 we show the same particle orbits as Fig. 5.16, but we start the orbit reconstruction 3 Gyr earlier, at $t \sim 6$ Gyr. We find that a lot more of the orbits are out of phase and are further out of phase, both in the projected coordinates and galactocentric radii. Again, most orbits appear to diverge from the n-body prediction after their first pericentre. After the orbits first deviate from the true orbit, their error continues to increase further.

We now want to analyse the accuracy of the orbit reproductions for a large sample of particles rather than analysis of a few random realisations. Sanders et al. (2020) introduced a measure of the error of the orbit reconstruction to quantify the accuracy of the orbits reconstructed in the BSE. They propose an error measure, $\mathcal{E}_i(t)$, which compares the relative position error of the reconstructed spatial path of the ith orbit, $\mathbf{r}_{i,\rm recon}(t)$, from that in the n-body simulation, $\mathbf{r}_{i,\rm orig}(t)$, at time after an interval of t,

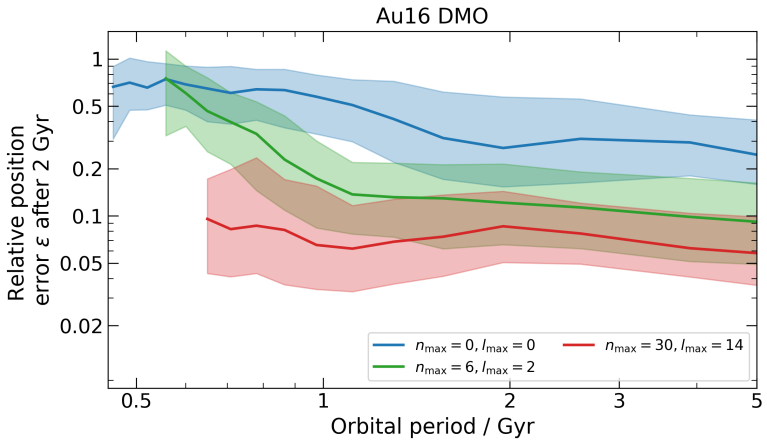

Figure 5.19: The same as Fig. 5.18 but for orbits which start at $t = 6$ Gyr.

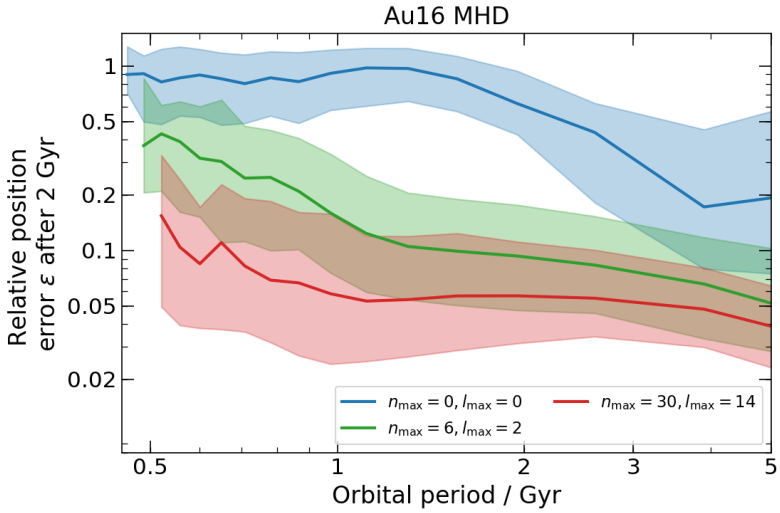

Figure 5.20: The same as Fig. 5.18 but for 25000 random dark matter particle orbits taken from the MHD Au16 halo and evolved with the coefficients generated from the baryonic halo.

$$\mathcal{E}_i(t) = \frac{|\mathbf{r}_{i,\mathrm{orig}}(t) - \mathbf{r}_{i,\mathrm{recon}}(t)|}{\overline{r}_{i,\mathrm{orig}}} \tag{5.4.1}$$

where $\overline{r}_{i,\mathrm{orig}}$ is the time-averaged galactocentric radius. This can be calculated at any time, t, during the reconstructed orbit. Sanders et al. (2020) calculate the error on the orbit after both 2 Gyr and one orbital period. However, measuring the error after a fixed number of orbital periods means that particles with longer periods naturally accumulate more error as they are integrated over a longer period. This choice leads to an almost linear relationship between the error and the orbital period. In this thesis, we choose to measure the error after 2 Gyr of integration.

Fig. 5.18 shows the median error, surrounded by an envelope of 16th to 84th percentiles, for particles binned by their orbital period. We calculate the orbital periods of each particle by taking a Fast Fourier Transform (FFT) of the particle's original galactocentric radius and identifying the frequency of the dominant period. If the period is longer than the simulated interval, we remove it from our analysis. Fig. 5.18 shows the results for reconstructed orbits that use progressively more terms in the BSE expansion starting at $n_{\mathrm{max}} = l_{\mathrm{max}} = 0$ ranging up to $n_{\mathrm{max}} = 30$ and $l_{\mathrm{max}} = 14$. We find that for orbital periods between $\approx (2 - 5)$ Gyr, the error is approximately constant. However, for orbits ≤ 2 Gyr the error tends to increase with decreasing orbital period, particularly when using a fewer number of terms in the BSE. The reduced error on orbits with longer periods may be lower as the particles are typically at larger radii, and thus, the orbits may be less sensitive to halo structure and more conditional on the enclosed mass. It could also be because the error is normalised using the mean orbital period, and thus, orbits with longer periods will have a much larger mean radius. The increase in the detail of the BSE from $n_{\mathrm{max}} = 6$ and $l_{\mathrm{max}} = 2$ to $n_{\mathrm{max}} = 30$ and $l_{\mathrm{max}} = 14$ only decreases the error by a factor about a factor of two across the whole range of orbital periods, despite a significant increase in the number terms.

Fig. 5.19 shows the same sample of particles but with their orbit integration starting ~ 3 Gyr earlier (at $z = 1$). The results of Fig. 5.19 are broadly similar to those that start at a later time. However, starting to evolve the orbits earlier leads to a

systematically higher error on the particles orbit, even when calculated with the same elapsed time. This indicates that the BSE reconstruction, or the inertial correction, is less accurate at earlier times. In Section 5.4.1 we see that the peculiar acceleration of the halo does appear to be higher at earlier times.

The MHD simulation of Au16 includes more non-spherically symmetric structure, mainly due to the galactic disc, and differs further from the zeroth-order Herquinst sphere due to the increased central density. These deviations from the spherically symmetric Hernquist should mean that more basic terms are required to achieve the same level of accuracy on the BSE reproduction of the density profile. This is supported by Fig. 5.20 which shows the error on a sample of dark matter particle orbits as shown in Fig. 5.18. The positional error on the orbits after 2 Gyr of evolution is systematically higher in the MHD simulation by about a factor of two. However, the error is not significantly different from the DMO results using the same number of terms in the expansion. This similarity in error suggests the Hernquist-Ostriker BSE is able to approximate the halo in the MHD simulation well. However, the similarity in error could also indicate that the limiting factor of the orbit integration accuracy is not the density approximation. Other factors can introduce error on the orbital reproductions, including the time interpolation between snapshots or the smoothed halo frame of reference and subsequent estimation of the peculiar velocity. Furthermore, the limiting factor of the accuracy of the reproduced orbits may be due to the massive subhalo, which appears to imprint the errors following the highest spherical harmonic term in both the MHD and DMO simulation.

We can compare the accuracy of the reconstructed orbits to those of previous BSE studies. Lowing et al. (2011) does not look at the error of a large sample of particles, but they do analyse the reconstructions of individual particle orbits. In general, our results appear to better reproduce the orbits taken from n-body cosmological simulations, which is unsurprising as they do not include the inertial correction. Furthermore, Lowing et al. (2011) does not smooth the trajectory of the halo; therefore, the inertial correction required in their work is likely much higher than required in this thesis. We can directly compare the results of Figs. 5.18-5.20 with those in

Sanders et al. (2020). general we find our errors are approximately a factor of two higher than found in Sanders et al. (2020). One of the reasons for their reduced error could be because they use a different basis expansion family than presented in this thesis. Using the basis set presented by Lilley et al. (2018b), can be tuned to yield an almost NFW profile at zeroth order. Furthermore, they calculate the coefficients with a much shorter sampling time than this thesis. Sanders et al. (2020) calculate the coefficients every ≈ 10 Myr, whereas in this thesis we compute the coefficients every ≈ 150 Myr. Therefore, it is likely they have a much smaller error introduced due to their temporal interpolation of the coefficients.

5.5 Further developments

This section presents further developments to the BSE method to study the potential around massive haloes taken from (baryonic) cosmological simulations. In Section 5.5.1 we introduce a novel method of accurately including a thin, time-dependent disc alongside the BSE of the remaining halo. We then propose a technique to efficiently model a population of massive satellite galaxies within the halo.

5.5.1 Modelling a thin disc

The Hernquist-Ostriker BSE is most efficient for modelling density distributions which are approximately spherically symmetric and are well fit by the zeroth-order Hernquist profile. This is a good approximation for haloes in dark matter only simulations. However, in cosmological hydrodynamical simulations, which also include a galaxy formation model, the BSE must also contend with both stellar and gaseous discs in the centre of galaxies. These discs can often be very thin and radially large. A large number of terms in the Hernquist-Ostriker BSE are required to accurately model these thin disc components.

Fig. 5.13 shows that the Herquinst-Ostriker BSE begins to reproduce the thin disc found in the Au16 MHD simulation. However, reproduction is not perfect. Namely,

the BSE is underdense in the centre and overdense above and below the plane of the disc. In effect, the BSE produces a smeared version of the original disc. While this does not appear to significantly hinder the ability of the BSE to reproduce orbits of point masses (see Section 5.4.3), it likely produces erroneous tidal forces. Thus, to study the tidal evolution of satellite galaxies falling into massive galactic haloes with a realistic galactic disc, we must either increase the number of terms in the BSE or find an alternative method to include the disc.

A possible approach to model the disc is to use a different family of basis expansion which is better suited to modelling the thin, extended discs. Alternatively, we propose a simpler solution in this thesis. We suggest that the disc can be modelled using a traditional analytic disc model and that this component can be removed from the BSE. Therefore, in this approach, we are only using the Herquinst-Ostriker basis expansion to model the halo and the small residual between the analytic disc and true disc.

We start by choosing an analytic model which which will be used to represent the disc component of our n-body simulations. There are a variety of analytic models which have been used to model galactic discs within the literature. The most common model in use today is the Miyamoto & Nagai (1975) model which is a modified version of the infinitely thin discs described by Kuzmin (1956) and Toomre (1963). The model is of the form,

$$\Phi_{\rm disc}(R,z,M,a,b) = \frac{GM}{\left[R^2+[a+(z^2+b^2)^{1/2}]^2\right]^{1/2}}\ , \tag{5.5.1}$$

$$\rho_{\rm disc}(R,z,M,a,b) = \frac{b^2M}{4\pi}\frac{aR^2+[a+3(z^2+b^2)]^{1/2}[a+(z^2+b^2)^{1/2}]^2}{\left[R^2+[a+(z^2+b^2)^{1/2}]^2]\right]^{5/2}(z^2+b^2)^{3/2}}\ , \tag{5.5.2}$$

where R is the cylindrical radius, z is the distance from the origin along the z-axis, a is the disc scale radius, b is the disc scale height, and M is a measure of the mass of the disc. The Miyamoto & Nagai (1975) disc model is preferred as it is free from singularities everywhere in space, and it is better suited to capturing discs that are not infinitely thin. The Miyamoto & Nagai (1975) model is also very flexible,

when $b/a \gg 1$ it produces an approximately spherical distribution with a density profile similar to that of a Plummer sphere Plummer (1911), and when $b/a \ll 1$ it corresponds to a significantly flattened disc distribution, similar to that of Kuzmin (1956) and Toomre (1963). The best-fit values of the parameters a, b and M can be extracted from hydrodynamical simulations using various techniques, such as a maximum likelihood estimation technique.

The complete density profile of the system can be constructed from a BSE representation of the halo, $\rho_{\rm halo,BSE}$, alongside an analytic model of the disc, $\rho_{\rm analytic\ disc}$,

$$\rho(r,\theta,\phi) = \rho(r,\theta,\phi)_{\rm particles} = \rho_{\rm halo,\ BSE}(r,\theta,\phi) + \rho_{\rm analytic\ disc}\ , \tag{5.5.3}$$

where the $\rho_{\rm halo,\ BSE}$ can be accurately represented using the Hernquist-Ostriker BSE presented in Section 5.2.1. We can therefore calculate $\rho_{\rm halo,\ BSE}$ using all of the particles within a spherical region of interest, and subsequently removing the contribution which is already accounted for by the analytic disc. This prevents the double counting of disc contribution,

$$\begin{aligned}
\rho_{\rm halo,\ BSE} &= \rho(r,\theta,\phi)_{\rm particles} - \rho_{\rm analytic\ disc}(R,z,M,a,b) \\
&= \sum_k \frac{m_k}{r_k^2 sin\theta_k}\delta(r-r_k)\delta(\theta-\theta_k)\delta(\phi-\phi_k) - \rho_{\rm analytic\ disc}(R,z,M,a,b) \\
&= \sum_{l=0}^{\infty}\sum_{m=0}^{l}\sum_{n=0}^{\infty} N_{lm}(\cos\theta)\rho_{nl}(r)[S_{{\rm halo},nlm}\cos(m\phi) + T_{{\rm halo},nlm}\sin(m\phi)]\ .
\end{aligned} \tag{5.5.4}$$

We can then calculate the coefficients $T_{{\rm halo},nlm}$ ($S_{{\rm halo},nlm}$) by multipying both sides of Eq. 5.2.15 by $[N_{lm}(\cos\theta)\Phi_{nl}(r)\cos(m\phi)]$ ($[N_{lm}(\cos\theta)\Phi_{nl}(r)\sin(m\phi)]$) and integrating over all space. We start with the particles and analytic potential of Eq. 5.5.4,

$$\begin{aligned}
&\int \text{LHS} \times [\text{N}_{\text{lm}}(\cos\theta)\Phi_{\text{nl}}(\text{r})\cos(\text{m}\phi)] \ \ \text{d}\mathbf{V} \\
&= \int [\rho_{\text{particles}}(r,\theta,\phi) - \rho_{\text{analytic disc}}(R,z,M,a,b)] N_{lm}(\cos\theta)\Phi_{nl}(r)\cos(m\phi)\ d\mathbf{V} \\
&= \sum_k m_k N_{lm}(\cos\theta_k)\Phi_{nl}(r_k)\cos(m\phi_k) - \\
&\int \rho_{\text{analytic disc}}(R,z,M,a,b) N_{lm}(\cos\theta)\Phi_{nl}(r)\cos(m\phi)\ d\mathbf{V}.
\end{aligned} \tag{5.5.5}$$

The RHS of Eq. 5.5.4 can be reduced, following the steps in Section 5.2.1, to

$$\begin{aligned}
&\int \sum_{l=0}^{\infty}\sum_{m=0}^{l}\sum_{n=0}^{\infty} N_{lm}(\cos\theta)\rho_{nl}(r)[S_{\text{halo},nlm}\cos(m\phi) + T_{\text{halo},nlm}\sin(m\phi)] \\
&\times [N_{lm}(\cos\theta)\Phi_{nl}(r)\cos(m\phi)]\ d\mathbf{V} = \frac{1}{2\pi} I_{nl} S_{\text{halo},nlm}(1+\delta_{m0})\pi\ ,
\end{aligned} \tag{5.5.6}$$

Therefore the coefficient $S_{halo,nlm}$ can be written as,

$$\begin{aligned}
S_{\text{halo},nlm} = (2-\delta_{m0})A_{nl}\Bigg[&\sum_k m_k N_{lm}(\cos\theta_k)\Phi_{nl}(r_k)\cos(m\phi_k) - \\
&\int \rho_{\text{analytic disc}}(R,z,M,a,b) N_{lm}(\cos\theta)\Phi_{nl}(r)\cos(m\phi)\ d\mathbf{V}\Bigg]\ .
\end{aligned} \tag{5.5.7}$$

We can re-write integral term of Eq. 5.5.7 as

$$F_{\text{disc},nlm}(R,z,M,a,b) = \int \rho_{\text{analytic disc}}(R,z,M,a,b) N_{lm}(\cos\theta)\Phi_{nl}(r)\cos(m\phi)\ d\mathbf{V}\ , \tag{5.5.8}$$

where $F_{\text{disc},nlm}(R,z,M,a,b)$ can be computed via numerical integration. Therefore, Eq. 5.5.7 simplifies to,

$$S_{\text{halo},nlm} = (2-\delta_{m0})A_{nl}\Bigg[\sum_k m_k N_{lm}(\cos\theta_k)\Phi_{nl}(r_k)\cos(m\phi_k) - F_{\text{disc},nlm}(R,z,M,a,b)\Bigg]\ , \tag{5.5.9}$$

which we see is,

$$S_{\text{halo},nlm} = S_{nlm} - F_{\text{disc},nlm}(R, z, M, a, b) \ , \tag{5.5.10}$$

where S_{nlm} is the coefficient calculated from the contribution of all of the particles in the simulation within the region of interest. In qualitative terms, we calculate the BSE from all of the particles within a spherical region. This can be a combination of contributions from gas, dark matter and stars, thus including the contribution of the disc. As the BSE includes contributions from the disc, naively adding an analytic disc potential would cause the disc to be double-counted. Namely, some contribution of the disc would be included by the coefficients of the BSE, as well as being included by the analytic disc. Thus, we must remove the analytic disc contribution from the BSE to ensure that we do not double-count the disc contribution.

The motivation for including the disc as an analytic model is that the BSE of Hernquist & Ostriker (1992) generally struggles to reproduce the thin, extended discs. Therefore, the term $F_{\text{disc},nlm}(R, z, M, a, b)$ is not necessarily removing the thin disc; rather, it is removing a poorly modelled version of the thin disc from the BSE, such that it can be re-introduced by a well fit analytic model.

An alternative technique is to separate the particles in the region of interest into two categories: disc particles and non-disc particles. The BSE coefficients can then be calculated from the non-disc particles, and an analytic disc model can be fit to the disc particles. These can be summed to produce a total density function for the region. The disadvantage of this method is that any change in the definition of the disc particles requires the coefficients of the BSE to be recomputed. Whereas, in the method described in this thesis, the coefficients are trivially calculated once for all of the particles in the region of interest, and the analytic representation of the disc can be applied in post-processing. Thus, different disc models could be trialled without the need to recompute the coefficients. This makes it much cheaper to prototype different disc models.

As described, the best fit values of the analytic disc model can be extracted from

hydrodynamical simulations. The parameters can be extracted at each snapshot of interest, as are the coefficients of the BSE. The disc's properties can then be approximated at any point in time by interpolating the best-fit model parameters between two snapshots. This can be combined with the coefficients of the BSE to allow a reconstruction of the BSE following Eq. 5.5.3. The forces at any point in the halo can be calculated as a combination of the BSE and the analytic disc forces. Therefore, the tidal forces from the disc are accurately included, thus allowing accurate modelling of the tidal evolution of infalling satellite galaxies. Furthermore, as the disc is being included via the analytic model, the BSE only needs to represent the remaining mass distribution. As shown in both Sections 5.3 and 5.4.2, the Hernquist-Ostriker BSE can accurately and cheaply reproduce MW-mass haloes in the absence of the galactic disc (and nearby massive satellites).

5.5.2 Modelling massive subhaloes

Section 5.2.6 demonstrated that increasing the number of radial and angular terms to resolve massive neighbours is prohibitive. This section describes an efficient method to include the massive subhaloes in the BSE of a cosmological simulation.

In Section 5.4.2 we demonstrated that the Herquinst-Ostriker BSE fails to accurately model a nearby, massive satellite within the halo of Au16 in both the MHD and DMO simulation. Moreover, the abrupt truncation of the BSE leads to spherical harmonic artefacts in the density profile corresponding to the highest order angular terms. These artefacts cause the density profile to deviate significantly from the true value. In Figs 5.8 and 5.11 we show that removing the subhaloes from the simulation significantly increases the accuracy of the BSE reproduction. Namely, removing the subhalo reduces the error on the projected density from values exceeding $\pm 50\%$ to values of order $\pm 5\%$. We could increase the accuracy of the BSE reproduction of the massive satellite by increasing the number of radial and angular terms; however, this becomes computationally prohibitive.

Following the method described in Section 5.4.2 the modelling of the halo can be split into two sections, modelling the satellite free halo and modelling the satellites.

A halo finder can be used to identify all particles associated with a massive satellite. These particles are then ignored when calculating the coefficients of the BSE of the main halo. Secondly, the particles associated with each massive satellite can be used to calculate an approximate representation. This representation could be a Herquinst-Ostriker BSE centred around the centre of the potential of the satellite or a simple spherically-symmetric radial distribution such as the NFW profile. These density profiles can then be combined to reproduce the total density profile of the halo at a given time. In this technique, the whole density profile of the halo becomes,

$$\rho(\mathbf{r}) = \rho_{\mathrm{BSE}}(\mathbf{r}) + \sum_{i=1}^{n_{\mathrm{satellites}}} \rho_{\mathrm{satellite},i}(\mathbf{r} - \mathbf{x}_i) \tag{5.5.11}$$

$\rho_{\mathrm{BSE}}(\mathbf{r})$ is the BSE approximation of the halo with the satellites removed, $\rho_{\mathrm{satellite},i}(\mathbf{r}-\mathbf{x}_i)$ is the density profile of the i-th satellite with a centre of $\mathbf{x}_i$ in the reference frame of the main halo and $n_{\mathrm{satellites}}$ is the total number of satellites modelled individually. The calculation of the forces on a point in the main halo must combine the forces from the main halo, and a sum over the forces from each of the independently modelled massive satellites.

In this method, the coefficients of the BSE of the main halo are calculated from all of the particles in the simulation, except those associated with a massive satellite. The particles associated with each of the massive satellites can then be used to independently calculate approximate profiles for each satellite. The profiles of the individual satellites can either be analytic, spherically-symmetric models such as the NFW or independent BSEs around their centre using an appropriate scale length. We suggest that the massive satellites can be accurately modelled using spherically symmetric profiles, such as the NFW profile, where the best-fit parameters are calculated at each snapshot and interpolated at any point in time. Any deviations from spherical symmetry with a massive satellite likely have no significant impact on the infall of other independent satellite galaxies.

While we do demonstrate it in this work, the results of Section 5.4.2 suggest that removing massive satellites from the BSE and re-introducing them with separate

analytic models will significantly increase the accuracy of the BSE method. Furthermore, in Section 5.4.2 we demonstrated that only a few BSE terms are required to accurately describe the DMO Au16 halo, with the nearby massive satellite removed. Thus, this method will be much more computationally efficient than increasing the number of terms in the main expansion to resolve the massive satellites.

5.6 Discussion and Conclusions

Self-consistent n-body and hydrodynamical simulations of the galaxy formation are extremely computationally expensive. Studying the infall of satellites into more massive haloes is highly inefficient as the main halo and the central galaxy dominate the compute resources. Therefore, we must find alternative methods to study the evolution of satellite galaxies falling into more massive haloes at the highest resolution. In this chapter, we described the basis function expansion technique (Hernquist & Ostriker, 1992; Clutton-Brock, 1972) which can efficiently approximate the potential of a simulated galactic halo. The basis function approximation of the potential can be used to study the infall of satellite galaxies into more massive haloes. Our main results are as follows:

- We have demonstrated that not only can the BSE technique be used to accurately reproduce the orbits of individual dark matter particles in DMO cosmological simulations, but also in full MHD simulations of realistic MW-mass galaxies at the present day. In general, we find that for a modest amount of terms in the BSE, the orbits in the full MHD simulation are only about a factor two less accurate than those in the DMO simulation.

- In Fig. 5.18 we show that the accuracy of the orbits increases quite significantly when including more terms in the BSE, up to a limit. We find that increasing the number of terms above $n_{\rm max} = 22$ and $l_{\rm max} = 10$ provides diminishing returns. We suspect that this is because another factor limits the error, for example, the limited temporal sampling of the coefficients or the inability of the

Hernquist-Ostriker BSE to faithfully reproduce the density profile of displaced massive satellites.

- The Herquinst-Ostriker basis set struggles to capture both a central NFW-like halo with massive, displaced satellites within the immediate environment. This is due to the form of the radial terms, which are most efficient when fitting profiles that decrease with increasing radius, and the cost of including more than a dozen angular terms. We suggest that satellites, those with masses above $\sim 1\%$ of the virial mass of the central halo, should be included via the addition of extra analytic profiles, like the NFW, or their own BSE's centred around their potential minimum.

- We find that the Herquinst-Ostriker basis family is able to model the density of a thin galactic disc surprisingly well. However, the BSE struggles to produce a disc as thin as the one in the Au16 MHD simulation. The BSE approximation tends to produce a disc that is not dense enough in the centre and too dense around the edges. We advise the use of a thin analytic disc component alongside the BSE. This will reduce the computational cost, as fewer terms will be required in the BSE, and increase the accuracy of the disc density and therefore force calculations within the halo.

This thesis shows that the Herquinst-Ostriker BSE can successfully reproduce the orbits of particles taken from n-body simulations of both dark matter only haloes and those with full hydrodynamics. However, the BSE must also accurately reproduce the tidal force to follow infalling satellites' evolution correctly. While the tidal forces are unimportant for evolving point particles, they are crucial in following the mass and size of extended structures like satellite galaxies. The recent work of van den Bosch et al. (2018) claims that most modern cosmological n-body simulations overestimate the number of satellite galaxies that are disrupted. They claim that over-softening of the gravitational force is the most likely cause of artificial disruption. The methods that we have introduced in this thesis can counter the effects of over-merging by allowing the force softening in the model satellite galaxies to be

reduced significantly without making the calculations infeasible expensive. However, further work is required to investigate the accuracy of the tidal forces predicted by the BSE technique before it can be applied to investigate to study the issue of subhalo disruption.

While the BSE technique appears to be an extremely powerful tool to study a whole host of problems, several limitations hinder the method. The BSE technique does not explicitly model the effects of dynamical friction. For some situations, dynamical friction is not a dominant effect. In particular, Boylan-Kolchin et al. (2008) claim that the effects of dynamical friction are unimportant for satellites that are less than 10% of the mass of the host halo. The BSE approximation can potentially include the effects of dynamical friction when the satellite of interest is selected from the original n-body simulation. In this case, the BSE approximation to the density may be able to capture the gravitational wake along the orbit, assuming the orbit in the BSE reconstruction does not differ significantly from that in the original simulation. Alternatively, the effects of dynamical friction could also be included with a simplified model.

Another limitation of the BSE method, as presented in this thesis, is that it does not include the hydrodynamical effects on the orbits. In Chapters 3 and 4 we demonstrated that hot haloes around MW-mass haloes are massive and contain a rich interplay of inflowing and outflowing gas. Therefore, infalling satellites that pass through this medium will interact with the hot ambient atmospheres and possibly even with some of the driven outflows. While the methods presented in this chapter do not include these hydrodynamical interactions, the hydrodynamical effects could be included in future works using various different techniques.

The effects of hydrodynamical interactions could be included by placing the infalling satellite into a 'wind tunnel'. In this approach, we effectively put a rectangular box around the satellite galaxy and allow gas to stream onto the galaxy with a prescribed density, velocity and temperature, matched to what we expect from the current position and velocity of the satellite in the frame of the halo. The satellite's orbit would still be evolved as described in this chapter; however, the hydrodynamical

effects would be solved in the frame of the satellite. This technique means that only a very small region of the halo would need to be hydrodynamically resolved and thus drastically lowers the computational expense. Possibly even more importantly, the simplification brought around by such a controlled setup allows the properties of the galaxies halo to be controlled, thus allowing the separation of effects due to different properties. The 'wind tunnel' technique has previously been applied to follow the properties of satellite galaxies as they fall into more massive haloes (Heß & Springel, 2012) and have been shown to yield results in good qualitative agreement with full hydrodynamical n-body results.

An alternative approach to include hydrodynamical effects without huge computational expense is to use a simulation with an adaptive resolution. We propose that the BSE gravitational force approximation, used in this thesis, could be coupled with an adaptive resolution hydrodynamical simulation, which is resolved at a much higher resolution around the satellite galaxy of interest. The most efficient implementation would allow the high-resolution region to follow the orbit of the orbiting satellite galaxy. This technique is best suited to grid simulation techniques, such as `AREPO`. A similar adaptive resolution hydrodynamic technique has been applied by van de Voort et al. (2019). They introduced an extra scalar field to the fluid to identify the regions of the simulation, which should be resolved with high resolution. The satellite galaxy would be seeded with the scalar field in this method. As the satellite galaxy evolves through the halo, the scalar field will advect along with the satellite, ensuring that the resolved region follows the orbit of the satellite.

More work is required to ensure that the BSE method used in this thesis accurately recovers the tidal forces present in the halo and includes hydrodynamical effects. However, the results of this thesis suggest the BSE method is a good starting point on which to build a complete model of satellite galaxy orbits in the immediate environments of massive haloes. The techniques described and proposed in this thesis allow the computational resources to be focused on the satellite galaxies of interest, and the idealised configuration allows the exploration of the entire parameter space.

Chapter 6

Conclusions

6.1 Summary

The presence of hot accreted X-ray luminous gaseous atmospheres in quasi-hydrostatic equilibrium around late-type galaxies in halos of mass $\geq 10^{12}$ $M_{\odot}$ is a fundamental prediction of galaxy formation models within ΛCDM (White & Frenk, 1991). While it is generally accepted that hot atmospheres exist around clusters, $M_{200} \geq 10^{14}$ $M_{\odot}$ the observational evidence around lower-mass haloes is less compelling. After numerous failed searches for diffuse X-ray emission from these galaxies over the years, detections were finally forthcoming in the early 2000s. Since then, various observational detections have indicated that the origin of this X-ray emitting gas is feedback from recent SNe rather than hot accreted haloes.

In Chapter 3 we use the large-volume, cosmological hydrodynamics EAGLE simulations to investigate the origin and properties of the hot, X-ray emitting gas around disc galaxies. The EAGLE simulations predict that MW-mass halos are baryon deficient relative to the mean baryon fraction. Specifically, they contain only $\approx 40\%$ of the mean cosmic baryon fraction within their halo virial radius, and about half of the baryons are in the form of a hot, ($T > 10^{5.5}$ K), gaseous halo. This baryon deficiency is attributed to feedback which can drive halo-wide winds. In EAGLE, the central halo X-ray emission is dominated by winds triggered by SNe feedback

for almost all halo masses. However, the X-ray emission in the outer regions is generally produced by an accreted, quasi-hydrostatic hot gaseous halo (see Fig. 3.2). Excising the inner $0.10R_{\rm vir}$ of the halo is sufficient to remove the majority of the hot gas heated by SNe feedback in halos of mass $\geq 10^{12}$ $\rm M_{\odot}$, thus allowing us to probe the emission from hot, accreted atmospheres predicted in a ΛCDM framework. The EAGLE simulations reproduce the observed general trend of $L_{\rm X} - M_{\rm vir}$ relation. We also predict that any steepening of the logarithmic slope of the $L_{\rm X} - M_{\rm vir}$ relation, above the self-similar value, $\alpha = 5/3$, is due to a varying hot gas fraction with halo mass. We show that the logarithmic slope of the power-law relationship between gas baryon fraction and halo mass can be inferred from the observed $L_{\rm X} - M_{\rm vir}$ relation using an analytical relation we derived, Eq. 3.2.3. This relation holds across several different EAGLE simulations, suggesting that this methodology can be applied to future X-ray observations to constrain the slope, normalisation and scatter of the halo gas fraction as a function of halo mass.

In summary, we find that in the EAGLE simulations, late-type galaxies of halo mass $\geq 10^{12}$ $\rm M_{\odot}$ do host hot, accreted atmospheres as predicted by White & Frenk (1991). However, feedback in the innermost region of the halo can produce substantially more X-ray emission in agreement with observations. Despite this, future X-ray observations of the outer regions of the halo may be able to infer the baryonic, and thus halo mass, from the X-ray emission.

The inclusion of feedback in cosmological hydrodynamical simulations is critical to reproducing galaxies' observed statistical properties. The complexity of baryon physics, together with the limited resolution of cosmological simulations, makes it impossible to include feedback *ab initio* from SNe or AGN. Therefore, these processes are included with a subgrid model; however, there is no standard implementation for modelling the effects of feedback. Generally, SNe feedback is dominant in lower mass galaxies, and AGN feedback becomes more significant in higher mass galaxies. The transition between these two regimes appears to coincide with the transition between haloes which host hot, quasi-hydrostatic atmospheres and those which do not, which is a halo mass $\rm M_{200} \approx 10^{12}$ $\rm M_{\odot}$. This makes MW-mass haloes an ideal

laboratory to investigate the differences arising from different subgrid models.

In Chapter 4 we analysed the emergent baryon cycle around two Local Group-like volumes centred around a pair of MW-mass haloes. We investigated how the baryon cycle varied when using the different subgrid models with the same initial conditions. We used the Auriga and Apostle galaxy formation models, which, among other differences, have significantly different implementations of SNe feedback. Apostle injects all the energy from SNe in the form of a thermal energy 'dump', whereas Auriga uses hydrodynamically decoupled 'wind' particles.

We found the minimum baryon fraction within a sphere around a primary Apostle galaxy to be $\approx 40\%$ of the cosmic baryon budget (the same as that found in the EAGLE simulations in Chapter 3), which is approximately half the value found in Auriga. Furthermore, the Apostle simulations exhibit a baryon deficiency of $\geq 10\%$ extending to ≈ 2 Mpc at the present day. The feedback processes can be classified into two broad categories: ejective and preventative. The Auriga simulations are dominated by ejective feedback with relatively short recycling times. Thus, most of the ejected gas cannot leave the virial radius of the halo, and if it does, it often re-accretes at later times. However, in Apostle feedback can eject a large mass of gas beyond R_{200}. This outflowing gas has such a large covering fraction and outward velocity that it can prevent the cosmological accretion of gas from the local environment.

These results in Chapter 4 highlight a fundamental difference in the outcome of the feedback processes in various subgrid implementations. We also identified a range of future observations of FRBs and CGM ion absorption lines that could constrain different galaxy formation models by identifying the signatures of galactic fountains and hot outflows capable of preventative feedback.

The large dynamic mass range of cosmological structure formation makes it computationally expensive to run simulations of galaxy formation. The mass of haloes in the Universe ranges from approximately 10^{-5} $M_\odot$ to 10^{15} $M_\odot$ (Wang et al., 2020), therefore studying the interaction of some of the lowest mass haloes in the immediate environment of massive haloes is prohibitive using traditional n-body techniques.

Therefore, we must use alternative methods to study these problems accurately.

In Chapter 5 we described the basis function expansion technique (Hernquist & Ostriker, 1992; Clutton-Brock, 1972) which can efficiently approximate the potential of a simulated galactic halo. We re-derived the BSE for the Herquinst-Ostriker basis, following Hernquist & Ostriker (1992) and Lowing (2011) including more detail, and correcting previous mistakes. We also demonstrated that the BSE technique is used to accurately reproduce modelled haloes of both DMO and full MHD cosmological simulations of realistic MW-mass galaxies. We also demonstrated that the BSE technique could accurately reproduce the orbits of point masses using the approximate potential BSE. Increasing the number of terms in the expansion above a specific number provides diminishing returns.

We find that the Herquist-Ostriker basis set struggles to capture both a central NFW-like halo with massive, displaced satellites within the immediate environment. We also demonstrate that the Hernquist-Ostriker BSE fails to accurately reproduce the thin galactic disc found in the Au16 MHD simulation. Namely, the BSE is underdense in the centre and overdense above and below the plane of the disc. In effect, the BSE produces a smeared version of the original disc. This will likely produce erroneous tidal forces, thus preventing an accurate study of the tidal evolution of satellite galaxies falling into massive galactic haloes with a realistic galactic disc. In Section 5.5 we present two novel further developments to the BSE method to study the potential around massive haloes taken from (baryonic) cosmological simulations. We outline a novel method of accurately including a thin, time-dependent disc alongside individual models of massive satellite galaxies within the halo.

To summarise, we demonstrate Herquinst-Ostriker BSE can successfully reproduce the orbits of particles taken from n-body simulations of both dark matter only haloes and those with full hydrodynamics. However, further developments are required to accurately study the tidal evolution of the infalling satellites correctly. We propose and describe two further developments, including a thin, time-dependent disc and a method to efficiently model a population of massive satellite galaxies within the halo.

In this thesis, we answered three main research aims, which we summarise below.

I) Do large volume, state-of-the-art cosmological simulations produce hot, accreted haloes around MW-mass haloes and above, as predicted by White & Rees (1978)?

The EAGLE simulations predict that late-type galaxies of halo mass $\geq 10^{12}$ $M_{\odot}$ do host hot, accreted atmospheres as predicted by White & Frenk (1991). However, SNe feedback in the innermost region of the halo can produce substantially more X-ray emission. However, we find that the X-ray emission in the outer regions of the halo is dominated by the hot, accreted haloes, and thus the analysis of the X-ray emission in the outer regions allows us to infer the mass of the hot halo.

II) Do different galaxy formation simulations, using different subgrid models, produce the same baryon cycle around galaxies?

We find that different galaxy formation simulations, which both produce realistic MW-mass galaxies at present-day, can produce very different baryon cycles. We show that the Apostle simulations produce large halo-wide outflows, which both eject gas and prevent the cosmological accretion of pristine gas. In comparison, the Auriga simulations produce much smaller outflows like a galactic fountain that can suppress star formation without significantly reducing the baryon fraction. We identify a range of future observations that could constrain these two degenerate regimes.

III) Are there viable computational methods to study the infall of high-resolution low-mass galaxies into higher mass haloes?

The self-consistent field technique provides a highly efficient way to accurately represent time-evolving haloes extracted from cosmological simulations. The Herquinst-Ostriker BSE can successfully reproduce the orbits of point masses of n-body simulations of both dark matter only haloes and those with full hydrodynamics. However,

the technique struggles to accurately capture the thin discs found in MW-like galaxies and thus will fail to faithfully include the tidal forces exhibited by the disc. Furthermore, the method fails to accurately model nearby massive satellite galaxies, which will be more important when modelling higher mass haloes. We proposed and described two further developments to overcome these problems, thus making the SCF technique suitable to model the infall of high-resolution low-mass galaxies into higher mass haloes.

6.2 Further Work

The conclusions in Chapter 3 show that the EAGLE simulations reproduce the theoretically predicted hot halo. In particular, the EAGLE simulations suggest the X-ray emission in the halo's outer regions is produced by hot, accreted haloes and could therefore be used to infer the baryon fraction of the haloes. Possible future work could answer the following questions:

- Do other large-volume cosmological simulations also predict that the accreted, hot haloes should be detectable? The results of Chapter 4 show that different galaxy formation models can produce vastly different baryon cycles and baryon fractions.

- Could our method of using the excess logarithmic slope of the $L_{\rm X}-M_{\rm vir}$ relation, above the self-similar value, $\alpha = 5/3$, be used to infer the hot gas fraction in a) other independent cosmological simulations, and b) observations of the real Universe?

- Can future telescopes be able to detect the lower surface brightness X-ray emission in the outer region of haloes? Mock observations could be produced, including background X-ray sources and instrumentation limitations.

- Do our findings of the origin of the X-ray emission also extend to the thermal Sunyaev-Zel'dovich (SZ) effect (Sunyaev & Zeldovich, 1970), which is also used to probe hot gas around galaxies?

- Would a more modern reproduction of the analysis of White & Rees (1978) and White & Frenk (1991) predict the correct X-ray luminosities? Historically, White & Frenk (1991) over-predicted the X-ray luminosity by two orders of magnitude.

Chapter 4 highlights a fundamental difference in the baryon cycle around MW-mass galaxies using two different galaxy formation simulations of the same initial conditions. Further work could investigate the following:

- While our analysis focused on the difference in SNe feedback, there were other differences in the simulations, namely hydrodynamical solver and AGN feedback. Further work could repeat this analysis by modifying the SNe feedback and ensuring other aspects of the simulations are identical.

- Neither the Apostle nor Auriga simulations have been used to simulate a large volume; therefore, it is not clear if they reproduce many observables of the real Universe such as the stellar-mass halo-mass relation. A follow-up project could apply these models to large volume simulations and thus allow an analysis of a larger range of halo masses.

- In Section 4.8 we identify a range of observables that could be used to distinguish between ejective and preventative feedback. Follow up work could produce mock observables and thus explore if current instruments can distinguish between the two models.

- Do the Auriga and Apostle galaxy formation models predict different baryon cycles around haloes of either higher or lower mass? As demonstrated in this thesis, MW-mass haloes are particularly complex as they are typically the transition mass between haloes with hot atmospheres and those without and the transition between SNe dominated feedback and AGN dominated feedback.

Finally, we demonstrate that the SCF method can successfully reproduce the orbits of point masses taken from n-body simulations of both dark matter only haloes and

those with full hydrodynamics. A range of further developments could be applied to this technique.

- A further natural work would be to include the further developments proposed in this thesis, both the analytic disc and separate massive satellite models. Do these developments improve the accuracy of point mass orbits? Can they accurately reproduce the tidal forces experienced by an extended object found in cosmological n-body simulations?

- We have shown in this work that an abrupt truncation can lead to visible artefacts corresponding to the highest order terms included. Would reducing the weighting of the higher-order terms improve the density profile's accuracy?

- Can the SCF technique be coupled to either an idealised 'wind tunnel' setup or an adaptive resolution hydrodynamical simulation to include the effects of complex hot atmospheres surrounding galaxies?

Bibliography

Alpher, R.A., Bethe, H., Gamow, G. *The Origin of Chemical Elements.* Physical Review, **73**(7) (1948), 803.

Anders, E., Grevesse, N. *Abundances of the elements - Meteoritic and solar.* Geochim. Cosmochim. Acta, **53** (1989), 197.

Anderson, M.E., Bregman, J.N. *Do Hot Halos Around Galaxies Contain the Missing Baryons?* ApJ, **714**(1) (2010), 320. 1003.3273.

Anderson, M.E., Churazov, E., Bregman, J.N. *A deep XMM-Newton study of the hot gaseous halo around NGC 1961.* MNRAS, **455** (2016), 227. 1508.01514.

Anderson, M.E., Gaspari, M., White, S.D.M., et al. *Unifying X-ray scaling relations from galaxies to clusters.* MNRAS, **449**(4) (2015), 3806. 1409.6965.

Bachman, P. *Die analytische zahlentheorie.* Teubner, Leipzig, **147** (1894), 148.

Bahé, Y.M., Crain, R.A., Kauffmann, G., et al. *The distribution of atomic hydrogen in EAGLE galaxies: morphologies, profiles, and H I holes.* MNRAS, **456**(1) (2016), 1115. 1511.04909.

Barnes, J., Efstathiou, G. *Angular Momentum from Tidal Torques.* ApJ, **319** (1987), 575.

Barnes, J., Hut, P. *A hierarchical O(N log N) force-calculation algorithm.* Nature, **324**(6096) (1986), 446.

Baugh, C. *A primer on hierarchical galaxy formation: The semi-analytical approach.* Rep. Progress Phys., **69** (2006).

Behroozi, P., Wechsler, R., Wu, H.Y. *Rockstar: Phase-space halo finder* (2012). 1210.008.

Behroozi, P.S., Wechsler, R.H., Conroy, C. *The Average Star Formation Histories of Galaxies in Dark Matter Halos from z = 0-8.* ApJ, **770** (2013), 57. 1207.6105.

Benítez-Llambay, A., Navarro, J.F., Frenk, C.S., et al. *The properties of 'dark' ΛCDM haloes in the Local Group.* MNRAS, **465**(4) (2017), 3913. 1609.01301.

Benson, A.J., Bower, R.G., Frenk, C.S., et al. *Diffuse X-ray emission from late-type galaxy haloes.* MNRAS, **314** (2000), 557. astro-ph/9903179.

Bird, S., Vogelsberger, M., Sijacki, D., et al. *Moving-mesh cosmology: properties of neutral hydrogen in absorption.* MNRAS, **429**(4) (2013), 3341. 1209.2118.

Bogdán, Á., Bourdin, H., Forman, W.R., et al. *Probing the Hot X-Ray Corona around the Massive Spiral Galaxy, NGC 6753, Using Deep XMM-Newton Observations.* ApJ, **850** (2017), 98. 1710.07286.

Bogdán, Á., Forman, W.R., Kraft, R.P., et al. *Detection of a Luminous Hot X-Ray Corona around the Massive Spiral Galaxy NGC 266.* ApJ, **772** (2013), 98. 1306.0643.

Bogdán, Á., Vogelsberger, M., Kraft, R.P., et al. *Hot Gaseous Coronae around Spiral Galaxies: Probing the Illustris Simulation.* ApJ, **804**(1) (2015), 72. 1503.01107.

Böhringer, H., Dolag, K., Chon, G. *Modelling self-similar appearance of galaxy clusters in X-rays.* A&A, **539** (2012), A120. 1112.5035.

Borrow, J., Anglés-Alcázar, D., Davé, R. *Cosmological baryon transfer in the SIMBA simulations.* MNRAS, **491**(4) (2020), 6102. 1910.00594.

Borrow, J., Kelly, A.J. *Projecting SPH Particles in Adaptive Environments.* arXiv e-prints (2021), arXiv:2106.05281. 2106.05281.

Bosma, A. *The distribution and kinematics of neutral hydrogen in spiral galaxies of various morphological types.* Ph.D. thesis, - (1978).

Bower, R.G., Schaye, J., Frenk, C.S., et al. *The dark nemesis of galaxy formation: why hot haloes trigger black hole growth and bring star formation to an end.* MNRAS, **465**(1) (2017a), 32. ISSN 0035-8711. 1607.07445, URL https://doi.org/10.1093/mnras/stw2735.

Bower, R.G., Schaye, J., Frenk, C.S., et al. *The dark nemesis of galaxy formation: why hot haloes trigger black hole growth and bring star formation to an end.* MNRAS, **465**(1) (2017b), 32. 1607.07445.

Boylan-Kolchin, M., Ma, C.P., Quataert, E. *Dynamical friction and galaxy merging time-scales.* MNRAS, **383**(1) (2008), 93. 0707.2960.

Bregman, J.N., Anderson, M.E., Miller, M.J., et al. *The Extended Distribution of Baryons around Galaxies.* ApJ, **862** (2018), 3. 1803.08963.

Brooks, A.M., Governato, F., Quinn, T., et al. *The Role of Cold Flows in the Assembly of Galaxy Disks.* ApJ, **694** (2009), 396. 0812.0007.

Bryan, G.L., Norman, M.L., O'Shea, B.W., et al. *ENZO: An Adaptive Mesh Refinement Code for Astrophysics.* ApJS, **211**(2) (2014), 19. 1307.2265.

Burchett, J.N., Tripp, T.M., Prochaska, J.X., et al. *The COS Absorption Survey of Baryon Harbors (CASBaH): Warm-Hot Circumgalactic Gas Reservoirs Traced by Ne VIII Absorption.* ApJ, **877**(2) (2019), L20. 1810.06560.

Callingham, T.M., Cautun, M., Deason, A.J., et al. *The mass of the Milky Way from satellite dynamics.* MNRAS, **484**(4) (2019), 5453. 1808.10456.

Christensen, C.R., Davé, R., Brooks, A., et al. *Tracing Outflowing Metals in Simulations of Dwarf and Spiral Galaxies.* ApJ, **867**(2) (2018), 142. 1808.07872.

Clutton-Brock, M. *The Gravitational Field of Flat Galaxies.* Ap&SS, **16**(1) (1972), 101.

Cole, S. *Modeling Galaxy Formation in Evolving Dark Matter Halos.* ApJ, **367** (1991), 45.

Cole, S., Lacey, C.G., Baugh, C.M., et al. *Hierarchical galaxy formation.* MNRAS, **319**(1) (2000), 168. astro-ph/0007281.

Collette, A. *Python and HDF5.* O'Reilly (2013).

Connor, L., Lin, H.H., Masui, K., et al. *Constraints on the FRB rate at 700-900 MHz.* MNRAS, **460**(1) (2016), 1054. 1602.07292.

Cordes, J.M., Chatterjee, S. *Fast Radio Bursts: An Extragalactic Enigma.* ARA&A, **57** (2019), 417. 1906.05878.

Correa, C.A., Schaye, J., van de Voort, F., et al. *The impact of feedback and the hot halo on the rates of gas accretion on to galaxies.* MNRAS, **478**(1) (2018), 255. 1804.01537.

Crain, R.A., McCarthy, I.G., Frenk, C.S., et al. *X-ray coronae in simulations of disc galaxy formation.* MNRAS, **407**(3) (2010), 1403. 1005.1642.

Crain, R.A., Schaye, J., Bower, R.G., et al. *The EAGLE simulations of galaxy formation: calibration of subgrid physics and model variations.* MNRAS, **450**(2) (2015), 1937. 1501.01311.

Crain, R.A., Theuns, T., Dalla Vecchia, C., et al. *Galaxies-intergalactic medium interaction calculation - I. Galaxy formation as a function of large-scale environment.* MNRAS, **399** (2009), 1773. 0906.4350.

Creasey, P., Theuns, T., Bower, R.G., et al. *Numerical overcooling in shocks.* MNRAS, **415**(4) (2011), 3706. 1106.0306.

Cullen, L., Dehnen, W. *Inviscid smoothed particle hydrodynamics.* MNRAS, **408**(2) (2010), 669. 1006.1524.

Dalcin, L.D., Paz, R.R., Kler, P.A., et al. *Parallel distributed computing using Python.* Advances in Water Resources, **34**(9) (2011), 1124. ISSN 0309-1708. New Computational Methods and Software Tools, URL http://www.sciencedirect.com/science/article/pii/S0309170811000777.

Dalla Vecchia, C., Schaye, J. *Simulating galactic outflows with thermal supernova feedback.* MNRAS, **426**(1) (2012), 140. 1203.5667.

Davies, J.J., Crain, R.A., McCarthy, I.G., et al. *The gas fractions of dark matter haloes hosting simulated $\sim L^\star$ galaxies are governed by the feedback history of their black holes.* MNRAS, **485**(3) (2019), 3783. 1810.07696.

Davies, J.J., Crain, R.A., Oppenheimer, B.D., et al. *The quenching and morphological evolution of central galaxies is facilitated by the feedback-driven expulsion of circumgalactic gas.* MNRAS, **491**(3) (2020), 4462. 1908.11380.

Davies, J.J., Crain, R.A., Pontzen, A. *Quenching and morphological evolution due to circumgalactic gas expulsion in a simulated galaxy with a controlled assembly history.* MNRAS, **501**(1) (2021), 236. 2006.13221.

Davis, M., Efstathiou, G., Frenk, C.S., et al. *The evolution of large-scale structure in a universe dominated by cold dark matter.* ApJ, **292** (1985), 371.

DeFelippis, D., Genel, S., Bryan, G.L., et al. *The Impact of Galactic Winds on the Angular Momentum of Disk Galaxies in the Illustris Simulation.* ApJ, **841**(1) (2017), 16. 1703.03806.

Dolag, K., Borgani, S., Murante, G., et al. *Substructures in hydrodynamical cluster simulations.* MNRAS, **399**(2) (2009), 497. 0808.3401.

Dubinski, J., Carlberg, R.G. *The Structure of Cold Dark Matter Halos.* ApJ, **378** (1991), 496.

Efstathiou, G., Sutherland, W.J., Maddox, S.J. *The cosmological constant and cold dark matter.* Nature, **348**(6303) (1990), 705.

Erkal, D., Belokurov, V., Laporte, C.F.P., et al. *The total mass of the Large Magellanic Cloud from its perturbation on the Orphan stream.* MNRAS, **487**(2) (2019), 2685. 1812.08192.

Faerman, Y., Sternberg, A., McKee, C.F. *Massive Warm/Hot Galaxy Coronae as Probed by UV/X-Ray Oxygen Absorption and Emission. I. Basic Model.* ApJ, **835** (2017), 52. 1602.00689.

Fath, E.A. *The Spectra of Some Spiral Nebulæ and Globular Star Clusters.* PASP, **21**(126) (1909), 138.

Fattahi, A., Navarro, J.F., Sawala, T., et al. *The APOSTLE project: Local Group kinematic mass constraints and simulation candidate selection.* MNRAS, **457** (2016), 844. 1507.03643.

Ferland, G.J., Porter, R.L., van Hoof, P.A.M., et al. *The 2013 Release of Cloudy.* Rev. Mexicana Astron. Astrofis., **49** (2013), 137. 1302.4485.

Flynn, C., Holmberg, J., Portinari, L., et al. *On the mass-to-light ratio of the local Galactic disc and the optical luminosity of the Galaxy.* MNRAS, **372**(3) (2006), 1149. astro-ph/0608193.

Ford, A.B., Davé, R., Oppenheimer, B.D., et al. *Tracing inflows and outflows with absorption lines in circumgalactic gas.* MNRAS, **444** (2014), 1260. 1309.5951.

Foster, A., Smith, R.K., Brickhouse, N.S., et al. *AtomDB and PyAtomDB: Atomic Data and Modelling Tools for High Energy and Non-Maxwellian Plasmas.* In *American Astronomical Society Meeting Abstracts #227*, volume 227 of *American Astronomical Society Meeting Abstracts* (2016), page 211.08.

Foster, A.R., Ji, L., Smith, R.K., et al. *Updated Atomic Data and Calculations for X-Ray Spectroscopy.* ApJ, **756** (2012), 128. 1207.0576.

Frenk, C.S., White, S.D.M., Davis, M., et al. *The Formation of Dark Halos in a Universe Dominated by Cold Dark Matter.* ApJ, **327** (1988), 507.

Fridman, A., Morozov, A., Polyachenko, V. *The destruction of a continuous ring revolving around a gravitating center.* Astrophysics and Space Science, **103**(1) (1984), 137.

Fukugita, M., Peebles, P.J.E. *The Cosmic Energy Inventory*. ApJ, **616**(2) (2004), 643. astro-ph/0406095.

Furlong, M., Bower, R.G., Crain, R.A., et al. *Size evolution of normal and compact galaxies in the EAGLE simulation*. MNRAS, **465**(1) (2017), 722. 1510.05645.

Furlong, M., Bower, R.G., Theuns, T., et al. *Evolution of galaxy stellar masses and star formation rates in the EAGLE simulations*. MNRAS, **450**(4) (2015), 4486. 1410.3485.

Genel, S., Bryan, G.L., Springel, V., et al. *A Quantification of the Butterfly Effect in Cosmological Simulations and Implications for Galaxy Scaling Relations*. ApJ, **871**(1) (2019), 21. 1807.07084.

Genel, S., Nelson, D., Pillepich, A., et al. *The size evolution of star-forming and quenched galaxies in the IllustrisTNG simulation*. MNRAS, **474**(3) (2018), 3976. 1707.05327.

Genel, S., Vogelsberger, M., Nelson, D., et al. *Following the flow: tracer particles in astrophysical fluid simulations*. MNRAS, **435**(2) (2013), 1426. 1305.2195.

Gingold, R.A., Monaghan, J.J. *Smoothed particle hydrodynamics - Theory and application to non-spherical stars*. MNRAS, **181** (1977), 375.

Goldbaum, N.J., ZuHone, J.A., Turk, M.J., et al. *unyt: Handle, manipulate, and convert data with units in Python*. Journal of Open Source Software, **3**(28) (2018), 809. URL https://doi.org/10.21105/joss.00809.

Grand, R.J.J., Gómez, F.A., Marinacci, F., et al. *The Auriga Project: the properties and formation mechanisms of disc galaxies across cosmic time*. MNRAS, **467** (2017), 179. 1610.01159.

Grand, R.J.J., van de Voort, F., Zjupa, J., et al. *Gas accretion and galactic fountain flows in the Auriga cosmological simulations: angular momentum and metal redistribution*. MNRAS, **490**(4) (2019), 4786. 1909.04038.

Guillochon, J., Parrent, J., Kelley, L.Z., et al. *An Open Catalog for Supernova Data.* ApJ, **835**(1) (2017), 64. 1605.01054.

Gupta, A., Mathur, S., Galeazzi, M., et al. *Probing the mass and anisotropy of the Milky Way gaseous halo: sight-lines toward Mrk 421 and PKS 2155-304.* Ap&SS, **352**(2) (2014), 775. 1307.6195.

Gupta, A., Mathur, S., Krongold, Y., et al. *A Huge Reservoir of Ionized Gas around the Milky Way: Accounting for the Missing Mass?* ApJ, **756** (2012), L8. 1205.5037.

Haardt, F., Madau, P. *Radiative Transfer in a Clumpy Universe. IV. New Synthesis Models of the Cosmic UV/X-Ray Background.* ApJ, **746**(2) (2012), 125. 1105.2039.

Hafen, Z., Faucher-Giguère, C.A., Anglés-Alcázar, D., et al. *The origins of the circumgalactic medium in the FIRE simulations.* MNRAS, **488**(1) (2019), 1248. 1811.11753.

Hafen, Z., Faucher-Giguère, C.A., Anglés-Alcázar, D., et al. *The fates of the circumgalactic medium in the FIRE simulations.* MNRAS, **494**(3) (2020), 3581. 1910.01123.

Hayward, C.C., Torrey, P., Springel, V., et al. *Galaxy mergers on a moving mesh: a comparison with smoothed particle hydrodynamics.* MNRAS, **442**(3) (2014), 1992. 1309.2942.

Henden, N.A., Puchwein, E., Shen, S., et al. *The FABLE simulations: a feedback model for galaxies, groups, and clusters.* MNRAS, **479**(4) (2018), 5385. 1804.05064.

Hernquist, L., Katz, N. *TREESPH: A Unification of SPH with the Hierarchical Tree Method.* ApJS, **70** (1989), 419.

Hernquist, L., Ostriker, J.P. *A Self-consistent Field Method for Galactic Dynamics.* ApJ, **386** (1992), 375.

Hernquist, L., Springel, V. *An analytical model for the history of cosmic star formation.* MNRAS, **341**(4) (2003), 1253. astro-ph/0209183.

Heß, S., Springel, V. *Gas stripping and mixing in galaxy clusters: a numerical comparison study.* MNRAS, **426**(4) (2012), 3112. 1208.0351.

Hockney, R., Eastwood, J. *Computer Simulation Using Particles.* Computer Simulation Using Particles (1981).

Hodges-Kluck, E.J., Bregman, J.N., Li, J.t. *The Hot, Accreted Halo of NGC 891.* ApJ, **866** (2018), 126. 1810.04680.

Holmberg, E. *On the Clustering Tendencies among the Nebulae. II. a Study of Encounters Between Laboratory Models of Stellar Systems by a New Integration Procedure.* ApJ, **94** (1941), 385.

Hopkins, P.F. *A general class of Lagrangian smoothed particle hydrodynamics methods and implications for fluid mixing problems.* MNRAS, **428**(4) (2013), 2840. 1206.5006.

Hopkins, P.F. *A new class of accurate, mesh-free hydrodynamic simulation methods.* MNRAS, **450**(1) (2015), 53. 1409.7395.

Hopkins, P.F., Wetzel, A., Kereš, D., et al. *FIRE-2 simulations: physics versus numerics in galaxy formation.* MNRAS, **480**(1) (2018), 800. 1702.06148.

Hou, J., Lacey, C.G., Frenk, C.S. *A comparison between semi-analytical gas cooling models and cosmological hydrodynamical simulations.* MNRAS, **486**(2) (2019), 1691. 1803.01923.

Hoyle, F. *On the Cosmological Problem.* MNRAS, **109** (1949), 365.

Hubble, E. *A Relation between Distance and Radial Velocity among Extra-Galactic Nebulae.* Proceedings of the National Academy of Science, **15**(3) (1929), 168.

Hubble, E.P. *Extragalactic nebulae.* ApJ, **64** (1926), 321.

Hummels, C.B., Smith, B.D., Silvia, D.W. *Trident: A Universal Tool for Generating Synthetic Absorption Spectra from Astrophysical Simulations.* ApJ, **847** (2017), 59. 1612.03935.

Hunter, J.D. *Matplotlib: A 2D graphics environment.* Computing in Science & Engineering, **9**(3) (2007), 90.

Irodotou, D., Fragkoudi, F., Pakmor, R., et al. *The effects of AGN feedback on the structural and dynamical properties of Milky Way-mass galaxies in cosmological simulations.* arXiv e-prints (2021), arXiv:2110.11368. 2110.11368.

Jenkins, A. *Second-order Lagrangian perturbation theory initial conditions for resimulations.* MNRAS, **403**(4) (2010), 1859. 0910.0258.

Jones, E., Oliphant, T., Peterson, P., et al. *SciPy: Open source scientific tools for Python* (2001). URL http://www.scipy.org/.

Kahn, F.D., Woltjer, L. *Intergalactic Matter and the Galaxy.* ApJ, **130** (1959), 705.

Kaiser, N. *Evolution and clustering of rich clusters.* MNRAS, **222** (1986), 323.

Kauffmann, G., Heckman, T.M., Tremonti, C., et al. *The host galaxies of active galactic nuclei.* MNRAS, **346** (2003), 1055. astro-ph/0304239.

Keller, B.W., Wadsley, J., Benincasa, S.M., et al. *A superbubble feedback model for galaxy simulations.* MNRAS, **442**(4) (2014), 3013. 1405.2625.

Keller, B.W., Wadsley, J.W., Wang, L., et al. *Chaos and variance in galaxy formation.* MNRAS, **482**(2) (2019), 2244. 1803.05445.

Kelly, A.J., Jenkins, A., Frenk, C.S. *The origin of X-ray coronae around simulated disc galaxies.* MNRAS, **502**(2) (2021), 2934. 2005.12926.

Kereš, D., Katz, N., Weinberg, D.H., et al. *How do galaxies get their gas?* MNRAS, **363**(1) (2005), 2. astro-ph/0407095.

Kereš, D., Vogelsberger, M., Sijacki, D., et al. *Moving-mesh cosmology: characteristics of galaxies and haloes.* MNRAS, **425**(3) (2012), 2027. 1109.4638.

King, A. *Black Holes, Galaxy Formation, and the M_{BH}-σ Relation.* ApJ, **596**(1) (2003), L27. astro-ph/0308342.

Kormendy, J., Richstone, D. *Inward Bound—The Search For Supermassive Black Holes In Galactic Nuclei.* ARA&A, **33** (1995), 581.

Kravtsov, A.V., Klypin, A.A., Bullock, J.S., et al. *The Cores of Dark Matter-dominated Galaxies: Theory versus Observations.* ApJ, **502**(1) (1998), 48. astro-ph/9708176.

Kuzmin, G. *A stationary galaxy model admitting triaxial velocity distribution.* Astron. Zh, **33** (1956), 27.

Lacey, C., Cole, S. *Merger Rates in Hierarchical Models of Galaxy Formation - Part Two - Comparison with N-Body Simulations.* MNRAS, **271** (1994), 676. astro-ph/9402069.

Lacey, C., Silk, J. *Tidally Triggered Galaxy Formation. I. Evolution of the Galaxy Luminosity Function.* ApJ, **381** (1991), 14.

Lacey, C.G., Baugh, C.M., Frenk, C.S., et al. *A unified multiwavelength model of galaxy formation.* MNRAS, **462**(4) (2016), 3854. 1509.08473.

Lagos, C.d.P., Crain, R.A., Schaye, J., et al. *Molecular hydrogen abundances of galaxies in the EAGLE simulations.* MNRAS, **452**(4) (2015), 3815. 1503.04807.

Lam, S.K., Pitrou, A., Seibert, S. *Numba: A LLVM-based Python JIT Compiler.* In *Proceedings of the Second Workshop on the LLVM Compiler Infrastructure in HPC*, LLVM '15. ACM, New York, NY, USA (2015). ISBN 978-1-4503-4005-2, pages 7:1–7:6. URL http://doi.acm.org/10.1145/2833157.2833162.

Larson, R.B. *Dynamical models for the formation and evolution of spherical galaxies.* MNRAS, **166** (1974), 585.

Li, J.T., Bregman, J.N., Wang, Q.D., et al. *The Circum-Galactic Medium of Massive Spirals. II. Probing the Nature of Hot Gaseous Halo around the Most Massive Isolated Spiral Galaxies.* ApJS, **233** (2017), 20. 1710.07355.

Li, J.T., Crain, R.A., Wang, Q.D. *Chandra survey of nearby highly inclined disc galaxies - III. Comparison with hydrodynamical simulations of circumgalactic coronae.* MNRAS, **440** (2014), 859. 1402.4471.

Li, J.T., Wang, Q.D. *Chandra survey of nearby highly inclined disc galaxies - I. X-ray measurements of galactic coronae.* MNRAS, **428** (2013a), 2085. 1210.2997.

Li, J.T., Wang, Q.D. *Chandra survey of nearby highly inclined disc galaxies - II. Correlation analysis of galactic coronal properties.* MNRAS, **435** (2013b), 3071. 1308.1933.

Li, Y., Bregman, J. *The Properties of the Galactic Hot Gaseous Halo from X-Ray Emission.* ApJ, **849** (2017), 105. 1710.02116.

Li, Z., Wang, Q.D., Hameed, S. *Chandra and XMM-Newton detection of large-scale diffuse X-ray emission from the Sombrero galaxy.* MNRAS, **376**(3) (2007), 960. astro-ph/0701487.

Licquia, T.C., Newman, J.A. *Improved Estimates of the Milky Way's Stellar Mass and Star Formation Rate from Hierarchical Bayesian Meta-Analysis.* ApJ, **806**(1) (2015), 96. 1407.1078.

Lilley, E.J., Sanders, J.L., Evans, N.W. *A two-parameter family of double-power-law biorthonormal potential-density expansions.* MNRAS, **478**(1) (2018a), 1281. 1804.11190.

Lilley, E.J., Sanders, J.L., Evans, N.W., et al. *Galaxy halo expansions: a new biorthogonal family of potential-density pairs.* MNRAS, **476**(2) (2018b), 2092. 1802.03350.

Lin, Y.T., Stanford, S.A., Eisenhardt, P.R.M., et al. *Baryon Content of Massive Galaxy Clusters at z = 0-0.6.* ApJ, **745**(1) (2012), L3. 1112.1705.

Lorimer, D.R., Bailes, M., McLaughlin, M.A., et al. *A Bright Millisecond Radio Burst of Extragalactic Origin.* Science, **318**(5851) (2007), 777. 0709.4301.

Lovell, M.R., Pillepich, A., Genel, S., et al. *The fraction of dark matter within galaxies from the IllustrisTNG simulations.* MNRAS, **481**(2) (2018), 1950. 1801.10170.

Lowing, B. *Interactions between Dark Matter Substructure and Galaxies.* Ph.D. thesis, Durham University (2011). URL http://etheses.dur.ac.uk/3358/.

Lowing, B., Jenkins, A., Eke, V., et al. *A halo expansion technique for approximating simulated dark matter haloes.* Monthly Notices of the Royal Astronomical Society, **416**(4) (2011), 2697–2711. ISSN 0035-8711. URL http://dx.doi.org/10.1111/j.1365-2966.2011.19222.x.

Lucy, L.B. *A numerical approach to the testing of the fission hypothesis.* AJ, **82** (1977), 1013.

Lynden-Bell, D. *Galactic Nuclei as Collapsed Old Quasars.* Nature, **223**(5207) (1969), 690.

Lynden-Bell, D. *Gravity power.* Phys. Scr, **17** (1978), 185.

Lynden-Bell, D., Rees, M.J. *On quasars, dust and the galactic centre.* MNRAS, **152** (1971), 461.

Madau, P., Dickinson, M. *Cosmic Star-Formation History.* Annual Review of Astronomy and Astrophysics, **52**(1) (2014), 415. https://doi.org/10.1146/annurev-astro-081811-125615, URL https://doi.org/10.1146/annurev-astro-081811-125615.

Maddox, S.J., Efstathiou, G., Sutherland, W.J., et al. *Galaxy correlations on large scales.* MNRAS, **242** (1990), 43.

Magorrian, J., Tremaine, S., Richstone, D., et al. *The Demography of Massive Dark Objects in Galaxy Centers.* AJ, **115**(6) (1998), 2285. astro-ph/9708072.

Marinacci, F., Grand, R.J.J., Pakmor, R., et al. *Properties of H I discs in the Auriga cosmological simulations.* MNRAS, **466**(4) (2017), 3859. 1610.01594.

Mathews, W.G., Baker, J.C. *Galactic Winds*. ApJ, **170** (1971), 241.

Matthee, J., Schaye, J., Crain, R.A., et al. *The origin of scatter in the stellar mass-halo mass relation of central galaxies in the EAGLE simulation*. MNRAS, **465**(2) (2017), 2381. 1608.08218.

McAlpine, S., Helly, J.C., Schaller, M., et al. *The EAGLE simulations of galaxy formation: Public release of halo and galaxy catalogues*. Astronomy and Computing, **15** (2016), 72. 1510.01320.

McMillan, P.J. *Mass models of the Milky Way*. MNRAS, **414**(3) (2011), 2446. 1102.4340.

McQuinn, M. *Locating the "Missing" Baryons with Extragalactic Dispersion Measure Estimates*. ApJ, **780**(2) (2014), L33. 1309.4451.

Michaux, M., Hahn, O., Rampf, C., et al. *Accurate initial conditions for cosmological N-body simulations: minimizing truncation and discreteness errors*. MNRAS, **500**(1) (2021), 663. 2008.09588.

Miller, M.J., Bregman, J.N. *Constraining the Milky Way's Hot Gas Halo with O VII and O VIII Emission Lines*. ApJ, **800**(1) (2015), 14. 1412.3116.

Mitchell, P.D., Schaye, J. *Baryonic mass budgets for haloes in the EAGLE simulation, including ejected and prevented gas*. MNRAS(2021a). 2112.08244.

Mitchell, P.D., Schaye, J. *How gas flows shape the stellar-halo mass relation in the EAGLE simulation*. arXiv e-prints (2021b), arXiv:2103.10966. 2103.10966.

Mitchell, P.D., Schaye, J., Bower, R.G. *Galactic inflow and wind recycling rates in the EAGLE simulations*. MNRAS, **497**(4) (2020a), 4495. 2005.10262.

Mitchell, P.D., Schaye, J., Bower, R.G., et al. *Galactic outflow rates in the EAGLE simulations*. arXiv e-prints (2019), arXiv:1910.09566. 1910.09566.

Mitchell, P.D., Schaye, J., Bower, R.G., et al. *Galactic outflow rates in the EAGLE simulations*. MNRAS, **494**(3) (2020b), 3971. 1910.09566.

Miyamoto, M., Nagai, R. *Three-dimensional models for the distribution of mass in galaxies.* PASJ, **27** (1975), 533.

Moster, B.P., Naab, T., White, S.D.M. *Galactic star formation and accretion histories from matching galaxies to dark matter haloes.* MNRAS, **428**(4) (2013), 3121. 1205.5807.

Muratov, A.L., Kereš, D., Faucher-Giguère, C.A., et al. *Gusty, gaseous flows of FIRE: galactic winds in cosmological simulations with explicit stellar feedback.* MNRAS, **454**(3) (2015), 2691. 1501.03155.

Navarro, J.F., Frenk, C.S., White, S.D.M. *Simulations of X-ray clusters.* MNRAS, **275**(3) (1995), 720. astro-ph/9408069.

Navarro, J.F., Frenk, C.S., White, S.D.M. *A Universal Density Profile from Hierarchical Clustering.* ApJ, **490** (1997), 493. astro-ph/9611107.

Navarro, J.F., White, S.D.M. *Simulations of Dissipative Galaxy Formation in Hierarchically Clustering Universes - Part One - Tests of the Code.* MNRAS, **265** (1993), 271.

Nelson, D., Genel, S., Vogelsberger, M., et al. *The impact of feedback on cosmological gas accretion.* MNRAS, **448**(1) (2015), 59. 1410.5425.

Nelson, D., Pillepich, A., Springel, V., et al. *First results from the IllustrisTNG simulations: the galaxy colour bimodality.* MNRAS, **475**(1) (2018), 624. 1707.03395.

Nelson, D., Springel, V., Pillepich, A., et al. *The IllustrisTNG simulations: public data release.* Computational Astrophysics and Cosmology, **6**(1) (2019), 2. 1812.05609.

Nelson, D., Vogelsberger, M., Genel, S., et al. *Moving mesh cosmology: tracing cosmological gas accretion.* MNRAS, **429**(4) (2013), 3353. 1301.6753.

Nicastro, F., Senatore, F., Gupta, A., et al. *X-ray detection of warm ionized matter in the Galactic halo.* MNRAS, **457** (2016), 676. 1512.03611.

Oppenheimer, B.D., Bogdán, Á., Crain, R.A., et al. *EAGLE and Illustris-TNG Predictions for Resolved eROSITA X-Ray Observations of the Circumgalactic Medium around Normal Galaxies*. ApJ, **893**(1) (2020a), L24. 2003.13889.

Oppenheimer, B.D., Davé, R., Kereš, D., et al. *Feedback and recycled wind accretion: assembling the z = 0 galaxy mass function*. MNRAS, **406**(4) (2010), 2325. 0912.0519.

Oppenheimer, B.D., Davies, J.J., Crain, R.A., et al. *Feedback from supermassive black holes transforms centrals into passive galaxies by ejecting circumgalactic gas*. MNRAS, **491**(2) (2020b), 2939. 1904.05904.

Ostriker, J.P., Mark, J.W.K. *Rapidly rotating stars. I. The self-consistent-field method*. ApJ, **151** (1968), 1075.

Owen, R.A., Warwick, R.S. *X-ray emission from the extended discs of spiral galaxies*. MNRAS, **394**(4) (2009), 1741. 0901.4263.

Pearce, F.R., Jenkins, A., Frenk, C.S., et al. *A Simulation of Galaxy Formation and Clustering*. ApJ, **521**(2) (1999), L99. astro-ph/9905160.

Peebles, P. *The large-scale structure of the universe*. Large-Scale Structure of the Universe by Phillip James Edwin Peebles. Princeton University Press (1980).

Perlmutter, S., Aldering, G., Goldhaber, G., et al. *Measurements of Ω and Λ from 42 High-Redshift Supernovae*. ApJ, **517**(2) (1999), 565. astro-ph/9812133.

Petroff, E. *Fast radio bursts: recent discoveries and future prospects*. arXiv e-prints (2017), arXiv:1709.02189. 1709.02189.

Pillepich, A., Nelson, D., Hernquist, L., et al. *First results from the IllustrisTNG simulations: the stellar mass content of groups and clusters of galaxies*. MNRAS, **475**(1) (2018), 648. 1707.03406.

Pillepich, A., Springel, V., Nelson, D., et al. *Simulating galaxy formation with the IllustrisTNG model*. Monthly Notices of the Royal Astronomical Society, **473**(3)

(2017), 4077–4106. ISSN 1365-2966. URL http://dx.doi.org/10.1093/mnras/stx2656.

Planck Collaboration, Ade, P.A.R., Aghanim, N., et al. *Planck intermediate results. XI. The gas content of dark matter halos: the Sunyaev-Zeldovich-stellar mass relation for locally brightest galaxies.* A&A, **557** (2013), A52. 1212.4131.

Planck Collaboration, Ade, P.A.R., Aghanim, N., et al. *Planck 2013 results. I. Overview of products and scientific results.* A&A, **571** (2014), A1. 1303.5062.

Plummer, H.C. *On the problem of distribution in globular star clusters.* MNRAS, **71** (1911), 460.

Pratt, G.W., Croston, J.H., Arnaud, M., et al. *Galaxy cluster X-ray luminosity scaling relations from a representative local sample (REXCESS).* A&A, **498**(2) (2009), 361. 0809.3784.

Price, D.J. *splash: An Interactive Visualisation Tool for Smoothed Particle Hydrodynamics Simulations.* PASA, **24**(3) (2007), 159. 0709.0832.

Price, D.J. *Modelling discontinuities and Kelvin Helmholtz instabilities in SPH.* Journal of Computational Physics, **227**(24) (2008), 10040. 0709.2772.

Price, D.J. *Smoothed particle hydrodynamics and magnetohydrodynamics.* Journal of Computational Physics, **231**(3) (2012), 759. 1012.1885.

Putman, M.E., Peek, J.E.G., Joung, M.R. *Gaseous Galaxy Halos.* ARA&A, **50** (2012), 491. 1207.4837.

Rees, M.J. *Black Hole Models for Active Galactic Nuclei.* ARA&A, **22** (1984), 471.

Rees, M.J., Ostriker, J.P. *Cooling, dynamics and fragmentation of massive gas clouds: clues to the masses and radii of galaxies and clusters.* MNRAS, **179** (1977), 541.

Riess, A.G., Filippenko, A.V., Challis, P., et al. *Observational Evidence from Supernovae for an Accelerating Universe and a Cosmological Constant.* AJ, **116**(3) (1998), 1009. astro-ph/9805201.

Roberts, M.S., Rots, A.H. *Comparison of Rotation Curves of Different Galaxy Types.* A&A, **26** (1973), 483.

Rosas-Guevara, Y., Bower, R.G., Schaye, J., et al. *Supermassive black holes in the EAGLE Universe. Revealing the observables of their growth.* MNRAS, **462**(1) (2016), 190. 1604.00020.

Rosas-Guevara, Y.M., Bower, R.G., Schaye, J., et al. *The impact of angular momentum on black hole accretion rates in simulations of galaxy formation.* MNRAS, **454**(1) (2015), 1038. 1312.0598.

Rubin, V.C., Ford, W. K., J., Thonnard, N. *Rotational properties of 21 SC galaxies with a large range of luminosities and radii, from NGC 4605 (R=4kpc) to UGC 2885 (R=122kpc).* ApJ, **238** (1980), 471.

Rubin, V.C., Ford, W. Kent, J. *Rotation of the Andromeda Nebula from a Spectroscopic Survey of Emission Regions.* ApJ, **159** (1970), 379.

Rupke, D. *A Review of Recent Observations of Galactic Winds Driven by Star Formation.* Galaxies, **6**(4) (2018), 138. ISSN 2075-4434. URL http://dx.doi.org/10.3390/galaxies6040138.

Sales, L.V., Navarro, J.F., Theuns, T., et al. *The origin of discs and spheroids in simulated galaxies.* MNRAS, **423**(2) (2012), 1544. 1112.2220.

Salpeter, E.E. *Accretion of Interstellar Matter by Massive Objects.* ApJ, **140** (1964), 796.

Sanders, J.L., Lilley, E.J., Vasiliev, E., et al. *Models of distorted and evolving dark matter haloes.* MNRAS, **499**(4) (2020), 4793. 2009.00645.

Sarazin, C.L. *X-ray emission from clusters of galaxies.* Reviews of Modern Physics, **58** (1986), 1.

Sawala, T., Frenk, C.S., Fattahi, A., et al. *The APOSTLE simulations: solutions to the Local Group's cosmic puzzles.* MNRAS, **457** (2016), 1931. 1511.01098.

Schaller, M., Dalla Vecchia, C., Schaye, J., et al. *The EAGLE simulations of galaxy formation: the importance of the hydrodynamics scheme.* MNRAS, **454**(3) (2015a), 2277. 1509.05056.

Schaller, M., Frenk, C.S., Bower, R.G., et al. *Baryon effects on the internal structure of ΛCDM haloes in the EAGLE simulations.* MNRAS, **451**(2) (2015b), 1247. 1409.8617.

Schaye, J., Crain, R.A., Bower, R.G., et al. *The EAGLE project: simulating the evolution and assembly of galaxies and their environments.* MNRAS, **446** (2015), 521. 1407.7040.

Schaye, J., Dalla Vecchia, C. *On the relation between the Schmidt and Kennicutt-Schmidt star formation laws and its implications for numerical simulations.* MNRAS, **383**(3) (2008), 1210. 0709.0292.

Schmidt, M. *3C 273 : A Star-Like Object with Large Red-Shift.* Nature, **197**(4872) (1963), 1040.

Sérsic, J.L. *Influence of the atmospheric and instrumental dispersion on the brightness distribution in a galaxy.* Boletin de la Asociacion Argentina de Astronomia La Plata Argentina, **6** (1963), 41.

Seyfert, C.K. *Nuclear Emission in Spiral Nebulae.* ApJ, **97** (1943), 28.

Shapley, H., Curtis, H.D. *The Scale of the Universe.* Bulletin of the National Research Council, **2**(11) (1921), 171.

Shull, J.M., Danforth, C.W. *The Dispersion of Fast Radio Bursts from a Structured Intergalactic Medium at Redshifts $z < 1.5$.* ApJ, **852**(1) (2018), L11. 1712.01280.

Sijacki, D., Vogelsberger, M., Kereš, D., et al. *Moving mesh cosmology: the hydrodynamics of galaxy formation.* MNRAS, **424**(4) (2012), 2999. 1109.3468.

Silk, J., Rees, M.J. *Quasars and galaxy formation.* A&A, **331** (1998), L1. astro-ph/9801013.

Smith, B.D., Bryan, G.L., Glover, S.C.O., et al. *Grackle: Chemistry and radiative cooling library for astrophysical simulations* (2016). 1612.020.

Smith, M.C., Sijacki, D., Shen, S. *Supernova feedback in numerical simulations of galaxy formation: separating physics from numerics.* Monthly Notices of the Royal Astronomical Society, **478**(1) (2018), 302. ISSN 0035-8711. https://academic.oup.com/mnras/article-pdf/478/1/302/24971782/sty994.pdf, URL https://doi.org/10.1093/mnras/sty994.

Smith, R.K., Brickhouse, N.S., Liedahl, D.A., et al. *Collisional Plasma Models with APEC/APED: Emission-Line Diagnostics of Hydrogen-like and Helium-like Ions.* ApJ, **556**(2) (2001), L91. astro-ph/0106478.

Smith, S. *The Mass of the Virgo Cluster.* ApJ, **83** (1936), 23.

Snowden, S.L., Egger, R., Freyberg, M.J., et al. *ROSAT Survey Diffuse X-Ray Background Maps. II.* ApJ, **485**(1) (1997), 125.

Sokołowska, A., Babul, A., Mayer, L., et al. *The Complementary Roles of Feedback and Mergers in Building the Gaseous Halo and the X-Ray Corona of Milky-Way-sized Galaxies.* ApJ, **867**(1) (2018), 73. 1708.07820.

Somerville, R.S., Primack, J.R. *Semi-analytic modelling of galaxy formation: the local Universe.* MNRAS, **310**(4) (1999), 1087. astro-ph/9802268.

Sommer-Larsen, J., Gelato, S., Vedel, H. *Formation of Disk Galaxies: Feedback and the Angular Momentum Problem.* ApJ, **519**(2) (1999), 501. astro-ph/9801094.

Spitzer, Jr., L. *On a Possible Interstellar Galactic Corona.* ApJ, **124** (1956), 20.

Springel, V. *The cosmological simulation code GADGET-2.* MNRAS, **364**(4) (2005), 1105. astro-ph/0505010.

Springel, V. *E pur si muove: Galilean-invariant cosmological hydrodynamical simulations on a moving mesh.* MNRAS, **401**(2) (2010), 791. 0901.4107.

Springel, V., Hernquist, L. *Cosmological smoothed particle hydrodynamics simulations: the entropy equation.* MNRAS, **333**(3) (2002), 649. astro-ph/0111016.

Springel, V., Hernquist, L. *Cosmological smoothed particle hydrodynamics simulations: a hybrid multiphase model for star formation.* MNRAS, **339**(2) (2003), 289. astro-ph/0206393.

Springel, V., Wang, J., Vogelsberger, M., et al. *The Aquarius Project: the subhaloes of galactic haloes.* MNRAS, **391**(4) (2008), 1685. 0809.0898.

Springel, V., White, S.D.M., Tormen, G., et al. *Populating a cluster of galaxies - I. Results at [formmu2]z=0.* MNRAS, **328** (2001), 726. astro-ph/0012055.

Strickland, D.K., Heckman, T.M. *Iron Line and Diffuse Hard X-Ray Emission from the Starburst Galaxy M82.* The Astrophysical Journal, **658**(1) (2007), 258–281. ISSN 1538-4357. URL http://dx.doi.org/10.1086/511174.

Strickland, D.K., Heckman, T.M., Colbert, E.J.M., et al. *A High Spatial Resolution X-Ray and Hα Study of Hot Gas in the Halos of Star-forming Disk Galaxies. I. Spatial and Spectral Properties of the Diffuse X-Ray Emission.* ApJS, **151** (2004), 193. astro-ph/0306592.

Sun, M., Voit, G.M., Donahue, M., et al. *Chandra Studies of the X-Ray Gas Properties of Galaxy Groups.* ApJ, **693**(2) (2009), 1142. 0805.2320.

Sunyaev, R.A., Zeldovich, Y.B. *Small-Scale Fluctuations of Relic Radiation.* Ap&SS, **7**(1) (1970), 3.

Suresh, J., Nelson, D., Genel, S., et al. *Zooming in on accretion - II. Cold circumgalactic gas simulated with a super-Lagrangian refinement scheme.* MNRAS, **483**(3) (2019), 4040. 1811.01949.

Sykes, C., Fumagalli, M., Cooke, R., et al. *Fluorescent rings in star-free dark matter haloes.* MNRAS, **487**(1) (2019), 609. 1905.00430.

Teyssier, R. *Cosmological hydrodynamics with adaptive mesh refinement. A new high resolution code called RAMSES.* A&A, **385** (2002), 337. astro-ph/0111367.

Thacker, R.J., Couchman, H.M.P. *Star Formation, Supernova Feedback, and the Angular Momentum Problem in Numerical Cold Dark Matter Cosmogony: Halfway There?* ApJ, **555**(1) (2001), L17. astro-ph/0106060.

The EAGLE team. *The EAGLE simulations of galaxy formation: Public release of particle data.* arXiv e-prints (2017), arXiv:1706.09899. 1706.09899.

Tollet, É., Cattaneo, A., Macciò, A.V., et al. *NIHAO XIX: how supernova feedback shapes the galaxy baryon cycle.* MNRAS, **485**(2) (2019), 2511. 1902.03888.

Toomre, A. *On the Distribution of Matter Within Highly Flattened Galaxies.* ApJ, **138** (1963), 385.

Torrey, P., Vogelsberger, M., Genel, S., et al. *A model for cosmological simulations of galaxy formation physics: multi-epoch validation.* MNRAS, **438**(3) (2014), 1985. 1305.4931.

Torrey, P., Vogelsberger, M., Marinacci, F., et al. *The evolution of the mass-metallicity relation and its scatter in IllustrisTNG.* MNRAS, **484**(4) (2019), 5587. 1711.05261.

Torrey, P., Vogelsberger, M., Sijacki, D., et al. *Moving-mesh cosmology: properties of gas discs.* MNRAS, **427**(3) (2012), 2224. 1110.5635.

Trayford, J.W., Camps, P., Theuns, T., et al. *Optical colours and spectral indices of z = 0.1 eagle galaxies with the 3D dust radiative transfer code skirt.* MNRAS, **470**(1) (2017), 771. 1705.02331.

Trayford, J.W., Theuns, T., Bower, R.G., et al. *Colours and luminosities of z = 0.1 galaxies in the EAGLE simulation.* MNRAS, **452**(3) (2015), 2879. 1504.04374.

Tüllmann, R., Pietsch, W., Rossa, J., et al. *The multi-phase gaseous halos of star forming late-type galaxies. I. XMM-Newton observations of the hot ionized medium.* A&A, **448** (2006), 43. astro-ph/0510079.

Tumlinson, J., Peeples, M.S., Werk, J.K. *The Circumgalactic Medium.* ARA&A, **55** (2017), 389. 1709.09180.

Tumlinson, J., Thom, C., Werk, J.K., et al. *The COS-Halos Survey: Rationale, Design, and a Census of Circumgalactic Neutral Hydrogen.* ApJ, **777**(1) (2013), 59. 1309.6317.

van de Hulst, H.C., Raimond, E., van Woerden, H. *Rotation and density distribution of the Andromeda nebula derived from observations of the 21-cm line.* Bull. Astron. Inst. Netherlands, **14** (1957), 1.

van de Voort, F., Bieri, R., Pakmor, R., et al. *The effect of magnetic fields on properties of the circumgalactic medium.* MNRAS, **501**(4) (2021), 4888. 2008.07537.

van de Voort, F., Quataert, E., Hopkins, P.F., et al. *The impact of stellar feedback on hot gas in galaxy haloes: the Sunyaev-Zel'dovich effect and soft X-ray emission.* MNRAS, **463**(4) (2016), 4533. 1604.01397.

van de Voort, F., Schaye, J., Booth, C.M., et al. *The drop in the cosmic star formation rate below redshift 2 is caused by a change in the mode of gas accretion and by active galactic nucleus feedback.* MNRAS, **415**(3) (2011a), 2782. 1102.3912.

van de Voort, F., Schaye, J., Booth, C.M., et al. *The rates and modes of gas accretion on to galaxies and their gaseous haloes.* MNRAS, **414**(3) (2011b), 2458. 1011.2491.

van de Voort, F., Springel, V., Mandelker, N., et al. *Cosmological simulations of the circumgalactic medium with 1 kpc resolution: enhanced H I column densities.* MNRAS, **482**(1) (2019), L85. 1808.04369.

van den Bosch, F.C., Ogiya, G., Hahn, O., et al. *Disruption of dark matter substructure: fact or fiction?* MNRAS, **474**(3) (2018), 3043. 1711.05276.

van der Walt, S., Colbert, S.C., Varoquaux, G. *The NumPy Array: A Structure for Efficient Numerical Computation*. Computing in Science Engineering, **13**(2) (2011), 22.

Van Rossum, G., Drake, F.L. *Python 3 Reference Manual*. CreateSpace, Scotts Valley, CA (2009). ISBN 1441412697.

Vanderlinde, K., Crawford, T.M., de Haan, T., et al. *Galaxy Clusters Selected with the Sunyaev-Zel'dovich Effect from 2008 South Pole Telescope Observations*. ApJ, **722**(2) (2010), 1180. 1003.0003.

Vasiliev, E. *A new code for orbit analysis and Schwarzschild modelling of triaxial stellar systems*. MNRAS, **434**(4) (2013), 3174. 1307.8116.

Vikhlinin, A., Kravtsov, A., Forman, W., et al. *Chandra Sample of Nearby Relaxed Galaxy Clusters: Mass, Gas Fraction, and Mass-Temperature Relation*. ApJ, **640**(2) (2006), 691. astro-ph/0507092.

Vogelsberger, M., Genel, S., Sijacki, D., et al. *A model for cosmological simulations of galaxy formation physics*. MNRAS, **436**(4) (2013), 3031. 1305.2913.

Vogelsberger, M., Genel, S., Springel, V., et al. *Introducing the Illustris Project: simulating the coevolution of dark and visible matter in the Universe*. MNRAS, **444**(2) (2014), 1518. 1405.2921.

Vogelsberger, M., Marinacci, F., Torrey, P., et al. *Cosmological simulations of galaxy formation*. Nature Reviews Physics, **2**(1) (2020), 42. 1909.07976.

Vogelsberger, M., Sijacki, D., Kereš, D., et al. *Moving mesh cosmology: numerical techniques and global statistics*. MNRAS, **425**(4) (2012), 3024. 1109.1281.

Wang, J., Bose, S., Frenk, C.S., et al. *Universal structure of dark matter haloes over a mass range of 20 orders of magnitude*. Nature, **585**(7823) (2020), 39. 1911.09720.

Wang, Q.D. *X-raying galaxies: A Chandra legacy*. Proceedings of the National Academy of Science, **107** (2010), 7168. 1003.1282.

Wang, Q.D., Li, J., Jiang, X., et al. *Chandra survey of nearby highly inclined disk galaxies - IV. New insights into the working of stellar feedback.* MNRAS, **457**(2) (2016), 1385. 1512.02655.

Wang, Q.D., Whitaker, K.E., Williams, R. *An XMM-Newton and Chandra study of the starburst galaxy IC 10.* MNRAS, **362**(3) (2005), 1065. astro-ph/0507041.

White, S.D.M., Frenk, C.S. *Galaxy formation through hierarchical clustering.* ApJ, **379** (1991), 52.

White, S.D.M., Navarro, J.F., Evrard, A.E., et al. *The baryon content of galaxy clusters: a challenge to cosmological orthodoxy.* Nature, **366**(6454) (1993), 429.

White, S.D.M., Rees, M.J. *Core condensation in heavy halos - A two-stage theory for galaxy formation and clustering.* MNRAS, **183** (1978), 341.

Wiersma, R.P.C., Schaye, J., Smith, B.D. *The effect of photo-ionization on the cooling rates of enriched, astrophysical plasmas.* Mon. Not. Roy. Astron. Soc., **393** (2009), 99. 0807.3748.

Wiersma, R.P.C., Schaye, J., Theuns, T., et al. *Chemical enrichment in cosmological, smoothed particle hydrodynamics simulations.* MNRAS, **399**(2) (2009), 574. 0902.1535.

Wijers, N.A., Schaye, J., Oppenheimer, B.D. *The warm-hot circumgalactic medium around EAGLE-simulation galaxies and its detection prospects with X-ray and UV line absorption.* MNRAS, **498**(1) (2020), 574. 2004.05171.

Wijers, N.A., Schaye, J., Oppenheimer, B.D., et al. *The abundance and physical properties of O VII and O VIII X-ray absorption systems in the EAGLE simulations.* MNRAS, **488**(2) (2019), 2947. 1904.01057.

Wright, R.J., Lagos, C.d.P., Power, C., et al. *The impact of stellar and AGN feedback on halo-scale baryonic and dark matter accretion in the EAGLE simulations.* MNRAS, **498**(2) (2020), 1668. 2006.00924.

Zel'dovich, Y.B. *The Fate of a Star and the Evolution of Gravitational Energy Upon Accretion.* Soviet Physics Doklady, **9** (1964), 195.

Zheng, Z., Ofek, E.O., Kulkarni, S.R., et al. *Probing the Intergalactic Medium with Fast Radio Bursts.* ApJ, **797**(1) (2014), 71. 1409.3244.

Zwicky, F. *Die Rotverschiebung von extragalaktischen Nebeln.* Helvetica Physica Acta, **6** (1933), 110.